

**Investigation and Propagation of Defects in the
Membrane Electrode Assembly of Polymer Electrolyte
Membrane Fuel Cells: Quality Control Analysis**

by

Arkhat Muneendra Prasad

A thesis

presented to the University of Waterloo

in fulfillment of the

thesis requirements for the degree of

Doctor of Philosophy

in

Chemical Engineering

Waterloo, Ontario, Canada, 2019

©Arkhat Muneendra Prasad 2019

Examining Committee Membership

The following served on the examining committee for this thesis. The decision of the examining committee is by majority vote.

External Examiner	Professor Brant Peppley Chemical Engineering, Queen's University
Supervisor	Professor Mark Pritzker Chemical Engineering, University of Waterloo
Internal Member	Professor Michael Fowler Chemical Engineering, University of Waterloo
Internal Member	Professor Boxing Zhao Chemical Engineering, University of Waterloo
Internal-external Member	Professor Roydon Fraser Mechanical and Mechatronics Engineering, University of Waterloo

AUTHOR'S DECLARATION

This thesis consist of materials all of which I authored or co-authored: see Statement of Contributions included in the thesis. This is a true copy of the thesis, including any required final revisions, as accepted by my examiners.

I understand that my thesis may be made electronically available to the public.

Statement of Contributions

In Chapter 4, the author was responsible for developing the custom-design transparent single cell, conducting the non-destructive catalyst-coated membrane (CCM) analysis, carrying out infrared (IR) thermal analysis, preparing the results, graphs and manuscript. Co-op undergraduate students Jonathan Lepine, Kelly Zheng and Jake McGrory helped in stack assembly and setting up the experiments.

In Chapter 5, the author was responsible for developing the non-destructive catalyst layer defect analysis, conducting all experiments, preparing the results and graphs. while undergraduate Co-op students Kelly Zheng and Kelly Huang helped implement the MATLAB code for image processing and image stitching for CCM analysis.

In Chapter 6, the author was responsible for developing RH cycling set-up coupled with G-50 fuel cell test station, conducting all *in-situ* and *ex-situ* experimental analysis, preparing the results, and graphs while undergraduate Co-op students Aditi Sharma and Brandon Wong assisted in conducting some of the experiments.

Finally, in Chapter 7, the author was responsible for developing the vacuum stage IR set-up for detecting defects in gas diffusion layers (GDL) as a non-destructive tool, conducting aging experiments and quantifying defect propagation in GDL electrodes, preparing the results and graphs. while undergraduate Co-op students Zi Qi Chen and Haocheng Zhang assisted in conducting some experiments.

Abstract

Polymer electrolyte membrane fuel cells (PEMFC) have the potential to deliver high power density with a lower weight and volume compared to other fuel cells. However, some of the barriers to the successful commercialization of PEMFCs include problems associated with durability, stability and cost. Fuel cell defects that arise and propagate in the membrane electrode assembly (MEA) components during manufacturing and subsequent operation are the biggest factors limiting their durability and stability, leading to shortened lifetimes, reduced performance or cell failure. Defects in the production line must be minimized if PEMFCs are to become reliable electrochemical energy devices on a commercial scale.

A conventional PEMFC electrode consists of layers (CL) of nanoscale Pt catalyst particles mixed with an ionomer on a high surface area carbon support deposited on the polymer electrolyte membrane (PEM) and sandwiched between gas diffusion media (GDM). The defects in these components originate from the raw materials used in the catalyst layers, process conditions during catalyst mixing, coating techniques, drying process, thickness variations in the casting substrate and the temperature and humidity of the processing environment. These defects can lead to reduced performance and can increase fuel cell degradation, specifically in the MEA components. Understanding the MEA component defects that affect fuel cell performance and lifetime is integral to the successful development of an on-line quality control strategy.

Previous research studies have been conducted on defects in catalyst-coated membranes (CCMs) and gas diffusion layers (GDLs) with various dimensions that have been introduced artificially at specific locations, which does not satisfactorily mimic the situation with real manufacturing defects. Very few studies on real defects have been reported to date with limited work on localized effects on CL defects such as loss of catalyst, the morphology of defect growth or the effect of defect location within the CCM on the resulting cell performance. This has limited our fundamental and comprehensive understanding of the nature of defects in the beginning-of-life (BOL) state and the manner in which they may or may not propagate during PEMFC operation. The focus of this research is to analyze real catalyst layer defects and membrane pinholes on commercial CCMs that are developed during mass production.

Specifically, the objectives of this study are to: (i) develop a non-destructive method to identify and quantify defects in CCM electrodes, (ii) implement a defect analysis framework to age CCMs using open-circuit voltage(OCV)- accelerated stress tests (AST), (iii) characterize the

electrochemical performance of CCM/MEAs with varying extent of manufacturing defects (catalyst layer thickness, degree of catalyst non-uniformity) and compare this to a baseline, defect-free CCM/MEA using ASTs as well as *in-situ* and *ex-situ* methods and (iv) investigate defects on GDL-microporous layer (MPL) using infrared (IR) imaging and surface conductivity measurements.

The first set of quality control experiments were performed on CCMs by using optical microscopy to characterize catalyst layer defects. Defects such as micro/macro cracks, catalyst clusters, missing catalyst layer defects (MCLDs), void/empty areas, CL delamination and pinholes in the CCM were characterized in terms of areal dimension (size, shape, and orientation) prior to electrochemical analysis. The OCV-AST protocol was developed to age defected CCMs in a custom-designed test cell and track defect propagation and behavior during aging. The geometric features of the defects were quantified and their growth measured at regular time intervals from beginning-of-life (BOL) to end-of-life (EOL) until the OCV had dropped by 20% from its initial value (as per the DOE-designed protocol). Overall, two types of degradation were observed: surface degradation caused by catalyst erosion and crack degradation caused by membrane mechanical deformation. Furthermore, the catalyst layer defects formed during the decal transfer process exhibited a higher growth rate at middle-of-life (MOL-1) before stabilizing by EOL. The results of the crack propagation analysis during AST showed that the defected area covered under cracks increased from 2.4% of the total CL area at BOL to 10.5% by EOL with a voltage degradation rate of 2.55mV/hr. This type of analysis should provide manufacturers with baseline information that will allow them to select and reject CCMs, increasing the lifetime of fuel cell stacks.

Once the CCM defects were analyzed comprehensively, research was carried out on the MEA stack. MEAs containing defected CCMs (incomplete catalyst layer defects-MCLD), pinhole across sealant and artificial pinholes at inlet/middle/outlet were investigated using a cyclic open-circuit voltage (COCV)-AST. Different RH cycling periods from 80% RH to 20% RH with time delays from 5 mins to 30 mins were applied to the cathode to study the propagation of defects and their effect on overall cell performance. *In-situ* analysis included the measurement of polarization curves, linear sweep voltammetry (LSV) and electrochemical impedance spectroscopy (EIS) to measure electrode degradation. Non-destructive *ex-situ* analysis using IR thermography was conducted every 100 cycles to monitor the evolution of defects in the MEA. The growth of

pinholes was studied on the basis on hydrogen crossover curves. Sealing defects were found to have a major impact on performance loss compared to catalyst layer defects. It was also observed that MCLDs degraded within a short period of time and developed pinholes although the extent of this degradation depended on defect thickness. The MCLD defects were unstable and observed to continually grow due to gradual loss of catalyst particles inside the defected areas that accelerated pinhole formation in CCMs. This effect was clearly reflected in the continuous decay of OCV during the fuel cell operation. Therefore, CCMs leaving the production line with missing and /or thin portions of CL are not recommended for MEA fabrication as they ultimately affect the long-term stability of PEMFC.

The last set of quality control experiments was conducted on GDL-MPL defects in samples that were being aged by RH cycling in a custom-design test cell. Thermal image analysis using IR thermography was carried out by passing DC current through the GDL sheet mounted on a porous vacuum stage to identify hot and cold spots reflecting defective areas. The morphological features and surface conductivity of MPL cracks were characterized using optical microscopy and four-point probe conductivity measurements. Interestingly, the nature of defects/cracks propagation in the GDL-MPL was found to affect cell performance in the mass transfer region at high currents. Crack propagation in GDL-MPL increased mass transport losses due to water flooding on the cathode, which was clearly observed in the polarization curves.

Finally, the overall effects of catalyst layer defects, membrane pinholes and GDL defects on cell performance were compared. MEA sealant defects (pinholes) had such a negative effect on cell performance that EOL was reached after only ~ 50 hours of COCV operation at 80% - 20% RH cycling. Thus, the detection of such a defect in a CCM should be sufficient cause to reject it for use in a commercial stack. We also observed that CCMs with defects that led to 70% reduced thickness of the CL failed faster than those with the same type of defects that had resulted in 30% reduced thickness of the CL, presumably due to less available catalyst for electrochemical reactions. Clearly, CL defects should be given high priority in quality control inspection strategies devised by CCM electrode manufacturers and PEMFC operators.

Acknowledgements

*“Guru Brahma: Guru Vishnu: / Guru Devo Maheshwaraha: /
Guru Saakshat Para Brahma: / Tasmai Sree Gurave Namaha: ||”*

According to Hindu mythology, this holy Sanskrit verse says:

Guru (guide/professor/supervisor) is Creator (*Brahma*), Donor (*Vishnu*), Protector (*Maheshwara*) and the ultimate person (*Para brahma*). He creates, sustains knowledge and destroys the weeds of ignorance. Hence, I felicitate (*namaha*) him.

I take this rare opportunity to express my deep sense of gratitude to my supervisor Dr. Mark Pritzker the great mentor and great professor who have taught me an important aspect of life: “goodness can never be defied, and good human beings can never be denied”. He has been tremendous with free-hearted guidance and undying patience for my research work. I have been extremely lucky to have a supervisor with good support, encouragement and care for my research. His valuable feedback on my papers and thesis helped advance my technical knowledge and improve my learning skills. Without him, this research would never have been possible. From the bottom of my heart, I sincerely thank my supervisor Dr. Mark Pritzker and will be indebted for the rest of my life.

In addition, ‘thanks’ is too small a word to express my sincere gratitude to Dr. Michael Fowler for his invaluable suggestions and guidance in critical thinking, as well as teaching me how to approach any challenge with courage and determination. I greatly admire his vision and understanding on my research struggles. His continuous support helping me with co-op students has given me an opportunity to strengthen my leadership skills and improve my patience during my research study. He is a great inspiration for me on both research level as well as a professional level.

I acknowledge my heartfelt thanks to Dr. Jeff Gostick, who supervised me for the GDL quality control research. His motivation and trust have been very helpful in gaining a scientific mindset

and raising the bar on the quality of my work. It has been a pleasure and a privilege working with him.

I also express my sincere thanks to my committee members Dr. Brand Peppley, Dr. Rayon Fraser and Dr. Boxin Zhao for their valuable suggestions during my research as well as the kind cooperation in providing thermal camera and four-point probe instruments for my research work.

Furthermore, I would like to thank my industrial associates, Dr. Sumit Kundu, Dennis Sun and Francine Berretta from Automotive Fuel Cell Cooperation (AFCC) and Alex Quing Ni from Hydrogenics for their cooperation and technical support during my PhD program. Our samples were provided through collaborations with AFCC and the University of Waterloo. I acknowledge the financial support from the Natural Sciences and Engineering Research Council of Canada (NSERC), Toyota Canada Automotive Safety Graduate Scholarship and AFCC, Burnaby, Canada.

I would like to thank all the co-op students: Rob Koller, Jonathan Lepine, Jordan Alves, Kelly Zheng, Kelly Huang, Jack McGrory, Zi Qi Chen, Murtaza, Aditi Sharma, Christoph Hass, Haocheng, Brandon Wong and Phillip Pattison. Their assistance and cooperation have been extremely valuable to this work. I would also like to make a special thanks to Jennifer Moll, who illuminated my teaching potential during my time as a lab TA and offered me the use of optical microscopes whenever it was needed for my research. Her encouraging words lead me to become one of the best TA's in 2017. I also wish to thank the staff of the Department of Chemical Engineering, especially Judy Caron and Rose Guderian, for their constant support during my stay at Waterloo.

Friendship is a golden chain, each link forged of memories and friends so dear. The unforgettable moments become the gold links that I will treasure in my heart forever. I will treasure great memories of my friend, Manoj Mathew, who always had a helping hand in sharing ideas and instruments in the fuel cell lab. It has been a pleasure working with such a great and wonderful friend who always leaves with a beautiful saying: "let me know if you need any help". I would also like to thank Lathankan, Ushnik, Sannan, Ariful (Anna!), Manan, Tharun, Piyush (Raja!), Lokesh, Mohammad Farkhondeh, Zhiyu Mao, Zachary Cano, Qing Hao Kong (John), Meharam,

Shashi and Mahad Hassan. I would like to thank my senior research partners in the lab, Shankar Raman Dhanushkodi and Satyam Panchal, for being supportive throughout my time here and for helping me as if they were my elder brothers. I express my thanks to my office mates, Yiyi Yang, Kiana Amini, Jing Fu, Pouyan Zamani and Timothy, for making my stay in the University of Waterloo a memorable one. Special thanks are extended to the moral support and ever caring nature of my Indian friends: K.D.V.Prasad, V.V.L.Kishan, Ravi Krishna, Nara Siva Kumar, Sravan, Koushik, Satish, Chaithanya Prasad, Bhanu Prasad, Santosh and Vikas Bommerla. They were always beside me during the happy and hard moments.

I would like to express my special thanks to master's supervisor Dr. A.Nirmala Grace, Professor and director, Centre of Nanotechnology Research, VIT University who is greatly inspirational and motivation for my PhD. I would also thank Dr. G.Velayutham from Sainergy Fuel Cell India Pvt Ltd for giving me an opportunity to start my carrier in PEM Fuel Cells and Jayachandran from IIT Madras who trained me in Fuel Cell Materials.

Every effort is motivated by ambition and all ambitious have an inspiration behind. I owe this place to the dearest person Dr. Bharathi who inspired and motivated me to keep things in perspective. I greatly value her contribution and deeply appreciate her encouragement. Words would never say how grateful your memories are and I thank the Almighty for having your presence in my life.

Saving the best for the last, all of my gratefulness goes to my parents, Arcot Krishna Reddy and Arcot Saraswathi, as well as my sister Muni Lakshmi for showing faith in me and giving me liberty to choose what I desired. I salute my family for the selfless love, care, pain and sacrifice that they have given in order to shape my life. I would never be able to pay back the love and affection showered upon me by my parents. My heart-felt regards goes to my cousins, Vara Lakshmi, Suman, Anitha, Draksha and Sai, for their love and affection. I finally thank God for everything that has been given to me.

*I Dedicate This Thesis to My Beloved Parents,
My sister, Dr. Michael Fowler and
My supervisor Dr. Mark Pritzker*



Table of Contents

Abstract.....	V
Acknowledgements	VIII
List of Figures.....	XVIII
List of Tables	XXIV
List of Abbreviation.....	XXV
1 Introduction.....	1
1.1 Overview.....	1
1.1.1 Definition of MEA component defects.....	2
1.1.2 Defect identification in the CCM and GDL.....	3
1.2 Motivation.....	4
1.2.1 Scope of defect analysis.....	5
1.3 Research Objectives.....	5
1.4 Thesis Outline	6
2 Background and Literature Review.....	9
2.1 Fuel Cell Technology.....	9
2.2 Performance of PEM Fuel Cells	11
2.3 Components of PEM fuel cells	13
2.3.1 Catalyst Layer (CL)	13
2.3.2 Polymer Electrolyte Membrane (PEM)	13
2.3.3 Gas Diffusion Layer (GDL).....	15
2.3.4 Micro-Porous Layer (MPL)	15
2.3.5 Bipolar Plate (BPP).....	15
2.4 Method of fabricating MEA.....	16
2.4.1 Fabrication of CCM using decal transfer method.....	17
2.5 Sources of defect formation in MEA electrodes.....	18
2.5.1 Manufacturing Defects.....	19
2.5.2 Operational Aging Defects	20
2.5.2.1 Formation of defects via degradation mechanism in MEA	22

2.5.2.1.1	Chemical/electrochemical degradation	23
2.5.2.1.2	Mechanical and thermal degradation	25
2.6	Durability problems for PEMFC stacks in automotive operation	26
2.6.1	Effect of local degradation of MEA components in automotive environments	27
2.6.2	Sources of mechanical stresses in PEMFC stack.....	28
2.7	Categorization of local defects in MEA components	29
2.8	Summary.....	33
3	Materials and Experimental Methods	34
3.1	Fuel Cell Test Station Apparatus	34
3.1.1	Leak test.....	35
3.1.2	Fuel cell operating conditions.....	35
3.1.3	Accelerated stress tests (AST)	36
3.2	MEA Characterization techniques	37
3.2.1	<i>In-situ</i> characterization: electrochemical analysis	38
3.2.1.1	Open-circuit voltage AST.....	38
3.2.1.1.1	Effect of OCV at constant low RH.....	38
3.2.1.1.2	Effect of OCV at cyclic RH	39
3.2.1.2	Polarization analysis	40
3.2.1.3	Linear sweep voltammetry - H ₂ crossover	41
3.2.1.4	Electrochemical impedance spectroscopy (EIS).....	41
3.2.1.5	ECSA measurement using cyclic voltammetry (CV).....	43
3.2.1.6	Ion chromatography	43
3.2.2	<i>Ex-situ</i> characterization.....	44
3.2.2.1	Non-destructive methods	44
3.2.2.1.1	Optical microscopy	44
3.2.2.1.2	IR thermography for inspection of MEA components.....	45
3.2.2.1.2.1	IR examination of MEA defects.....	45
3.2.2.1.2.2	IR examination of GDL defects	45
3.2.2.1.3	Electrical measurements.....	46
3.2.2.2	Destructive methods.....	47

3.2.2.2.1	Scanning electron microscopy	47
3.2.2.2.2	X-ray tomography analysis	48
4	Non-Destructive Method of Investigating Catalyst Layer Defects in CCM.....	49
4.1	Introduction.....	49
4.2	Research Framework	52
4.3	Experimental.....	52
4.3.1	CCMs for defect investigation.....	52
4.3.2	Microscopic inspection of CL defects in CCM	53
4.3.3	IR thermography characterization.....	55
4.3.4	Design of custom-built test cell	55
4.3.4.1	Custom-built test cell for OCV analysis	56
4.3.5	Operational aging of the CCM.....	57
4.3.6	Accelerated stress test (AST).....	58
4.4	Results and Discussion	59
4.4.1	Characterization tools	59
4.4.1.1	CCM examination using optical microscopy.....	59
4.4.1.2	Detection of MEA defects by IR thermography	61
4.4.2	Investigation of defects in CCMs	63
4.4.2.1	Identification of defects (CL micro-cracks) in BOL-LTS reinforced CCMs ...	63
4.4.2.2	Propagation of defects (CL macro-cracks) in EOL-LST reinforced CCM.....	64
4.4.2.3	Comparison of defects in BOL-LST and EOL-LST samples.....	66
4.4.3	Defects in non-reinforced CCM at BOL.....	69
4.4.3.1	Electrode pores and scratches	69
4.4.3.2	Defect (missing/thin CL) caused by improper decal transfer of catalyst.....	71
4.4.3.3	Propagation of defects in EOLP	73
4.4.4	OCV analysis of defective CCMs.....	74
4.4.5	Classification of Defects.....	75
4.5	Conclusions.....	76
5	Characterization of Catalyst Layer Defects in CCM and Resulting Cell Performance	78
5.1	Introduction.....	78

5.2	Research Framework	80
5.3	MCLD defect analysis framework.....	80
5.3.1	Test protocol for non-destructive CCM defect analysis	82
5.4	Results and Discussion	85
5.4.1	Microscopic investigation of CCM defects and image processing.....	85
5.4.2	OCV analysis of initially defective CCMs	87
5.4.3	Degradation of catalyst layer defect – MCLD	89
5.4.3.1	Propagation of manufacturing defect - MCLD of CCM-1	90
5.4.3.2	Propagation of manufacturing defects - MCLD of CCM-2.....	93
5.4.3.3	Degradation mechanism of catalyst layer defects.....	95
5.4.3.3.1	Surface degradation (chemical) of catalyst layer defects	95
5.4.3.3.1.1	Catalyst erosion	97
5.4.3.3.1.2	Effect of ionomer leaching in catalyst layer.....	100
5.4.3.3.2	Crack degradation (mechanical) of catalyst layer	100
5.4.4	IR investigation of MCLD propagation.....	104
5.5	Conclusions.....	105
6	Effect of RH AST on Manufacturing Defects: Catalyst Layer Defects and Sealant Interface Defects in PEMFC Electrode.....	107
6.1	Introduction.....	107
6.2	Research Framework	110
6.3	Test Procedure	110
6.4	OCV-hold diagnostic test at low RH	113
6.4.1	Performance of MEA-1.....	117
6.4.2	Performance of MEA - 3.....	121
6.4.3	Performance of MEA - 4.....	125
6.4.4	Performance of MEA – 5.....	130
6.5	COCV diagnostic test during RH cycling.....	134
6.5.1	Performance of MEA-2.....	138
6.5.2	Performance of MEA-6.....	141
6.5.3	Effect of RH cycling on catalyst layer defects.....	145

6.5.4	Performance of MEA-7 and MEA-8.....	146
6.6	Effect of constant and cyclic RH on membrane degradation observed by fluorine emission analysis	152
6.7	Effect of constant and cyclic RH on CCM observed by SEM.....	153
6.8	Conclusions.....	154
7	Defect Analysis in Gas Diffusion Layers (GDL): Quality Control Approach.....	156
7.1	Introduction.....	156
7.1.1	Fabrication of GDL/MPL substrates.....	157
7.2	Research Framework	160
7.2.1	Objective of GDL defect analysis.....	160
7.3	IR Examination of GDL Defects	161
7.3.1	Experimental set-up: DC excitation using vacuum stage	161
7.4	MPL Crack Analysis.....	166
7.4.1	Implementation of AST	167
7.4.2	Microscopic investigation of MPL cracks	168
7.4.3	Effects of crack propagation in MPL.....	174
7.4.4	Effect of GDL degradation on polarization performance	176
7.5	Electrical Characteristics of GDL/MPL Substrates	177
7.5.1	In-plane electrical measurements.....	178
7.6	Conclusions.....	179
8	Conclusions and Recommendations.....	181
8.1	Conclusions.....	181
8.2	Contributions to MEA quality control development	184
8.3	Recommendations for future work	185
8.3.1	Catalyst layer development.....	185
8.3.2	GDL-MPL development	186
9	References.....	187
10	Appendix.....	202
10.1	Leak test.....	202
10.2	MATLAB for Image Stitching:	203

10.3	IR thermography of catalyst layer defects: CCM-2	205
10.4	COCV decay curves.....	205
10.5	Overview of defect locations in CCM- CCL	206
10.6	Scratch/deep cuts in catalyst layer – CCL	206
10.7	IR thermography set-up for GDL defect detection	207
10.8	X-ray tomography of GDL-MPL substrates	207

List of Figures

Figure 1-1: Various defects observed in CCM/MEA components during the fabrication process.	3
Figure 1-2: Outline of thesis results organized for chapter 4,5,6 and 7.....	7
Figure 2-1: (a) Various components of PEMFC stack in a fuel cell vehicle [27]; (b) cross-section of a single-cell PEMFC consisting of BPP, GDL, MPL, CL and PEM.....	9
Figure 2-2: Schematic of polarization curve indicating the major cell voltage losses: mixed potential/open circuit (η_{ocv}), activation overpotential (η_{act}), ohmic overpotential (η_{ohm}) and concentration overpotential (η_{conc}).	11
Figure 2-3: (a) Cross-sectional view of reinforced membrane [41]. (b) Chemical structure of the Nafion polymer and (c) microscopic structure of Nafion membrane [44].....	14
Figure 2-4: MEA fabrication methods [50].	17
Figure 2-5: Categorization, cause and effect of defects formed in PEMFC components.....	19
Figure 2-6: Percentage of catalyst transfer from decal substrate to polymer membrane, the dotted circles indicate incomplete catalyst transfer leading to void spaces and missing catalyst areas in CCM [59].	20
Figure 2-7: Degradation mechanism of defect formation in MEA components during AST.....	22
Figure 2-8: Oxygen reduction reaction on metals.....	24
Figure 2-9: Schematic illustration of four different mechanisms of hydrogen peroxide formation. ...	25
Figure 2-10: Impact and estimation of losses in PEMFC stacks due to three major electrode degradation modes: start-stop, idling and load cycling[12].	28
Figure 2-11: Categorization of defects based on severity and priority.	29
Figure 2-12: (a) Top and side views of CL showing distribution, length and depth of cracks. (b) Missing catalyst regions/thin catalyst area (manufacturing defects) in CCM; the dark line indicates major cracks in CL due to expansion of membrane. (c) Delamination of CL leaving bare membrane. (d) Membrane thinning. (e) Pt band formation in membrane causing radicals. (f) Mechanism of pinhole formation caused by chemical, mechanical and thermal degradation. Note: (a), (b), and (c) are examples obtained from GORE CCM (Prime series 5510) & AFCC CCMs operated at the University of Waterloo.	32
Figure 3-1: G50 fuel cell test station and ancillary components for PEMFC testing. Refer to the text for identification of the numbered components.	34
Figure 3-2: (a) Equivalent circuit of electrochemical processes occurring in PEMFC. (b) Nyquist plot (EIS) of PEMFC showing how the membrane resistance $R_{\Omega,mem}$, cathode charge transfer resistance $R_{Ct,Ca}$ and cathode mass transfer resistance $R_{mt,Ca}$ are determined. The charge transfer resistance of anode is neglected due to the fast kinetics of the hydrogen oxidation reaction (HOR).	Error!
Bookmark not defined.	
Figure 3-3: (a) Schematic of four-point probe method used to measure the surface resistance of MPL with cracks (b) Schematic of electron flow path across the MPL crack; red region outlines a surface crack.	47

Figure 3-4: (a) Experimental setup of x-ray tomography whereby a detector measures the attenuation of x-rays penetrating through the stack of GDL samples to generate cross-sectional images of the internal structure features of GDL-MPL, as shown in (b). 48

Figure 4-1: Framework for CCM defect analysis followed in this part of study. 52

Figure 4-2: (a) Schematic of reflected light microscopy experimental setup. (b) Reflected microscopy setup for investigating catalyst layer defects in CCMs. 54

Figure 4-3: (a) Cross-sectional view of TSA for CCM analysis, (b) top view of the CCM#1 assembled in TSA device with an active area of $\sim 48 \text{ cm}^2$, (c) microscopic stitched image of CCM#1 operated in TSA device after 85 hours of OCV test. (Hardware and experimental set up was designed at the University of Waterloo). 57

Figure 4-4: (a) Orientation of CCM in test cell jig showing gas flow directions and gasket sealants in contact with the GDLs. (b) Single large stitched image of a reinforced CCM in the BOL state of the cathode. Magnified image of an individual block of the stitched image captured at 5x magnification showing (c) BOL cracks and (d) EOL cracks aged for 40 hours. 60

Figure 4-5: (a) Schematic diagram of the side view of MEA and location of defects in non-reinforced CCM at BOL; (b) thermal image of defected MEA viewed on cathode side (c) temperature profile along the red line shown in Figure 4-5b. Note that 590 pixels along x-axis correspond to a length of 12 cm. 62

Figure 4-6: (a) Optical image (5x magnification) of a portion of reinforced CCM; (b) optical image of enclosed region of macro-crack in (a) at higher magnification (50x); (c) visualization of cracks along the blue line in (a); (d) Z-profile showing depth profile of crack along the blue arrow in (b). 65

Figure 4-7: Section of cracked area selected from Figure 4-4a (spatial resolution of $1.83 \mu\text{m}$ and 5x magnification) to demonstrate the boundaries of cracks, (a) RGB microscopic image, (b) 8-bit (black & white) image, where dark areas indicate cracks and white areas indicate dents, (c) boundaries of cracks corresponding to Figure 4-7b, where crack number 32 represents the larger area ($8570 \mu\text{m}^2$) of the crack. 66

Figure 4-8: (a) Distributions of number of cracks and percentage of the total defect area covered by BOL-LST cracks, (b) distributions of EOL-LST cracks after aging for 40 hours and (c) comparison of BOL and EOL crack distributions. 67

Figure 4-9: Microscopic image of non-reinforced CCM in the BOL state captured at 5x magnification showing (a) electrode pores of various sizes as labeled, (b) comparison of electrode pore distribution (micro- and macro-pores) on pristine CCM, (c) catalyst layer scratch and (d) missing portion of catalyst layer with height/depth profile captured at 50x magnification. 70

Figure 4-10: Optical microscope images of missing catalyst layer due to improper manufacturing viewed from the (a) cathode side and (b) anode side in non-reinforced CCM captured in the BOL state at 5x magnification. Two regions of interest in (a) are shown at 50x magnification in (c) ROI-1 and (d) ROI-2. Scale markers are included on the images. 72

Figure 4-11: (a) Stitched microscopic image of non-reinforced CCM after aging for 40 hours; (b) 3D view (height map) of the portion of the CL indicated with dashed line in (a); (c) magnified image of the defected area showing crack formation and delamination of the CL captured at 50x magnification; (d) Z-profile obtained along the yellow line in Figure 4-11c. 74

Figure 5-1: Research framework on morphological characterization of CCM defects. 80

Figure 5-2: (a) Steps involved in fabrication of CCM/MEA. (b) Schematic showing missing catalyst layer defects (MCLD) in the CCM fabricated using the decal transfer method. 81

Figure 5-3: Non-destructive CCM defect analysis framework combined with electrochemical analysis. 82

Figure 5-4: Stitched optical microscopic image of CCL of defected (a) CCM-1 showing 1 MCLD observed after (a) 10 hours (MOL-1) and (b) 100 hours of OCV-AST (EOL); regions ROI-1 and ROI-2 are specifically selected for further investigation of crack propagation and delamination of CL. (c) CCM-2 showing 2 MCLDs (Defect-1 and Defect-2) 86

Figure 5-5: OCV test results of CCM-1, CCM-3 and CCM-baseline operated in the test cell over a duration of 100 hours. The green curve represents the OCV decay curve of CCM-2 which was operated for only 25 hours due to pinhole formation inside the MCLD defect..... 88

Figure 5-6: Microscopic images of defect growth in an MCLD in a defected CCM-1 (a) BOL at 0 hours, (b) MOL-1 after 10 hours OCV-AST, (c) MOL-2 after 50 hours OCV-AST, (d) EOL after 100 hours OCV-AST, (e) 3D graphical view of MCLD with active area of $757016 \mu\text{m}^2$ on CCL (f) cross-sectional view of MCLD showing dimensions of depth and (g) schematic view of MCLD in CCL across the CCM-1. 90

Figure 5-7: (a) Areal growth of MCLD in CCM-1 (black curve represents the total area of MCLD (triangular area) and pink curve represents the degraded catalyst area inside MCLD), (b) fluoride emission rate (FER) at the cathode over the course of 100-hour OCV-AST and areal growth of MCLD in (c) defect-1 and (d) defect-2 of CCM-2..... 93

Figure 5-8: Microscopic image of defect growth of MCLD in CCM-2 (see the location of defect in Figure 5-4c): defect -1 on cathode captured at (a) 0, (b) 12 and (c) 25 hours; defect-2 on anode at (d) 0, (e) 12 and (f) 25 hours of OCV AST. 93

Figure 5-9: (a)Microscopic image of catalyst layer defect (zero catalyst area/bare membrane) selected from defect-2 in Figure 5-8f (ROI-1) showing surface view of bare membrane, where catalyst dissolution into polymer matrix in the bare membrane; (b) membrane cracks/tears (region-1) and pinhole (region-2) in the bare membrane. Plots in red below (b) and (c) correspond to Z-profiles along the blue arrows in microscopic images. 95

Figure 5-10: (a) Reflected microscope image of MCLD at MOL-2 indicating selected regions ROI-3 and ROI-4; (b) transmitted light microscope image of MCLD with pink area indicating degraded catalyst due to chemical degradation during fuel cell operation; 3D microscopic visualizations of enlarged regions (c) ROI-3 and (e) ROI-4; (d) Z-profile/height profile showing variation in thickness of degraded catalyst layer surface at ROI-3 along the red line in Figure 5-10c; (f) colour mapping of morphological features of degraded catalyst layer at ROI-4: blue represents thinnest catalyst, green represents uneven surface of degraded catalyst layer, orange represents non-degraded catalyst layer. 96

Figure 5-11: Schematic showing the possible ways that defects in the cathode layer can propagate via chemical and mechanical degradation and eventually lead to gas crossover through pinholes..... 99

Figure 5-12: Microscopic images of crack propagation on the CCLs at EOL: (a) delaminated catalyst layer at ROI-2, (b) multiple crack propagation at ROI-1; the pink area in the image represents the thinnest region, (c) 3D enlarged view of delaminated and degraded catalyst layer at ROI-5 and (d) color mapping of delaminated area at ROI-5 showing catalyst layer pores. 102

Figure 5-13: IR thermographic response of CCM containing a MCLD at (a) BOL, (b) MOL-2 and (c) EOL (after polarization analysis). (d) Surface temperature profiles along the dashed arrow line indicated in (a) and (b).....	105
Figure 6-1: Modes of degradation in MEA operated under constant-low RH and RH cycling during OCV causing defects in PEMFC electrode.....	109
Figure 6-2: Framework for MEA analysis followed in this part of study.....	110
Figure 6-3: Experimental AST protocol for MEA degradation analysis.....	110
Figure 6-4: Schematic of various RH cycles used during electrode/stack conditioning (blue-100%RH), steady-state OCV (green-30%RH) and RH cycling (red – 80% - 20% RH).	112
Figure 6-5: OCV degradation curves of defected and non-defected MEAs: (a) MEA-1 baseline (no defects) (b) MEA-3, 1 intentional pinhole introduced at 70 hours (c) MEA-4, 2-MCLD in CCL as shown in Figure 5-4c. (d) MEA-5, 1 scratch defect.....	114
Figure 6-6: Analysis of the OCV curve for MEA-1 during the first period (MOL-1) to differentiate the reversible and irreversible losses. The irreversible voltage loss is indicated in green (A to C) and the reversible loss in red (B to C).	116
Figure 6-7: MEA-1 performance: (a) breakdown of irreversible (blue), reversible (orange) and total (green) OCV decay rates during the AST, (b) polarization curves and (c) H ₂ crossover current measured at different points during the AST. (d) Schematic of voltage recording from total cell and across pinhole/defect region.	118
Figure 6-8: MEA-1 (a) Schematic of sealant/gasket/CCM/GDL interface defects in MEA (i) BOL initiation of defects across sealant (orange circles) interface area (ii) MOL propagation of defects (radicals/H ₂ O ₂ generation) (iii) EOL pinhole formation (H ₂ /O ₂ crossover); IR image of MEA-1 captured at (b) MOL-2 and (c) EOL. (d) Digital image of MEA-1 captured after EOL; magnified image shows burned area of MEA due to H ₂ /O ₂ combustion and calcium contaminant precipitated on the GDL (white).....	120
Figure 6-9: MEA-3 IR examination at (a) BOL, (b) MOL-4 and (c) EOL; (d) SEM image of artificial pinhole (~90µm) in CCM formed using a micro-needle and; (e) variation of H ₂ crossover current density during the course of aging.	122
Figure 6-10: MEA-3 performance: (a) breakdown of irreversible (blue), reversible (orange) and total (green) OCV decay rates during the AST; (b) polarization curves obtained during the AST; red arrow indicates the drop in OCV after artificial pinhole is introduced, the black dashed circle shows the voltage difference between total cell voltage (blue curve) and voltage drop across pinhole region (green curve) the schematic of voltage measuring points is shown in Figure 6-7d (c) EIS spectra and (d) polarization curves across artificial pinhole region at various RHs.....	123
Figure 6-11: MEA-4 (a) Schematic of chemical and mechanical stress on catalyst layer defect (zero catalyst area/bare membrane – cross sectional view) in CCM causing defect to develop into cracks and pinholes; (b) Microscopic image of degraded catalyst layer defect (MCLD), showing the surface view of bare membrane/zero catalyst area, the white dots inside the red dotted circle represents the dissolution Pt-particles from the catalyst layer in to the membrane during the OCV AST; (c) represents the 3D view of color mapping of defect in Figure (b), where orange represents the catalyst layer, green represents the bare membrane and purple represents the degraded area in the membrane developing into micro-pinholes. (d) Z-profile along the blue arrow in Figure (a), (e) degraded areas in the membrane developing into micro-pinholes. (f) 3D view of image in Figure (e).	127

Figure 6-12: MEA-4 performance: (a) breakdown of irreversible (blue), reversible (orange) and total (green) OCV decay rates during the AST; (b) polarization curves obtained during the AST; red dotted area indicates the difference in the ohmic portion of curves. (c) H₂ crossover currents and (d) Nyquist EIS plots during the course of aging. 129

Figure 6-13: MEA-5 (a) Optical image showing scratches on the catalyst layer; the dotted circle area indicates a deep cut, while the dark line denotes a surface scratch; (b) Z-profile across the blue arrow in (a) showing a deep scratch with depth of 4 μm; (c) layout of MEA-5 showing location of defect in CCM; IR images of MEA-5 at BOL (d) and EOL (e) showing two pinholes 1 and 2. 131

Figure 6-14: MEA-5 performance: (a) breakdown of irreversible (blue), reversible (orange) and total (green) OCV decay rates during the AST; (b) polarization curves, (c) H₂ crossover currents and (d) Nyquist EIS plots (@ 100 mA cm⁻²) obtained during aging. 133

Figure 6-15: RH cycle waveform (black) and OCV response (red) of MEA-2 (baseline) during AST. 135

Figure 6-16: Comparison of (a) membrane resistance R_Ω obtained from EIS; (b) EIS spectra obtained at 80% and 20% RH; (c) performance loss with respect to RH time delay and; (d) comparison of COCV curves from BOL to EOL, showing the effect of extended dry operation on steady decrease in OCV. 136

Figure 6-17: OCV decay curves isolated from the COCV curves shown in Figure 6-15 during the course of RH cycling AST; black line represents the voltage response at 80% RH, red line represents the voltage response at 20% RH. 138

Figure 6-18: MEA-2 performance: (a) breakdown of irreversible (blue), reversible (orange) and total (green) OCV decay rates during the AST; (b) polarization curves, (c) H₂ crossover currents and (d) Nyquist EIS plots (@ 100 mA cm⁻²) obtained during aging. 139

Figure 6-19: MEA-2 IR thermographs captured at (a) 74, (b) 130 and (c)157 hrs of AST. 141

Figure 6-20: MEA-6 performance: (a) breakdown of irreversible (blue), reversible (orange) and total (green) OCV decay rates during the AST; (b) polarization curves, (c) H₂ crossover currents and (d) Nyquist EIS plots (@ 100 mA cm⁻²) obtained during aging. 143

Figure 6-21: MEA-6 IR investigation captured at (a) BOL (b) MOL-1 and (c) EOL. IR thermographs of MEA-6 captured at (a) prior to COCV test, (b) after 96 RH cycles (32 hrs) and (c) after 162 RH cycles (54 hrs of AST). 144

Figure 6-22: MEA-6 - Optical images of MCLD at (a) BOL, (b) after 100 hrs of OCV at 60°C and 100%RH, (c) after 54 hrs of COCV at 90°C (162 RH cycles) (d) schematic of MCLD during OCV and COCV ASTs. 145

Figure 6-23: MEA-7 (a) Graphical view of catalyst layer defect(MCLD) located in CCL in CCM, (b) optical image of MCLD, (c) edge of MCLD (dashed region in (b)) magnified at 50X resolution and (d) Z-profile along the blue arrow in (c) showing the depth of the defect. 147

Figure 6-24: MEA-7 performance: (a) breakdown of irreversible (blue), reversible (orange) and total (green) OCV decay rates during the AST; (b) polarization curves, (c) H₂ crossover currents and (d) Nyquist EIS plots (@ 100 mA cm⁻²) obtained during aging. 148

Figure 6-25: MEA-8 performance: (a) breakdown of irreversible (blue), reversible (orange) and total (green) OCV decay rates during the AST; (b) polarization curves, (c) H₂ crossover currents and (d) Nyquist EIS plots (@ 100 mA cm⁻²) obtained during aging. 151

Figure 6-26: MEA-8 (a) Optical image of catalyst layer defect; IR images of MEA-8 at (a) MOL-1 – 50 hours, (b) MOL-2 – 100 hours and (c) EOL- 110 hours.....	152
Figure 6-27: (a) Cumulative fluoride ion release for MEA operated under constant low RH and cyclic RH (b) Comparison of irreversible voltage decay rate of MEA-1 and MEA-2 operated under OCV and COCV-AST.....	152
Figure 6-28: Cross sectional view of (a) CCM at BOL; (b) CCM (MEA-4) operated under constant low RH for 75 hours of OCV-AST (white dotted circle indicates micro-hole in cathode ionomer developed at end of catalyst layer crack); CCM (MEA-2) operated at cyclic RH (80% -20%) for 150 hours of COCV-AST shown at two magnifications (c) and (d).....	Error! Bookmark not defined.
Figure 7-1: Steps used to fabricate the GDL and MPL. The red dotted area indicates steps where defects/cracks in the MPL can develop.....	158
Figure 7-2: Framework for research on GDL quality control in this chapter.	160
Figure 7-3: (a) Schematic of experimental setup designed with vacuum stage for IR investigation of GDL defects. (b, c) Digital images of GDL showing defects 1-7 within the active area of 12 cm x 4 cm. Table 7-1 lists dimensions of defects shown in figures b and c.....	162
Figure 7-4: IR images of defected GDLs: (a) and (c) are captured without a vacuum, (b) and (d) are captured with a vacuum.	164
Figure 7-5: IR image of GDL showing defects D-5 to D-7. (b) Temperature line profile across the defects shown in Figure 7-5a.	165
Figure 7-6: (a) Schematic of custom-design test cell for RH cycling AST. (b) Digital image of test cell connected to fuel cell test station. Images of GDL surface when operating cell under (c) 0% and (d) 80% RH.....	168
Figure 7-7: Microscopic images of MPL surface at BOL showing (a) deep cracks (through-plane crack) (b) surface cracks (in-plane cracks) (c) SEM image of MPL surface cracks (d) SEM image of interlayer inside the crack.	170
Figure 7-8: Stitched image of MPL surface: (a) fresh MPL surface covered with surface cracks and carbon clusters, (b) aged MPL surface after AST-2, (c) frequency distribution of the number of cracks according to crack area and (d) frequency distribution of the area covered by cracks according to crack area.	172
Figure 7-9: (a) Microscopic image of cracked MPL surface under channel and land regions. (b) Schematic of crack propagation in the MPL during typical PEMFC operation under RH cycling...	174
Figure 7-10: (a) Schematic of MEA showing cracks in MPL that lead to interfacial gaps between the CCM and catalyst layer. (b) Schematic of in-plane and through-plane cracks causing diffusion barriers for gas and electron transport to the catalyst layer.....	175
Figure 7-11: (a) Polarization and power density curves of fresh and aged GDLs. (b) EIS curves obtained at low current (5 A) and (c) high current (60 A).....	176
Figure 7-12: (a) Schematic of MPL surface (top view) divided into 10 regions or slots for in-plane resistance measurements, (b) In-plane resistance measurements obtained in the 10 slots using the four-point probe, the red arrows indicate the resistance at inlet and outlet.	178
Figure 8-1: Defect chart summarizing the impacts of various defects in MEA components on overall cell performance and life-time as determined in this study.	184

List of Tables

Table 2-1: Different types of local defects formed in MEA components.	31
Table 2-2: Currently available methods to detect defects in PEMFC components.	32
Table 3-1: Operating conditions for MEA conditioning at BOL.	36
Table 3-2: Protocols of MEA degradation ASTs used in this study.	40
Table 4-1: Experimental conditions of AST, IR imaging and OCV test.	59
Table 4-2: Comparison of BOL-LTS and EOL-LTS cracks in reinforced CCM.	68
Table 4-3: Classification of CCM Defects.	76
Table 5-1: Summary of CCMs investigated in this chapter.	84
Table 5-2: Average width of cracks in the CCL of CCM-1 formed during OCV-AST.	101
Table 6-1: Summary of MEAs used in this chapter.	112
Table 6-2: Description of overall test analysis and samples used for OCV hold test.	113
Table 6-3: OCV and H ₂ crossover current density at different stages during the AST.	119
Table 6-4: OCV, H ₂ crossover current density, HFR and LFR of MEA-3 during course of AST. ...	125
Table 6-5: OCV, H ₂ crossover current density, HFR and LFR of MEA-4 during course of AST. ...	130
Table 6-6: OCV, H ₂ crossover current density, HFR and LFR of MEA-5 during course of AST. ...	133
Table 6-7: Description of overall test analysis and samples used for COCV test.	137
Table 6-8: OCV, H ₂ crossover current density, HFR and LFR of MEA-2 during course of AST. ...	140
Table 6-9: OCV, H ₂ crossover current density, HFR and LFR of MEA-6 during course of AST. ...	144
Table 6-10: OCV, H ₂ crossover current density, HFR and LFR of MEA-7 during course of AST. ...	148
Table 6-11: OCV, H ₂ crossover current density, HFR and LFR of MEA-8 during course of AST. ...	151
Table 7-1: Dimensions of defects shown in Figure 7-3b and c.	162
Table 7-2: Comparison of temperature response on MPL defects with literature values.	166
Table 7-3: Operating conditions applied for aging GDLs.	168
Table 7-4: Polarization performance and parameters obtained from EIS analysis of cells containing fresh and aged GDLs.	177

List of Abbreviation

ACL	Anode Catalyst Layer
AFCC	Automotive Fuel Cell Cooperation
AST	Accelerated Stress Test
BOL	Beginning-Of-Life
BPP	Bipolar Plate
CC	Crossover current
CCL	Cathode Catalyst Layer
CCM	Catalyst Coated Membrane
CL	Catalyst Layer
COCV	Cyclic Open Circuit Voltage
CV	Cyclic Voltammetry
DOE	Department of Energy
ECSA	Electrochemical Active Surface Area
EIS	Electrochemical Impedance Spectroscopy
EOL	End-Of-Life
FCV	Fuel Cell Vehicles
FER	Fluoride emission rate
GDE	Gas Diffusion Electrode
GDL	Gas Diffusion Layer
H ₂ crossover	Hydrogen Crossover
HOR	Hydrogen Oxidation Reaction
Ionomer	Electrolyte Membrane
IR	Infrared
LSV	Linear Sweep Voltammetry
MCLD	Missing Catalyst Layer Defect
MEA	Membrane Electrode Assembly
MOL	Middle-Of-Life
MPL	Micro-Porous Layer

O ₂ Crossover	Oxygen Crossover
OCV	Open Circuit Voltage
OP	Optical Microscopy
ORR	Oxygen Reduction Reaction
PEM	Polymer Electrolyte Membrane
PEMFC	Polymer Electrolyte Membrane Fuel Cell
PFSA	Perfluorosulfonic Acid
Pt	Platinum
PTFE	Polytetrafluoroethylene
QC	Quality Control
R&D	Research and Development
RH	Relative Humidity
ROI	Region of Interest
SEM	Scanning Electron Microscopy
SLPM	Standard Liters per Minute – 0°C, 1 atm
TEM	Transmission Electron Microscopy
Z-profile	Depth/Height Profile

1 Introduction

1.1 Overview

As resources continue to diminish and energy demand continues to rise, effective energy management and utilization have become increasingly important. In order to minimize the socio-ecological impacts of climate change, 21st century energy systems must rely on technology that is free of greenhouse gas emissions [1]. Polymer electrolyte membrane fuel cells (PEMFCs) are promising energy systems that meets this need by converting fuel directly into electricity with high efficiency, less fuel consumption and zero emissions (with only water as a by-product). Nonetheless, they require an infrastructure that supports the widespread use of hydrogen [2].

Durability and reliability are major challenges limiting their commercialization and competitiveness with conventional fossil fuel energy-based alternatives [3]. Material durability is one of the key issues limiting the commercialization of fuel cells. Further improvement in durability of fuel cell components by minimizing defects developed during the manufacturing process is needed in order to reduce the cost and extend the lifetime of fuel cell electrodes. One of the potential challenges for improving durability and long-term stability of fuel cell systems is the formation of defects (i.e. catalyst layer cracks, irregularities in the catalyst layer, empty catalyst layers, delamination of catalyst layers, thickness variations, scratches, sealant interface defects and membrane pinholes) that occur in the membrane electrode assembly (MEA) components during fabrication and operation via chemical, mechanical and thermal degradation [4]. These defects shorten PEMFC life, reduce performance and can ultimately cause catastrophic failure of the cell. The identification of defects at different stages of a fuel cell life (BOL, MOL and EOL) should provide insight into the behavior of materials under various operating conditions over time [5]. The development of an efficient non-contact and non-destructive technique is not only essential to improve quality control, but would also enable manufacturers to better predict the long-term stability and lifetime of fuel cell components [6]. The primary motivation behind such research is to develop a quality control technique to measure defect growth and propagation in MEA components (e.g., CCM and GDL) during typical fuel cell operation. This would provide useful information for fuel cell manufacturers, developers and suppliers to select/reject a defective electrode prior to the stack installation and thereby reduce manufacturing costs as well as improve

the life span of fuel cells. Therefore, the focus of this research will be on identifying the propagation of defects in CCMs and GDLs for PEMFC applications.

1.1.1 Definition of MEA component defects

CCMs and GDLs are two major components in an MEA. The defects in CCM/GDL are defined as imperfections, irregularities or non-uniformities in the thickness of the catalyst layers and MPL that can cause losses in PEMFC performance. These defects include cracks, missing/empty catalyst, catalyst agglomerates, scratches, voids, delaminated portions, uneven thickness coatings and membrane pinholes. Examples of MEA defects are shown in Figure 1-1. As defects grow larger in size, shape and extent, failure becomes more likely [7,8]. More precautions should be taken specifically during the fabrication of CCMs to produce defect-free electrodes since it is expected that manufacturing defects grow at a faster rate than defects that form during the subsequent operation due to chemical, mechanical and thermal degradation [8,9]. Although advances in CCM fabrication technology have enabled PEMFCs to operate at higher power densities in recent years, operation at these higher rates can leave the CCM more prone to develop electrode defects that lead to catastrophic failure. Once defects such as pinholes become large enough, the direct reaction of the fuel and oxidant can produce hydroxyl and hydroperoxyl radicals that accelerate the chemical degradation of the polymer membrane [9,10]. The research presented here has attempted to gain a better understanding of the origin and evolution of various defects in CCMs and GDLs, classify defects according to the physical characteristics, correlate these defects with PEMFC performance loss under different operating conditions and develop a quality control system for improving MEA technology.

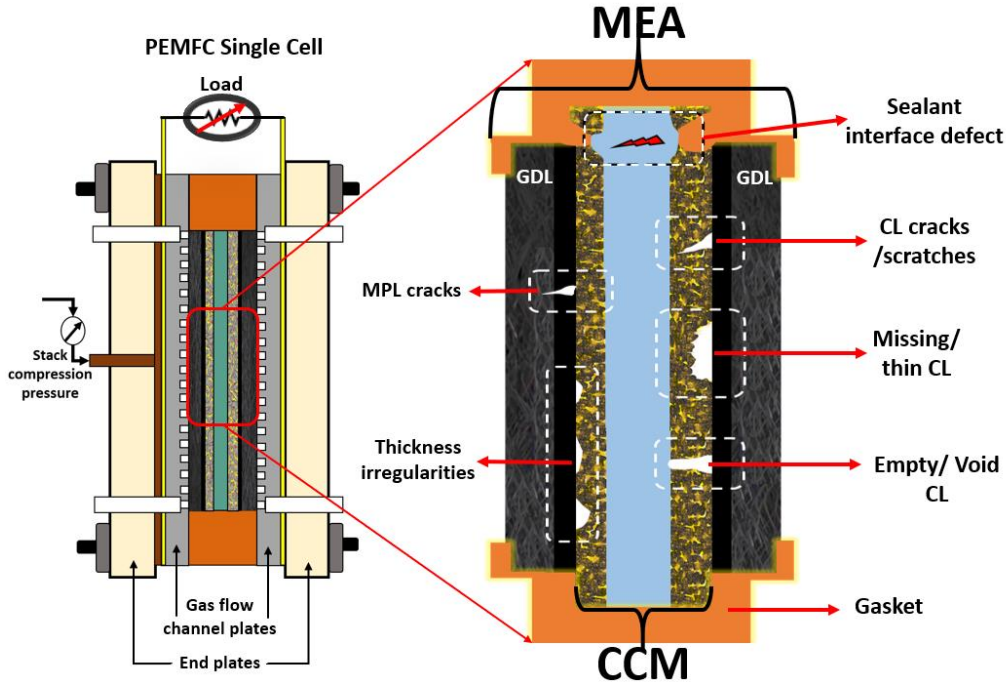


Figure 1-1: Various defects observed in CCM/MEA components during the fabrication process.

1.1.2 Defect identification in the CCM and GDL

The detection of defects is a major target for fuel cell manufacturers to improve fuel cell durability. The ability to investigate defects in MEA/CCM components is important for preventing the failure of fuel cell stacks, increasing durability and ensuring that the produced material is as defect-free as possible [7]. Defects that form during the fabrication of the CCM are catalyst layer cracks, void spaces in the catalyst layers, delamination between the catalyst layer and polymer membrane and membrane pinholes. Defects that form during the fabrication of the GDL are micro-porous layer cracks, thickness variations in the GDL/MPL, non-uniform distribution of hydrophobic material (i.e, PTFE) and MPL surface roughness. Defects can be characterized in terms of length, width, area, aspect ratio and criticality. These are useful parameters to measure and estimate the defect behavior and performance loss under typical conditions such as load cycling, potential cycling and RH cycling. Although MEA defects can have a profound effect on cell performance loss, the mechanisms involved are not clearly understood. The previous research on this topic has included both experimental and modeling studies and utilized electrochemical testing, physical destructive and simulations to investigate the degradation mechanisms operating in the catalyst layer and polymer membrane [11–15]. Visual inspection is the most common method of detecting defects during the production process but is not ideal because (1) the defects

formed within the MEA are not directly visible due to the presence of the GDL and (2) point measurements involve destructive methods such as SEM and TEM and so samples cannot be reused for further analysis which causes precious material waste. The recent investigation of defects using IR thermography enables pinholes to be detected by measuring hotspots on the MEA [8,16], but this technique cannot provide information regarding surface morphology, thickness measurement and defect characteristics. In this research, a non-destructive approach using optical microscope and IR thermography is used to detect surface and internal defects in the electrode and classify defects according to shape, size, extent, location and aspect ratio of the defects.

1.2 Motivation

The widespread of manufacturing fuel cell components demands a comprehensive quality control system that accurately inspects material defects in MEA [17]. The formation of defects in MEA components can be related to the raw materials, mechanical and process parameters during the fabrication process (i.e., mixing, coating and drying), flaws in the casting substrate and conditions during PEMFC operation (e.g., current, temperature and humidity). Defects on the catalyst layer, in particular, can have dramatic effects on fuel cell performance, cost and stability [7][18]. Recently, the US DOE released data showing that the component rejection rate due to imperfections formed during manufacturing production process are 2.5% from catalyst production, 2.5% from catalyst coatings, 3.0% from decal transfer, 3.0% from die cutting and 0.5% from hot pressing [17]. Better quality control inspection could help reduce CCM imperfections that stem from errors such as inconsistencies associated with catalyst ink preparation and catalyst coating methodology[19][20][21][22] as well as thickness variation in catalyst layers and electrolyte membranes [23][24]. Fuel cell manufacturers spend unnecessary time and money to disassemble fuel cell stacks and remove a single faulty cell. Thus, defects developed during fuel cell production must be examined and characterized prior to assembly with the hope of differentiating between fatal and minor defects. Perhaps the most important challenge for the mass production of fuel cell components is the improvement of the quality control inspection to identify CCM defects and predict their lifetime [25][26]. Thus, it would be advantageous for fuel cell manufacturers to develop online quality control procedures to ensure the production of defect-free MEA components. A better understanding of the effect of MEA component defects on fuel cell performance and lifetime is crucial to the development of these online quality control procedures.

1.2.1 Scope of defect analysis

One of the major challenges faced by CCM electrode manufacturers is associated with catalyst layer defects developed during fabrication. Despite being sub-micrometer to sub-millimeter in size, catalyst layer irregularities have a huge impact on degradation and their behaviour is hard to predict after a MEA is formed by hot pressing. Many researchers have examined the effect of artificial defects at specific locations on overall cell performance but a research gap still exists in analyzing real defects and how they evolve during aging. In this research, realistic catalyst layer defects developed in CCM production lines have been analyzed with respect to their morphology at various stages of aging.

1.3 Research Objectives

The overall objective of this research is to develop non-destructive techniques and quality control diagnostics for catalyst-coated membrane (CCM) and gas diffusion layer components and to investigate the effects of defects on PEMFC performance. To achieve this,

1. First, a custom-design transparent single cell device has been fabricated in order to operate CCMs in a safe mode that prevents external damage to the catalyst layer due to compression by the GDL, gas flow channels and ribs. Catalyst layer defects such as cracks, thin catalyst layers and empty/void/bare catalyst regions in the CCM will be analyzed at various stages of operation using an optical microscope. This methodology will potentially be very useful for fuel cell manufacturers to define and ensure a certain level of CCM quality.
2. A secondary objective in this research is to investigate chemical and mechanical degradation of the catalyst layer and membrane under accelerated stress conditions (AST) in order to identify potential failures and their mechanisms. This will potentially enable membrane material loss in MEA to be monitored. The MEA will be characterized by *ex-situ* and *in-situ* electrochemical tests. The results from this research will provide insight into the behaviour of defects in the CCM/MEA at various stages of operation. This will have long-term benefits of enabling better estimation of the lifetime of defected and defect-free electrodes.
3. The final objective of the research is to develop a non-destructive technique to detect defects on the GDL/MPL substrates using thermal, electrical and optical measurements.

- a. Thermal measurements using infrared thermography experiments are aimed at detecting defects as small as $\sim 500 \mu\text{m}$ on the MPL substrate. The developed setup can be implemented as an in-line diagnostic tool for GDL quality control.
- b. The electrical conductivity and optical appearance of MPL cracks are investigated at BOL and EOL. This should enable a better understanding of crack propagation in MPLs and its impact on overall cell performance.

1.4 Thesis Outline

The chapters of the thesis are organized as follows:

- **Chapter 2: Background** – This chapter provides relevant background information from a literature review on the main research topics covered in this work. It will first cover the basic components of fuel cells and the fabrication methods for CCM/MEA electrodes. It will then focus on the causes of defect formation in CCM/MEA during manufacturing and operation. This chapter provides an overview of various degradation mechanisms responsible for defect formation in MEA components.
- **Chapter 3: Experimental** – This chapter discusses the experimental procedure that will be utilized. The first part describes the main measurements and procedures for non-destructive testing of CCMs. The second part describes the accelerated stress testing and subsequent characterization techniques used for CCM/MEA and GDL analysis.

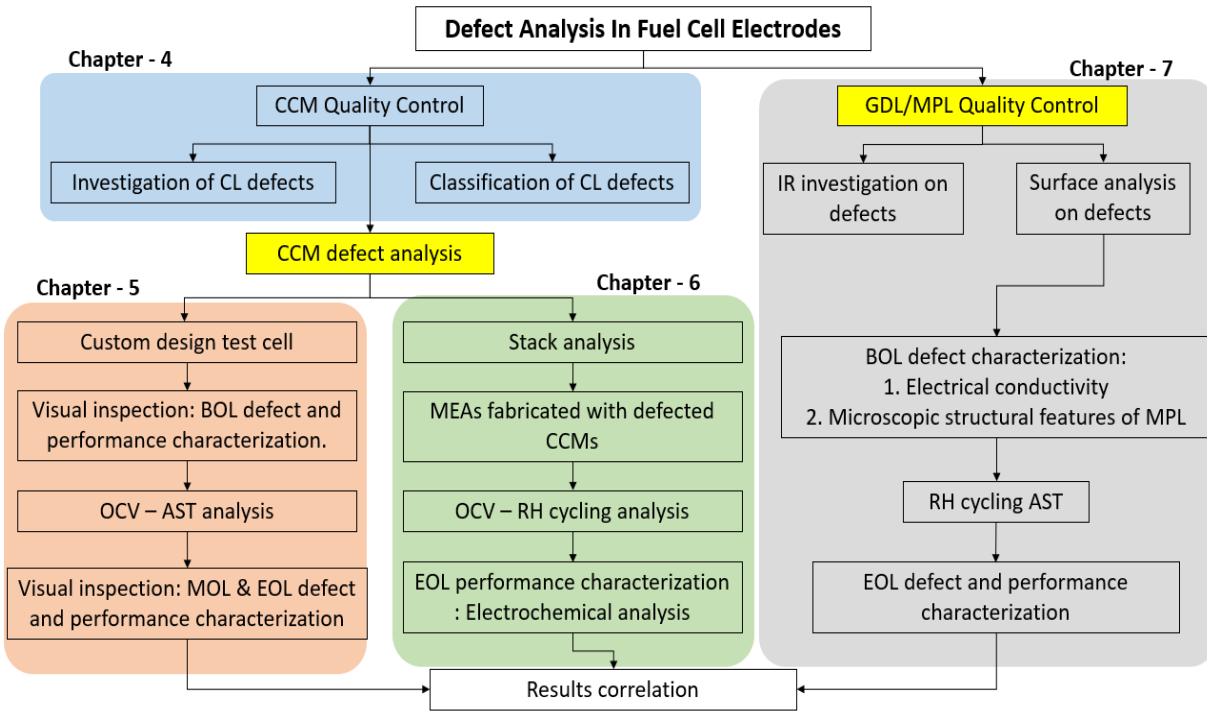


Figure 1-2: Outline of thesis results organized for chapter 4,5,6 and 7.

- Chapter 4: Investigation of catalyst layer defects in CCM** – In this chapter, a non-destructive method of investigating defects in CCM electrode is presented for quality control purposes. The first section is concerned with image analysis to characterize the defects in CCMs. The second section focuses on identifying the various catalyst layer defects (cracks, scratches, missing and empty CL) that form in the CCM and classifying them based on the size, shape and orientation. The mechanical propagation of real defects in the MOL condition is also monitored.
- Chapter 5: Morphological characteristics of catalyst layer defects** – This chapter describes the investigation of morphological changes of missing/thin catalyst layer defects formed during the decal transfer method. The growth of defects due to chemical and mechanical propagation and their effect on performance loss are discussed. Surface delamination and crack propagation on cathode catalyst layer are studied on aged CCMs. The electrochemical cell performances of defected and non-defected CCMs are measured and compared.

- **Chapter 6: Effect of load cycling on CCM defects** – In this chapter, we present a case study which employs typical chemical and mechanical ASTs in single cell operation to characterize the behaviour of 3 CCM manufacturing defects: (1) missing catalyst layer defects (MCLD), (2) gasket/CCM interface defects (sealant pinhole defects) and (3) scratches/deep cuts. The durability of MEAs with and without defects is tested at low RH under steady-state conditions and during cycling under low/high RH conditions at high stack temperature.
- **Chapter 7: Assessment of quality control in GDL/MPL substrates** – This chapter extends the quality control research to defects on GDL/MPL electrodes. In the first stage of the research, an IR thermal setup is developed to detect defects in the MPL substrate with size less than ~1 mm and monitoring the defect with in less than 1 minute of time. The second stage of the research focuses on MPL crack propagation, electrical conductivity and electrochemical performance of GDL/MPL samples at BOL and EOL to understand the impact of defects on overall cell performance.
- **Chapter 8: Conclusions and future work** – This chapter includes a summary of the main conclusions of this study and the research contributions to the PEMFC literature and a discussion of possible directions for future research.

2 Background and Literature Review

2.1 Fuel Cell Technology

Fuel cells are electrochemical devices similar to a primary battery in that they directly convert chemical energy into electricity. Unlike primary batteries that must be recharged or replaced after discharge, fuel cells are fed a continuous supply of reactants and therefore can produce power continuously as long as the reactants are available. The use of fuel cells in automobiles and small stationary applications has received increased attention as their advantages have come to light. These advantages include the fact they have no moving parts, generate comparatively high-power density, operate with high efficiency and low noise and exhibit fast start-up capability and simple scalability. Fuel cells are categorized based on the type of fuel used, composition of the electrolyte and operating temperature. Examples include solid oxide, direct methanol, molten carbonate, phosphoric acid and polymer electrolyte membrane fuel cells.

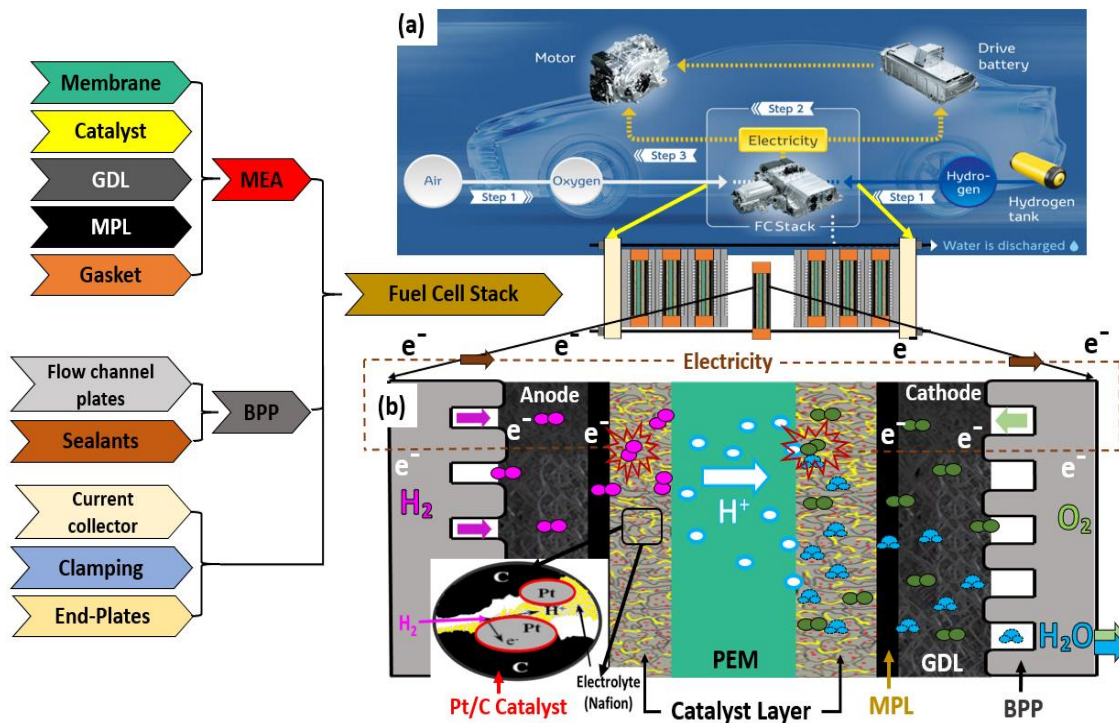


Figure 2-1: (a) Various components of PEMFC stack in a fuel cell vehicle [27]; (b) cross-section of a single-cell PEMFC consisting of BPP, GDL, MPL, CL and PEM.

This research focuses on PEMFCs which consist of a solid polymer electrolyte sandwiched between an anode where the oxidation of hydrogen occurs and a cathode where the reduction of

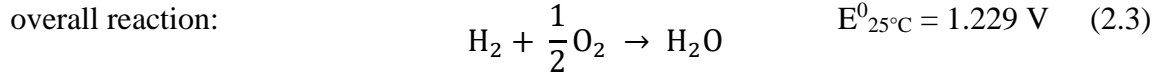
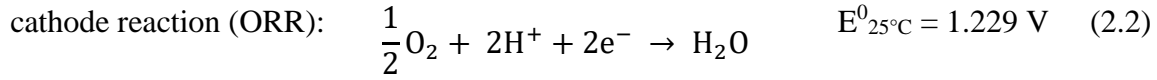
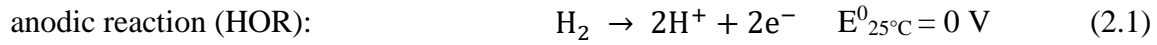
oxygen occurs [28]. Figure 2-1 shows the typical assembly of fuel cell stack components and single cell configuration of PEMFC.

To increase the power output, cells are assembled in a series or sequence of electrodes called a stack. At the anode, hydrogen fuel is supplied through the bipolar plate to enable uniform gas distribution across the electrode, then transported through the porous electrocatalyst layer to the platinum-carbon catalyst and finally oxidized electrochemically to form H^+ ions and electrons. The electrons travel through the external circuit and provide electric power to the load while the H^+ ions are conducted through a polymer electrolyte membrane to the cathode. At the cathode, these H^+ ions combine with the electrons from the external circuit and O_2 fed from the other bipolar plate to form water and heat.

In addition to serving as the ionically conducting electrolyte selective for H^+ , the solid polymer membrane also serves as an electron insulator and gas barrier between the anode and cathode so that the reactant gases H_2 and O_2 cannot freely combine with each other. The membranes are usually made from perfluorosulfonic acid (PFSA) polymer, most commonly the commercial product Nafion supplied by DuPont. The Teflon-like backbone of Nafion provides structural stability while its hydrophilic surface acid groups absorb the water. The expansion and contraction of the membrane depends on its water content. The composite material formed by the anode catalyst layer (ACL), cathode catalyst layer (CCL) and the polymer electrolyte membrane is typically called the catalyst-coated membrane (CCM). The gas diffusion layers are typically combined with the CCM to comprise the membrane electrode assembly (MEA) [28].

In order for the electrochemical reactions to occur and power be generated, the catalyst must provide a triple phase boundary (TPB) condition where (1) reaction gases meet active metal catalyst, (2) electrons must have a conduction path to and from the active metal catalyst sites and (3) an ionic conductor must be available to transport the H^+ ions to/from metal catalyst sites. The electronic conductor and ionic conductor must also be in contact with the catalyst site to make this region electrochemically active.

The basic reactions in a PEMFC are as follows:



From the overall electrochemical reaction, each single cell will theoretically produce 1.229V at 25°C, $P_{\text{O}_2} = 1 \text{ atm}$ and $P_{\text{H}_2} = 1 \text{ atm}$. During fuel cell operation, the cell potential is dependent on several factors such as temperature, pressure and stoichiometry of reactants [29–31]. The cell emf at different conditions can be calculated using the Nernst equation:

$$\Delta E = \Delta E^0 - \frac{RT}{nF} \ln \left(\frac{a_{\text{H}_2\text{O}}}{a_{\text{H}_2} a_{\text{O}_2}^{1/2}} \right) \quad (2.4)$$

where R is the gas constant, T is the temperature (K), n is the number of electrons transferred in the reaction, F is the Faraday constant, while $a_{\text{H}_2\text{O}}$, a_{H_2} , and a_{O_2} are the activities of water, hydrogen and oxygen, respectively.

2.2 Performance of PEM Fuel Cells

Typically, a polarization curve is considered to be the main measure of fuel cell performance. A polarization curve depicts the dependence of cell potential or voltage on the current density. Three regions which mark the onset of the voltage losses due to electrode kinetics (activation), ohmic resistance and mass transfer can be identified on these curves, as shown in Figure 2-2.

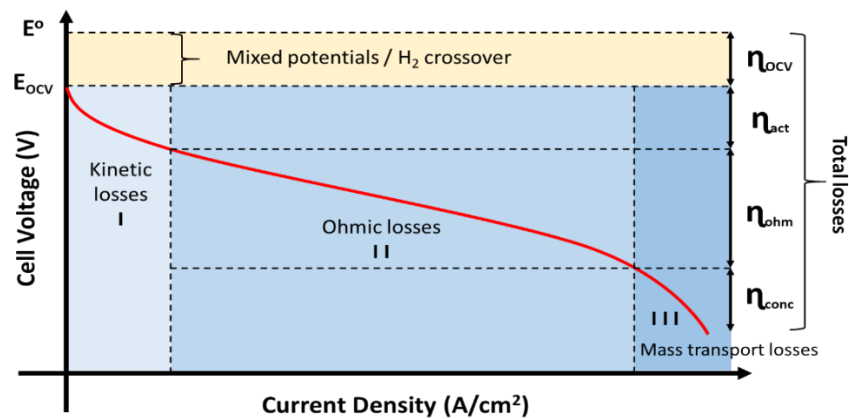


Figure 2-2: Schematic of polarization curve indicating the major cell voltage losses: mixed potential/open circuit (η_{ocv}), activation overpotential (η_{act}), ohmic overpotential (η_{ohm}) and concentration overpotential (η_{conc}).

The actual cell voltage is less than the cell potential determined from the Nernst equation during fuel cell operation. This is due to the losses shown in Eqn (2.5): open-circuit voltage (η_{OCV}), activation/charge transfer losses (η_{act}), ohmic losses (η_{ohm}) and concentration/mass transfer losses (η_{conc}). As the current density increases, the magnitudes of the last three voltages increase

$$V_{cell} = E^0 - \eta_{OCV} - \eta_{act} - \eta_{ohm} - \eta_{conc} \quad (2.5)$$

Open-Circuit Voltage (η_{OCV}): The open-circuit voltage E_{OCV} ($E^0 - \eta_{OCV}$) is typically between 0.95 V and 1 V. At zero current, the cell potential V_{cell} should approach the ideal equilibrium potential (E^0), but due to phenomena such as leakage of H_2 from the anode to cathode and Pt oxidation, the highest achievable voltage under open circuit conditions (i.e., OCV) is only ~ 0.95 V to 1 V [31,32].

Activation losses (η_{act}): Activation polarization is the voltage overpotential necessary to overcome the electrochemical reaction activation energy on the catalyst surface. Activation polarization is the dominant source of voltage loss that is required to initiate electrochemical reactions controlled by slow electrode kinetics. In addition to electrode kinetics, these losses are related to the total surface area of the active catalyst where the reactants are converted at a three-phase boundary between the catalyst, carbon support and Nafion. The catalyst promotes the reaction, the carbon support allows electrons to be conducted to and from the catalyst and the Nafion (recast ionomer) allows protons to be conducted to and from the catalyst. Activation losses at the cathode electrode dominate over the anode electrode due to the sluggish nature of oxygen reduction (ORR). Overall utilization of the catalyst is decreased when at least one of the three phases is not available.

Ohmic losses (η_{ohm}): The ohmic overpotential is significant at intermediate current densities and is associated with the resistance to ionic transport through the membrane electrolyte and to electronic transport through the gas diffusion layers (GDL), micro-porous layer (MPL) and graphite plate. The resistance to ionic flow through the membrane usually is dominant over the resistance to electronic flow. Additionally, the losses are also related to contact resistance at the interfaces between the fuel cell components.

Concentration losses (η_{conc}): Mass transfer limitations become important at high current density when the supply of reactants to the active catalyst sites at high current densities cannot keep pace with electrode reaction kinetics. Products must be continuously removed from the catalyst layers in order to achieve maximum fuel cell efficiency; otherwise the electrode will undergo water

flooding. The over-potential concentration may lead to very large drop in cell potentials due to insufficient reactants [33,34].

2.3 Components of PEM fuel cells

2.3.1 Catalyst Layer (CL)

The CLs affect the performance of MEAs in fuel stacks and must have high electrocatalytic activity for the electrode reactions, good electronic conductivity, good ionic conductivity and high porosity for efficient transport of reactants and products. Pure and alloyed platinum is used as catalysts for hydrogen oxidation and oxygen reduction in the catalyst layer of PEMFCs. Since platinum is a very expensive noble metal and accounts for 25-40% of the total fuel cell cost, an increase in the efficiency of platinum utilization is critical [35]. To achieve satisfactory utilization, the electrochemically active surface area of platinum must be approximately $60\text{-}120\text{ m}^2\text{ g}_{\text{Pt}}^{-1}$ [36,37] and platinum particles, typically 2-7 nm in diameter, must be dispersed on a high surface area carbon support with a loading of approximately 20 – 50 wt.%. The platinum-carbon is then uniformly mixed with an ionic conductor such as Nafion which acts as a binding agent and deposited to form a porous catalyst layer with thickness of 1 – 50 μm [35]. The electrochemical reactions occur at the three-phase boundary where the platinum particles, ionomer and gas phase contact each other. The H^+ ions are transported through the ionomer phase, while electrons are transferred by the carbon support. If the catalyst layer is coated on the GDL-MPL, it is referred to as a gas diffusion electrode (GDE); if it is coated on the solid polymer membrane, it is referred to as a catalyst-coated membrane (CCM). Platinum loading is typically increased to $0.2\text{-}0.5\text{ mg}_{\text{Pt}}\text{ cm}^{-2}$ at the cathode, but only $0.1\text{ – }0.2\text{ mg}_{\text{Pt}}\text{ cm}^{-2}$ at the anode because the ORR has much slower kinetics than the HOR (by ~ 3 orders of magnitude) [12].

2.3.2 Polymer Electrolyte Membrane (PEM)

The polymer electrolyte membrane has two functions: i) provides conductive path for H^+ from the anode to the cathode, while forcing electrons to travel through the external circuit and ii) serves as a gas barrier between the anode and cathode. Its structural stability is important for proper fuel cell operation. In PEMFCs, the electrolyte is made of a thin solid polymer (10 – 200 μm thick) such as Nafion. It should have high chemical stability and proton conductivity, low cost, good thermal stability, high durability, good water uptake and low coefficient of expansion. High ionic conductivity for H^+ which depends on the water content and ion exchange capacity of the

membrane is essential to complete the electrochemical circuit and minimize the ohmic overpotential. The more hydrated a PEM is, the higher is its proton conductivity. At the same time, the water-saturated membrane swells and the microstructure of the ionic clusters increases in volume and diameter as the water content increases [31,38]. However, it should not expand too much since this will put pressure on the bipolar plates, cause the membrane to buckle or tear and lead to defects such as cracks or pinholes [13]. During fuel cell operation, chemical attack of the membrane from peroxy radicals, hydrogen ions, oxygen and contaminants in the gas streams may occur. This chemical attack degrades the polymer and consequently reduces the energy output of the fuel cell. If a break in the membrane occurs, the oxidant and fuel will have a path to react directly rather than electrochemically. Liu et al. [39] showed that the chemical and mechanical stability of membranes is improved by reinforcing them with porous polytetrafluoroethylene (PTFE) fiber. The operating lifetime of reinforced membranes can be increased by as much as five-fold due to the presence of the strong PTFE backbone [40,41]. Other studies have shown that local variations in the thickness of the CCM and GDL originating during MEA fabrication can lead to cracks that function as stress concentrating points in the membrane and ultimately cause pinholes to form [42,43].

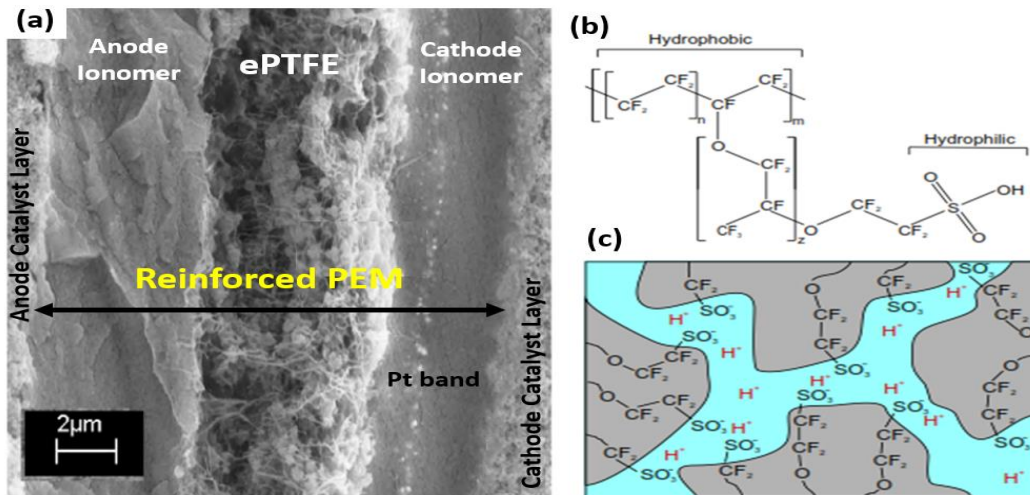


Figure 2-3: (a) Cross-sectional view of reinforced membrane [41]. (b) Chemical structure of the Nafion polymer and (c) microscopic structure of Nafion membrane [44].

Figure: 2-3a shows the cross-sectional view of a membrane where the ePTFE layer is reinforced between the anode and cathode ionomer layers, while Figure 2-3b shows the chemical structure of PFSA membrane which is amphiphilic due to the presence of hydrophobic and hydrophilic side

chains. Short hydrophilic chains made of sulfonic acid groups connect long hydrophobic chains of polytetrafluoroethylene. The sulfonic acid groups increase the proton conductivity. The amphiphilic nature of the PFSA membrane causes the polymer phase to separate into clusters and leave behind a proton conductive network, as shown in Figure 2-3c. The proton conductive network is provided by water (blue) which fills the hydrophilic phase [44].

2.3.3 Gas Diffusion Layer (GDL)

The function of the GDL is to: (1) act as a gas diffuser, (2) provide mechanical support to the CL and (3) provide an electrical pathway for electrons. The GDL provides a frame for the catalyst layer and promotes uniform mass transport of reactants over the active catalyst surface. The GDL typically has a thickness of $\sim 100 - 250 \mu\text{m}$ and is made from carbon fibers (6-10 μm diameter) woven into a cloth or paper with a high porosity of about 40 – 70% [14,45]. Electrons are conducted by the GDL from the electrode to the bipolar plate. The GDL is treated with 30 wt% of either polytetrafluoroethylene (PTFE) or fluoroethylenepropylene to enhance its hydrophobicity and promote water transport away from the cathode [14].

2.3.4 Micro-Porous Layer (MPL)

A microporous layer (MPL) is applied to the GDL to improve the electrical contact with the catalyst layer and facilitate product water removal from the cathode to reduce water flooding at high current densities. The MPL consists of a porous carbon-polymer/PTFE composite network that has a higher density than the GDL as well as different wetting behavior. For effective mass/thermal management, losses at the MPL|CL, MPL|GDL and GDL|bipolar plate interfaces play significant roles. Among these, the MPL|CL interface is particularly important since it acts as a bridge between the reacting and non-reacting components. Poor contact can lead to considerable ohmic losses, electrical resistance and thermal contact resistance [42,46].

2.3.5 Bipolar Plate (BPP)

Bipolar plates isolate the individual cells, conduct both heat and electrical current between the cells, facilitate water and thermal management throughout the cell and evenly distribute reactant gases over the electrode surface within the stack. Bipolar plates receive electrons from the gas diffusion layers, provide structural stability to the cell and conduct electrons to current collectors or to adjacent cells in a stack. The current collectors conduct electrons from the bipolar

plate to the external load through highly conductive copper plates that are often coated with thin layers of gold. The most recently developed BPPs are composites made from graphitized carbon and polymer, giving them excellent corrosion resistance, low contact resistance and good electrical conductivity [47–49].

2.4 Method of fabricating MEA

The MEA is a key stack component and requires state-of-art fabrication. The MEA is composed of a catalyst-coated membrane (CCM) hot-pressed to GDLs on either side [50]. Each CCM consists of a polymer electrolyte membrane that is coated with the anode catalyst layer (ACL) and cathode catalyst layer (CCL) on either side. The MEA performance is typically dependent on the properties of the CL and the contact interfacial resistance between CL and the polymer electrolyte membrane in CCM. An important factor in preparation of CLs is the selection of coating procedures to minimize their roughness and contact resistance. Several coating techniques have been tested in recent years to improve MEA performance such as spraying, blading, deckling, ink-jetting and brushing. The most common methods are classified into three categories [51–53]:

- (1) Direct coating of catalyst on membrane (DCM),
- (2) Decal transfer of catalyst onto membrane (DTM)
- (3) Coating of catalyst on substrate (CCS).

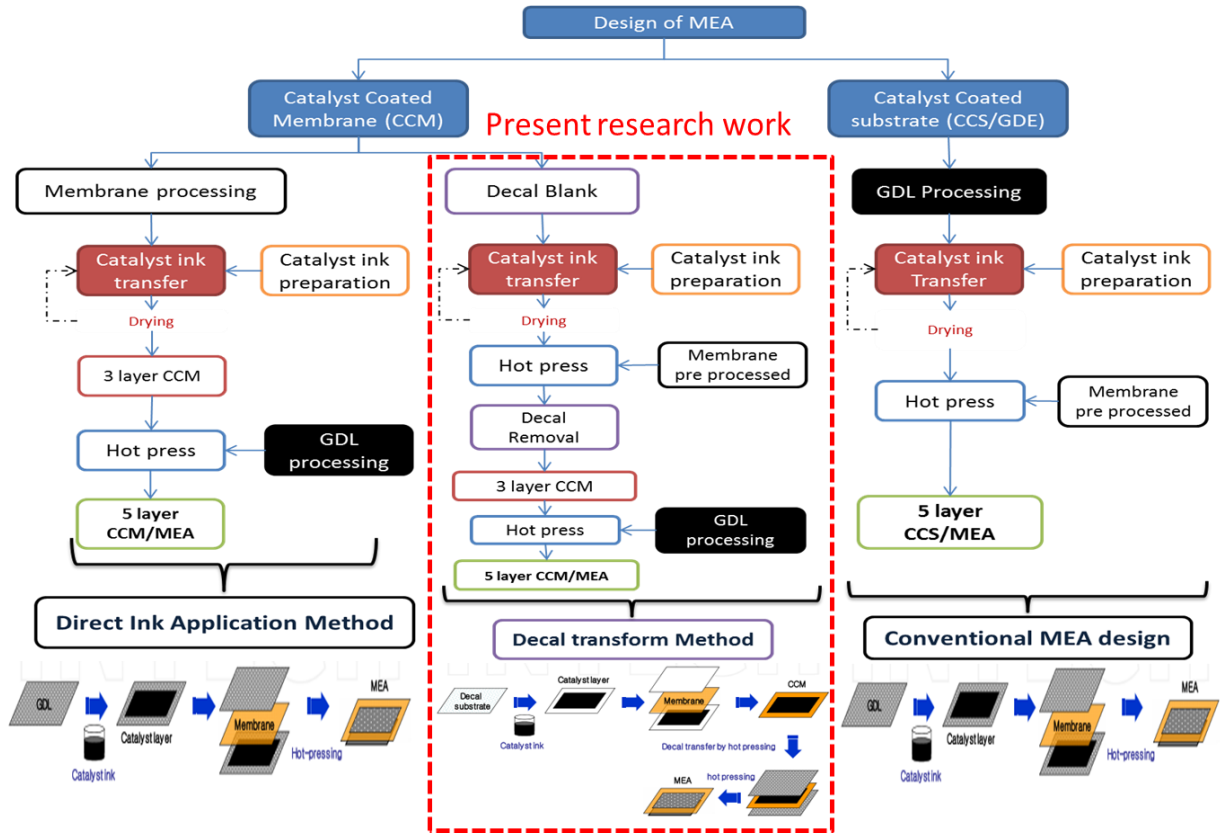


Figure 2-4: MEA fabrication methods [54].

2.4.1 Fabrication of CCM using decal transfer method

CCM-based MEA fabrication has many advantages compared to conventional GDE-based MEAs (gas diffusion electrodes with catalyst coated on GDLs) such as lower contact resistance between the catalyst layer and electrolyte membrane, easier gas transport, more effective catalyst utilization and thinner electrodes. The CCM is the key component of PEMFCs since it contains the expensive platinum electrocatalyst, which must provide high-active-surface area on the order of $70 - 120 \text{ m}^2\text{g}^{-1}$ to achieve the desired results [55][56]. The development of high surface area catalysts has helped reduce the amount of platinum required per unit area and reduce the thickness of the catalyst layer to $0.2 \mu\text{m}$ from $10 \mu\text{m}$ [57]. Several studies have demonstrated the advantages of a thinner catalyst layer in lowering the electron and proton transport resistances, increasing the O_2 concentrations within the cathode, reducing the amount of platinum usage and minimising the overall cost of the system [58][59][19]. In addition, thin catalyst layers are beneficial for the 3-phase catalyst reaction, gas permeability, fluid transport, electrical conductivity and ionic conductivity [60]. If any of these properties is hindered, fuel cell performance suffers significantly.

In addition, research has shown that thin catalyst layers are advantageous because they improve the kinetics of the oxygen reduction reaction, minimize catalyst loading, reduce electrode resistance and increase current density [22].

The research in this PhD project will focus on the CCM-fabricated DTM technique. This technique involves loading the catalyst layer ink uniformly onto the decal substrate as shown in Figure 2-4 (indicated in red dotted rectangle). The CLs of both electrodes are then transferred from the decal substrates to the Nafion membrane by hot pressing at 100 to 120 kg cm⁻² loaded pressure and temperatures of 110°C-140°C for a specific amount of time. The decal substrates are then peeled away from the CCM to leave behind the catalyst layer on the membrane, yielding a three-layer CCM. Finally, teflon-treated GDL or GDE (MPL + GDL) is then added to the CCM by hot-pressing, as mentioned earlier [54].

DTM is an advanced technique that improves catalyst utilization and forms a better-connected ionomer network compared to that achieved using the CCS method. This has a significant effect on the performance and long-term durability of the MEA due to low interfacial resistance between the CL and the PEM. DTM produces a thinner catalyst layer with lower mass transfer resistance and better contact between the electrode components [61]. However, the DTM method is more complex than the CCS method. Properties such as CL microstructure porosity and thickness are difficult to control using DTM due to dehydration of the membrane during decal transfer and the possibility that sintering of the catalyst will occur. Furthermore, ionomer segregation can occur on the outside of the CL and catalyst can be incompletely transferred from the decal substrate to Nafion if the pressing temperature becomes too high in an effort to transfer more of the CL onto the membrane, as shown in Figure 2-6. The present research work focuses on identifying defects that occur during DTM fabrication and the behavior of such defects during the subsequent operation of the fuel cell.

2.5 Sources of defect formation in MEA electrodes

The manufacturing costs of the various components must be reduced for fuel cells to become competitive in modern markets. Often, PEMFC failure has been attributed to defects that originate in the CCM during the fabrication and assembly stages. This has led to a growing demand for more stable manufacturing processes and more advanced methods of quality control and defect

detection methods [25]. In the fabrication of MEA/CCM electrodes, for example, defects such as micro-cracks, missing catalyst, uneven loading of catalyst, voids and pinholes can occur during the various DTM stages and sandwiching of the MEA between the GDEs. This eventually increases the interfacial contact resistance and/or ohmic polarization in the MEA [42]. Online quality control would facilitate continuous production of defect-free MEA components [6,9]. This research focuses on investigating the effects of manufacturing defects and operational aging defects on MEA endurance and performance. Some of the common defects that occur in PEMFC components are categorized below in Figure 2-5. These defects which can occur due to manufacturing processes or operational aging of the fuel cell have been shown to decrease PEMFC performance and increase the probability of PEMFC failure [7,25,26,42,43,62].

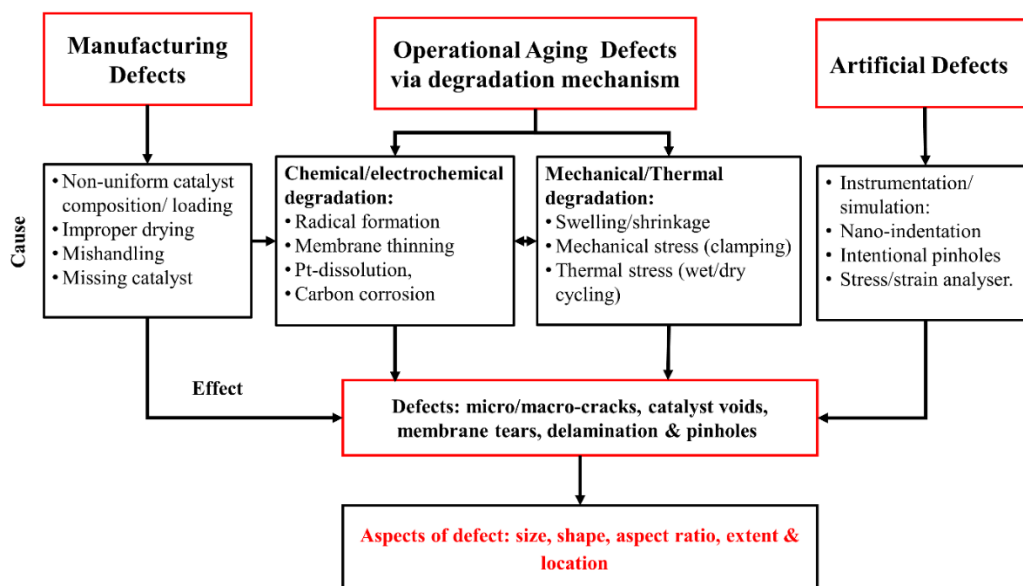


Figure 2-5: Categorization, cause and effect of defects formed in PEMFC components.

2.5.1 Manufacturing Defects

Manufacturing methods used to fabricate the CL can lead to defects which can propagate further during PEMFC operation due to chemical and mechanical stress. For example, the preparation of the CL by the DTM involves the formation of a homogenous mixture of solvents in catalyst ink. Incorrect mixing can lead to defects during the drying and transformation processes, as shown in Figure 2-5. Catalyst ink is a dispersion of Pt-C catalyst in a mixture of Nafion ionomer solution, solvent and deionized (DI) water [63]. The most important aspects of ink formulation are the selection of the appropriate weight ratio of 1:3 of ionomer to catalyst and the proper distribution

of the ionomer in the catalyst, which can minimize electrode resistance and maximize ionomer contact with Pt catalyst nanoparticles [49,54,64]. Non-uniform mixtures of solvents can lead to uneven drying of the CL surface in which the top layer dries faster than lower layers. This causes the solvent vapor from the lower regions to penetrate to the top and develop defects such as micro-cracks and delamination between CL and PEM [7]. Defects can also form as the catalyst dries on the decal or the catalyst layer is transferred on to the membrane. Over-compression of areas with uneven CL thickness can damage local areas of the membrane [15]. Incomplete transfer of catalyst layer from decal to membrane causes non-uniform distribution of catalyst, void regions and missing catalyst areas, as shown in Figures 2-1c and 2-6. These areas degrade at accelerated rates under chemical and mechanical stress and develop into defects such as pinholes in the CCM/MEA electrode which are very detrimental to cell performance. Identification and classification of defects that lead to poor performance or sudden shutdown of fuel cells and characterization of the behavior of these defects under various accelerated conditions are primary goals of this research.

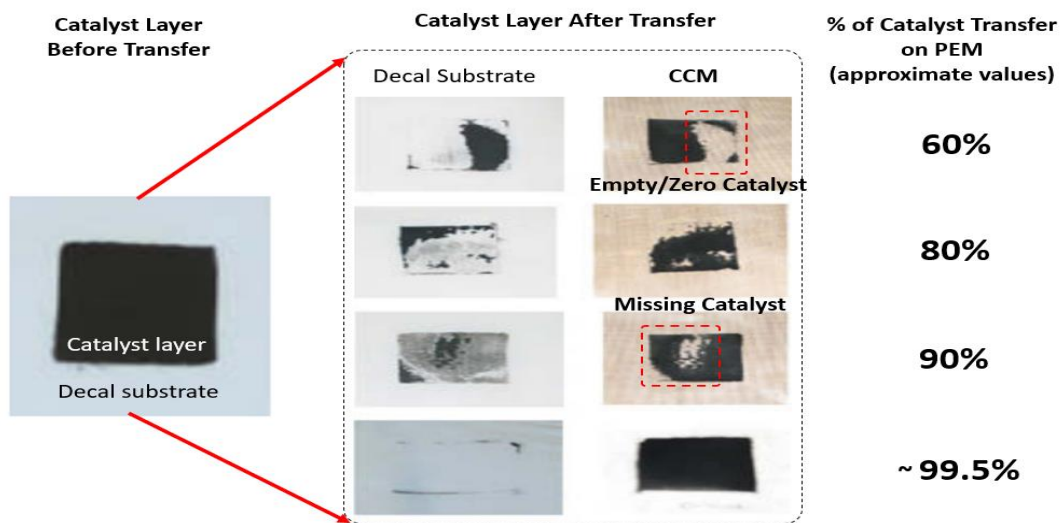


Figure 2-6: Percentage of catalyst transfer from decal substrate to polymer membrane, the dotted circles indicate incomplete catalyst transfer leading to void spaces and missing catalyst areas in CCM [63].

2.5.2 Operational Aging Defects

Defects caused by degradation of material components limit the service life of the electrode and impair main electrode functions such as electron conduction, proton conduction, electrode thickness, gas separation and electron insulation. CL degradation can lead to defect formation and may be caused by external pressure, membrane shrinkage or the operating environment [65]. The external pressure from the bipolar plates and internal stress due to swelling and shrinkage of

membrane can cause micro-cracks to form in the surface of the CL, thereby increasing ohmic losses. Operating conditions such as high current density can cause local build-up of water that leads to material loss via carbon corrosion and Pt oxidation and/or voltage degradation. Since the membrane is electrically insulating and separates the anode and cathode reactions, the loss of membrane material strongly influences cell performance. Membrane defects formed during the production process and cell assembly or during PEMFC operation shorten cell life, decrease cell performance and reduce cell efficiency. Operational aging defects arise due to the harsh operating conditions of the cell in which membranes undergo chemical and mechanical stresses during hydration cycling and differ from manufacturing defects that are formed during fabrication of electrodes.

The complex series of heterogeneous and local degradation processes in the CCM/MEA can be categorized into chemical/electrochemical, mechanical and thermal mechanisms [66]. Chemical/electrochemical degradation is caused by loss of chemical components in the electrode which leads to membrane thinning, loss of ionomer network in the CL, Pt dissolution and carbon corrosion. The stress caused by the swelling and shrinking of the Nafion membrane due to changes in temperature, relative humidity (RH) or load cycling is the main cause of mechanical degradation and failure through the initiation and propagation of microscopic cracks, creep and delamination. These defects can also lead to gas crossover through the membrane [67]. Temperature cycling can significantly increase the rate of membrane degradation and cause thermal degradation. This is considered to be a sub-category of the mechanical degradation mechanism. Obviously, the combined effects of chemical, mechanical and thermal stress cause defects that lead to degradation of cell performance and even to complete failure [65].

2.5.2.1 Formation of defects via degradation mechanism in MEA

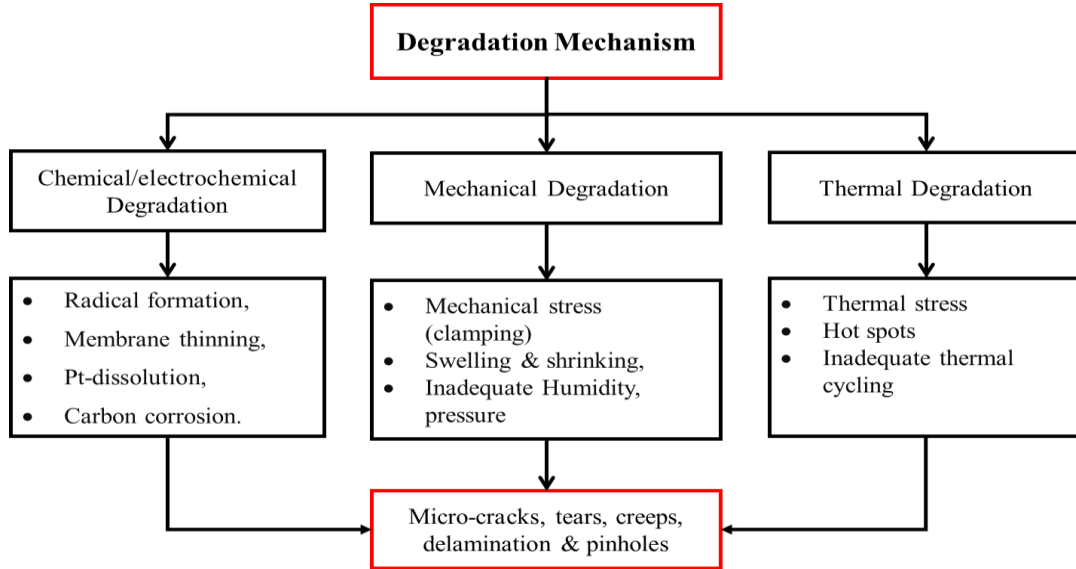
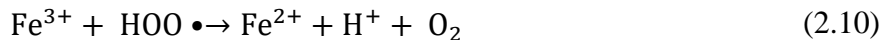
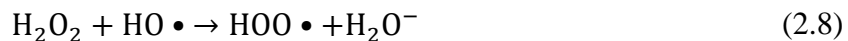
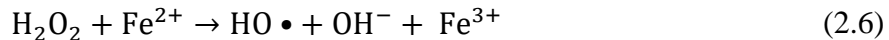


Figure 2-7: Degradation mechanism of defect formation in MEA components

Various authors have found that chemical, mechanical and thermal degradation mechanisms can combine to form defects in the MEA during PEMFC operation. Kundu et al categorized the morphological features of defects according to their causes, modes and effects during manufacturing and PEMFC operation [7]. Placca and Kouta investigated 37 individual events responsible for ‘cell degradation’ in PEMFC systems by using ‘fault-tree analysis’ (FTA) [65]. Kreitmeier et al. investigated artificial defects by relating pinholes of known size to their effects on cell performance under accelerated stress test (AST) conditions and analyzing gas crossover [68]. Kusoglu and Weber developed a mechanical model for pinhole growth in polymer membranes under humidified cycle loads and correlated the growth of pinhole to measure the crossover in order to estimate the lifetime of the membrane [13]. Ulsch and Bender used IR thermography to identify defects in fuel cell electrodes by measuring hotspots across the local defects such as pinholes and micro-cracks in the MEA [9,69]. Dhanushkodi et al investigated chemical degradation causing dissolution of platinum nanoparticles to form bands in the PEM responsible for PEMFC performance loss [70]. Other studies and investigations have involved polymer fracturing, polymer melting, catalyst sintering and carbon corrosion that enhance and propagate the defects in the electrode [71–73].

2.5.2.1.1 Chemical/electrochemical degradation

Chemical degradation can be a very complex process that can lead to other events and problems. Regardless of the specific details, most experimental research has found that chemical processes play important roles in membrane degradation [74]. The membrane life is affected by the formation of highly reactive radical species that attack the polymer. This is believed to be main cause of membrane thinning and pinhole formation in the CCM [75]. The radicals can attack the anode CLs, cathode CLs and the membrane electrolyte, damaging the polymer structure and leading to irreversible damage. The formation of radicals such as peroxide (HO•) and hydroperoxide (HOO•) triggers several chemical and electrochemical reactions in the catalyst layer and the membrane. *In-situ* and *ex-situ* analyses confirmed that free radical attack during fuel cell operation was responsible for the chemical degradation of ionomer in both the membrane and CL [76]. Corrosion of fuel cell components and external impurities originating from gas tubing or humidifiers or other parts can contaminate the cell with small quantities of metal cations and ultimately cause blistering of the membrane. Ca²⁺, Fe²⁺, Cu²⁺, Mg²⁺ and Pt²⁺ have been identified in the membrane after long-term operation [77]. These contaminants can attach to the side chain of the polymer membrane and form crystals that grow and create blisters. These crystals often form at the inlet where the cation concentration is higher. This also forms voids in the membrane, which become filled with water. The presence of cations lowers the membrane ionic conductivity, reduces the ORR activity of the catalyst and accelerates the chemical decomposition of polymer as shown in below equations [78]. This process can increase the rate of membrane thinning and pinhole formation.



Hydrogen peroxide has a longer lifetime than hydroxyl radicals and may be transported by diffusion and decompose to radicals far from the production site although the location and production mechanism of hydrogen peroxide formation is still under debate. Currently, the main question regarding polymer membrane decomposition is whether it mainly occurs at the anode or

the cathode or in the core of the membrane [41]. Figure 2-9 shows four chemical/electrochemical processes that cause hydrogen peroxide formation in the fuel cell CCM. In process I, the incomplete reaction of electrons and H^+ (step 4 in Figure 2-8) forms hydrogen peroxide, which is generated electrochemically by the two-electron reduction of oxygen at potentials below 0.695 V shown in Eqn. (2.12). This is catalyzed by both platinum particles and the carbon support. LaConti et al. proposed that radicals are initially generated by the formation of H_2O_2 through the addition of a proton to an incomplete water structure as shown in Figure 2-8. The four-electron reduction reaction of oxygen to form water as product at the cathode is shown in Step 1 and Eqn. 2.11. This overall process likely does not occur all at once. H_2O_2 can form according to steps 1 and 2 via two-electron reduction and then go onto form water in step 4 or desorb from the catalyst surface into the bulk in step 3 [79].

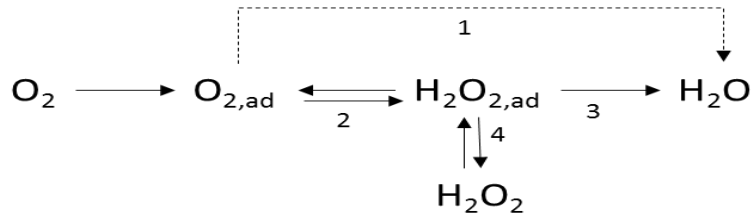


Figure 2-8: Oxygen reduction reaction on metals.



Due to the permeable nature of the membrane, gas crossover of hydrogen from the anode to the cathode and oxygen cross-over from the cathode to the anode can occur (processes II and IV in Figure 2-9). In both cases, gases can react chemically to produce hydrogen peroxide in the cathode catalyst layer (II) and the anode catalyst layer (IV). This can reduce the proton conductivity of the ionomer and weaken the mechanical strength of the catalyst layer and polymer membrane [79]. One way to estimate the rate at which the polymer degrades is to measure the concentration of fluoride ions in the effluent water from the fuel cell [41]. In process III (Figure 2-9), the removal of the carbon support structure in the CL can promote the agglomeration or dissolution of Pt nanoparticles. The free Pt nanoparticles can migrate and become embedded in the membrane to form a Pt band which can promote pinhole formation and enhance peroxide generation in the

membrane core, effectively ending the cell useful life [70]. This degradation mechanism leads to non-uniform membrane thinning and eventual pinhole formation and gas crossover, decreases the effectiveness of the cell and increases the degradation rate [7,67]. The removal of the Nafion ionomer in CL can enable micro-cracks to develop on the electrode surface and in the CL [80].

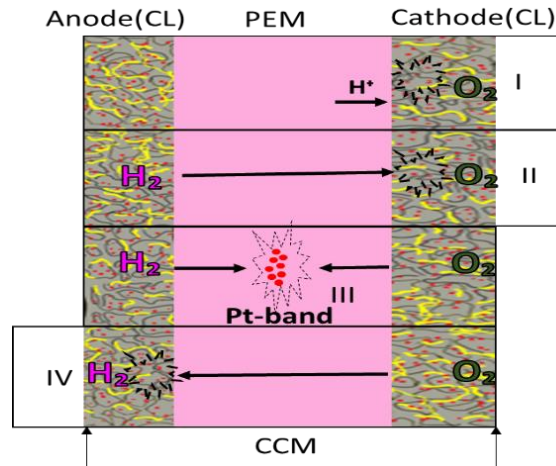


Figure 2-9: Schematic illustration of four different mechanisms of hydrogen peroxide formation.

2.5.2.1.2 Mechanical and thermal degradation

Since chemical degradation gradually breaks down the electrode components, it tends to affect the long-term performance of the fuel cell stacks. Mechanical degradation is considered a major cause of sudden membrane failure that can lead to cracks, tears, delamination and pinholes in the CCM/MEA. The combined effects of mechanical stress due to external and internal pressures and thermal stress caused by temperature cycling causes mechanical degradation. Stress is initially applied through the clamping pressure during the assembly of the fuel cell stack to ensure good electrical connection between the fuel cell components, as mentioned earlier. The mechanical degradation can be accelerated by numerous factors: (1) manufacturing imperfections in the fuel cell components, (2) non-uniformity of the applied pressure, (3) roughness of the GD, microporous layer (MPL) and/or CL, (4) high temperature, (5) high pressure and (6) low humidity. Inadequate humidification causes mechanical stress in the membrane and continuous cycling of its volume due to swelling and shrinking. The volume change of the Nafion membrane disrupts its crystalline structure and tends to shrink the ion channels in the membrane and thereby reduce its ionic conductivity. Upon initial contact with water, the MEA swells 10-20% but is limited in its movement due to compressive forces imposed by the bipolar plates. Consequently, the portions

under the lands are constricted and tend to buckle. If the cell becomes dehydrated, the MEA may stretch and tear [81].

Membrane integrity degrades irreversibly once the mechanical stress exceeds the local yield strength. Polymer creep induced by pressure on the membrane in the strain-hardening region decreases the membrane thickness and in turn accelerates membrane creep [82]. Cracks can also occur at the intersection of the land and channel (crazing sites) and can propagate through the membrane leading to tears, creep or pinholes at ultimate stress points. Both membrane creep and crack formation processes increase gas crossover. If the mechanical stress becomes large enough, delamination of the catalyst layer from the polymer membrane can occur [83].

Other examples of non-homogeneous degradation occur due to pressure gradients across the MEA. This effect is exacerbated by the high gas concentration at the edges of the flow channels and synergy between the chemical and mechanical effects leading to degradation. Therefore, chemical degradation significantly reduces membrane toughness, leading to membrane failures at mechanical stress areas [83]. As a result, the formation of defects such as micro-cracks, tears, creep and pinholes as well as delamination are more likely to occur in these areas.

A high operating temperature has the benefit of enhancing ORR and HOR reaction kinetics, but also significantly facilitates membrane degradation, affecting its stability, hydration and polymer chain nanostructure. Nafion degrades rapidly as temperature increases and irreversibly loses its mechanical integrity. Increasing temperature above approximately 90°C dehydrates the membrane and may induce changes in the nanostructure associated with increased crystallinity [84] and dissociation of ionic clusters. Catalytic combustion of hydrogen and oxygen through defects such as pinholes may create local hotspots at platinum particles and induce thermal decomposition of the ionomer and further degradation of the membrane. Significant increase in gas crossover during long-term operation of PEMFCs is thus often correlated with thermal polymer decomposition due to local hot-spots at pinholes [65,68,85].

2.6 Durability problems for PEMFC stacks in automotive operation

The durability or degradation rate of materials in a PEMFC stack is affected by modes of operation of the fuel cell, environmental conditions, choice of materials and cell design. The mode

of operation of a fuel cell is defined by the load or drive cycle that it is strongly dependent on the driving habits of the vehicle operator. The stack experiences a variety of loads that may be constant or cyclic under normal vehicle operation. A rapid increase in power from 10% to 90% power in 1 second, for example, can be achieved but may lead to material degradation and the formation of defects. Shimoi and co-workers from Nissan have reported on extensive experimental studies to predict electrode degradation rate in terms of start-stop, load cycling and idling modes [86,87]. The principal modes of operation of PEMFCs in automobiles that cause electrode degradation are: (1) start-up/shut-down cycling, (2) OCV/idling/low-load, (3) acceleration and deceleration, (4) ambient air quality and (5) sub-zero temperatures [12,86]. Different environmental conditions such as pressure, temperature and humidity and air quality, also affect the rate of material degradation.

2.6.1 Effect of local degradation of MEA components in automotive environments

Figure 2-10 illustrates three major impacts and estimates of losses in PEMFC stacks causing electrode degradation. Most of this degradation occurs due to rapid start-ups and shut-downs of an automotive device due to short interval. This leads to differences in oxygen concentration that can cause cathode potentials to spike by as much as 1.5 V. These repeated changes in cathode potential have detrimental effects on the fuel cell electrodes such as carbon corrosion, Pt agglomeration, crossover and leaks, resulting in ~44% of the total electrode degradation [87]. Operation of fuel cell stacks under idling OCV conditions causes irreversible degradation and irreversible material loss due to generation of peroxide radicals that can increase membrane thinning and Pt-ECSA losses. Operational losses under these low-load conditions contribute ~ 28% of the total electrode degradation. Continuous ‘ramp-up’ and ‘ramp-down’ cycling also contributes to 28% of MEA degradation due to the loss of surface area via Pt dissolution and water flooding at the cathode when operating at high current densities. This causes continuous mechanical and chemical stress in the polymer membrane and catalyst layers and accelerates degradation[12].

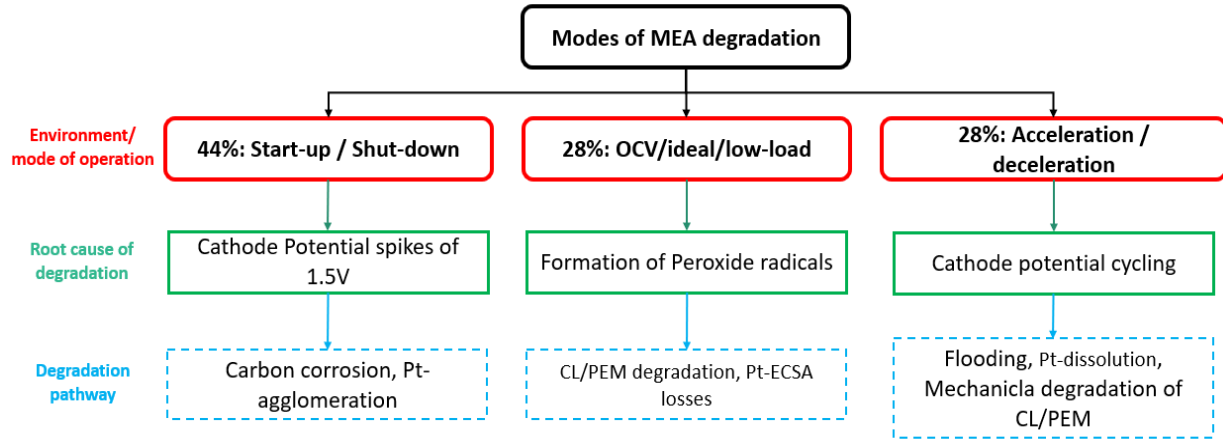


Figure 2-10: Impact and estimation of losses in PEMFC stacks due to three major electrode degradation modes: start-stop, idling and load cycling[12].

2.6.2 Sources of mechanical stresses in PEMFC stack

Fuel cell components may also degrade due to environmental conditions and mechanical stresses from cell construction and design. Mechanical stresses are imposed on fuel cell components via several mechanisms such as compressive forces, shearing forces, temperature variations, MEA hydration and contaminants. The compression of the MEA by the endplates to reduce gas leaks and contact resistant losses causes mechanical stress. This affects softer fuel cell materials such as the membrane and catalyst layer which are compressed under the raised areas (flow channel) of the bipolar plate tends to crack and delaminate. Shear forces due to fluid flow can also mechanically stress and adversely affect fuel cell components. Typical fluids include gases and liquid water which flow through the channels of the bipolar plates and GDL. The pressure within the flow field can cause pressure differences across the membrane, which also stress the materials and lead to cracks forming in parallel to the shear force, especially in the electrolyte [15].

Temperature variations also cause mechanical stress both on large and small scales. Large-scale temperature variations cause differences in material expansion throughout the cell, which in turn causes mechanical stress. Small-scale temperature effects occur when hot-spots form on the MEA surface when reactions proceed at a high rate. They tend to occur in local areas that have higher amounts of catalyst or area dehydrated and so experience higher ohmic losses and localized heating that burn the polymeric components of the fuel cell. Small holes burnt through the polymer electrolyte membrane are referred to as pinholes [88].

Contaminants can also cause mechanical stress if they are inadvertently introduced into the fuel cell during hydration of the reactant gases. When hydration methods such as bubble columns or gas stream misting are used, tiny droplets or aerosols are introduced into the gas stream. This may contain contaminants such as calcium, corrosion products of the metallic bipolar plates such as magnesium and other ions that can enter into polymer membrane and cause local stress in the membrane [12].

2.7 Categorization of local defects in MEA components

Defects can be categorised based on their severity and priority. Defect severity refers to the impact on fuel cell performance and can be categorized as being critical, major, minor and low. Defect severity is an important characteristic because it is directly related to functionality [89]. If a pinhole develops in the membrane, the MEA can no longer function in a stack and would thus be classified as a defect of critical severity [71]. Hu and Cao analysed the evolution of pinhole growth affecting the long-term stability of MEA [90][33]. On the other hand, priority represents the attention which should be paid to the defect and is classified as being immediate, high, medium, and low. For example, micro-cracks have little immediate effect on overall performance but have the potential to propagate into a defect that does require immediate attention. Thus, they are classified as defects of high priority [91][92]. Figure 2-11 shows a detailed categorization of various defects based on their severity and priority.

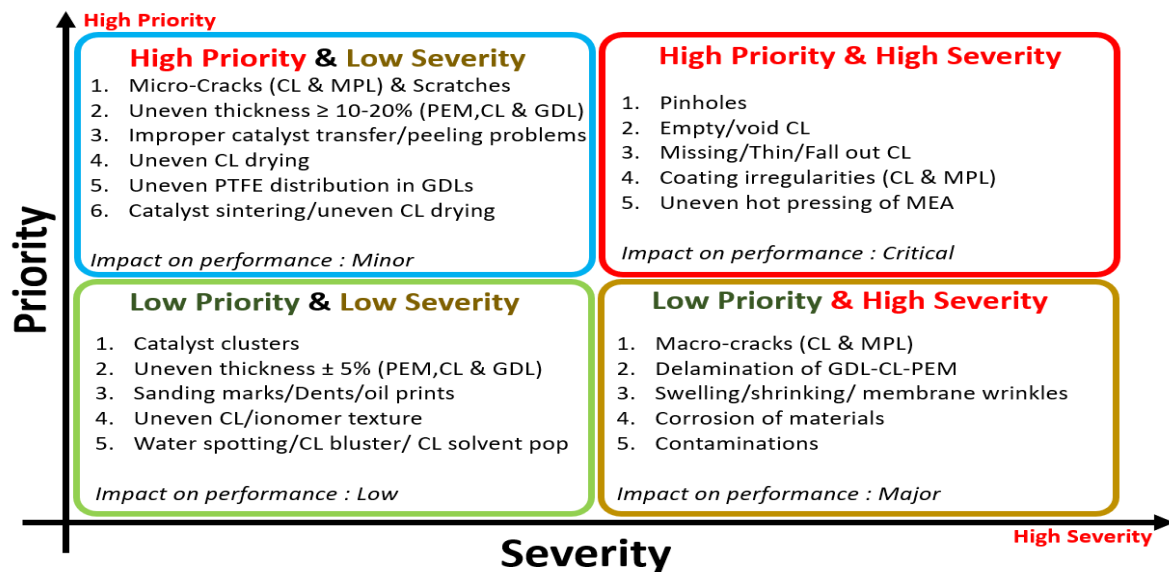


Figure 2-11: Categorization of defects based on severity and priority.

High severity and high priority: A defect that falls in this category will cause the failure of a fuel cell. This defect completely damages or changes the structure of the electrode to the point where operation can no longer continue [89]. Other examples of high severity and high priority defects are pinholes and empty catalyst layers. Pinholes result in the failure of the fuel cell, while the presence of empty catalyst layers which do not promote the electrochemical reactions can lead to large pressure, concentration and thermal gradients and non-uniform heat distributions during operation that can lead to the development of pinholes, particularly at high current densities [93]. These gradients also tend to facilitate gas crossover and enhance radical formation which further decomposes the polymer in the membrane.

Low severity and high priority: Any defect of low severity that has the potential to affect performance is placed in this category. Such a defect does not immediately affect performance in a significant way but could eventually propagate at later stages of operation. This defect should be addressed during the initial stages of the fabrication process. For example, micro-cracks fall in this category because they can eventually develop into macro-cracks [94][77].

High severity and low priority: Any defect that is not predictable at BOL but significantly affects functionality is a high severity and low priority defect. This defect can develop during fuel cell operation during MOL or can propagate from previous defect stages. Eventually, this defect can develop into a pinhole or a similar defect that can be catastrophic. Examples include delamination of GDL-CL-PEM due to shrinking/swelling of membranes[18]. Since it is difficult to predict the delamination of CL at BOL, this defect is considered low priority as opposed to a higher priority.

Low priority and low severity: Low priority and low severity defects have negligible effects on functionality and performance. It should be noted that low priority and low severity defects contribute towards a lower electrode standard. Catalyst clusters, small variations in catalyst layer thickness on the order of $\pm 5\%$, sanding marks and dents are examples of low priority and low severity defects[7][4].

The influence of other defects such as voids, membrane thinning, creep, tears and delamination on cell performance affects long-term stability of the stacks. Smaller defects may not have an immediate effect on cell performance but can eventually cause dangerous gas crossover and ultimately failure if they become large enough. Various authors have investigated operational

defects [7,41,80,95–97] and artificial defects [68] under accelerated stress conditions. Classification of defects in the different MEA components are shown in the table below.

Table 2-1: Different types of local defects formed in MEA components.

Defect type	Material affected	Impact of defect in CCM
Cracks (Fig. 2-12a)	Catalyst layer: separation of catalyst layer without breaking of membrane. Membrane: creeping or tearing inside the solid polymer.	<ul style="list-style-type: none"> • Breaking of catalyst layer • Defect propagation through mechanical stress • Non-homogeneous current distribution • Areas subject to free radical attack • Increased resistance in catalyst area • Growth of defect to a pinhole
Voids (Fig. 2-12b)	Catalyst layer: areas where no catalyst is loaded or missing catalyst regions	<ul style="list-style-type: none"> • Improper catalyst transfer onto the membrane • Increase in surface resistance of CL • Higher chance of water flooding
Delamination (Fig. 2-12c)	Catalyst layer/membrane: separation of catalyst layer from PEM	<ul style="list-style-type: none"> • Separation of CL due to mechanical changes of the PEM • Higher chance of water flooding • Partition of CL and membrane across micro-crack and pinhole areas • Increase in activation losses
Membrane thinning (Fig. 2-12d)	Membrane: variations in CCM thickness	<ul style="list-style-type: none"> • Mechanical weakness of polymer structure inside the PEM • Areas with high radical concentration • Variation of resistance at different locations • Areas of high gas crossover
Platinum dissolution [58] (Fig. 2-12e)	Membrane: separation of Pt nanoparticles and Pt band within membrane	<ul style="list-style-type: none"> • Formation of thin Pt-band within the membrane • Loss of ECSA over entire active area • Damage due to carbon corrosion • Slow catalytic activity affecting long-term stability
Pinholes (Fig. 2-12f)	Membrane: void spaces within membrane that are larger than 10 microns allow gas crossover of fuel and oxidant.	<ul style="list-style-type: none"> • Major effect on performance loss in CCM • Exothermic reaction between H₂ and O₂. • Areas where chemical, mechanical and thermal stresses combine • Instant electrode short-circuits • Develops at flooded areas

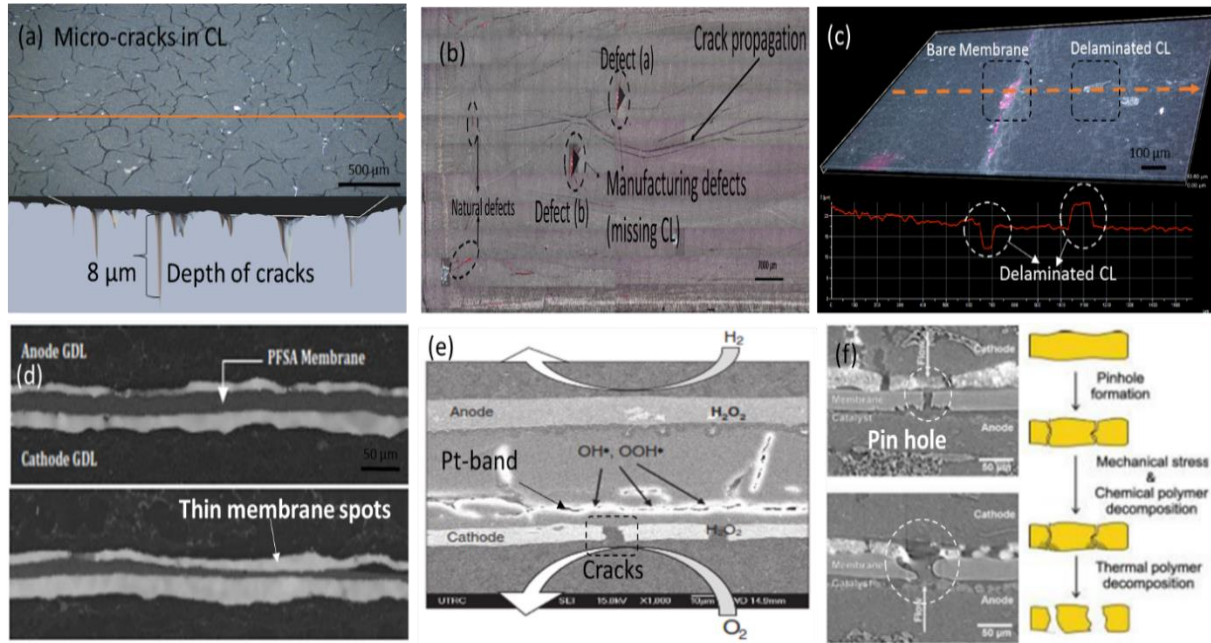


Figure 2-12: (a) Top and side views of CL showing distribution, length and depth of cracks. (b) Missing catalyst regions/thin catalyst area (manufacturing defects) in CCM; the dark line indicates major cracks in CL due to expansion of membrane. (c) Delamination of CL leaving bare membrane. (d) Membrane thinning. (e) Pt band formation in membrane causing radicals. (f) Mechanism of pinhole formation caused by chemical, mechanical and thermal degradation.

Table 2-2: Currently available methods to detect defects in PEMFC components.

Technique	Defect Identification	Size Resolution		References
		Surface resolution	Depth resolution	
Optical microscopy (reflected light)	Surface defects	30 – 2500 μm	10 – 100 μm	[25] [98–100]
Stylus profilometry	Surface defects	10 – 100 μm	0.1 – 10 μm	[42]
Scanning electron microscopy (SEM)	Surface and cross-sectional defects	0.0005 – 1000 μm	0.0001 – 10 μm	[62,101,102]
IR thermography	Surface thermography of defects	~20 cm	–	[25][69,103] [83,104]
Low energy x-ray imaging	Surface defects	0.1 – 2 cm	–	[105]
Electrochemical impedance spectroscopy (EIS)	<i>In-situ</i> measurements	–	–	[101,106]

2.8 Summary

Research in this thesis focuses on identification of abnormalities and defect points on CCM components. Defects such as micro-cracks that are prone to forming during CL fabrication in fresh electrodes or in aged MEAs involve breakage of the CL. Fuel cells can operate in the presence of these defects although their performance and durability can be significantly affected. CCM defects are interconnected. For example, micro-cracks can propagate into macro-cracks that can delaminate entirely from the catalyst layers [80]. As the delaminated area increases, defects force the current to flow away from the void region. In this case, the current is directed around the delaminated areas which become hotspots and develop pinholes [107]. Additionally, void areas can also lead to water flooding in the catalyst layer causing cell productivity to diminish. These areas allow the reaction gases to permeate through the membrane, causing gas cross-over and H_2O_2 formation. The peroxide decomposes the polymer both in the catalyst layer and membrane, causing electrode thinning and ultimately pinhole formation in the CCM, which in turn can cause failure and shutdown of the fuel cell [107]. However, if defects are developed during the manufacturing process, it is suspected that local stress across the defects accelerates faster and can lead to failure or significantly affect the electrode lifetime. The main focus of the proposed research is to investigate the potential correlation between the propagation of defects and performance loss measured under various accelerated conditions.

3 Materials and Experimental Methods

3.1 Fuel Cell Test Station Apparatus

Fuel cell experiments were conducted using a FCAT single cell designed by AFCC with a geometric active area of 48.4 cm². As discussed in section 2.4, the MEAs used in this research work consisted of a 3-layer CCM made of DTM sandwiched between anode and cathode GDLs coated with MPLs on one side. This 5-layer MEA was held in place using 150 µm thick Teflon gasket on either side to form a 7-layer structure. A schematic diagram of the MEA is shown in Figure 1-1 and Figure 4-5. For some experiments, MEAs were put together here at the University of Waterloo from 5 proprietary commercial CCMs; for other experiments, 8 proprietary commercial MEAs were used. Of these, MEA-1, MEA-2, MEA-3, MEA-5 and MEA-8 were manufactured at AFCC, while defected samples MEA-4, MEA-6 and MEA-7 were fabricated at the University of Waterloo.

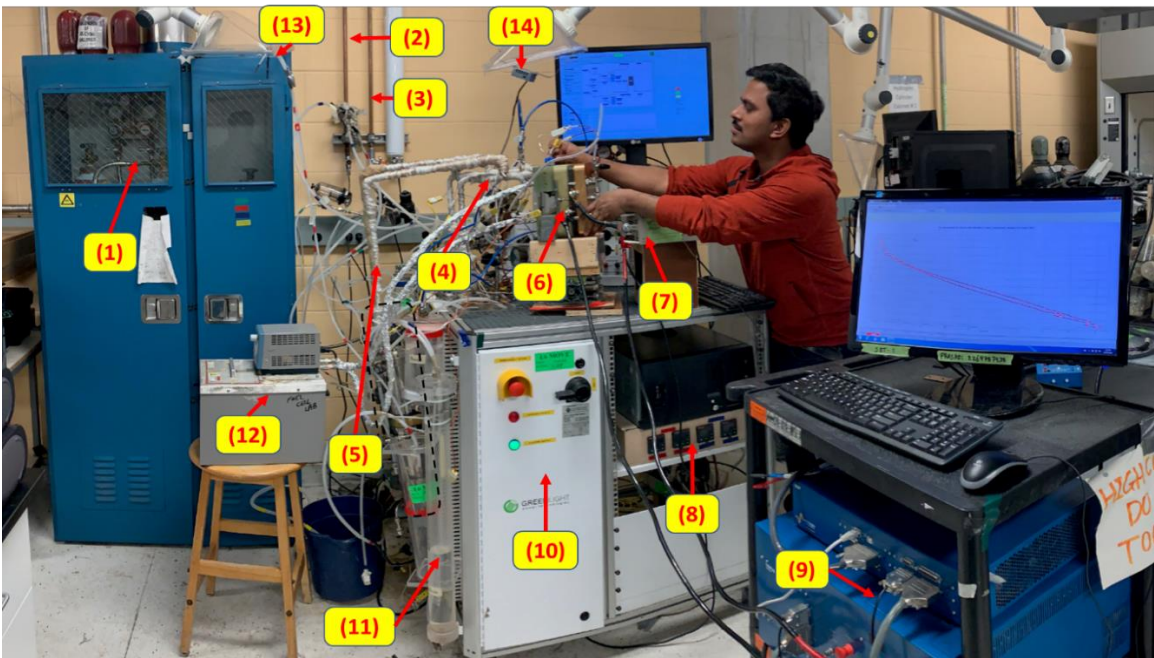


Figure 3-1: G50 fuel cell test station and ancillary components for PEMFC testing. Refer to the text for identification of the numbered components.

All experiments in this research study were conducted using a G-50 fuel cell test station to investigate PEMFC performance. The test station contained the following components (refer to

numbered items in Figure-3-1): 1. hydrogen fuel tanks (99.9995% purity), 2. air supply line, 3. nitrogen supply line, 4. anode and cathode inlet gases from internal humidification bottles (wet), 5. anode and cathode inlet gases from external humidification bottles (dry), 6. FCAT cell (see schematic of single cell in Figure 1-1), 7. external power supply (5 V, 120 A) connected in parallel to the FCAT cell and external electrical RBL 232- TDL load box (Note that the load box was located below the computer monitor), 8. Temperature controllers for humidification bottles, 9. BioLogic Science VMP3 potentiostat with HCP-1005/100A booster and EC lab V10.39 software, 10. Greenlight model fuel cell control chamber (G-50), 11. water outlet bottles to collect condensed water from the fuel cell stack for fluoride ion release analysis. 12. water bath to maintain the stack temperature at 90°C, 13. hydrogen outlet connected to fume extractors, 14, hydrogen sensor to detect any H₂ leaks from the stack.

3.1.1 Leak test

Stacks must be a leak-free to eliminate pressure drops across the MEA and ensure a uniform reactant supply. Internal and external leak tests were regularly carried out at BOL, MOL and EOL to measure the total gas leak rate from all sources: coolant, fuel and oxidant ports and hydrogen cross-over. The procedure for the leak tests is described in Appendix 10-1.

3.1.2 Fuel cell operating conditions

The following operating procedure was followed for all MEAs:

Prior to assembly in the FCAT cell, each MEA was examined using IR thermography to identify BOL defects, as discussed later in section 3.2.2.1.2.1. Once the MEA was incorporated into the cell, a leak test was performed to confirm that the assembly was properly done. If any leak was observed, the cell was re-assembled with new silicone gaskets, Swagelok fittings or bipolar flow plates until the leak test was passed. Once this was accomplished, the FCAT cell was carefully connected to the inlet and outlets gas streams to the G-50 test station shown in Figure 3-1. Hot deionised water was supplied to the stack water inlet port from the external water bath (12) to heat the cell to 90 ± 5 °C.

The operating parameters such as gas flow rate, stack pressure, humidification bottle and line temperatures were set through HyWareII software. Two humidification bottles were used to control the RH levels of the gas streams - an internal humidification bottle supplied wet gas and external humidification bottle supplied dry gas. Once the stack reached the cell temperature, the

nitrogen flow was stopped, and reaction gases were supplied to the anode and cathode using Bronkhorst EL- mass flow controllers (MFC) and pressure transducers. The dew point temperature of the internal and external humidifiers was set by the user. As the gases exited from the humidifiers, they entered a stainless-steel tube wrapped with heaters. The temperature of gas stream tubes was adjusted to achieve the desired relative humidity. Internal thermocouples were used to monitor the temperatures of the gas streams inside the stack. An external power supply (5V and 120 A) was connected in parallel to the cell and load box to provide additional voltage to drive the current above 50 A. Two load boxes (9) were used in this study based on the requirements of the experiments. All the electrochemical analyses (e.g., polarization curves, LSV, CV and EIS) were carried out using a BioLogic Science VMP3 potentiostat with an HCP-1005/100A booster. As current was applied to the cell, the reactions progressed, and water and heat were generated as by-products. The water from the anode and cathode outlets was collected in knockout drums. In some experiments, this water was further analysed for its fluoride ion content using ion chromatography to assess the extent of ionomer degradation. During the OCV and COCV ASTs (detail ASTs were discussed in section 6.3), water was collected every 8 – 16 hours of operation. As discussed earlier, the cell temperature was controlled by the circulating external water bath. The operating parameters used to condition the MEAs for BOL are listed in Table 3-1.

Table 3-1: Operating conditions for MEA conditioning at BOL.

BOL conditioning	Anode	Cathode
Fuel	H ₂ (99.995%)	Air
Inlet Pressure (Kpag)	270	250
Cell Temperature	60°C	60°C
Stoichiometry	1.2	3
Inlet Relative Humidity	100%	100%
Current Density	1.5 A/cm ²	
Duration of test	12 hours	

3.1.3 Accelerated stress tests (AST)

Accelerated stress tests reduce the time and cost needed to assess the durability of fuel cell systems and estimate the life time of fuel cell stack in heavy-duty automotive applications [108]. Membranes and catalyst layers are critical components of fuel cell stacks operating in automotive systems. They must be highly durable and tolerate a wide range of operating conditions including

high and low voltages, temperature ranging, relative humidity (RH) and variable gas compositions. AST protocols are important for targeting and understanding specific degradation mechanisms. ASTs must be designed to cause failure modes similar to those observed under actual operating conditions in order to provide meaningful insight into the causes and effects of failure in real-time operation of fuel cells. These failure modes vary depending on whether they are being operated for automotive or stationary applications. The primary aim of the ASTs used in this study was to conduct experiments compatible with steady state operation that has been shown to significantly affect MEA performance in automotive systems. Factors that accelerate degradation of the MEA are temperature, relative humidity, freeze-thaw cycling, load cycling and startup-shutdown. Standard protocols developed by the US Department of Energy (DOE) will be followed in this research for specific analysis [109].

Considering the sensitivity and mechanical stability of CCMs (catalyst layer – membrane – catalyst layer, three-layer electrode without GDL) and MEAs (GDL – catalyst layer – membrane – catalyst layer – GDL, five-layer electrode), experiments were conducted in two different types of cells. The first set of experiments was carried out in a custom-built test cell designed and fabricated at the University of Waterloo to investigate CL defects in defected CCMs. A detailed description of this test cell is given in section 4.3.4. Aging experiments on CCM samples (Chapters 4 and 5) and GDL samples (Chapter 7) were performed using this custom-built test cell. The second set of aging experiments on the MEAs (Chapter 6) was done in a standard FCAT fuel cell designed and supplied by AFCC.

3.2 MEA Characterization techniques

To investigate the chemical degradation of CCMs and MEAs, experiments were carried out under open-circuit voltage (OCV) conditions, as discussed in Section 3.2.1.1.1. To characterize the mechanical durability of CCMs and MEAs, an AST consisting of RH cycles was applied, as discussed in Section 3.2.1.1.2. Degradation tendencies of a cell were gleaned by examining its resulting polarization curves at regular intervals. The electrochemical performance of the MEAs was measured using *in-situ* characterization tests throughout the AST. The extent of membrane degradation was also assessed by measuring the fluoride ion release rate in water samples collected

in the anode and cathode outlets. Fresh samples and degraded samples after fuel cell operation were also inspected using *ex-situ* characterization techniques.

3.2.1 *In-situ* characterization: electrochemical analysis

In situ diagnostic techniques were employed in this research to investigate the degradation of the CCM/MEAs. These included open-circuit voltage (OCV) analysis with the RH maintained at a fixed low level or cycled between dry and wet levels, polarization analysis, linear sweep voltammetry (LSV), electrochemical impedance spectroscopy (EIS), cyclic voltammetry (CV) and ion chromatography. These procedures or techniques are described in the following sub-sections [110].

3.2.1.1 Open-circuit voltage AST

Open-circuit voltage accelerated stress tests (denoted here as OCV-AST) were used to examine the chemical degradation of CCM/MEA electrodes. These conditions promote the homogeneous degradation of electrode active areas by inducing reactant crossover through operation of a stack under no load (zero current) and maximum catalyst potential for extended periods of time [111]. In addition, the high electrode potential at the cathode under open-circuit conditions can lead to dissolution of the Pt catalyst. During the operation, as the membrane degraded, the OCV of the cell decreased until it reached the pass/fail criteria, which was set to be 0.8 V in this study. Two sets of OCV AST were used:

1. The first OCV-AST test was conducted in a custom-built test cell and aimed at accelerating catalyst layer defects in the CCM. The details of CCM-AST are discussed in section 4.3.6.
2. The second OCV-AST was conducted in the FCAT cell and aimed at accelerating defects in the MEA. It involved two sets of experiments in which the RH was held at a constant low level and cycled between wet and dry conditions. The operating conditions for MEA-AST are shown in Table 3-2 and implementation of this AST procedure is described in section 6.3.

3.2.1.1.1 Effect of OCV at constant low RH

Numerous electrode degradation studies have shown that the chemical degradation rate of the membrane is accelerated when a cell is held at the OCV at high temperature and low RH. Thus, these are good conditions for evaluating the chemical durability of an electrode [112–115]. The OCV-hold test at constant low RH in this work was designed to accelerate the chemical

degradation of MEA that decomposes the polymer in the reinforced membrane matrix and catalyst layers. This would cause several events to occur inside the fuel cell: gas crossover generating H_2O_2 that initiates free radical formation and membrane thinning and eventually the formation of micro-cracks and pinholes. Common consequences of chemical degradation are loss of ionomer in the anode and cathode CLs, membrane thinning and pinhole formation. The AST in our study was carried out at high temperature ($90^\circ C$), high gas inlet pressure of anode/cathode (250/270Kpa), high flow rates (2/10 SLPM) and low humidity (30/30 %RH). Therefore, we would expect these AST conditions to significantly accelerate aging of the CCM/MEA components. Similar observations were also reported in the literature [5,12,17].

3.2.1.1.2 Effect of OCV at cyclic RH

The RH cycling protocol in this research work was designed and implemented to accelerate both chemical and mechanical degradation of the membrane and catalyst layer defects. ASTs involving the application of RH cycles (wet/dry) over short intervals at high temperature were particularly useful for assessing membrane durability (in PEMFC stacks operating under realistic conditions) in real life operation. Under high RH conditions, the membrane tends to swell and buckle in-plane due to the constraining pressure of the bipolar plates, leading to catalyst layer cracks and delamination of GDL/catalyst layer/membrane interface. On the other hand, at low relative humidity, the membrane should shrink and lose stiffness and strength. Also, when not highly hydrated, the membrane is more prone to chemical degradation and a weaker interlayer bond strength of MEA components. The repeated humidity cycling of high and low conditions induces internal and external stress on the membrane.

Throughout these experiments, the RH of the reaction gases was cycled from 80% (wet) to 20% (dry) on the cathode side and maintained at 80% on the anode side. The decision to select 80% RH rather than 100% was to reduce the possibility of water flooding in the membrane. On the other hand, 20% RH was selected over 0% to prevent excessive drying of the membrane which could lead to large residual tensile stresses at $90^\circ C$ [119][118]. This approach of testing MEAs is of great interest to electrode developers and membrane researchers and so commonly used [67]. The AST operating conditions implemented in this research is listed in Table 3-2.

Table 3-2: Protocols of MEA degradation ASTs used in this study.

AST condition	OCV at constant low RH	OCV at cyclic RH	Polarization curves
AST duration	≤20% loss in OCV or ≤0.8V	≤20% loss in OCV or ≤0.8V	data collected at every OCV interruption
Current Density	0 A cm ⁻²	0 A cm ⁻²	0 – 2 A cm ⁻²
Cell temperature	90°C (±2%)	90°C (±2%)	90°C (±2%)
Fuel/Oxidant	99.995% H ₂ /air	99.995% H ₂ /air	99.995% H ₂ /air
Gas flow	anode: 2 slpm H ₂ cathode: 10 slpm Air	anode: 2 slpm H ₂ cathode: 10 slpm Air	anode: 2 slpm H ₂ cathode: 10 slpm Air
Pressure	270/250 kPa	270/250 kPa	270/250 kPa
Relative Humidification	anode: 30% RH (±2%) cathode: 30% RH (±5%)	anode: 80% RH (±2%) cathode: 20% - 80% RH (±6%)	anode: 80% RH (±2%) cathode: 80% RH (±2%)
F⁻ ion release	monitored at least every 8 - 16 hours		no target

3.2.1.2 Polarization analysis

Polarization (*I-V*) measurements were conducted using the G-50 fuel cell test station with an RBL 232 (TDL electronic device) electronic load box. Hydrogen gas and air were fed to the anode and cathode at stoichiometric ratios of 1.5 and 3, respectively, while the cell was kept at a constant temperature of 90°C using a water coolant plate. *V-I* curves were obtained at a temperature of 90°C with the same relative humidity at both the anode and cathode. The polarization curves were obtained by applying a given current density and measuring the resulting cell voltage after 1 minute. Current densities of 1.5, 1.2, 1, 0.8, 0.6, 0.4, 0.2 and 0 A cm⁻² were applied. When fresh unconditioned MEAs were tested, the stack was conditioned by applying a load of 1.5 A cm⁻² for a minimum of 12 hours. If the cell voltage dropped below 0.15 V for more than 30 seconds, the fuel cell was considered to be unable to maintain the maximum current density and the current was immediately decreased in order to raise the cell voltage to 0.3 V. The resulting polarization curve was constructed by plotting cell voltage against the current density. We conducted a preliminary set of experiments at different fixed RH values ranging from 50% to 100% to determine the level that yielded the best cell performance at high current densities since RH shows strong influence on mass transport losses in the cell. An RH of 80% was found to yield the best fuel cell performance and so was used for the remainder of the study. The operating conditions for polarization analysis are listed in Table 3-2.

3.2.1.3 Linear sweep voltammetry - H₂ crossover

Hydrogen crossover is an important indicator to assess the health of the MEA at different stages. Because the rate of oxygen crossover tends to be lower, the rate of hydrogen crossover is typically of greater interest. The flux of hydrogen crossover is obtained by measuring the crossover current and converting this to a mass flow through the membrane using Faraday's law [118]. Equation (3.1) relates the molar flux N_{H_2} of H₂ (moles cm⁻² s⁻¹) through the membrane to the crossover current density i_{H_2} (A cm⁻²):

$$N_{H_2} = \frac{i_{H_2}}{2F} \quad (3.1)$$

where F is the Faraday constant (96485 C mol⁻¹). The rate of hydrogen crossover depends on the membrane thickness, microstructure and partial pressure. As membranes thin, gas crossover increases. The rate can be calculated using Fick's law:

$$N_A = \frac{P_M(P_1 - P_{11})}{\delta} \quad (3.2)$$

where N_A is the gas flux, δ is the membrane thickness, P_M is the membrane permeability and P_1 and P_{11} are the partial pressures of the reactant gases on the anode and cathode sides. As the extent of gas crossover increases, pinhole formation leading to sudden shutdown of the cell becomes more likely.

The hydrogen crossover current was measured using linear sweep voltammetry using a BioLogic Science VMP3 potentiostat with a HCP-1005/100A booster and EC lab V10.39 software. Inert nitrogen gas was passed through the cathode (working electrode), while hydrogen was fed on the anode side (counter electrode). As the MEA aged, H₂ from the anode side begins to cross over through defects and reacts at the cathode to generate crossover current. To isolate the effects of hydrogen crossover, the voltage was scanned from 0.05 V to 0.7 V at a scan rate of 2 mV s⁻¹. Any H₂ permeating through to the cathode would be oxidized immediately and its current at 0.4 V was measured and taken to be the crossover current [12]. At potentials higher than 0.4 V, the rate of hydrogen oxidation became limited by hydrogen permeation rates.

3.2.1.4 Electrochemical impedance spectroscopy (EIS)

Galvanostatic EIS was used to characterize the effect of aging of the MEA using a BioLogic VMP3 impedance analyzer with the HCP-1005/100A booster over a range of 10 μ Hz to 10 kHz. EIS is a powerful technique to measure the ohmic resistance, charge transfer resistance

and mass transfer resistance of a PEMFC. Functionally, the membrane of an MEA acts as a resistor, while the anode and cathode CLs act similarly to capacitors in a circuit consisting of the cathode working electrode and anode counter electrode. Figures 3-2a and b show the equivalent circuit describing electrochemical processes and a typical Nyquist plot, respectively, of the PEMFC. Each of the anode and cathode catalyst layers can be modelled as an R-C element with capacitor C and a resistor R_{ct} in parallel. R_{ct} represents the charge transfer resistance in the catalyst layer and C represents the capacitance of the electrochemical double layer at the electrode/electrolyte interface. The two R-C elements are connected in series to $R_{\Omega, mem}$ which represents the membrane resistance. Since the anode reaction is notably faster than the cathode reaction, the cathode reaction is rate controlling and of greater interest.

The factors contributing to the voltage loss can be quantified by determining the characteristic parameters of the equivalent circuit. The capacitors in the circuit act as ideal conductors at high frequencies, resulting in the elimination of the imaginary components of the impedance. Since $R_{\Omega, mem}$ is the only element limiting the flow of current in the equivalent circuit at high frequencies, the resistance of the membrane can be determined by the point of intersection of the impedance curve with the x-axis (real impedance) at the high frequency end. The capacitors can be assumed to be perfect insulators at low frequencies. Therefore, the voltage drop across the single cell MEA is determined by the sum of the remaining resistors. Similar to the membrane resistance, the total resistance of the cell is obtained from the intersection of resistance with the real impedance axis (x-axis) in the low frequency region [120].

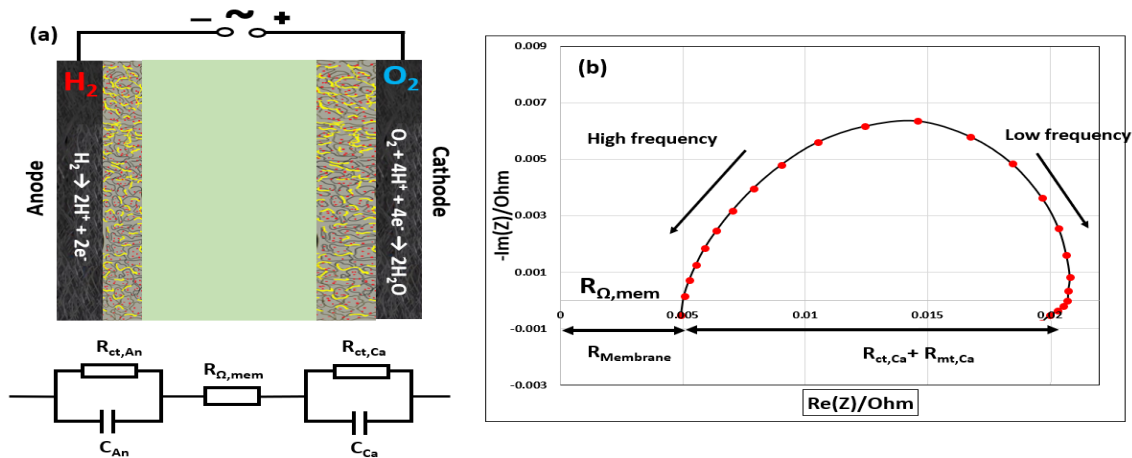


Figure 3-2: (a) Equivalent circuit of electrochemical processes occurring in PEMFC. (b) Nyquist plot (EIS) of PEMFC showing how the membrane resistance $R_{\Omega, mem}$, cathode charge transfer resistance $R_{ct, Ca}$

and cathode mass transfer resistance $R_{mt,Ca}$ are determined. The charge transfer resistance of anode is neglected due to the fast kinetics of the hydrogen oxidation reaction (HOR).

The electric resistance of the anode serves as a reference, allowing charge transfer resistance due to the oxygen reduction reaction (ORR) at the cathode to be studied through AC impedance [121]. The experiments were carried out in the galvanostatic mode by applying a signal with a DC bias current of 5 A (0.1 A/cm²) and a 10% AC amplitude of 500 mA at frequencies ranging from 100 KHz to 100 mHz at intervals of 6 points per decade.

3.2.1.5 ECSA measurement using cyclic voltammetry (CV)

Cyclic voltammetry (CV) is perhaps the most versatile electroanalytical technique for the study of electroactive species. CV allows measurement of the electrochemically active surface area (ECSA). ECSA is calculated using the relation given in Eqn (3.3) at different time intervals to yield an estimate of the active surface area of the Pt catalyst based on the charge associated with H₂ adsorption. This area is an important measure of the degree of degradation of the CL. The potential is cycled typically at a scan rate of 5 or 10 mV s⁻¹ over a potential range between 0 and 1.2 V (vs. RHE). The number of Pt surface atoms is estimated from the columbic charge Q_H for hydrogen adsorption/desorption assuming the charge to cover the surface with 1 cm² of Pt is $210 \frac{\mu C}{cm^2_{Pt}}$ [28].

$$ECSA \left(\frac{m^2_{Pt}}{g_{Pt}} \right) = \frac{Q_H \left(\frac{C}{cm^2} \right)}{\left[210 \left(\frac{\mu C}{cm^2_{Pt}} \right) * L_{Pt} \left(\frac{g_{Pt}}{cm^2} \right) \right]} \quad (3.3)$$

where L_{Pt} represents the Pt loading in the electrode.

3.2.1.6 Ion chromatography

Measurements of the fluoride emission rate (FER) and the conductivity of water were used to characterize the degree of chemical degradation due to ionomer leaching in the catalyst layers and membrane. The FER was determined by using ion chromatography (Dionex DX 500 ion chromatographic analyzer) on samples collected in the water discharged from the anode and cathode. The effluent water from the anode and cathode outlets was collected from the stack during OCV ASTs approximately every 8 – 16 hours, typically at the beginning and end of each day.

3.2.2 *Ex-situ* characterization

In order to map the defects caused by degradation, samples were examined *ex-situ* by optical microscopy, SEM, TEM, profilometry and IR thermography. The development of a non-destructive technique to monitor the propagation of defects in the CCM/MEAs at different stages of operation is one of the main goals of the research. Conventional methods of measuring defects in the CCM/MEA using destructive methods i.e., SEM and TEM electron microscopy help fuel cell electrode developers to monitor defects during BOL and EOL, but cause irreparable physical damage to samples. Thus, with this approach, it is impossible to measure cell performance loss and correlate it directly with the propagation of defects in CCMs during the operation of fuel cell at MOL. A non-destructive technique to inspect the MOL defects that affect PEMFC performance is therefore required for fuel cell manufactures and developers to better understand the causes of electrode degradation and failure of the CCM/MEA.

3.2.2.1 Non-destructive methods

3.2.2.1.1 Optical microscopy

CCMs electrodes are manufactured at industrial production site. Defected CCMs are separated from the production line and supplied to University of Waterloo by the industrial partners AFCC to investigate the effect of manufacturing defects in catalyst layers on cell performance. Samples were carefully examined using an Eclipse MA 200-inverted-metallurgical-reflected light microscope to identify defects on the catalyst layers. The CCMs with defects were separated from non-defected CCMs for further microscopic analysis. NIE software was used to image the surface morphology and generate details on defects such as surface profiles, orientation, dimensions and aspect ratios. In addition, 3D defect maps were produced using the digital information obtained from Z-profile scanning. This procedure was used throughout the life of a CCM electrode to characterize the defects at BOL and monitor their evolution at MOL and EOL. Finally, the defects were characterized with respect to their area, length, width and aspect ratio. The experimental setup developed for investigating CCM defects using optical reflected microscopy are discussed later in section 4.3.2.

3.2.2.1.2 IR thermography for inspection of MEA components

Infrared thermography is a useful technique for characterizing surface properties of materials that cannot be identified from their visible appearance. Due to its high resolution and very sensitive detection, it is considered to be a good choice for quality control. Its application is widely used in various research fields to characterize defects in metal surfaces, membrane folds, catalyst layer defects, concrete structures and conduct surface analysis [8,16,122,123]. Previous studies have shown that the detection limit of defects is in the centimeter-to-millimeter range with certain limitations in accurately determining defect shape and length. For example, Aieta et al.[16] and Vengatesan et al.[67] used IR thermography to detect the location of defects in MEAs and GDEs, but they did not clearly report defect shape and size. Fuel cell manufacturers are often interested in identifying sub-millimeter defects in catalyst layers and GDL substrates. Therefore, the aim of IR detection technique is to identify GDL defects membrane, catalyst layer defects in the CCM/MEA and sub-millimeter defects in the GDL/MPL in less than 1 minute of inspection time. The improved IR technique is discussed in section 7.3.1.

3.2.2.1.2.1 IR examination of MEA defects

Our use of IR thermography to detect MEA defects is based on the idea that any pinholes in the membrane or leak areas would facilitate hydrogen crossover from the anode to the cathode. The direct combustion of the crossover H_2 and O_2 in the presence of the Pt catalyst would generate heat (infrared energy) that appears as a hotspot on the IR image at the location of the pinhole. The software in the camera converts the IR image into a thermal image. We conducted IR thermography by passing H_2 gas (20% H_2 diluted with 80% N_2) over the anode and exposing the cathode to the air. The IR camera and the electrode were placed inside a dark environmental chamber to eliminate external light reflections and the camera lens was positioned 1 meter away from the cathode. The thermography image was displayed by assigning a specific color to each thermal energy level. More details on the IR thermography setup developed to investigate membrane pinholes in the MEA are given in section 4.3.3.

3.2.2.1.2.2 IR examination of GDL defects

IR examination was also used to detect defects in the GDL/MPL substrates. To do this, we modified the procedure from that described above in order to improve its sensitivity from that used to examine MEA defects. Our approach was to accentuate temperature differences over the

GDL/MPL surface that would already arise during normal IR thermographic examination. To achieve this, we used DC excitation to heat the GDL-MPL surface, while cold air was pulled through the GDL using a vacuum pump located below a porous ceramic plate at the bottom of the set-up. The developed setup is discussed in section 7.3.1. More air would be expected to be pulled through the thinner defected areas, thereby making these areas cooler than the areas with no defects. Based on this idea, we monitored temperature variations with an IR camera placed 1 meter away from the setup in a dark environment as the DC current was passed through the sample. From careful measurement of the temperature differences over the MPL surface, we identified the defected areas from the cold spots appearing on the IR thermograph. This method allowed MPL defects larger than 1 mm to be detected in less than 1 min. More details on the IR thermography setup to detect defects in GDL-MPL substrates are presented in section 7.3.

3.2.2.1.3 Electrical measurements

This research also focused on measuring the in-plane electrical conductivities of GDL-MPL substrates using a four-point conductivity probe device. The in-plane electrical sheet resistance was measured using the standard four-point probe technique. This method works best for applications with low surface resistance where the contact resistance between the MPL surface and probes is negligible and does not significantly affect the measurements. This contrasts with the two-probe technique, where the contact resistance has an influence on resistance measurements [124–126]. The measurements are accurate when the distance between the probes is small compared to the size of the sample and none of the probes are placed too close to the edge of the sample. A schematic of the four-point probe technique used in this study is shown in Figure 3-3a. The distance between each probe is set to 1 mm. A DC current of 60 mA was applied between the two outside probes using a 4-wire Kelvin meter and the resulting voltage drop along the surface between the two inner probes was measured. With corresponding current and the voltage readings, the resistivity (ρ) of the sample could be calculated using Eqn (3.4):

$$\rho = 2\pi S \frac{V}{I} \quad (3.4)$$

where I is the current flowing along the sample surface from probe 1 to 4, V is the voltage drop between inner probes 2 and 3 and S is the distance between the probes.

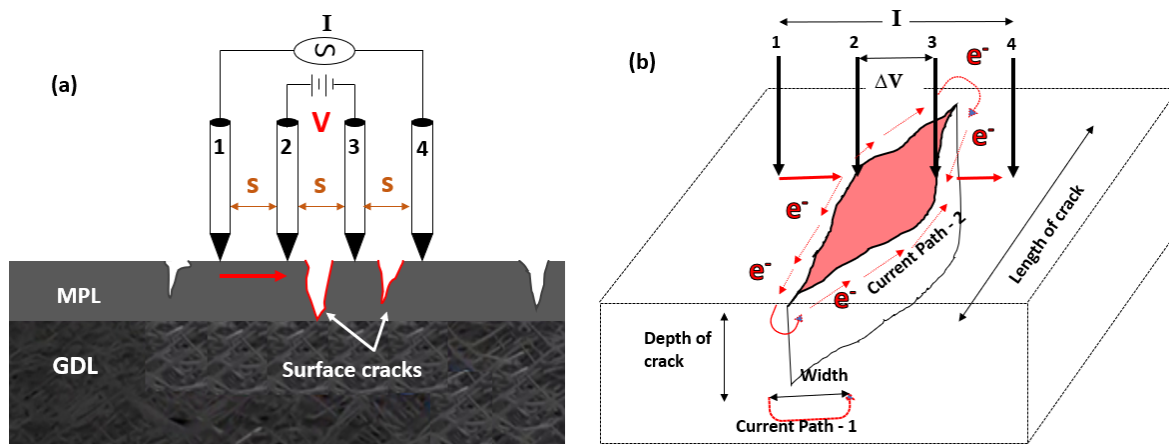


Figure 3-3: (a) Schematic of four-point probe method used to measure the surface resistance of MPL with cracks (b) Schematic of electron flow path across the MPL crack; red region outlines a surface crack.

The GDL samples were cut to be exactly the same size as the cathode active area (i.e., 12 x 4 cm). The surface resistance was determined by placing the GDL on top of a vacuum stage to ensure that the surface remained flat during measurements. The in-plane resistance was determined before and after the GDL was subjected to the AST. Figure 3-3b shows a schematic indicating the electron flow path across a crack on the MPL surface along both its width (current path 1) and length (current path 2). The voltage drop corresponding to the in-plane resistance depends upon the geometry of the cracks and rises as the geometric area of the crack increases [127]. At BOL, it is expected that the MPL cracks are small in area and so this voltage drop would be lower. As samples are aged during RH cycling, the cracks tend to grow significantly more along their lengths than their widths. Therefore, the electrode resistance increases with MPL crack propagation and this should lead to an increase in the in-plane resistance on an aged MPL surface.

3.2.2.2 Destructive methods

3.2.2.2.1 Scanning electron microscopy

CCM samples at EOL were examined using scanning electron microscopy (Phillips XL30 scanning electron microscope with backscattering detection at 350x magnification and 15 KV) to examine and determine in particular thickness variations, Pt dissolution in the membrane and other structural damage caused by degradation. After reaching the EOL during the ASTs, the MEAs

were prepared for SEM analysis by first carefully removing GDLs from the aged MEAs. To do this, sections of CCM were submerged in liquid N₂. Once frozen, the CCM samples were broken into small sections while still submerged. For better cross-sectional analysis, samples were mounted on the side of stainless-steel nuts or SEM stages so that the fractured side was exposed for SEM analysis.

3.2.2.2.2 X-ray tomography analysis

The internal microstructure of the GDL/MPL was studied using x-ray micro-computed tomography (Zeiss Xradia 520 3D x-Ray microscope). The GDL/MPL interfaces and cross-sectional images were generated by measuring the attenuation of x-rays penetrating through the sample. The GDL stack was rotated and moved along the axial direction during the scanning process to generate a stack of sliced images, as shown in Figure 3-4. From these stacks of sliced images, a 3D visualization of the internal structure of the GDL/MPL (i.e., intrusion of MPL into GDL, thickness variations in GDL/MPL, in-plane and through-plane MPL cracks) was constructed using Dragonfly and ImageJ image processing software.

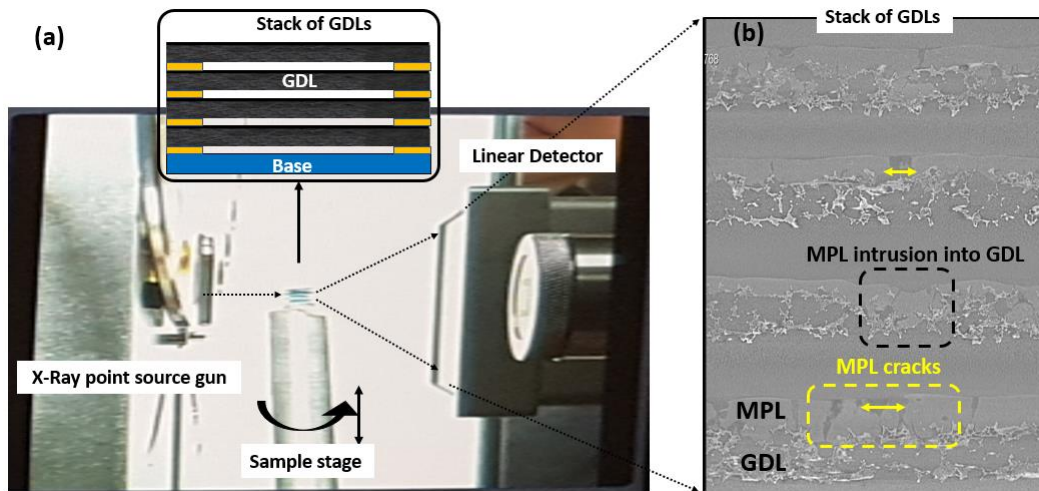


Figure 3-4: (a) Experimental setup of x-ray tomography whereby a detector measures the attenuation of x-rays penetrating through the stack of GDL samples to generate cross-sectional images of the internal structure features of GDL-MPL, as shown in (b).

4 Non-Destructive Method of Investigating Catalyst Layer Defects in CCM

The following chapter is adapted from the paper by Muneendra Prasad Arcot, Kelly Zheng, Jake McGrory, Michael Fowler and Mark Pritzker published in *International Journal of Energy Research*: “Investigation of catalyst layer defects in catalyst-coated membrane for PEMFC application: Non-destructive method”. 42.11(2018): 3615–3632.

The author’s specific contribution was to develop a non-destructive technique to inspect catalyst layer and membrane defects in the CCM/MEA that negatively affect PEMFC performance, particularly in the early stages of operation. In this research, the experimental setup using optical microscopy and IR thermography were developed, defect analysis experiments were conducted on 48 cm² CCMs and these defects were classified and categorized based on area, size and orientation for quality control and assessment that could be of use to industrial operators. Undergraduate Co-op students Kelly Zheng and Jake McGrory assisted in the computer analysis of the microscopic images.

4.1 Introduction

The development of reliable and accurate methods for detection and characterization of defects is critical if the commercial adoption of PEMFCs is to become more widespread. In addition, the need will further grow as continuous, roll-to-roll manufacturing processes are adopted in order to produce CCMs on a commercial scale. The requirements of such a system are very demanding when one considers the large difference in scale of the initial size of defects (i.e., cracks, scratches/deep cuts, missing/thin/empty catalyst layer and membrane pinholes defects) relative to that of the entire CCM that must be monitored. To provide a sense of this difference in scales, the defects can typically be on the order of 0.04 – 2.0 cm² in area, whereas the dimensions of the rolls are ~ 15.4 x 70.0 cm and the linear speed of a electrode sheet scanned during manufacturing can be ~ 9 m min⁻¹ [25]. Since the current quality control techniques are limited to millimeter length, more sensitive detection methods are required to detect defects at the micrometer scale. Since the entire CCM area should be ideally characterized to ensure that no

potentially damaging defects are present, the detection techniques should be rapid, accurate and reliable with a resolution ranging from the micron scale to the millimeter scale.

The detection methods currently described in the literature are not able to satisfy all of these requirements. For example, the CCM thickness can be measured manually by cutting a sample or using laser-point measurements at specific locations, but cannot be done over the entire area in real time [25]. Novel techniques including optical reflectometry and IR imaging with DC excitation have been proposed in an attempt to meet some of these requirements [69,103]. Although several studies have been performed on defects artificially introduced at specific locations, very few studies on real defects in catalyst layers have been reported to date [7,8,25,43,69,94,105,128,129]. Furthermore, the studies on real defects were not concerned with localized effects that can have large effects such as increased surface resistance and loss of catalyst, the morphology of defect growth or the effect of the defect location within the CCM on the resulting cell performance. Consequently, many gaps in our fundamental and comprehensive understanding of the nature of these defects in the beginning-of-life (BOL) state and the manner in which they may or may not propagate during PEMFC operation still exist.

Although defects in the CL may not have a large impact at BOL, they grow in size and eventually degrade such properties as the in-plane resistance of the CL and reduce the performance of cell in the ohmic region. Although methods for detecting defects on newly-manufactured fuel cell components have been proposed, no reliable *in-situ* method to monitor their propagation in the CCM during fuel cell operation has been developed for two principal reasons.

- The majority of these methods have been developed using artificial defects that do not entirely mimic real manufacturing defects [130,131].
- Widely used defect detection techniques such as SEM and TEM are destructive methods and render the tested cell components unusable for further experimentation or operation.

These factors have limited our understanding of how these defects propagate from BOL during operation. Our focus in this phase of the research is to measure the propagation of defects in the CLs caused by deformation resulting from repeated expansion and shrinkage of the membrane.

Therefore, the specific objectives of this study are to:

- I. Develop a non-destructive method to investigate and characterize CL defects in CCM electrodes,
- II. Investigate and gain insight into the aging of various types of defects and their propagation and
- III. Classify defects in the CL with respect to their dimensional changes.

Toward the first objective, we have developed a method of defect detection aimed at overcoming the shortcomings of the previously reported approaches described above. We outline a non-destructive method to detect and monitor defects in the CL using reflected light microscopy that does not prevent the CCMs from being re-installed and re-used in the fuel cell. This method provides 100% areal inspection of the catalyst layers in CCMs.

The second objective is to investigate the aging of CCMs using a custom-built test jig that enables samples to be examined without any damage due to flow channel plates or indentation of the CL by GDLs. This safe operation allows the CL defects to be monitored at both MOL and EOL. This investigation is performed on two commercial CCMs. The defects in the first CCM can be attributed to its long-term storage under conditions of uncontrolled relative humidity, while those in the second CCM are caused by improper decal transfer of the catalyst during fabrication. This first CCM has been included in the study to highlight the importance of the proper storage conditions even prior to use. For best performance during operation, CCM electrodes should be shipped and stored in a sealed and specially designed container and environment to maintain stable moisture content and minimize dimensional changes prior to use. Ideally the electrodes should be kept out of direct sunlight in a climate-controlled environment at temperatures between 21°C and 27°C and relative humidity between 45% and 55% [132]. If CCMs are exposed to typical room conditions, the membranes will quickly equilibrate to ambient relative humidity and change their dimensions accordingly. As a result of deformation in the membranes, micro-cracks can form in the catalyst layer during this shipping and storage period even before the CCM is used. As a part of our quality control analysis, we have included in this study CCMs that had been stored for 2 years in a typical room environment where the relative humidity was uncontrolled and varied between 20% and 75% to investigate the effect that uncontrolled storage can have on the distribution of cracks in catalyst layers. The types of defects that can form include cracks, missing/empty catalyst layer, delamination and pinholes. It is important to understand the effect

of defects that develop during storage and how they propagate over time since membranes are commonly stored prior to use.

The third objective of this study is to classify the dimensions of these defects in CCMs on the basis of size and shape. The methods presented here should be of benefit to fuel cell manufacturers in characterizing defects that are formed during the manufacturing process and selecting the most effective electrodes for use in stacks and testing [34]. In addition, the methodology presented also provides a comprehensive approach for defect detection and propagation which may be beneficial in many industrial applications beyond those of PEMFCs.

4.2 Research Framework

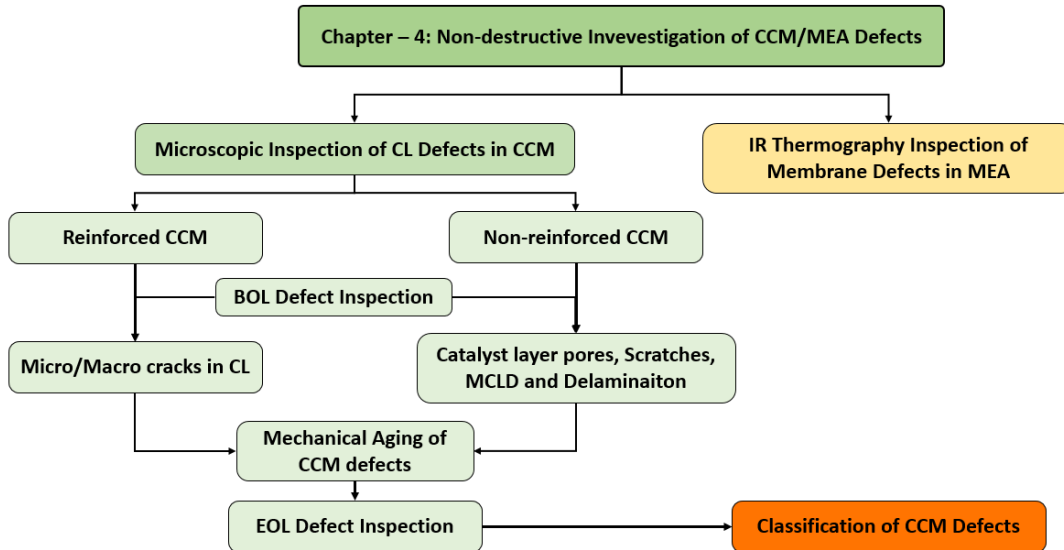


Figure 4-1: Framework for CCM defect analysis followed in this part of study.

4.3 Experimental

4.3.1 CCMs for defect investigation

Experiments were conducted on two different types of commercial CCMs fabricated using the decal transfer method (DTM) (see section 2.4) that have the same active area of 48 cm² and catalyst loading of 0.2 mg/cm² at the anode and 0.5 mg/cm² at the cathode (GoreTM PRIME® CCMs). The first type made with perfluorosulfonic acid (PFSA) membranes reinforced with PTFE fibers were stored for 2 years in the laboratory under ambient conditions prior to fuel cell operation in this study [41]. These samples are referred to as reinforced CCMs for our purposes here.

Samples of this type are examined in both BOL and EOL conditions and denoted as BOL_{LST} and EOL_{LST}, respectively, where LTS in the subscript denotes long-term-stored. Since these reinforced membranes have been stored in a non-inert dry atmosphere, one would expect the development of cracks in the BOL_{LST} state even before operation. The second type of CCM contains a non-reinforced membrane and so is termed a non-reinforced CCM. These CCMs are freshly manufactured and pristine and not stored prior to PEM fuel cell operation. These samples are also inspected at BOL and EOL and termed BOL_P and EOL_P, respectively, where P in the subscript denotes pristine. It is important to emphasize that the objective of this study is not to compare the behavior of these two CCMs, but to present case studies illustrating the non-destructive method, the types of defects that can be characterized and the types of measurements that can be made. The large difference in the histories of these two CCMs should ensure that these case studies capture a wide range of possible defects and phenomena.

4.3.2 Microscopic inspection of CL defects in CCM

The first step in this research is to develop a non-destructive and non-contact diagnostic tool to examine the defects in CCMs using reflected light microscopy. After batches of CCM electrodes are fabricated on the production line, the defected CCMs are separated from non-defected CCMs for further microscopic analysis. Each CCM sample is first fixed to a frame to flatten undulations in the membrane and facilitate the focusing of the microscope beam on the defects. To investigate the viability of the technique, a pristine CCM or aged CCM is mounted under the reflected microscope setup and images are captured under green light and auto white balance, as shown in Figure 4-2a. Defect was identified by passing a beam of light on one side of the electrode (anode/cathode) and capturing the transmitted light passing through the thinner area in electrode or defected areas. A complicating factor is that it is necessary to characterize entire CCM samples which have the dimensions with 12 cm length, 4 cm width and an overall active area of 48 cm², but at the same time detect defects which initially are very small with lengths in the range of 10 – 280 μm and areas of missing catalyst ranging from ~ 0.15 to 0.7 mm². Image analysis was conducted on a defected area by measuring the Z-profile/depth profile, intensity profile and 3D surface morphology to obtain quantitative data such as the length, width, depth and aspect ratio of the defect. A key requirement of this system is the ability to detect defects smaller than 50 microns, while scanning the entire active 48 cm² area on both sides of each sample. This is achieved using an Eclipse MA 200-inverted-metallurgical-microscope. Microscopic video

images of the CCMs are captured at 5x magnification while samples are moved at a speed of 0.7 cm/min to capture the video record the catalyst layer surface without any noise. Further video images are converted into a single, high-resolution image of the entire 48 cm² sample using image-stitching software (Image J). Auto-white balance (AWB) setting is applied to enable defected areas such as cracks, pinholes and other surface defects to be identified on the microscopic image via their color intensity. Magenta/pink areas in the images are considered to be defect spots caused by thinning of the CL or polymer membrane in the electrode. Several experiments are conducted to eliminate over-exposure of the pink areas to standardize the transmitted light intensity in defected areas from 80% - 1%. It is found that the adjustment of the intensity to 5% enables the best visualization of the defected areas of thin/zero catalyst layers. The CCM quality control operators should note that the transmitted light intensity varies depending on the thickness of the catalyst layers, catalyst loading, type of membrane used (reinforced or non-reinforced), electrode pores (as discussed in section 4.4.3.1) and coating type. All the CCMs investigated in this research work are examined using reflected light microscopy with 5% transmitted light intensity. Defects of interest are further characterized at higher (50x and 100x) magnification following the same procedure. The digital information from the top-view and cross-sectional images is then combined using the NIE software to generate 3D maps of the CCM defects and images showing the surface profiles, orientation, dimensions and aspect ratios of the defects. This procedure is routinely followed to characterize the sample defects at the BOL and then to monitor the evolution of these initial defects and any new ones that form upon aging.

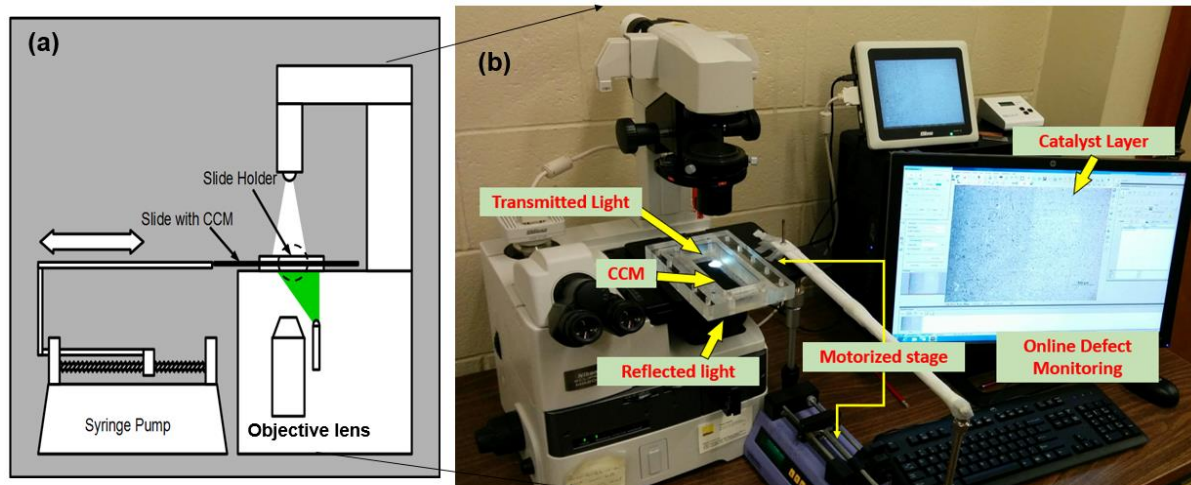


Figure 4-2: (a) Schematic of reflected light microscopy experimental setup. (b) Reflected microscopy setup for investigating catalyst layer defects in CCMs.

4.3.3 IR thermography characterization

The second non-destructive technique developed involves the use of infrared (IR) thermography imaging to detect defects in MEAs. Defects in MEA are developed during the fabrication process due to uneven compression of components (i.e., CCM, GDLs and gaskets) during hot pressing. Infrared (IR) imaging is performed on the non-reinforced CCM to investigate defects such as thin or empty catalyst spots or pinholes in the membrane developed during hot pressing of the MEA. CCMs with missing catalyst area are identified prior to MEA fabrication to investigate the impact of this type of defect on the subsequent behavior. A 640 x 480 FLIR T620 thermal imaging camera with a uniform emissivity of 0.95 for the GDL is placed 0.6-0.9 m above the top of the MEA. A 20/80 H₂/N₂ mixture is passed across the anode surface at a flow rate of 0.5 slpm for 1 min while the cathode is exposed to open air. Some of the H₂ can cross from the anode to the cathode side across pinholes or thin or empty catalyst spots. When some of this H₂ comes into contact with O₂ on the cathode side, it reacts and generates heat that is detected by the IR camera. Thus, hotspots in IR thermographs should occur at pinholes and thin or empty portions of the CL. This experiment is conducted in a dark area to prevent interference from ambient light. The experimental conditions used for the IR investigation to detect pinholes in the MEAs are listed in Table 4-1.

4.3.4 Design of custom-built test cell

The primary goal of the research is to investigate the behavior of the catalyst layer defects in CCMs during the aging process. Two challenges in identifying defects in MEAs are

1. Physical damage of the catalyst layer as the GDL is peeled away from the MEA to which it has been hot-pressed.
2. Indentation of GDL carbon fibers on the catalyst layer due to high compression during MEA fabrication.

Considering these two factors, we designed a custom-built test cell jig to study the impact of the CCM defects at BOL, MOL and EOL. Figure 4-3a shows the assembly of the test cell jig that has a 7-layered structure consisting of the CCM at the center sandwiched between two uncompressed GDLs, two 6-mm gaskets and two N₂ flow channel end-plates. This device is designed to age CCMs in an environment in which external factors due to compression by the flow channel plates [133] and GDL fibers are eliminated since this could cause indentations on the catalyst layer, which

may lead to further defects. Any additional stress developed in the membrane due to normal swelling and shrinkage act as external forces on the CCM that could accelerate the propagation of the defects. The GDLs on either side of the CCM are not confined on their outer edges to provide mechanical stability for the membrane during expansion and shrinkage. Anode and cathode GDLs (Toray TGP-H-060) with 15%-20% PTFE loading are selected and sized to match the active area of the electrode. The physical and mechanical properties of these GDLs have been reported in the literature [43]. The 6-mm gasket on either side serves as a frame to prevent the CCM from being compressed by the flow plates (i.e., rib and channel) of the jig. The flow channel plates of the jig are made with fully transparent polycarbonate which allows the thermal changes on the CCM to be monitored using IR thermography and the growth of defects such as pinholes to be tracked non-destructively during aging.

1. The test cell consists of polycarbonate transparent plates with dimensions of 120 mm in length, 2 mm in width and 1.5 mm in depth and a parallel flow field (Figure 4-4a) [4]. This design allows the user to monitor thermal changes on the electrode through IR thermography to easily identify leaks or pinholes.
2. Gaskets covering a range of thicknesses (0.5, 1, 3, 5, 6 and 8 mm) were tested in the cell to determine their effectiveness in minimizing the external compression forces exerted by the flow channel on the catalyst layer. The gaskets should provide enough space for the membrane to swell without being damaged by the flow paths. A 6-mm thick gasket was found to yield the best results without any external damage to the catalyst layers. Overall, this gasket thickness ensured that the formation of defects was caused solely by the mechanical deformation of the membrane and not by external mechanical forces.

4.3.4.1 Custom-built test cell for OCV analysis

In order to investigate the effect of defect propagation on the electrochemical performance of the CCMs, the anode and cathode was supplied with hydrogen and air, respectively, as fuels. To carry out the OCV experiments, the test cell was slightly modified so that the anode and cathode GDLs were extended by 1 cm (5 cm x 13 cm) larger than the catalyst layer active area (4 cm x 12 cm). Also, a 1.5 cm strip of each GDL was extended outside the test cell for connection to the potentiostat and measurement of the potential difference (OCV) between anode and cathode during the experiment. The OCV experiments were conducted without hot pressing the GDL to the CCM so that they can be separated to examine catalyst layer defects with the optical microscope without

further damage. Although this weakened the contact between the GDL and CL to some extent, the GDL was kept in contact with the entire active area of the CL. The test conditions for the OCV measurements are presented in Table 4-1. The main purpose of this AST was to study the morphological changes of catalyst layer defects that propagate during the aging process. Since the CCM is considered to be delicate and sensitive materials in fuel cells, aging it without being hot-pressed to the GDL in a custom-design test cell should be considered to be an extreme AST.

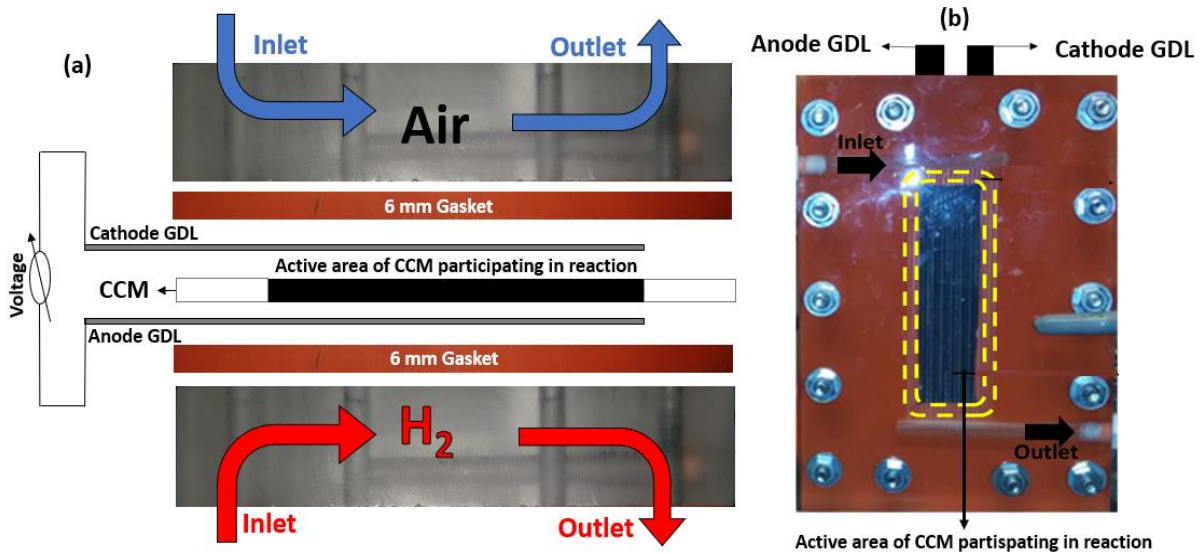


Figure 4-3: (a) Cross-sectional view of TSA for CCM analysis, (b) top view of the CCM#1 assembled in TSA device with an active area of $\sim 48 \text{ cm}^2$, (c) microscopic stitched image of CCM#1 operated in TSA device after 85 hours of OCV test. (Hardware and experimental set up was designed at the University of Waterloo).

4.3.5 Operational aging of the CCM

To study the propagation of manufacturing defects in the CCM without having to worry about effects arising from the GDL, each CCM was aged in the test jig described above by passing N_2 at 100% RH on either side of the electrode. Once the aging tests were completed, the CCMs were detached from the GDLs and mounted on the frame to examine defects on the CL with the optical microscope. It should be noted that the operating conditions such as flow rate, pressure and temperature applied to this test cell were the same as those that would be applied in a standard PEMFC single cell. All the aging experiments described in Chapters – 4 and 5 were carried out using this custom-built test cell.

4.3.6 Accelerated stress test (AST)

To monitor the defect propagation in the catalyst layer due to mechanical stresses induced by the membrane, a preliminary AST was conducted whereby each CCM was operated for 40 hours without the mechanical support from the gas flow channel plates. The 40-hour limit was selected based on the EOL of the reinforced CCMs. Although the non-reinforced CCMs did not reach their EOL by this point, the duration of operation was maintained the same in both cases. The uncompressed GDLs could still provide sufficient stability to resist the uneven forces on the membrane due to the incoming gases. The AST conditions are summarized in Table 4-1.

The gas crossover rate was used as a benchmark of the overall membrane health in both CCMs during the course of the 40 hours of operation and was monitored after aging for set times during each experiment. The crossover rate was measured by feeding a diluted 20/80 H₂/N₂ dry gas mixture into the anode inlet with 5 psi pressure while the anode outlet was closed. Tubing was connected to the cathode inlet and then submerged in a graduated cylinder, while the cathode outlet was sealed. The leakage between the fuel and oxidant sides was determined by measuring the volume of bubbles collected in the inverted graduated cylinder. A leakage rate of 1 mL min⁻¹ or less was acceptable; if it exceeded 2 mL/min, the test was stopped and the CCM was examined using the optical microscope to characterize the defects in its EOL condition. (Note: The 40-hour lifetime of the reinforced CCMs was determined in this way). An important aspect of this study was to assess the reproducibility of the non-destructive defect characterization methods presented. Consequently, the AST above was repeated on three different CCM samples of the same type.

Table 4-1: Experimental conditions of AST, IR imaging and OCV test.

AST condition	Reinforced and reinforced CCMs	non-reinforced CCM	IR Imaging: MEA made of non-reinforced CCM	OCV test conditions
AST duration	40 hours		60 seconds	BOL and EOL (1 hour)
Cell temperature	60°C (±2%)		21°C	65°C (±2%)
Gas flow	anode: 2 slpm N ₂ cathode: 2 slpm N ₂		anode: 0.5 slpm H ₂ cathode: open air	anode: 2 slpm H ₂ cathode: 4 slpm Air
Pressure	100/100 kPa		100 kPa	270 kpa/ 250 kpa
Humidification	100%:100% (±5%)		-	100%:100% (±5%)
Schematic of experimental setup				

4.4 Results and Discussion

In what follows, section 4.4.1 gives brief examples of the types of analyses and data that can be obtained using the tools of optical microscopy and IR thermography. This is followed in sections 4.4.2 and 4.4.3 with a presentation of the results of a detailed investigation using these tools to monitor the propagation of defects when the CCMs are subjected to the AST described in section 4.3.6.

4.4.1 Characterization tools

4.4.1.1 CCM examination using optical microscopy

Defect formed in the CL during coating, handling and storage process are crucial for the quality control of CCM fabrication. This focus led us to develop a quality control technique to investigate defects in large scale CCMs while samples are rolled under the microscope after fabrication. The primary goals of this work were to identify and quantitatively characterize defects that i) already appeared at BOL and ii) propagated after aging of the CCM in a non-reactive environment. The CCMs were examined at 5x magnification at different speed rates from 0.5 to 2 cm min⁻¹. At a speed of 0.7 cm min⁻¹, a clear image resolution could be achieved during the motion

of the sample. The use of higher magnification was not favorable for capturing acceptable images at this speed. Therefore, we chose a lower magnification (5x magnification) to analyze larger areas of the CCM in a reasonable time. The overall image analysis in this work was also performed at 5x magnification. From our investigation on catalyst layers, we observed that scratches and dents have 2-dimensional structures (length and width) that exhibit higher reflective light intensity than the surrounding CCM surface (white areas). On the other hand, cracks had a 3-dimensional structure (length, width and depth) with lower light intensity (dark areas) on the image. When scratches were sharp and penetrated through the catalyst layer, these areas were also considered to be cracks.

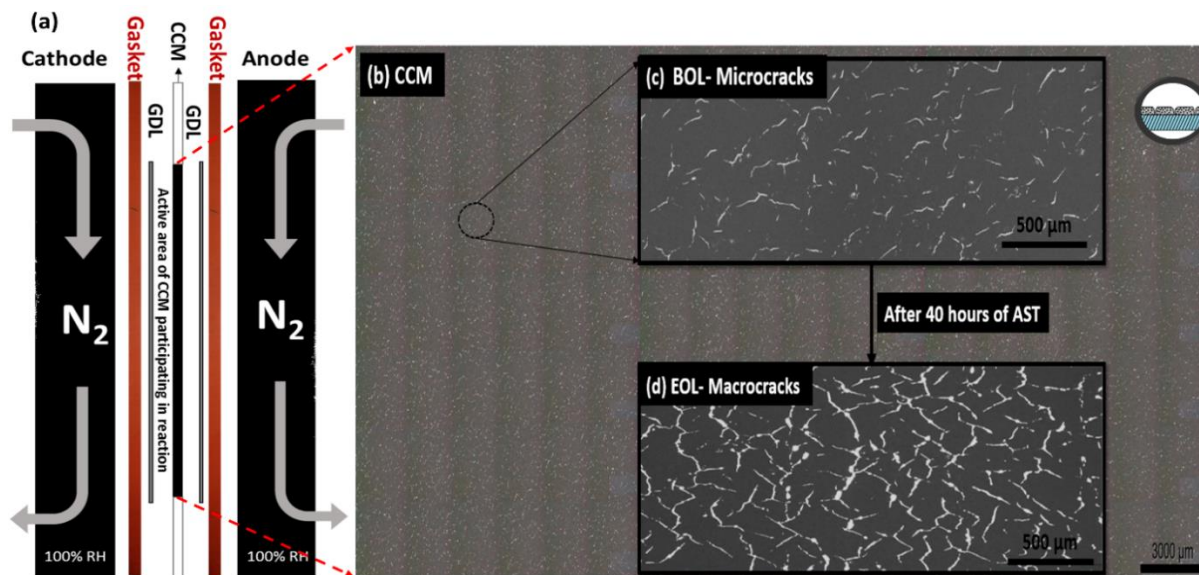


Figure 4-4: (a) Orientation of CCM in test cell jig showing gas flow directions and gasket sealants in contact with the GDLs. (b) Single large stitched image of a reinforced CCM in the BOL state of the cathode. Magnified image of an individual block of the stitched image captured at 5x magnification showing (c) BOL cracks and (d) EOL cracks aged for 40 hours.

Figures 4-4b-d show optical microscopy images of the cathode catalyst layer of a reinforced CCM at BOL after long-term storage (i.e., BOL_{LTS}) and later at EOL (i.e., EOL_{LTS}) after being subjected to the AST described in section 4.3.6. This AST was repeated three times on different reinforced CCM samples, as noted previously. Very similar results were obtained from these triplicate experiments. Figure 4-4b shows a single large image of an entire reinforced CCM in the BOL_{LTS} obtained by stitching 252 higher resolution optical images captured at 5x magnification. Figure 4-

4c shows a magnified view of a single block of the stitched image (Figure 4-4b) and highlights the extensive and irregular array of BOL cracks in the CL. This CCM was then aged in the test cell jig shown in Figure 4-4a by subjecting it to an accelerated test involving the passage of fully humidified N₂ to both the anode and cathode for 40 hours. Over this 40-hour period, the RH was closely controlled and ultimately led to CCM failure. The mechanical deformation of the membrane induced by the swelling and shrinkage leads to the propagation of the small cracks present at BOL [134] into larger cracks at EOL (Figure 4-4d). Possible causes of this swelling and shrinkage could be uneven gas and moisture distribution over the CL and the particular structure of the reinforced CCM whereby a relatively stiff PTFE reinforcement is sandwiched between the cathode and anode PFSA membranes. Some of this swelling and shrinkage could also be due to the unavoidable starting and stopping of the experiment every 10 hours to measure the gas cross-over.

Statistical analysis of the data from the images of the triplicate BOL_{LTS} samples indicates that the BOL cracks range from 10 to 280 μm in length and from 1 to 100 μm in width with aspect ratios between 1 and 10. These BOL cracks cover ~2.4 % ± 0.10 of the total active sample area. The structure and dimensions of the cracks in this sample change dramatically after 40 hours of aging. Analysis of the EOL_{LTS} image in Figure 4-4d shows that the dimensions of cracks now range from 10 to 700 μm in length and 1 to 250 μm in width with an aspect ratio of 1 to 12. The EOL cracks now cover ~10.5% ± 0.04 of the total active sample area in the EOL_{LTS} image. Comparison of the data obtained from Figure 4-4c and 4-4d reveals that the total defect area has increased by 8.1% and the crack length and width increased by ~150%.

4.4.1.2 Detection of MEA defects by IR thermography

Some of the defects formed during fabrication can be caused by uneven pressure/stress on the component layers after hot pressing or can include missing catalyst regions in the CCM. Such defects facilitate hydrogen crossover, leading to a large drop in the OCV and even to pinhole formation [69]. Monitoring defects in the CCM within an MEA is complicated by the fact that it is contained within the GDL layers. In this case, IR thermography has been shown to be effective at characterizing defects [8,103]. In this study, we use IR thermography to examine the cathode side of an MEA, as shown in the schematic side view in Figure 4-5a. It should be noted that the set-up shown in Figure 4-5a examines the actual 7-layered MEA used in commercial PEMFCs (not the same as the samples examined in the set-up shown in Figure 4-4a which is used to test

CCMs alone). Thus, the CCM in this image is hot-pressed to the GDL. Although this is an unused MEA, it contains typical defects formed during fabrication. In our setup, it is perfectly sealed and aligned along the edges of the GDL with a teflon gasket. Note that the CCM is slightly larger than the GDL in this sample, but the overhang portion is sealed with the teflon gasket.

Examination of the temperature profile in Figure 4-5b suggests that larger leaks through the defect are associated with higher temperature spots in the IR image. A higher temperature in the image reflects that more hydrogen has crossed from the anode to cathode and reacted with oxygen on the platinum catalyst surface to generate heat. The heat (infrared energy emitted) produced on the cathode is detected by the infrared detector of the IR camera and converted to an electrical signal which is precisely measured and processed by software that can automatically quantify the infrared energy and generate a thermal image. The images acquired using the camera are converted into visible images by assigning a color to each IR energy level to yield a false-color image called a thermogram. In this way, hotspots across pinholes and thin or empty portions of the CL can be determined using IR thermography.

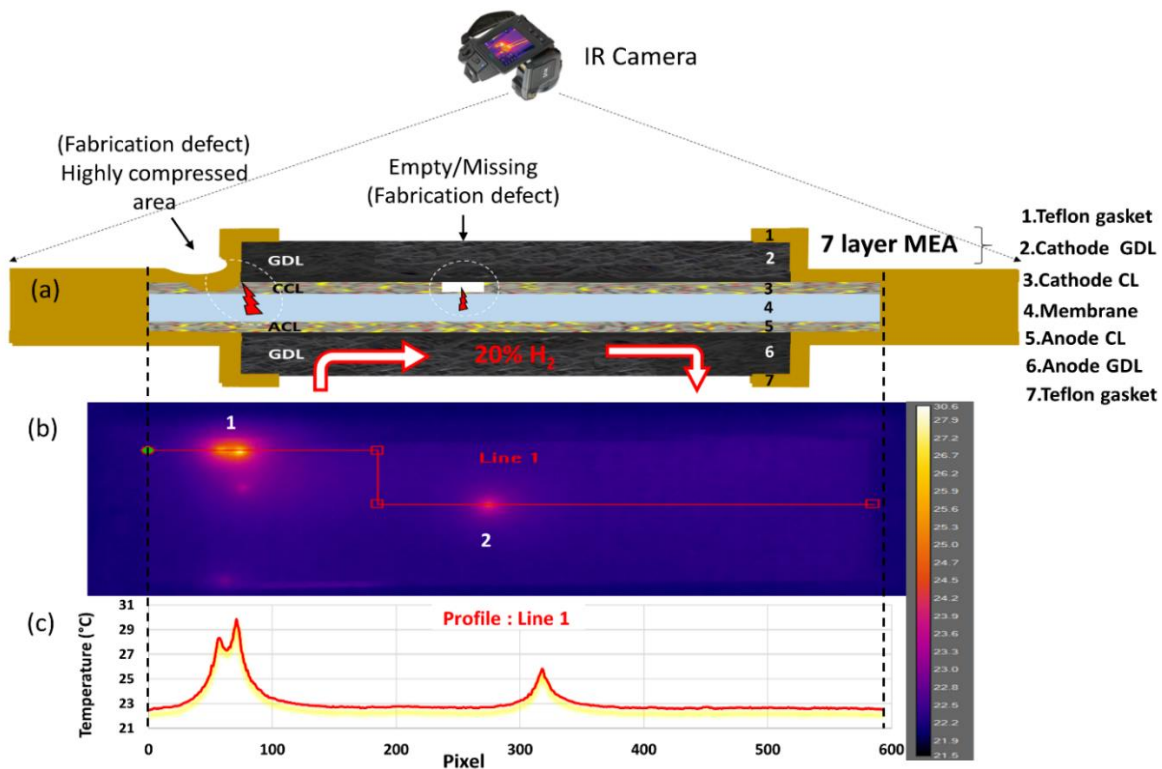


Figure 4-5: (a) Schematic diagram of the side view of MEA and location of defects in non-reinforced CCM at BOL; (b) thermal image of defected MEA viewed on cathode side (c) temperature profile along the red line shown in Figure 4-5b. Note that 590 pixels along x-axis correspond to a length of 12 cm.

An IR image of the top view of the non-reinforced MEA in the BOL shown in Figure 4-5b and the temperature profile along the two horizontal line segments drawn on the thermal image are combined along one line are shown in Figure 4-5c. The temperatures in this IR image span a range from 21°C (dark blue) to 31°C (pale yellow). This image reveals the presence of two hotspots. One hotspot is found near the upper edge of the MEA. The location of this fabrication defect is not surprising since the area between the active area, GDL and gasket (elliptical region indicated by the dashed lines in Figure 4-5a) is prone to developing defects at the edge of the MEA due to the large pressure and stress on the CCM applied by the GDL during hot pressing. The temperature profile across this hotspot shows peaks at temperatures of 30.6°C and 28.2°C. The second hotspot which reaches 26.1°C is located near the center of MEA and presumably is caused by missing catalyst or thinning of the catalyst. Missing or thinned catalyst can be caused either by the improper laying down or lift-off of a small portion of the CL during the decal transfer step or by the direct intrusion of carbon fibers from the GDL. Based on the maximum temperatures reached in the profile, defects due to missing CL appear to be less harmful than those near the edge of the MEA. The gas crossover in the defected MEA is measured to be 1.2 mL min⁻¹ at BOL. Although suppliers of CCMs are aware of such defects, their effects as well as their growth during fuel cell operation have not been studied. Therefore, it is important to quantify the amount of missing CL that has occurred prior to MEA fabrication. These IR results shows that these defects are also significant and should be of concern prior to MEA assembly. Although the hotspot defects do not initially appear to affect performance, they can potentially grow during cell operation and eventually cause shutdown of the PEMFC [69,103].

4.4.2 Investigation of defects in CCMs

4.4.2.1 Identification of defects (CL micro-cracks) in BOL-LTS reinforced CCMs

CCMs stored under a wide range of atmospheric conditions can experience mechanical stress and strain due to the uncontrolled relative humidity. A comparison of the results obtained for the two CCMs also shows that the storage conditions have a significant impact on the development of CL defects in the CCM electrodes. From our investigation, BOL cracks are the only defects detected on the reinforced CCMs. No evidence of pores in any of the images of the reinforced CCMs is found. Pores are typically introduced by CCM manufacturers during fabrication to improve gas transport and provide moisture, which is essential for proton transport in the catalyst layer. However, if the catalyst layer demonstrates high performance (high catalyst

surface area), electrode pores are not introduced since they can also have the negative effect of trapping water that can degrade the catalyst. Therefore, the manufacturer had no interest in introducing pores in these CLs. Examination of the depth of the cracks appearing at BOL (Figure 4-4c) using the Z-profile reveals that the cracks do not penetrate deeply into the CL and all lie between ~ 0.5 to $1.5 \mu\text{m}$ from the top surface. One would expect such a distribution of cracks to raise the in-plane resistance of the CL and ultimately reduce the performance of the PEMFC in the ohmic region [135][91].

4.4.2.2 Propagation of defects (CL macro-cracks) in EOL-LST reinforced CCM

To investigate the effect of aging on crack propagation, the reinforced CCM discussed in section 4.4.2.1 was subjected to an AST in the custom-built test cell jig (Figure 4-4a) for 40 hours according to the conditions listed in Table 4-1. At the end of the 40-hour AST, the CCM was re-examined to characterize its crack structure. Figure 4-6a shows an image of the EOL cracks in a portion of the EOL-LTS. In order to provide a closer view, we show the encircled area in Figure 4-6a at 50x magnification in Figure 4-6b. The bottom half of the graph (Figure 4-6c) gives a cross-sectional view of the cracks penetrating into the CL as one moves along the blue line shown in Figure 4-6a. The corresponding Z-profile along the blue arrow in Figure 4-6b is presented in Figure 4-6d to show the depth of the main cracks that are intersected in this region. The larger of the two cracks shown is measured to have a width of $\sim 20 \mu\text{m}$ and depth of $\sim 7 \mu\text{m}$. Since the nominal thickness of the cathode CL is $8 \mu\text{m}$, this crack essentially penetrates through the full depth of the CL and exposes the bare membrane below. Cracks that penetrate through the CL provide preferential water transport pathways and inhibit mass transport of the reactant gases [134]. As the defect area grows, the severity of the defect increases gradually and would be expected to reduce PEMFC performance [80,121].

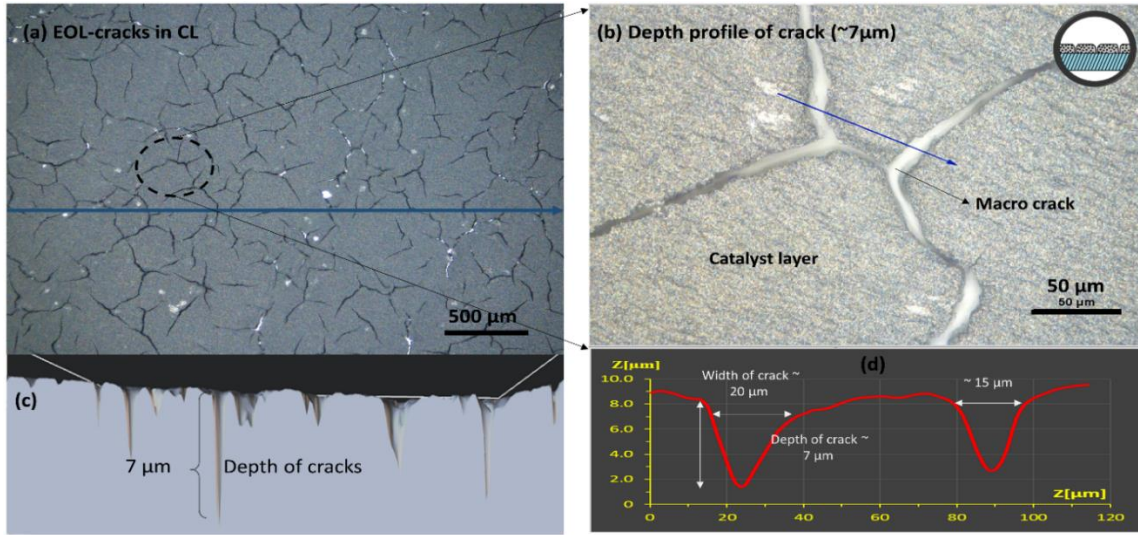


Figure 4-6: (a) Optical image (5x magnification) of a portion of reinforced CCM; (b) optical image of enclosed region of macro-crack in (a) at higher magnification (50x); (c) visualization of cracks along the blue line in (a); (d) Z-profile showing depth profile of crack along the blue arrow in (b).

The degree of crack propagation in the catalyst layer is investigated using the open-source imaging software ImageJ. The RGB (red, green and blue) microscopic image in Figure 4-7a is converted to an 8-bit (black and white) image shown in Figure 4-7b for easier detection of cracks. To eliminate distortions (shading or smoothing) in the image, a FFT-bandpass filter is applied to better visualize the image contrast. To analyze the length and areas of the cracks, the scale bar is firstly calibrated from the image with a known distance. Secondly, a threshold is adjusted by sliding the intensity bar so that all the cracks of interest are selected with respect to crack boundaries, as shown in Figure 4-7c. Resolution of the image has a major impact in this process by affecting the detection of some defect/crack details. The image resolution which is directly related to magnification of the microscope is an important and challenging factor that can influence the fine details of the smaller defect/micro-cracks. Accordingly, we have been careful to account for these effects in the image analysis. The spatial resolution r of the images is $1.83 \mu\text{m}$ obtained from the expression $r = 0.5\lambda/N.A$, where wavelength $\lambda=550 \text{ nm}$ and numerical aperture $N.A = 0.15$. The crack boundaries may cross smaller or newly generated cracks ($< 5 \mu\text{m}$) which may influence the number of cracks. However, the total area of defects is not significantly influenced. Thus, since the determination of the number of cracks is a complicated process at lower magnification, we have chosen to characterize the severity of defect on the basis of the total damaged areas in the CL. Finally, crack dimensions are obtained by selecting the Analyze Particle command in the ImageJ software, which

gives overall information on number, length and area of the cracks. The results of the overall crack analysis are discussed in section 4.4.2.3.

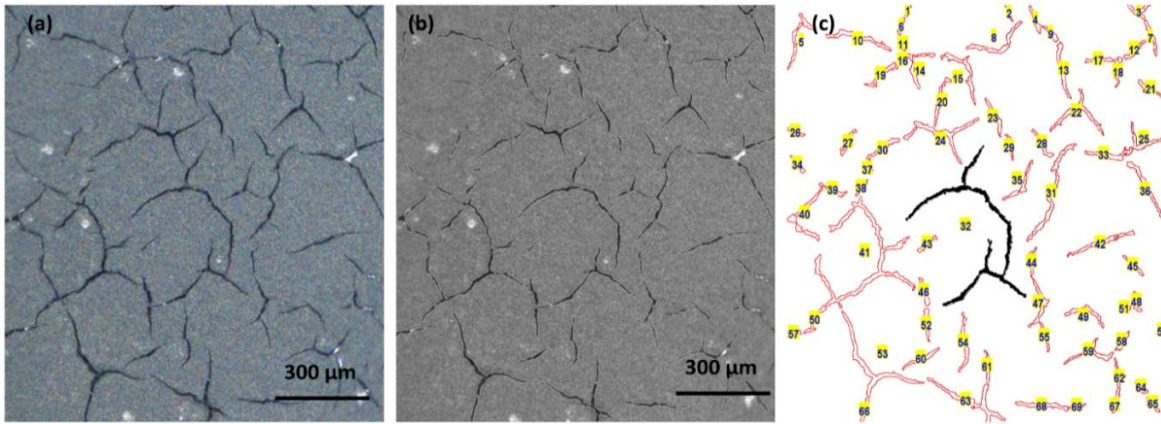


Figure 4-7: Section of cracked area selected from Figure 4-4a (spatial resolution of $1.83 \mu\text{m}$ and $5\times$ magnification) to demonstrate the boundaries of cracks, (a) RGB microscopic image, (b) 8-bit (black & white) image, where dark areas indicate cracks and white areas indicate dents, (c) boundaries of cracks corresponding to Figure 4-7b, where crack number 32 represents the larger area ($8570 \mu\text{m}^2$) of the crack.

4.4.2.3 Comparison of defects in BOL-LST and EOL-LST samples

The distributions of the cracks and defect area percentage of the BOL-LTS and EOL-LTS analyzed using the Image J software are presented in Figures 4-8a and 4-8b, respectively. The non-uniformity of the crack distribution increases sharply on going from the BOL-LTS state to the EOL-LTS state. The blue bars indicate the number distribution of cracks with respect to the area from $1 \mu\text{m}^2$ to above $10000 \mu\text{m}^2$ that they cover, while the orange bars show the distribution in terms of the percentage of the total defect area. It should be noted that these data are obtained over the entire 1 cm^2 active area of CCM. On the basis of numbers alone, these data reveal that the smallest cracks occur most frequently in the CCM when it is in the BOL-LTS state. However, medium-sized cracks from 100 to $750 \mu\text{m}^2$ dominate in terms of the area, covering $\sim 56.8\%$ of the total defect area (enclosed in the yellow dashed region in Figure 4-8a).

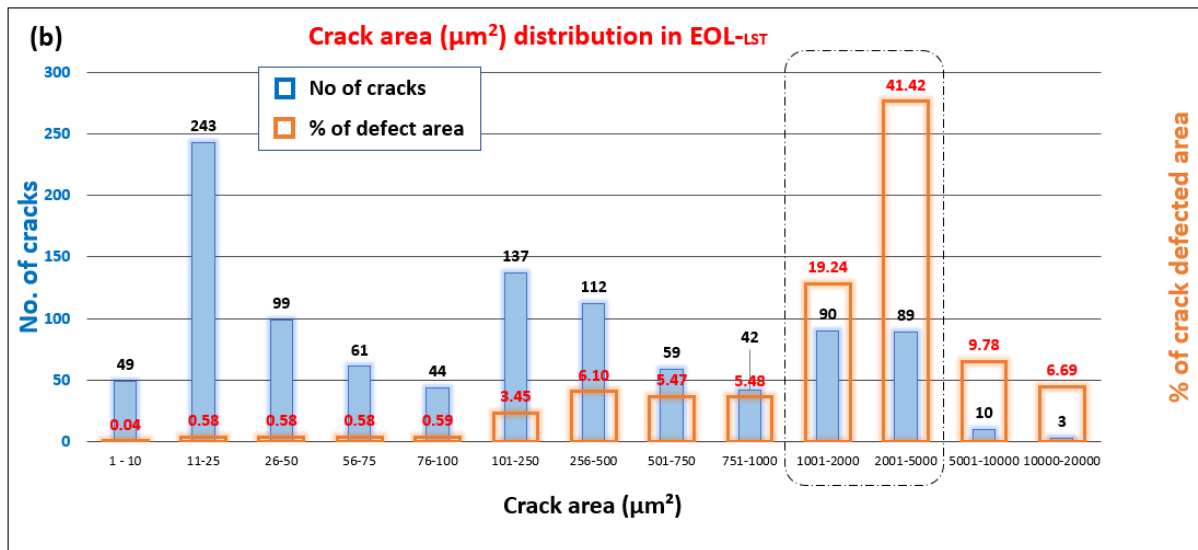
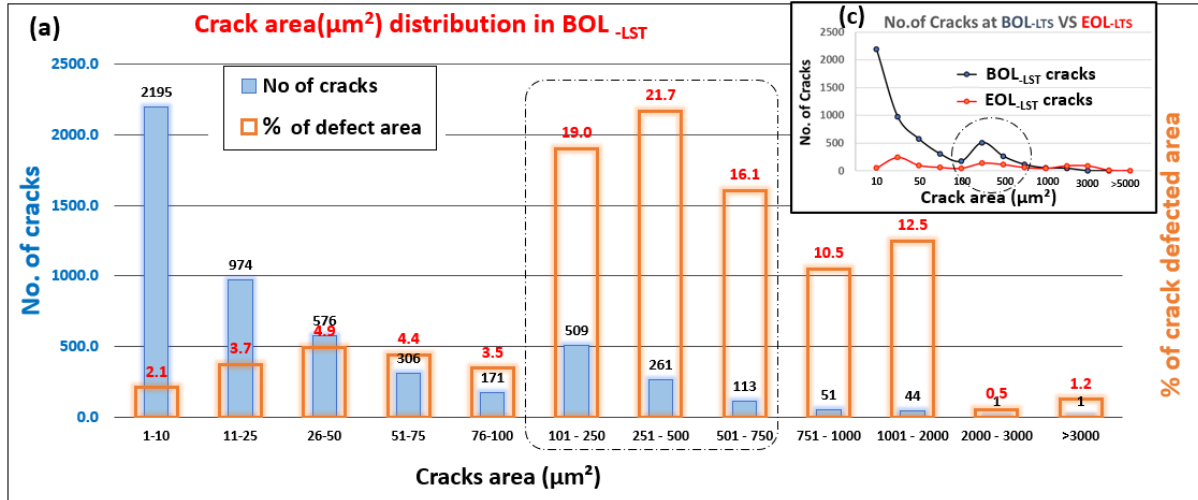


Figure 4-8: (a) Distributions of number of cracks and percentage of the total defect area covered by BOL-LST cracks, (b) distributions of EOL-LST cracks after aging for 40 hours and (c) comparison of BOL and EOL crack distributions.

When the CCM is aged, the plastic deformation of the membrane during hydration and dehydration causes the surface cracks in the BOL-LTS to grow downward into the CL and horizontally along its surface [135]. When undergoing dehydration, the membrane shrinks, causing cracks to close or migrate toward each other in the CL. When the membrane becomes more hydrated, compressive stress is developed in the membrane and pressure is released through the propagation of the macro-cracks. Table 4-2 shows the overall summary of defects found in the reinforced CCM from its BOL-LTS to EOL-LTS. After aging the sample, the density of cracks (both BOL and EOL) decreases significantly from $\sim 27613 \text{ cm}^{-2}$ to $\sim 10515 \text{ cm}^{-2}$ in its EOL state ($\sim 61.9\%$ decline). The blue curve

in Figure 4.8c presents the distribution of BOL cracks with respect to crack area, while the red curve shows the distribution of EOL cracks. Since many fewer cracks remain at EOL than at the start of aging, it appears that many BOL cracks have merged to form larger cracks after 40 hours of the AST. As much as 60.7% of the defected area is made up of cracks between 1000 and 5000 μm^2 in area after aging (represented by yellow dotted line in Figure 4-8b). A number of measures of the crack dimensions provide evidence of the dramatic growth in their size during aging. The total defect area has increased significantly from $\sim 2.4\% \pm 0.10$ (BOL-LTS) to $\sim 10.5\% \pm 0.04$ (EOL-LTS), while the maximum crack length has grown from 280 to 700 μm and width from 100 to 250 μm . Interestingly, the aspect ratios of the defects do not significantly change, indicating that the length and width of the cracks grow at similar rates. This fact suggests the cracks tend to merge isotropically rather than anisotropically and is consistent with the side-by-side comparison of the reinforced CCMs in Figure 4-4c and 4-4d which shows that the cracks tend to have a more branched structure at EOL than at BOL. This effect is clearly evident in the crack network in Figure 4-7c where the branches of crack 32 are extended and merged to adjacent cracks with an area of 8570 μm^2 . If new cracks form during aging, one would expect that the EOL distribution would include a large number that are $\sim 50 \mu\text{m}^2$ or less in area, similar to that observed in the BOL samples. However, as shown in Figures 4-8b and 4-8c, very few cracks smaller than 100 μm^2 are observed after aging. This strongly suggests that most of the cracks that grow are those that already appear at BOL-LTS, reflecting the importance of minimizing crack and defect formation during the manufacturing process or storage conditions of the CCMs. This is also confirmed by our direct observation of the entire CCM surface at BOL and EOL with the optical microscope.

Table 4-2: Comparison of BOL-LTS and EOL-LTS cracks in reinforced CCM.

Sample conditions	Density of cracks/cm ²	Range of crack length (μm)	Range of crack width (μm)	Aspect ratio	% of defect area
BOL-cracks (BOL-LTS)	27613 \pm 2650	10 – 280	1 – 100	1 – 10	2.4% \pm 0.10
EOL-cracks (EOL-LTS)	10515 \pm 440	10 – 700	1 – 250	1 – 12	10.5 % \pm 0.04

4.4.3 Defects in non-reinforced CCM at BOL

Since the non-reinforced CCMs examined in this study were freshly prepared and pristine prior to their use, we expect no defects such as BOL cracks caused by membrane deformation that occurs during storage, as is the case with the CCMs examined in the previous section. It should be noted that a comparison of the two CCMs (one reinforced and one non-reinforced) cannot be made as there are multiple factors that can lead to differences in defect propagation. Instead, the goal is to monitor the different types of defects that are developed during mass production of CCMs. Based on our examination of the non-reinforced CCMs at BOL_P using optical microscopy, we identify five types of defects/features: electrode pores, scratches, areas of missing/thin CL, empty/void/bare catalyst regions and delamination of the CL. These types of defects have not been observed in the CCMs examined in the previous sections. Each of these defect types is characterized in the following sections.

4.4.3.1 Electrode pores and scratches

Electrode pores are essential for active electrochemical interaction of reaction gases and catalyst and mass transport. They are intentionally introduced into the CCM by the manufacturer to improve gas transport, but their size distribution can be difficult to control. Consequently, it is important to measure the pore size distribution in the CL [136]. Figure 4-9a shows numerous electrode pores captured on the pristine non-reinforced CCM surface at BOL_P. The electrode pore distribution is obtained with ImageJ and shows that their diameters range from 1 to 30 μm . This range is similar to that reported by Hwang et al. [59] who also showed that pores smaller than 25 μm in diameter enable fast removal of water product away from the membrane. On the other hand, pores larger than 25 μm in diameter provide sites for water to collect, flood and facilitate gas crossover. In these situations, the large pore diameter can be considered as a defect that leads to mass transport losses and lower cell performance.

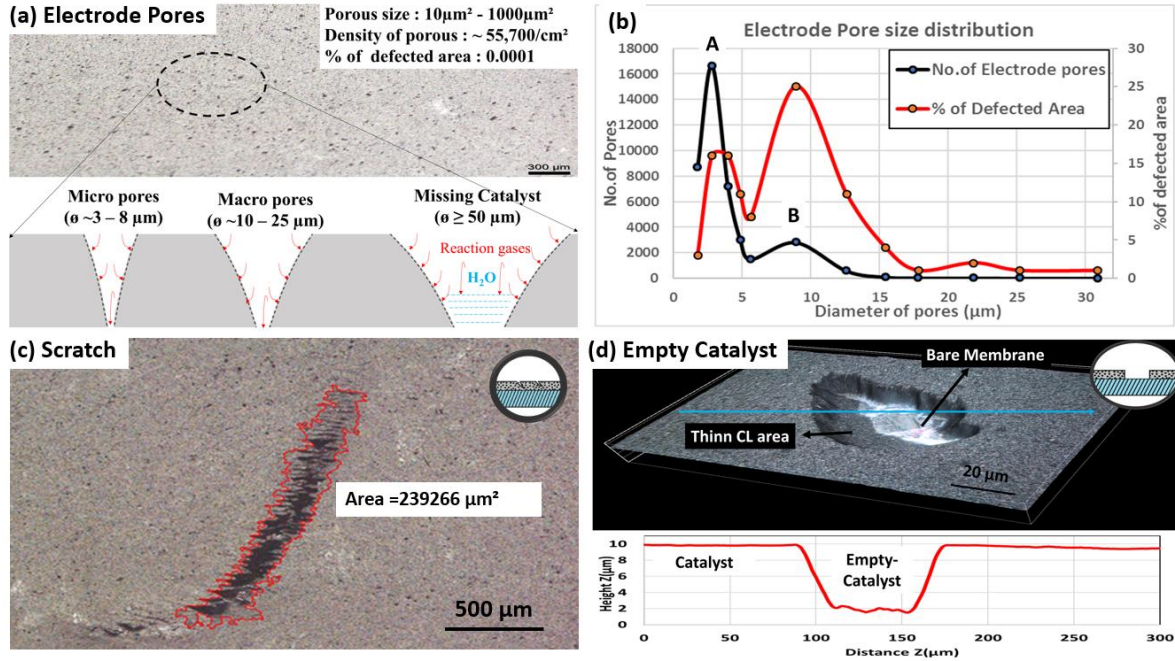


Figure 4-9: Microscopic image of non-reinforced CCM in the BOL state captured at 5x magnification showing (a) electrode pores of various sizes as labeled, (b) comparison of electrode pore distribution (micro- and macro-pores) on pristine CCM, (c) catalyst layer scratch and (d) missing portion of catalyst layer with height/depth profile captured at 50x magnification.

ImageJ particle analysis was conducted on the image in Figure 4-9a to convert the RGB microscope image to an 8-bit (black and white) image and distinguish pores that appear as darker areas from dents that appear brighter. The number density of pores is found to be $\sim 55,700 \text{ cm}^{-2}$ and the combined area of all pores makes up only a very tiny fraction ($\sim 0.0001 \%$) of the entire CCM surface. From the pore areas so determined, the pore diameters are estimated assuming they are perfectly circular. Since the circularity of the pores varies from 75 - 100%, this assumption only has a small influence on the diameter estimates.

For convenience, we designate micro-pores to have diameters less than 5 μm , macro-pores to have diameters between 5 and 25 μm and missing catalyst to be voids larger than 25 μm (see schematic at bottom of Figure 4-9a). Figure 4-9b shows the distributions of the number of pores and percentage of pore area with respect to pore diameter obtained from Figure 4-9a. The distributions show that 44% of the pores are micro-pores smaller than 5 μm in diameter, while macro-pores between 5 and 25 μm diameter make up 52% of the total pore area. Such a range of pore sizes is desirable and important for effective fuel cell operation. Mu et al. [80] showed that the CL pores

become larger when Nafion ionomer is lost and ultimately become CL layer defects. Examination of this CCM sample shows that five regions have pore sizes larger than 25 μm and comprise 4% of the total pore area. As noted above, these regions may be unfavorable for mass transport due to their large pore size [59].

Our analysis has identified other defects such as scratches on the CCMs. Scratches differ from cracks in that they are abrasions to the CL surface caused by mishandling during CCM assembly and can be distinguished by their irregular and non-uniform shapes. Figure 4-9c shows a scratch identified in at BOL_P with a defect area of $\sim 2.4 \times 10^5 \mu\text{m}^2$ and a length of $\sim 2150 \mu\text{m}$. The damage associated with scratches is sharp and penetrates through the CL and is classified as a crack. Interestingly, no scratches are observed in the reinforced CCM at BOL_{LTS} discussed in section 4.4.1.1.

4.4.3.2 Defect (missing/thin CL) caused by improper decal transfer of catalyst

Missing catalyst defects mainly originate from improper decal transfer and lead to a thinned area of CL on top of the membrane or a completely removed portion of CL that exposes bare membrane below. Figure 4-9d shows an example of an empty CL area on the non-reinforced CCMs at BOL_P and the corresponding Z-profile along the blue line. All of the CL in the central portion of the defect has been removed to expose bare membrane which appears bright in the reflected microscope light. Outside of this central region, but still within the defect, the CL is only partially missing. As one moves outward from this central bare region, the thickness of the CL increases until it reaches the 8 μm thickness of the intact CL at the outermost edge of the defect. No oxygen reduction would be expected to occur during fuel cell operation on the portion of the CCM on the cathode side where bare membrane is exposed (zero CL thickness). Ulsh et al. [69] showed that very little current flows across the empty catalyst layer defects and lowers the overall performance of the MEA. These missing catalyst areas can also be locations for the formation of dangerous pinhole defects during typical fuel cell operation.

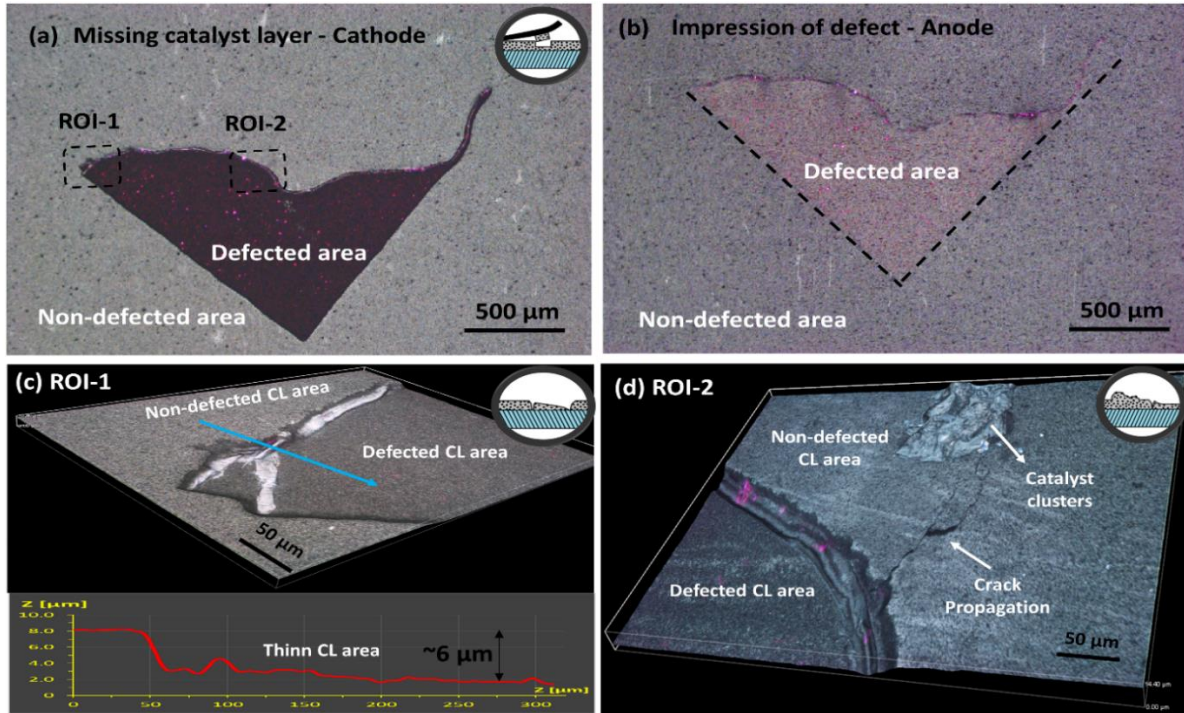


Figure 4-10: Optical microscope images of missing catalyst layer due to improper manufacturing viewed from the (a) cathode side and (b) anode side in non-reinforced CCM captured in the BOL state at 5x magnification. Two regions of interest in (a) are shown at 50x magnification in (c) ROI-1 and (d) ROI-2. Scale markers are included on the images.

Figure 4-10a shows a large manufacturing defect (missing catalyst layer defect - MCLD) in the CL of the non-reinforced CCM as viewed from the cathode side, while Figure 4-10b shows the same defect from the anode side. Defects identified on the cathode (Figure 4-10a) leave the same impression on the anode side (Figure 4-10b) due to overall thinning of CCM. The defect shown here can arise during the decal transfer step when catalyst is incompletely transferred onto the membrane or torn off when the decal substrate is removed. For a more detailed examination of this defect, two regions of interest labelled ROI-1 and ROI-2 in Figure 4-10a are shown at 50x magnification in Figure 4-10c and 4-10d, respectively. The pink colour of the defected areas corresponds to thinner portions of the CL. The intact CL outside the defect which appears grey has a thickness of $8 \pm 0.5 \mu\text{m}$ (Figures 4-10c and 4-10d). Figure 4-10d clearly shows a crack propagating just on the outside of the defected area. This indicates that cracks that have presumably propagated from these manufacturing defects in the CL are already present at BOL_P. Other defects that we have observed are clusters, one of which is shown in Figure 4-10d. They are very different in appearance from foreign particles such as dust or contaminants that have also been observed but

show up as bright white spots. In the images, the material making up these clusters reflect light similarly to the surrounding catalyst surface. Thus, we conclude that these clusters are likely made up of additional catalyst material deposited by excess spray pressure during the coating step. The greater thickness of the CL in this cluster would presumably raise its ohmic resistance and inhibit the flow of current across this defected portion of the MEA relative to that elsewhere. Obviously, such defects should be avoided during CCM fabrication.

4.4.3.3 Propagation of defects in EOLP

As with the reinforced CCMs, the non-reinforced CCMs have been subjected to the same 40-hour AST as described in section 4.3.6 in order to investigate the propagation of the defects present at BOL. We observe that the defects grow to a much smaller extent in the non-reinforced CCMs than in the reinforced CCMs. For one thing, the pore size distribution remains largely unaltered upon aging. For another, no significant growth of the manufacturing defects occurs. Some crack propagation is observed in the CL due to mechanical expansion and shrinkage of the membrane during the AST. The stitched-together image in Figure 4-11a of the aged CL in the non-reinforced CCM shows the presence of some cracks which appear as dark lines. This image is dominated by the presence of a large crack which appears as the heavier dark line (indicated with an arrow). This crack grows in the x-direction likely due to the expansion of the membrane in the y-direction during aging. Another defect that appears in the image of the CL in the aged CCM is an oil mark within the dotted circle, which likely is a contaminant originating from impurities in the air or gas tubing [137], dissolution of Nafion or PTFE or human contact during examination of the sample.

A selected portion of the CL containing this large crack (indicated by the dashed region in Figure 4-11a) is shown at higher magnification in Figures 4-11b-d and reveals that it contains smaller cracks extending out the delaminated region. Figure 4-11d shows a Z-profile measured in the direction along the yellow arrow in Figure 4-11c. In this situation, it appears that delamination is occurring as a result of crack propagation on the catalyst layer surface. As these cracks grow, it is likely that the portions of the defected CL behind their furthest advance begin to delaminate. It is interesting to note that this delamination does not necessarily lead to detachment of the entire CL to expose the membrane. Although the mechanical expansion of membrane creates pressure on the CL, the lower part of the CL is strongly bonded to the polymer membrane and can accommodate the pressure. However, the uppermost CL sections cannot withstand the pressure

and ultimately develop cracks and delaminate as shown in Figure 4-11c and 4-11b. As noted previously in section 4.3.6, the same pressure of 100 kPa is applied on both the anode and cathode sides of the reinforced and non-reinforced CCMs in this study. Thus, we do not expect an imbalance in the applied pressure in the z-direction (i.e., normal to the plane of the image) to cause the damage observed in Figure 4-11a. However, it is possible that this applied pressure causes the CCM to expand in the y-direction on the catalyst layer and a crack to propagate in the x-direction. The magnified image in Figure 4-11c shows clear evidence of a crack that has developed in the CL and leads to delamination. The 3D view of the damaged CL in Figure 4-11b shows a portion of the CL that is approximately 300 μm in length, 5 to 25 μm in width and 4 μm in depth. This behavior is not observed in the reinforced CCM where it appears that the expansion and contraction of the membrane is uniform in both the x- and y-directions, causing cracks to grow more evenly in these directions.

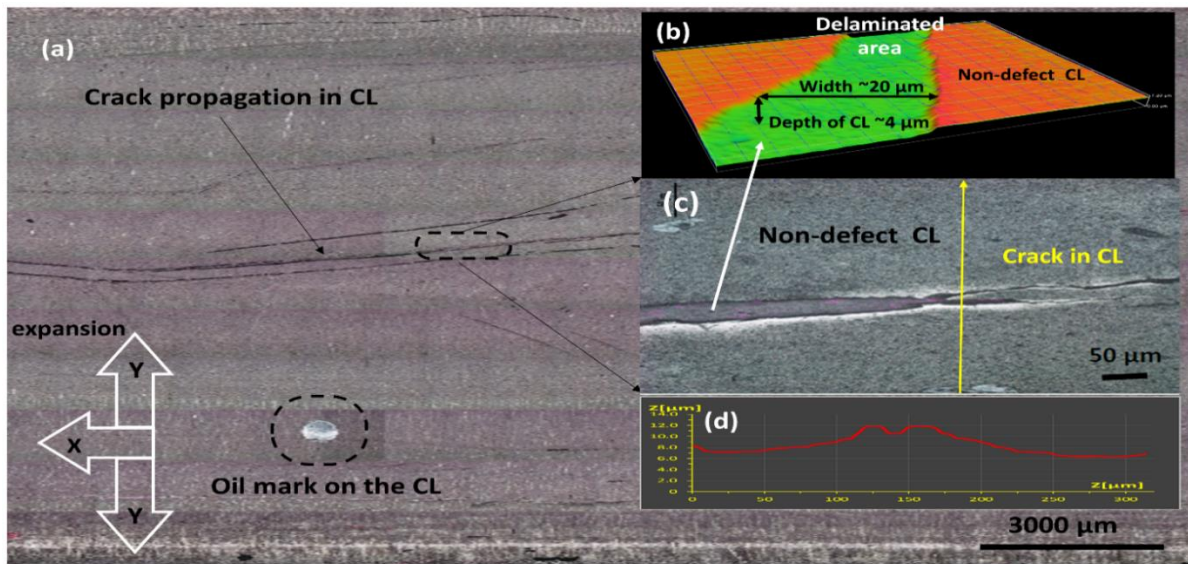


Figure 4-11: (a) Stitched microscopic image of non-reinforced CCM after aging for 40 hours; (b) 3D view (height map) of the portion of the CL indicated with dashed line in (a); (c) magnified image of the defected area showing crack formation and delamination of the CL captured at 50x magnification; (d) Z-profile obtained along the yellow line in Figure 4-11c.

4.4.4 OCV analysis of defective CCMs

As stated previously, the OCV of the cell described in section 4.3.4.1 is measured at BOL and EOL both before and after the AST to obtain some measure of the effect of defect propagation on electrochemical performance. As expected, the propagation of cracks in the CL has a major effect on OCV degradation, presumably due to gas crossover. CCMs with significant defects at

BOL such as cracks in the CL (i.e., reinforced CCM) exhibit higher voltage loss compared to the non-reinforced CCM with no cracks in the CL. The OCV of the reinforced CCM shown in Figure 4-4b decreases by 102 mV from 928 mV to 826 mV, whereas the OCV of the non-reinforced CCM shown in Figure 4-11a drops by 45 mV from 942 mV to 897 mV. The OCV drops as a result of mixed electrode potentials arising mainly due to hydrogen gas crossing through the defective areas and then being oxidized at the cathode where oxygen is present. These results are consistent with that of the optical image analysis in sections 4.4.1.1 and 4.4.2.3 which reveals that cracks grow in both length and width and that the defect (crack) area in the reinforced CCM increases by 8.1% from BOL to EOL. One would expect cracks to have grown in both dimensions in order for the amount of gas crossover through the membrane to rise significantly. On the other hand, no significant growth of BOL defects (Figures 4-9 and 4-10) is observed in the non-reinforced CCM indicating that it is still intact. The 45 mV drop could be due to the single large crack that has formed on the cathode CL (Figure 4-11). Small portions of the CL appear to be delaminated inside the cracked area, which could also contribute to this loss in OCV.

4.4.5 Classification of Defects

As a summary of the various types of defects observed in the two commercial CCMs examined in this study, we have classified them based on their appearance, length, area and characteristic features in Table 4-4. Based on this analysis, six types of defects are identified: BOL cracks, EOL cracks, scratches, delaminated CL, electrode pores and missing or empty CL portions. This classification of defect type, size and shape which is currently not available in the literature, can form the basis for the acceptance or rejection of CCMs by fuel cell stack assemblers and ultimate improvement of the quality control, reliability and cost of CCM manufacturing and PEMFC operation [34]. No doubt these aspects will become more important as attention increasingly turns toward CCM manufacturing on a commercial scale. The results summarized above should also be important for the research community in future studies on the mechanisms of CCM and stack degradation and failure.

As noted previously, the main focus of this study is to investigate the morphology of real defects that propagate in the CL due to mechanical deformation of membranes operated under the AST described in section 4.3.6. Real defects and their effect on cell performance are very difficult for PEMFC manufacturers to characterize once the fuel cell stacks are installed.

Table 4-3: Classification of CCM Defects.

Defect Type		Length (μm)	Area (μm^2)	Characteristic Feature
1. BOL cracks		1 – 280	1-1000	breakthrough of CL
2. EOL cracks		280 – 700	1000-5000	cracks propagated in CL
3. Scratches		> 700	> 5000	marks on CL due to mishandling
4. Delaminated CL		4 - 8	> 5000	removal of portion of CL due to crack propagation
5. Electrode pores	i. micro	dia $\leq 5\mu\text{m}$	< 250	pores exist in CL
	ii. macro	dia $\sim 5\text{-}25\mu\text{m}$	250–3000	
6. Missing or empty catalyst			> 5000	portion of CL missing or large damaged areas in CL

4.5 Conclusions

In this study, we present a novel, non-destructive and non-contact method to identify and characterize defects that have been generated during the fabrication of commercial CCM electrodes using the decal transfer method and classify the defects based on their dimensions. The main findings can be summarized as follows:

1. *Developing Non-destructive method*

The use of optical microscopy to examine and quantitatively characterize CL defects has been found to be particularly advantageous since it does not require the destruction of samples and so allows the evolution of defects to be monitored from BOL to its EOL. Our approach consists of first characterizing the defects in stored and freshly prepared CCMs at the BOL and then aging them in a non-reactive environment in a designed test cell and characterizing the defects once again at the MOL and EOL.

2. *Investigation of CL defects*

Two commercial CCMs with different types of defects were investigated. First, crack propagation in CL was studied in a reinforced CCM containing defects in its BOL state developed due to unstable storage conditions in an environment with uncontrolled humidity. This led to a significant number of BOL defects such as cracks formed during long-term storage of samples, which subsequently propagate into larger cracks during aging. Defect/crack propagation in this CL

sample was found to be rapid and caused the OCV to degrade at a rate of 2.55 mV/h. In contrast, freshly prepared non-reinforced CCMs with CL defects including missing or empty catalyst areas and scratches produced during the decal transfer step were also investigated. Follow-up examination of these samples revealed that these defects did not grow after 40 hours of aging. The major degradation observed included cracks and delaminated portions of the CL, presumably caused by expansion of the membrane during hydration. The performance of cells containing this CCM did not deteriorate as rapidly as those containing the first CCM stored at uncontrolled humidity, as reflected in an OCV degradation rate of 1.12 mV/h. As noted above, these cracks did not exist at BOL and formed during aging due to membrane deformation.

3. *Classification of CL defects*

Six types of defects on the CCMs have been identified based on their length, area and characteristic features. The most common defects observed were cracks and missing portions of the CL. Based on microscopic examination, it appeared that cracks at BOL propagated at a faster rate than do the other defects. IR thermography indicated that defects such as pinholes formed during the MEA fabrication likely had a more significant effect on fuel cell performance than other CL defects.

The method of investigating defects presented here as well as the classification of these defects in terms of their effect on long-term fuel cell degradation should prove helpful for fuel cell researchers and manufacturers to develop robust fuel cell systems. These techniques should allow them to identify the specific defects in CCMs and MEAs and better understand their degradation over time. Further work is currently underway in our laboratory on the influence of manufacturing defects on the chemical degradation of CCMs and the impact of manufacturing defects on CCM lifetime.

5 Characterization of Catalyst Layer Defects in CCM and Resulting Cell Performance

The main goal of the research described in this chapter is to investigate the evolution of catalyst layer defects such as missing/thin catalyst layer defects during aging process and provide a better understanding of their propagation and the resulting effect on cell performance. The propagation of catalyst layer defects due to mechanical and chemical degradation is analysed at BOL, MOL and EOL and related to the corresponding cell performance. This behaviour is compared to that of CCMs that initially are defect-free.

5.1 Introduction

Any damage to the fuel cell components during the manufacturing process ultimately leads to the failure of the electrode. Defects on the catalyst layer, in particular, can have dramatic effects on fuel cell performance, cost and stability [7][18]. Unnecessary time and money is spent tearing apart fuel cell stacks to remove a single faulty cell. Thus, defects developed during fuel cell production must be examined and characterized with the hope of differentiating between fatal and minor defects. Perhaps the most important issue regarding the mass production of fuel cell components is the improvement of the quality control inspection to identify CCM defects and predict their lifetime [25][26]. Better quality control inspection could help reduce CCM imperfections that stem from errors such as inconsistencies associated with catalyst ink preparation and catalyst coating methodology[19][20][21][22] as well as thickness variation in catalyst layers and electrolyte membranes [23][24].

Inconsistent catalyst ink preparation in the production line is one of the main contributors to CCM defects. Defects can arise when inconsistencies in slurry formulation cause non-uniformities in the catalyst coating. This in turn can lead to an uneven distribution of catalyst layer pores and micro-cracks in the catalyst layer after the ink is sprayed and dried on the decal substrate [138]. The next step in fabrication is to transfer the loaded catalyst layer on the decal substrate onto the electrolyte membrane by hot pressing the three layers comprising the CCM at a temperature of 130°C - 140°C. During this step, the ionomer in the catalyst layer develops strong bonds with the ionomer in the electrolyte membrane [22][139]. The bond formation between adjacent catalyst layers and the

electrolyte membrane reduces the contact resistance and improves catalyst utilization both of which play key roles in fuel cell performance. Any improper catalyst transfer from the decal onto the electrolyte membrane can lead to the formation of cracks, scratches, thin/missing catalyst layer and empty catalyst layer [4] which have the potential to develop into dangerous membrane pinholes [69]. Phillips and Bender et al showed that various artificial catalyst layer defects can lead to the non-uniform distribution of current in the electrode. In particular, negligible current was observed to flow across thin/zero catalyst sites. These areas can develop into hotspots during the electrochemical reaction and eventually pinholes [69][140].

Therefore, control of the catalyst layer structure and ideal catalyst transfer on the electrolyte membrane are some of the biggest challenges faced by CCM manufacturers. Another major quality control problem in catalyst layer research is tracking defect growth during MOL and EOL. Once the MEA has been hot pressed, the complex matrix of components can change the orientation of existing defects and cause the emergence of additional defects, making it difficult to characterize original defects. Therefore, it is very important to understand the sensible changes and growth of catalyst defects during fuel cell operation.

Understanding the morphologies of various types of defects, their origins during manufacturing and their impact on cell performance are extremely important in developing a quality control program [25]. If this information is combined with defect detection guidelines developed by electrode manufacturers, material suppliers, production engineers, research laboratories and the DOE, a systematic approach in quantifying defects can be developed. In the future, different parties should provide their own perspective on classifying defect severity and priority to eventually formulate a consistent decision-making process.

To achieve an accurate CCM quality control inspection system, this research focuses on real catalyst layer defects. In collaboration with industrial partners, different orientations and irregularities of catalyst layer defects developed during production were examined and CCMs with MCLD of interest are reported in this study. The objective of this work was to inspect morphological changes in the catalyst layer defects as they propagated throughout the aging process by implementing a non-destructive investigation method. The defected CCMs/MEAs were

then electrochemically tested in a stack to understand the behaviour of defects in a typical fuel cell environment. Key concerns of this study were the factors that led to defect propagation triggering catalyst layer failure. Figure 5-1 shows the research framework for investigating defects in CCMs.

5.2 Research Framework

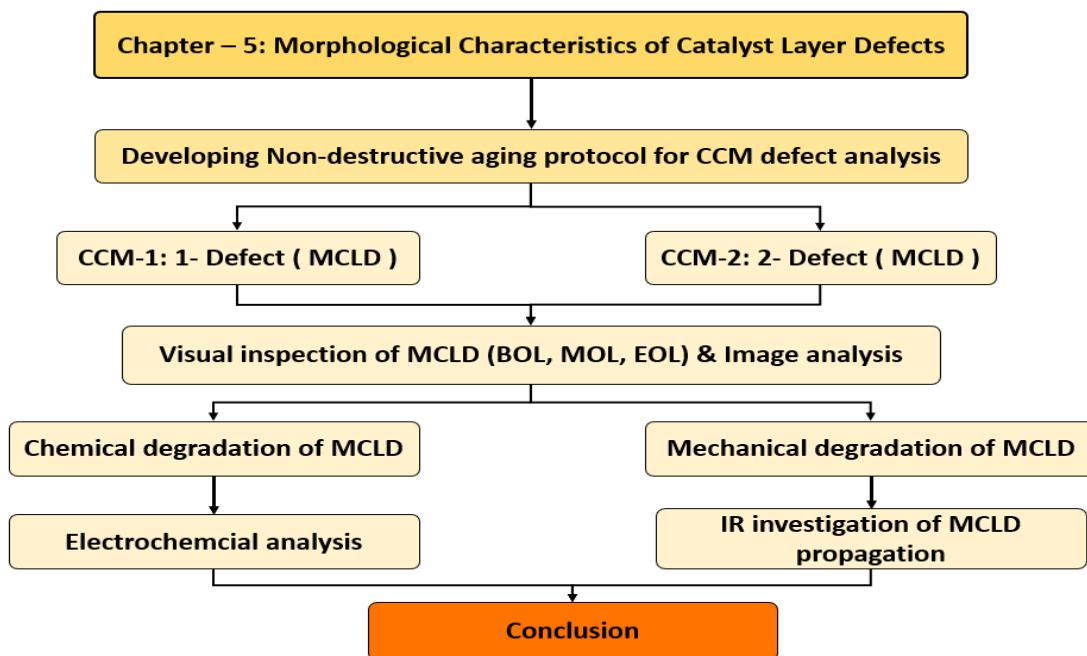


Figure 5-1: Research framework on morphological characterization of CCM defects.

5.3 MCLD defect analysis framework

Various defects that are commonly observed in commercial CCMs during the production line were identified and classified with respect to size, shape and area in Chapter 4. In the present chapter, we focus on the morphological features of missing/thin catalyst layer defects (MCLD) and their propagation during the aging process and the corresponding effect on electrochemical cell performance.

It is well known that the CL is a key component of the cathode in a PEMFC. The steps by which the CL is fabricated and incorporated into the MEA is presented schematically below in Figure 5-2a. The catalyst layers are made by mixing a Pt/C catalyst diluted with deionized water and ethanol mixed with ionomer binder solution. The catalyst ink is spray-coated onto a decal substrate

followed by drying at 80°C. The catalyst layer on the decal substrate is then transferred onto a PFSA Nafion membrane using the decal transfer method in a hot press at 140°C for 5 mins. During the decal peeling process, tiny portions of catalyst can be left over on the decal substrate, forming a catalyst irregularity defect on the catalyst layer. These defects are defined as missing catalyst layer, thin catalyst layer or zero catalyst layer.

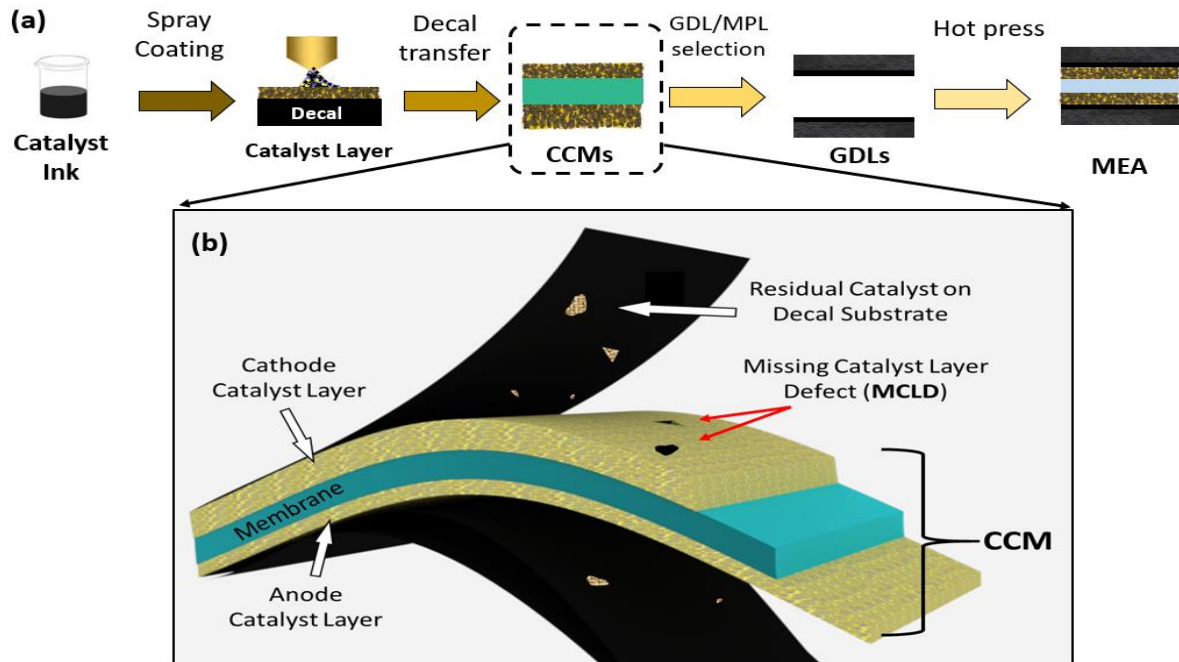


Figure 5-2: (a) Steps involved in fabrication of CCM/MEA. (b) Schematic showing missing catalyst layer defects (MCLD) in the CCM fabricated using the decal transfer method.

The MCLDs are one of the most common defects that form during the mass production of CCMs. An example of how such a defect can form during the decal transfer of the CL is shown schematically in Figure 5-2b. The red arrows on the image indicate two MCLDs formed on the CCL during the decal removal process when catalyst has not been transferred from the decal substrate to the CCL. For example, the catalyst transfer ratio of the catalyst layers from the decal onto the membrane in the CCMs investigated in this study were ~90 - 95%. Saha et al [63] reported catalyst transfer rates of 60%, 80%, 90% and 99% using the DTM technique. No research work to date has focused on investigating MCLDs and their impact on PEMFC performance. Therefore, the primary focus of the research is to investigate the behaviour of these catalyst layer defects during aging, which is a high priority topic in the fuel cell industry.

5.3.1 Test protocol for non-destructive CCM defect analysis

Figure 5-3 depicts the new framework for investigating real catalyst layer defects that would benefit the quality control procedure used by fuel cell manufacturers. This framework is novel because it provides manufacturers with a non-destructive CCM defect analysis tool. The details of this framework are discussed in this section.

A necessary aspect of evaluating the quality of the fuel cell electrode is the accurate measurement of defects arising during MEA manufacturing and the impact of such defects on cell performance. As discussed previously in section 5.3, the formation of manufacturing defects such as spots with excess or limited catalyst loading leads to a non-uniform catalyst layer thickness. This can lower fuel cell performance due to gas crossover through the defected zones in the membrane or uneven Pt catalyst thickness, especially across the defects. The problems in identifying defects in the CCM are complex because the catalyst layer is typically black and non-reflective so that identification of discrete defects in the large active area of the CCM is difficult. In addition, the time required to detect the defect is a key feature of any technique. Obviously, it is essential to detect all defects as early as possible to avoid cell failure and complete stack shutdown.

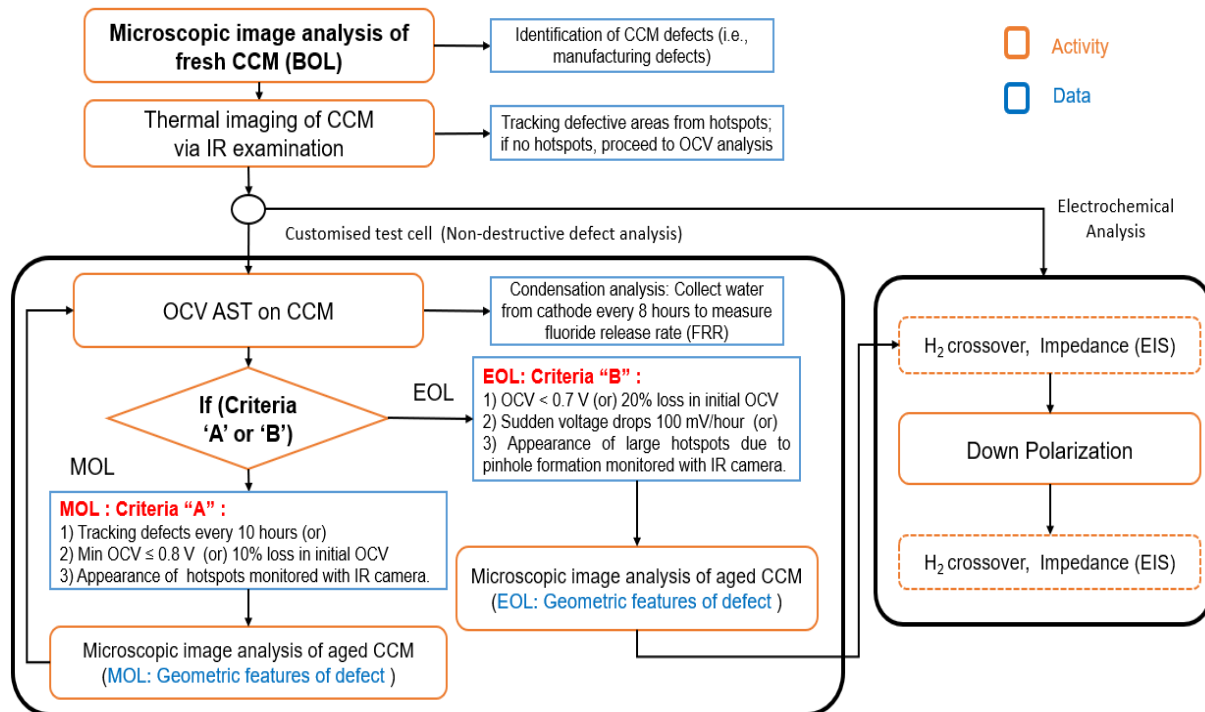


Figure 5-3: Non-destructive CCM defect analysis framework combined with electrochemical analysis.

Figure 5-3 shows the flowsheet of the various steps to monitor and characterize the aging of CCMs and the formation and growth of defects. As discussed in section 4.3.2, defects were identified using reflected microscopy at BOL in pristine CCMs. IR thermography of the sample was captured before the start of OCV analysis to confirm that no pinholes or leak spots were present at BOL, as discussed in Section 4.3.3. Only pinhole-free CCMs were allowed to proceed to the OCV-AST. DOE-recommended protocols were used for this OCV-AST operation [141][108]. MCLD defective CCMs were aged using the custom-designed test cell described in section 4.3.4. Operation of the CCMs in the test cell enabled the user to investigate defect propagation at MOL and EOL. During the OCV analysis, two criteria (A and B) were set to investigate the evolution of defects in the membrane.

Criterion A:

1. Experiments were stopped every 10 hours (or if any sudden drop in OCV was observed) to inspect the manufacturing defect (MCLD) growth during the AST. The growth of defects (i.e., total area of defects and total pink areas due to catalyst thinning/catalyst erosion/washout inside the defect) was tracked over time to estimate the loss of catalyst and correlate this in turn to the loss in overall cell performance, as measured by the loss OCV in the CCM.
2. OCV was monitored over an extended period of time until it had dropped by more than 10% of the initial value. The loss in voltage might be due to loss of catalyst, degradation of polymer in the membrane or due to gas crossover through defects (pinholes).
3. A periodic inspection (every 15 minutes) by IR imaging was conducted on the polycarbonate design test cell device to identify hotspot locations on the sample. Since even a small amount of hydrogen crossover from anode to cathode could severely damage the membrane, tracking hotspots was essential for safe operation of CCMs.

As the AST progressed, the degradation of materials at local areas rapidly increased and led to high gas crossover.

Criterion B:

1. If the OCV drop over the sampling period exceeded 20% of the initial value (EOL target set by the US DOE [141][108], EOL conditions were met and the experiment was terminated.

It should be noted that the primary focus of the research was to investigate the morphological changes of the catalyst layer defects during MOL aging and gain a better understanding of steps involved in defect (MCLD) propagation. This proposed testing method was found to be successful for investigating CCMs during MOL without any external damage. From our testing methods, we observed that the morphology of the catalyst layer defects was not affected by the GDL fibers and/or flow channel plates indentations during MOL and EOL. Therefore, it is expected that the propagation of defect during the aging process should be caused primarily by chemical and mechanical reactions of the reaction gases. After the completion of these two criteria, the aged CCM was hot-pressed to a GDL and then subjected to electrochemical analysis through RH cycling, polarization analysis, H₂ crossover measurements and AC impedance analysis.

In this chapter, 3 defective CCMs (CCM-1, CCM-2 and CCM-3) and 1 non-defective CCMs (CCM – baseline) were used for OCV-AST. A summary of the defects found in these CCMs after aging is provided in Table 5.1. The defects in CCM-1 and CCM-2 were examined at MOL, while CCM-3 was operated without any interruption during the OCV-AST until EOL. Then electrochemical analysis of CCM-1 and CCM-2 was carried out in the FCAT cell to study the effect of the MCLDs on typical cell operation at a constant low RH and while being subjected to wet/dry RH cycles. The results of the electrochemical analysis of CCM-1 and CCM-2 are discussed in section 6.5.2 and section 6.4.3, respectively.

Table 5-1: Summary of CCMs investigated in this chapter

Sample	No. of CL defects (MCLD)	Avg. CL thickness lost in MCLD (μm)	Microscopic defect inspections (h)	No. of hours operated (h)	Voltage degradation rate (mV h^{-1})
CCM – 1	1 – MCLD	~ 5.61	0, 10, 50, 100	100	1.6
CCM – 2	2 – MCLD	~ 3.82 ~ 4.78	0, 12, 25	25	2.98
CCM – 3	1 – MCLD	~ 2.50	1, 100	100	1.03
CCM – baseline	No defects	Baseline	-	100	0.6

5.4 Results and Discussion

5.4.1 Microscopic investigation of CCM defects and image processing

The reflected light microscope setup described in section 4.3.2 was used to investigate the catalyst layer defects. The CCM samples were first attached to a plastic frame to dampen any vibration of the membrane that might occur. To identify MCLD or any catalyst layer defects, a beam of white light with 20% intensity was directed (transmitted light) onto the ACL of the CCM by facing the CCL toward the reflected light microscope camera. Adjustment of the light intensity depending on the ACL and CCL thicknesses was an important factor in detecting the CL defects. A higher light intensity was recommended for the thicker CLs. Then the x-y plane of the microscope was connected to a motorized stage so that it could be rastered over the CCM sample at a uniform rate and the entire sample could be inspected. On non-defected catalyst areas, the thick CCL blocked the transmitted light from passing through the CCM. However, the transmitted light could pass through thinner defected catalyst areas (uneven catalyst, no catalyst, cracks and pinholes) in the CCM and merge with green reflected light from the objective lens to produce a magenta/pink color on these regions. This distinct colour allowed specific defects on the CCM to be identified and characterized; more intensely colored regions indicated thinner catalyst layers. Specific regions of interest (ROI) were further investigated in dark-field mode to provide more detail concerning the MCLDs and cracks in the catalyst layer. Finally, a complete areal inspection was carried out by rastering the microscope over the entire CCM sample and digitally stitching together the numerous microscopic video images of the CCMs into a high-resolution image using Image J image stitching software. To minimize the time of microscopic image stitching, a MATLAB program was developed to automate the input of the video file to the ImageJ imaging software to produce large stitched images. The MATLAB code is included in Appendix section 10.2.

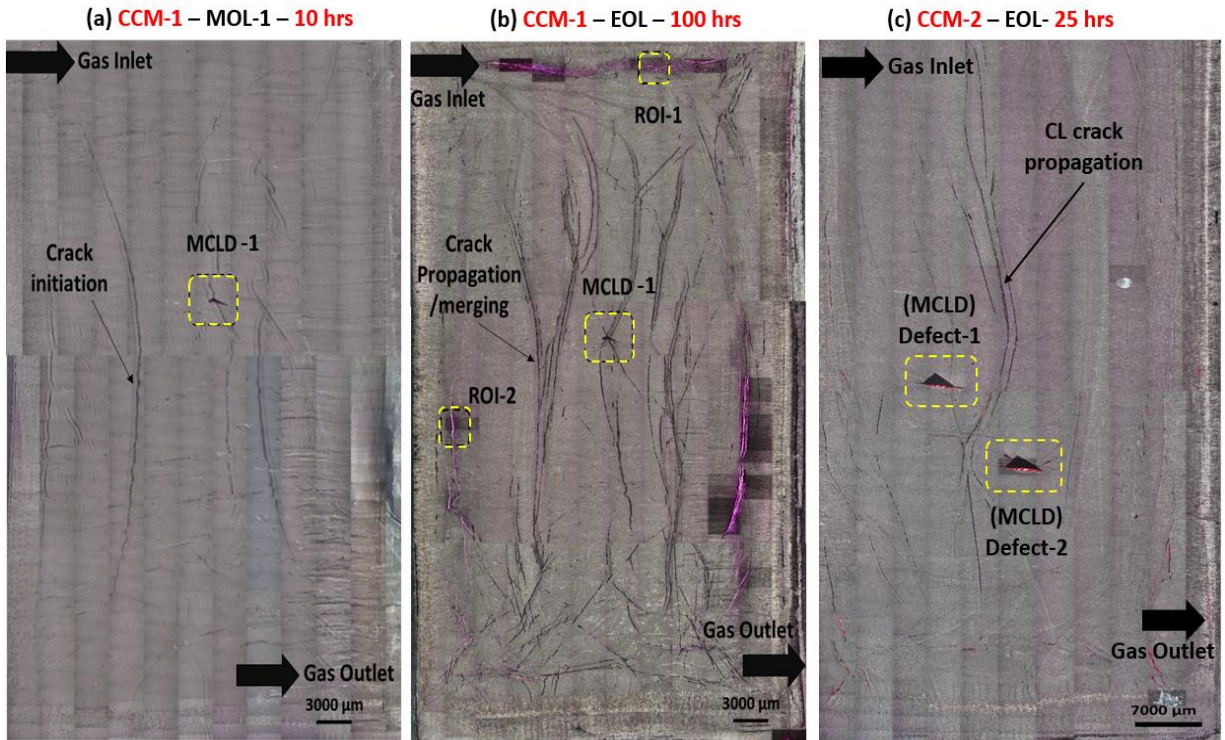


Figure 5-4: Stitched optical microscopic image of CCL of defected (a) CCM-1 showing 1 MCLD observed after (a) 10 hours (MOL-1) and (b) 100 hours of OCV-AST (EOL); regions ROI-1 and ROI-2 are specifically selected for further investigation of crack propagation and delamination of CL. (c) CCM-2 showing 2 MCLDs (Defect-1 and Defect-2)

Once inspected at BOL, CCMs to be aged proceeded to the OCV-AST conducted in the test cell discussed in section 4.3.4. The microscopic image analysis follows the procedure described in the flowchart/framework in Figure 5-3. The entire 48 cm² stitched active areas of the CCL of CCM-1 and CCM-2 are shown in Figure 5-4. The stitched optical images of CCM-1 after 10 and 100 hours aging by the OCV-AST appear in Figures 5-4a and b, respectively, while the image of CCM-2 after 25 hours of OCV-AST is presented in Figure 5-4c. The gas inlet and outlet directions are indicated at the top left and bottom right of the image. Three major changes were observed during the aging process:

1. A decrease in OCV as a result of growth of defects in CCMs during AST was observed. The results of the OCV analysis are presented in section 5.4.2.
2. Microscopic investigation of catalyst layer defects (MCLD) during MOL showed clear evidence of defect propagation and areas where catalyst particles were degraded inside MCLD. A detailed inspection of growth of MCLD is presented in section 5.4.3.

3. Propagation of new defects (i.e., cracks and delamination) in the CLs as a result of chemical and mechanical degradation was observed at MOL and EOL.

The dark line/arcs on the images in Figure 5-4 correspond to cracks propagating in the catalyst layers as a result of deformation of CCM after swelling and shrinkage of the membrane. Due to interruptions during the MOL could cause the membrane to expand and shrink and thereby develop cracks on the catalyst layer.

Crack initiation and propagation are observed at three stages in this study: crack initiation at MOL-1 (CCM-1 - 10 hours), crack propagation at MOL-2 (CCM-1 - 50 hours) and crack propagation/merging/delamination at EOL (CCM-1 - 100 hours). As shown in Figure 5-4a, no significant crack opening or propagation in the catalyst layer is observed at MOL-1 (CCM-1 – 10 hours). The stitched microscopic image of the aged CCM-1 after 100 hours of OCV-AST (Figure 5-4b) reveals evidence of extensive crack propagation at EOL. The crack that had just initiated after 10 hours grew deeper and developed a more branched structure after 100 hours. ROI-1 and ROI-2 are areas appearing in the EOL image specifically selected for closer examination of damage. ROI-1 represents an area where cracks have severely propagated in the catalyst layer. Two effects are clearly evident in this area: cracks with an average width of ~ 10 to 50 μm have formed and several adjacent cracks have merged together. ROI-2 is a delaminated area of the catalyst layer that has occurred as a crack propagates during membrane deformation. The depth of the catalyst layer defect in ROI-2 is further investigated using Z-profile and 3D imaging. This analysis shows that the catalyst layer in these areas has not been completely removed and that the material delaminated or detached amounts to ~50 – 70% of the original thickness over an average width of ~ 50 μm – 150 μm , leaving behind remaining thin portions of the catalyst attached to the electrolyte membrane. Furthermore, large catalyst layer pores with diameter of ~25 μm are observed in the leftover thin catalyst layers. A more detailed discussion of the crack growth behaviour in CCMs is given in section 5.4.3.3.2.

5.4.2 OCV analysis of initially defective CCMs

OCV-AST experiments were conducted on CCMs until its OCV dropped by ~ 20% from its initial value as discussed in section 5.3.1. The results obtained for 3 CCMs (CCM-1, CCM-2 and CCM-3) with initial defects and one with no defects (CCM-baseline) are reported in this

chapter. The OCV curves obtained using these CCMs over the course of their ASTs are presented in Figure 5-5. The OCV-AST was stopped at MOL in the case of CCM-1 (after 10 hours and again after 50 hours) and CCM-2 (after 12 and 25 hours) based on the criteria given in Figure 5-3 to examine the evolution of the MCLDs with the optical microscope. Although CCM-3 and CCM-baseline did not reach their EOL at the end of 100 hours, the experiments were terminated at this point in order to compare their rates of OCV degradation with that of CCM-1. CCM-2 was stopped due to hotspot identified across the defect-2 after 25 hours.

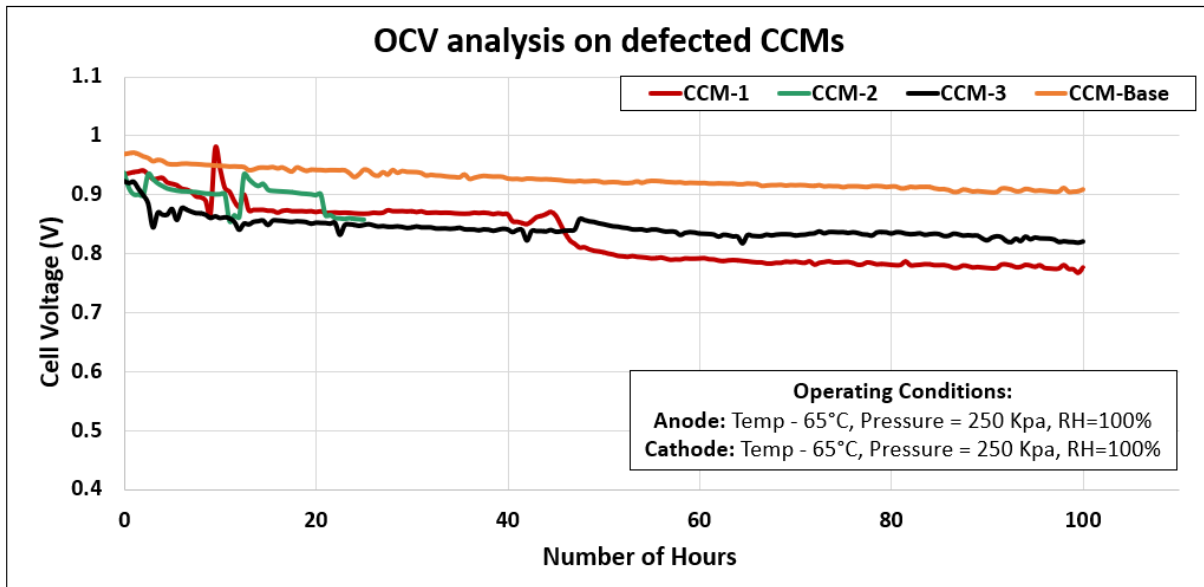


Figure 5-5: OCV test results of CCM-1, CCM-3 and CCM-baseline operated in the test cell over a duration of 100 hours. The green curve represents the OCV decay curve of CCM-2 which was operated for only 25 hours due to pinhole formation inside the MCLD defect.

The red curve in Figure 5-5 shows that the CCM-1 OCV is more severely affected over the course of the AST than CCM-3 and CCM-baseline – decreasing from 935 mV to 776 mV at an average rate of 1.6 mV/hr. On the other hand, the OCV of CCM-3 degrades from 923 mV to 820 mV at an average rate of 1.03 mV/hr. Two observations related to the voltage loss in CCM-1 were made:

- i) IR inspection detected a small hot spot across the MCLD in CCM-1 after 100 hours, as will be discussed in section 5.4.4.

ii) Microscopic inspection and quantitative analysis of the images reveals that some loss of catalyst inside the MCLD, crack formation in the catalyst layer and delamination of catalyst layer has occurred, as will be discussed in section 5.4.3.3.2.

To examine the evolution of MCLD in CCM-1, samples were removed from the test cell at intervals of 10, 50 and 100 hours. This stop/start procedure could affect the state of CCMs due to dehydration of membranes when exposed to atmosphere. Evidence that this occurred to some extent in the case of CCM-1 is evident from the permanent decrease in the OCV observed after the 50-hour point (Figure 5-5). To directly assess this, CCM-3 and CCM-baseline were operated under identical conditions as CCM-1, but without removing the CCM from the test cell until the very end of the experiment after 100 hours. The results shown in Figure 5-5 indicate that the average degradation rates of CCM-3 and CCM-baseline are 1.03mV/hr and 0.6mV/hr, respectively. In both cases, the degradation of voltage is less than in the case of CCM-1. This difference indicates that the stop/start interruptions to remove the CCM from the test cell for microscopic examination and then re-install it for subsequent testing have an effect on the OCV-time behavior of the CCMs. It is also observed that in both initially defected CCMs, similar types of catalyst degradation were observed inside the MCLD, as will be described in section 5.4.3.

Similar results (green curve in Figure 5-5) are observed for CCM-2 that contained two MCLDs in the CCL at BOL, as shown in Figures 5-4c. Over the course of the AST, the OCV degrades by 66 mV at a very high average rate of 2.98 mV/h. However, due to the formation of a hot spot in the location of MCLD -2 in Figure 5-4c (see IR thermograph in Appendix section 10.3), the sample met the EOL criteria after only 25 hours of AST. Obviously, the rapid decline in the OCV can be attributed to the severe physical damage of the membrane.

5.4.3 Degradation of catalyst layer defect – MCLD

One of the common fabrication defects observed in CCM is an uneven catalyst layer coating. The catalyst layer thickness and functional surface formed by one or more layers is very important in the fabrication of CCM. It is a complicated matter to identify the non-uniformity of the catalyst layer on the polymer membrane. As discussed earlier, the sources of non-uniformity can be improper catalyst spraying, transferring or drying conditions (e.g. temperature, humidity,

pressure and non-air gas environment). Figure 5-6a shows evidence of irregularities (i.e., missing catalyst loading/ thin catalyst spots) in the catalyst loading of CCM-1 presumably formed during the decal transfer step of fabrication. This defect is considered a manufacturing defect since it is present at BOL. The faster degradation of this CCM at its location during the AST indicates that it is an area that is most prone to develop into a failure point during subsequent PEMFC operation.

5.4.3.1 Propagation of manufacturing defect - MCLD of CCM-1

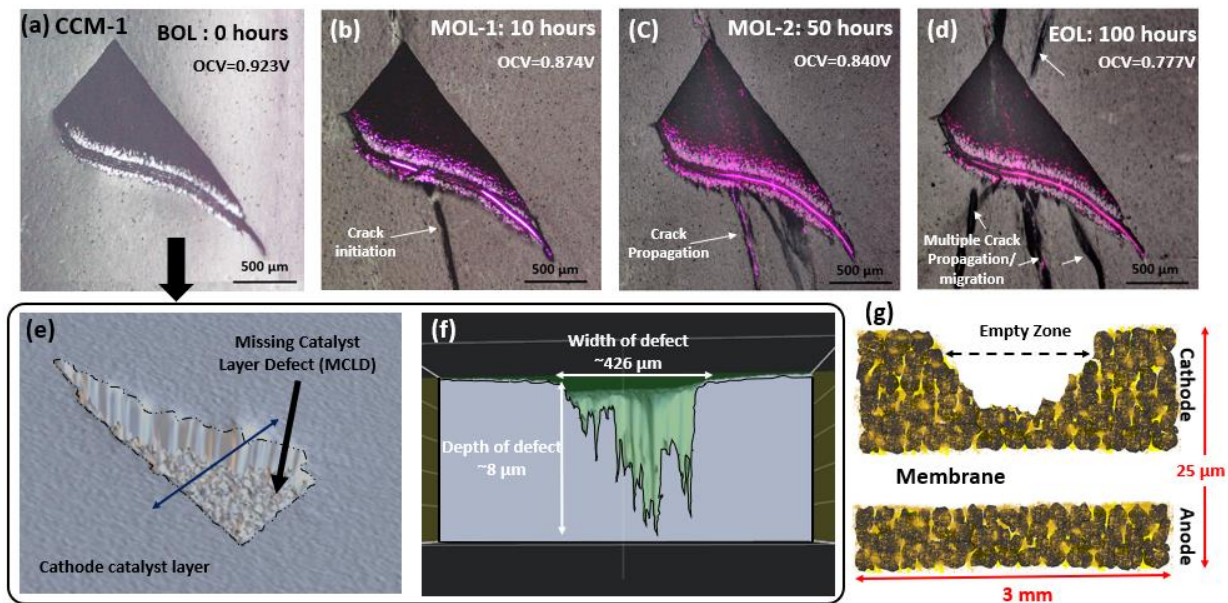


Figure 5-6: Microscopic images of defect growth in an MCLD in a defected CCM-1 (a) BOL at 0 hours, (b) MOL-1 after 10 hours OCV-AST, (c) MOL-2 after 50 hours OCV-AST, (d) EOL after 100 hours OCV-AST, (e) 3D graphical view of MCLD with active area of $757016 \mu\text{m}^2$ on CCL (f) cross-sectional view of MCLD showing dimensions of depth and (g) schematic view of MCLD in CCL across the CCM-1.

Figures 5-6a-d show the morphological changes of this MCLD (dark triangular area) at the 0-, 10-, 50- and 100-hour points of the AST. Based on the OCV curve in Figure 5-5, this defect does not significantly affect cell performance initially; however, as it grows and exposes more of the membrane, it accelerates local membrane degradation due to the direct reaction of fuel and oxidant. Decreased catalyst density also leads to slower reactions, decreasing voltage and ultimately cell performance. Examination of CCM-1 at BOL shows that the MCLD covers a geometric area of $\sim 757016 \mu\text{m}^2$, of which a small portion is a region of empty/thin catalyst (pink area that covers $\sim 7370 \mu\text{m}^2$) (Figure 5-6a). A 3-D diagram of the MCLD at BOL is depicted in Figure 5-6e, while a cross-sectional view showing the depth of the defect along the blue line in Figure 5-6e is

presented in Figure 5-6f. The width of the defect is measured to be $\sim 426 \mu\text{m}$ across the blue line. Note that the depth of the defect is not uniform presumably due to the non-uniform removal of catalyst during the decal transfer step. Figure 5-6g presents a schematic (not drawn to scale) of the cross-section of the MCLD to provide a better view of the defect. In this research project, all CCMs provided by our industrial partner contained defects only on the cathode side and not at all on the anode.

After BOL microscopic inspection, CCM-1 was further examined by IR thermography after 10, 50 and 100 hours of AST to make sure that no pinholes had formed. Since no pinholes had formed, it was re-connected to the workstation to resume the monitoring of its OCV. The pink areas in Figures 5-6b, c and d corresponding to very thin/absent catalyst regions in the MCLD continue to grow as the CCM ages.

A primary focus of this study is to investigate the relation between the evolution of the MCLD and its loss in OCV as the CCM ages. As shown in OCV curves in Figure 5-5 (red line), CCM-1-MCLD experiences a noticeable voltage degradation of 7.4% over the first 10 hours of operation as its voltage decreases from 935 mV to 865 mV. Particularly noticeable is the abrupt voltage drop of 36 mV from 901 mV to 865 mV between the 9th and 10th hours of the AST. To determine whether this loss in performance can be correlated to a change in the MCLD, we have carried out an image analysis of the CCM after the 10th hour (i.e., MOL-1). Further image analysis is conducted on the CCM after aging for 50 hours (MOL-2) and 100 hours (EOL) over which period the OCV is observed to have dropped by a cumulative amount of 10.1% and 17.8% with respect to its initial voltage. Figure 5-7a shows the areal growth of the MCLD (black curve) and degraded catalyst area inside the MCLD (pink curve) during the OCV AST. Prior to OCV testing, the pink area inside the MCLD detected is negligible (Figure 5-6a), as expected. As the AST proceeds, the catalyst in defect areas undergoes washout that leaves behind bare membrane or thin catalyst layer spots due to non-uniform bonding of catalyst across the defect. The cumulative area of the MCLD (dark triangular region in Figure 5-6) increases by 5.4% from BOL to MOL-1(10 hours), 11.25% between MOL-1 and MOL-2 (40 hours) and 1.58% between MOL-2 and EOL (50 hours) (Figure 5-7a). The pink area in Figures 5-6a-d drastically increases by a factor of ~ 17.7 over the 100 hours of the experiment. As a result, the voltage degrades at a rate of 1.6 mV/h over this duration. For

the first 10 hours of the AST, the pink area increases substantially by a factor of 13.5, indicating a high degree of catalyst degradation within the defect and the voltage decreases at a rate of 8.2 mV/h. This growth in pink area is attributed to the loss of catalyst or washout of catalyst inside the MCLD, leaving empty catalyst sites that presumably facilitate gas crossover across the MCLD and reduce the OCV. From 10 to 100 hours of the AST, only a very small change in the pink area is observed and the voltage drops at a lower rate of 1.3 mV/h. This suggests a strong relationship between irregularity in catalyst layer thickness and cell performance.

The areal growth of the entire MCLD (dark triangular area in Figures 5-6a-d) over the first 10 hours of the AST increases slightly to 5.94% total defect area. (black curve in Figure 5-7a), while the OCV decreases at the very high rate of 8.2 mV/h. From 10 hours to 100 hours, the total area of MCLD increases by 17% and the OCV decreases at a rate of 1.3 mV/h. Examination of the optical images in Figures 5-6b and c shows that most of the CCM damage appears to involve the propagation of cracks in the catalyst layer. Taken together, these observations suggest that no strong relationship exists between the growth of the entire MCLD and cell performance. As discussed above, it appears that the relationship between cell performance and catalyst layer thickness is much stronger than the relationship between cell performance and the growth of MCLD and other operational aging defects (CL cracks). However, more investigation is required on other samples with this type of defect and others to further corroborate this observation.

To conclude, the MCLD has been found to grow rapidly during MOL-1 due to chemical degradation causing loss of catalyst particles inside the defect, but its degradation stabilizes significantly over the remaining period until the EOL as shown by the pink curve in Figure 5-7a. In section 5.4.3.3, specific regions of the degraded area inside the MCLD are investigated at 100x magnification to more closely examine the changes in the defect morphology and possible mechanisms for degradation of the catalyst layer.

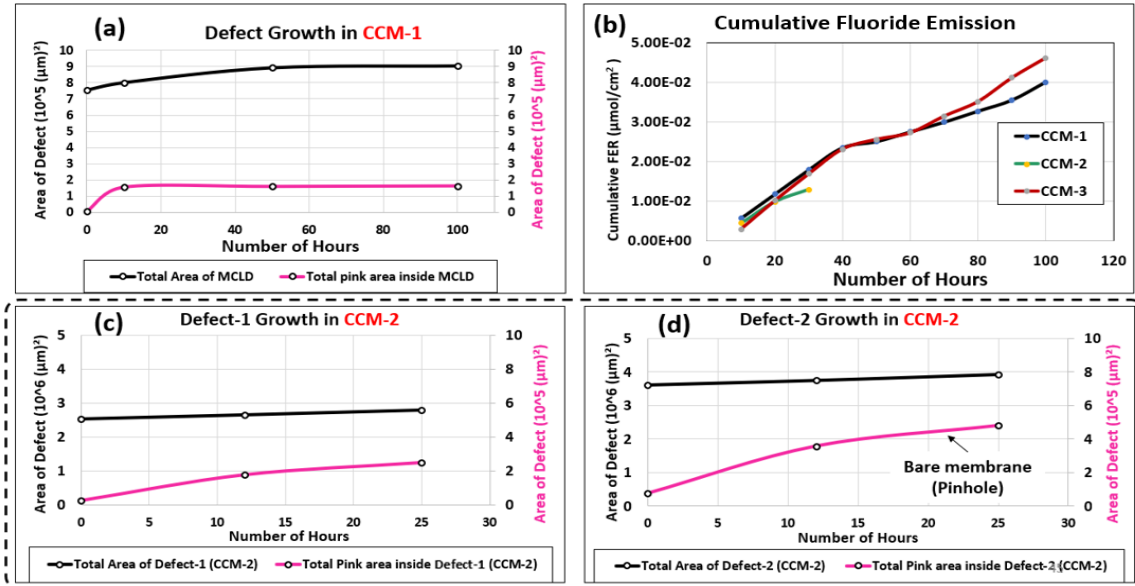
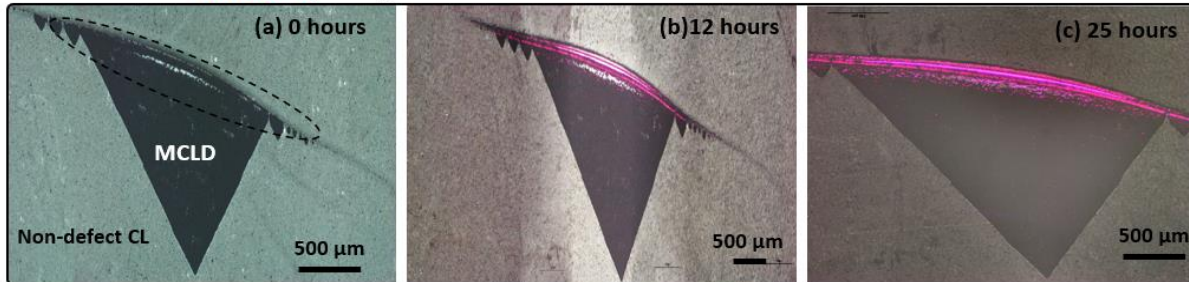


Figure 5-7: (a) Areal growth of MCLD in CCM-1 (black curve represents the total area of MCLD (triangular area) and pink curve represents the degraded catalyst area inside MCLD), (b) Cumulative Fluoride Emission at the cathode over the course of 100-hour OCV-AST and areal growth of MCLD in (c) defect-1 and (d) defect-2 of CCM-2.

5.4.3.2 Propagation of manufacturing defects - MCLD of CCM-2

CCM-2: Cathode : **Defect – 1 (MCLD)**



CCM-2: Anode : **Defect – 2 (MCLD)**

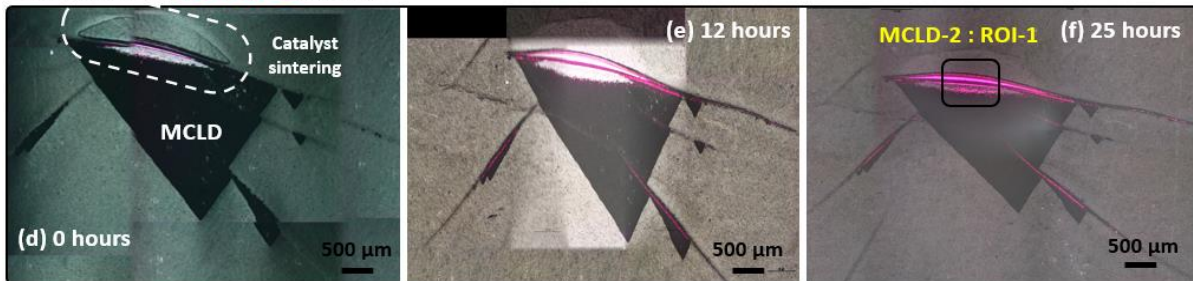


Figure 5-8: Microscopic image of defect growth of MCLD in CCM-2 (see the location of defect in Figure 5-4c): defect -1 on cathode captured at (a) 0, (b) 12 and (c) 25 hours; defect-2 on anode at (d) 0, (e) 12 and (f) 25 hours of OCV AST.

Figure 5-8 depicts a surface view of the morphological changes of defect-1 and defect-2 in CCM-2 on cathode at 0 hours, 12 hours and 25 hours of OCV-AST. Defect-1 is located on the cathode side, while defect-2 appears on the anode side in the locations indicated in Figure 5-4c over the entire $\sim 48 \text{ cm}^2$ area. The region in defect-2 designated as ROI-1 in Figure 5-8f is shown at higher magnification in Figure 5-9. The plots in red at the bottom of Figures 5-9 correspond to Z-profiles along the blue arrows indicated in the microscopic images in Figures 5-9a and b. Although CCM-2 was tested for only for 25 hours, the trend in the defect growth is similar to that of CCM-1. The bare membrane inside defect-2 in CCM-2 likely facilitates gas leakage through the membrane and the rapid decrease of the OCV at a rate of 2.95 mV/h. The aerial view and depth profile in Figure 5-9b reveals the presence of a micro-pinhole on a portion of this bare membrane. The proposal that gas has leaked through the bare membrane (via these micro-pinholes) is supported by the IR thermograph for this sample (see Appendix section 10.3) which reveals the presence of hotspots in the same region where the micro-pinholes appear. The pink area inside the MCLD increases by 942% due to catalyst washout, whereas the total area occupied by the MCLD increases by only 5.5% after 25 hours. The significant loss of the OCV is likely due to the formation of micro-pinhole or membrane cracks, as shown in Figure 5-9b. Once electrodes develop pinholes or leak zones, the criterion for EOL is met and the experiment is terminated. The following two additional observations can be made from this microscopic inspection of defect-2 in CCM-2.

1. By closely inspecting defect-2 at BOL from both the cathode and anode sides, a catalyst sintering area is found across the MCLD as represented by the white dotted circle in Figure 5-8d. Since the catalyst sintering is observed at BOL, it is expected that this defect presumably formed during the hot press ($\sim 140^\circ\text{C}$) of decal substrate and polymer membrane. As a result of the high temperature and pressure during the hot press across the defect-2, a small section of the catalyst layer is completely missing in the area denoted as ROI-1 in Figure 5-8f and Figure 5-9. Catalyst sintering presumably causes polymer melting in the membrane that might lead to cracks and pinhole in the membrane as shown in Figure 5-9b. A magnified surface view of ROI-1 in Figures 5-9a and 5-9b clearly shows a strip of bare membrane that would be exposed to the reaction gases during cell operation.
2. Although gas leakage across the defects in CCM-2 is not observed at BOL, IR thermography shows that gas leakage across the sintered area in defect-2 has likely occurred after 25 hours of OCV AST. Bare membrane inside the sintered region would

allow the permeation of H₂ from the anode that can react with O₂ on the surface of the Pt cathode catalyst particles and form local hotspots in the electrode. The elevated temperature during the operation can also cause polymer decomposition and micro-pinhole formation in the membrane. as shown in Figure 5-9b. [71,101,142].

CCM-2: MCLD-2 : ROI – 1 : Membrane cracks and pinhole

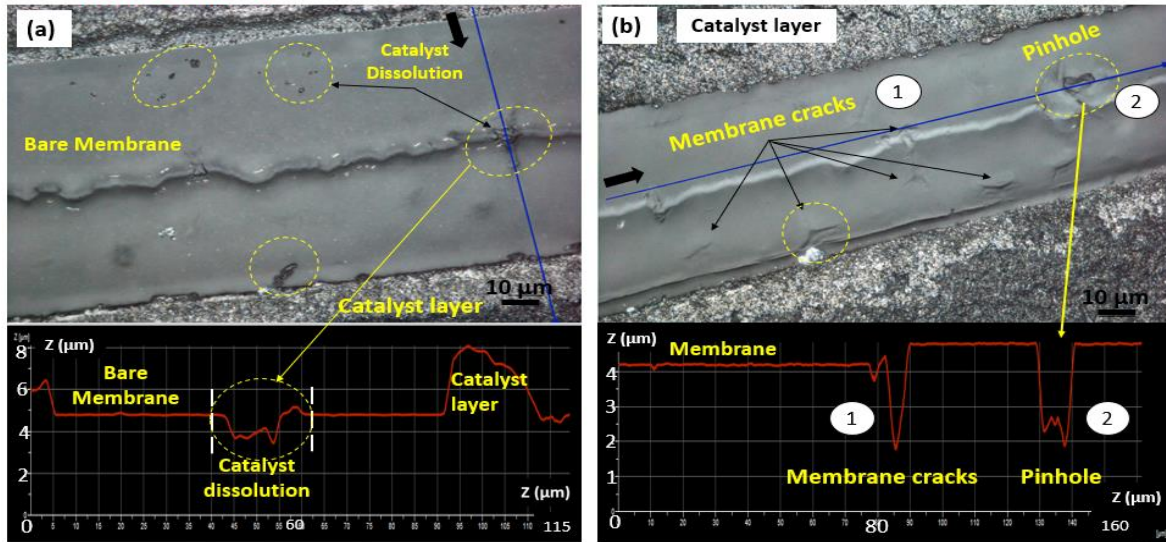


Figure 5-9: (a) Microscopic image of catalyst layer defect (zero catalyst area/bare membrane) selected from defect-2 in Figure 5-8f (ROI-1) showing surface view of bare membrane, where catalyst dissolution into polymer matrix in the bare membrane; (b) membrane cracks/tears (region-1) and pinhole (region-2) in the bare membrane. Plots in red below (b) and (c) correspond to Z-profiles along the blue arrows in microscopic images.

5.4.3.3 Degradation mechanism of catalyst layer defects

As fuel cells operate, their components break down by chemical and mechanical degradation [143]. Eventually, the degradation can lead to the formation of pinholes that terminate the life of the electrode. Reshetenko et.al showed that catalyst layer defects can facilitate gas crossover in the electrode that leads to pinhole formation [101][142][88]. Mu et.al. reported various events causing the chemical degradation of catalyst layers which could result in crack formation and pinhole formation across the MEA in areas where defects were the most likely to experience chemical degradation.

5.4.3.3.1 Surface degradation (chemical) of catalyst layer defects

To visualize the intensity of degradation inside the MCLD defect, we carried out a microscopic image analysis with and without transmitted light. Figure 5-10a shows the reflected

microscope image of the MCLD in CCM-1 obtained at MOL-2 (after 50 hours of aging) obtained without transmitted light. In this image, highly damaged sites in the CL are not completely visible. However, when this image is captured in transmission mode without reflected light (Figure 5-10b), the damaged areas become more evident. Now thin and completely missing catalyst zones and propagating cracks appear in the resulting image. The white pixels in Figure 5-10b correspond to the thinnest areas of the catalyst which presumably allow the transmitted light to pass through the defect.

Regions ROI-3 and ROI-4 located at the middle and edge of the defect (Figure 5-10a) have been selected for closer examination using transmitted and reflected light to characterize surface degradation within the MCLD. The catalyst surface in these two regions has clearly become irregular due to chemical/layer degradation inside the MCLD (Figures 5-10c, 5-10e and 5-10f). As previously shown, this effect can be caused by ionomer leaching from the catalyst layer and H_2O_2 formation at the defected catalyst sites [80].

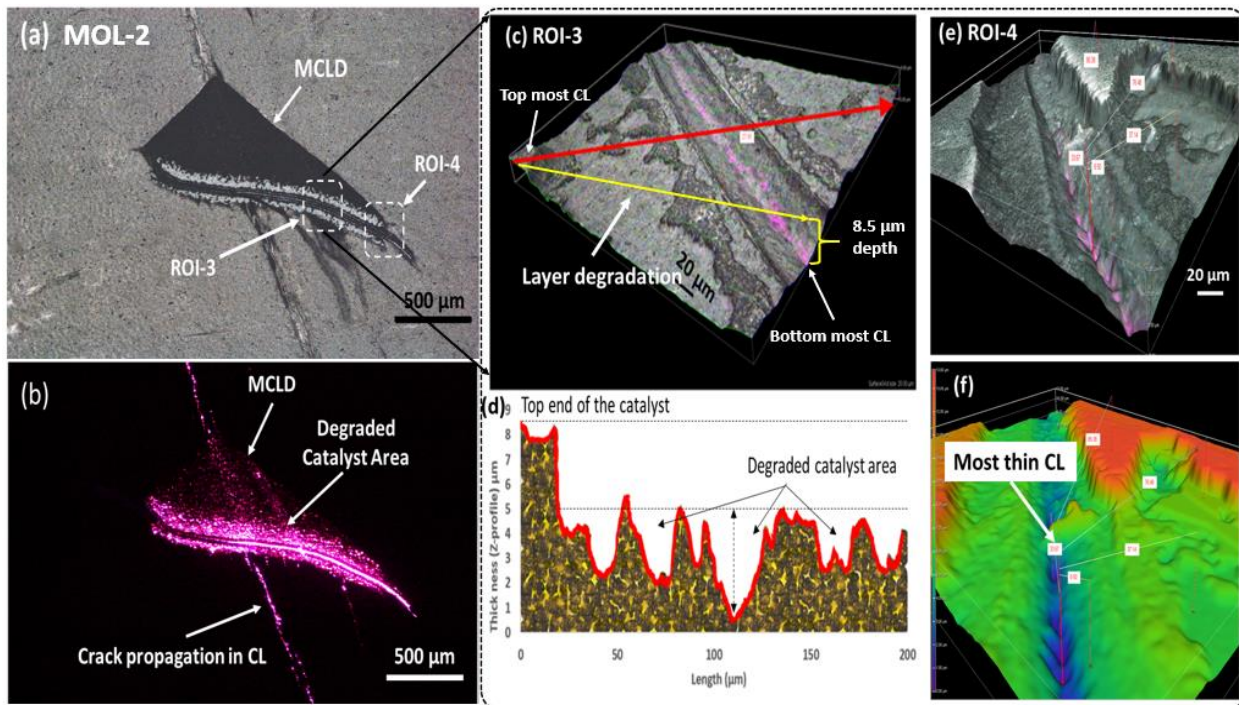


Figure 5-10: (a) Reflected microscope image of MCLD at MOL-2 indicating selected regions ROI-3 and ROI-4; (b) transmitted light microscope image of MCLD with pink area indicating degraded catalyst due to chemical degradation during fuel cell operation; (c) 3D microscopic visualizations of enlarged regions (c) ROI-3 and (e) ROI-4; (d) Z-profile/height profile showing variation in thickness of degraded catalyst layer surface at ROI-3 along the red line in Figure 5-10c; (f) colour mapping of morphological features of

degraded catalyst layer at ROI-4: blue represents thinnest catalyst, green represents uneven surface of degraded catalyst layer, orange represents non-degraded catalyst layer.

5.4.3.3.1.1 Catalyst erosion

Catalyst erosion is a major problem limiting the durability of the Pt/C catalyst contained in the fuel cell electrode. As discussed previously in section 5.1, the ionomer network in the catalyst layer is able to form strong interfacial bonds with catalyst particles and the electrolyte membrane as a result of hot pressing [22][139]. This is crucial to enhance the kinetics of the electrochemical reactions and effective transport of protons. Any non-uniform distribution of ionomer in the catalyst layer and non-uniform thermal compression during hot pressing will lead to incomplete transfer of catalyst layer onto the membrane as shown in Figures 5-2b and 5-6a. We have observed that catalyst particles located within the incomplete transfer zones (MCLD) gradually degrade during operation and are not as stable as catalyst particles in non-defected areas. Examination of CCM electrodes at MOL reveals that weak zones in the catalyst layer are more likely to erode as they are exposed to incoming reaction gases at different RH, pressure and temperature. For example, as we have shown previously, a significant amount of catalyst appears to have been lost within the MCLD (pink area indicates the loss of catalyst) during the growth of the MCLD in CCM-1 (Figure 5-6b). A potential cause of this catalyst loss is the weak interaction between the Pt/C and ionomer inside the MCLD since this area might not have been reinforced at the elevated temperatures. As a result, catalyst particles become detached from the thin layer, leading to discontinuities in electronic and ionic flow. Such sites would support little or no electrochemical reactions during fuel cell operation especially at high current densities.

The effect of catalyst erosion from BOL to EOL is observed mainly inside the MCLD (see Figures 5-6a – 5-6d, pink area inside MCLD) and decreases the density of catalyst inside the defect. In the case of CCM-1, the major damage occurs between BOL and MOL-1, as determined from the analysis of the growth of its area over time (Figure 5-7a). This area has increased to 2008% of its initial value at MOL-1, 2.7% between MOL-1 and MOL-2 and 0.8% between MOL-2 and EOL. This trend shows that the erosion rate of weakly bonded catalyst particles at defective sites is very high in the early stages of operation before quickly stabilizing. This observation suggests that catalyst particles inside the defected area are not completely impregnated as these areas do not

undergo uniform thermal compression during hot pressing. This causes poor bond strength between adjacent catalyst particles and intact sulphonic acid groups (ionomers) that enables gradual detachment of the catalyst during cell operation. A more complete view of the degraded area of MCLD is presented in Figure 5-10b captured under transmitted mode. The intensity of the light increases across thin areas where catalyst has been lost and gradually the pink area inside the MCLD grows. The valley shape inside the defects at ROI-3 (Figure 5-10c) and ROI-4 (Figure 5-10e) is due to partial removal of the catalyst layer. Figure 5-10d presents the Z-profile of the variation of thickness of the catalyst layer at ROI-3 along the line indicated by the red arrow in Figure 5-10c. This profile clearly shows that the degradation of the catalyst layer inside the defect is non-uniform. From the depth profile in Figure 5-10d, it appears that degradation occurs in a particular way. A small portion of the CL remains intact with its initial thickness of 8.5 μm . However, over a large part of the layer, the top portion between 5 and 8.5 μm is uniformly removed. It is not clear whether this portion was removed during the formation of the defect prior to its use in the cell or after its use in the cell. Most of the layer is very uneven with a thickness between 0 and 5 μm , reflecting the non-homogeneous nature of degradation that could be due to catalyst erosion. Figure 5-10f gives a 3D color graphical view of the degraded catalyst layer that corresponds to Figure 5-10e. Although not included here, our investigation of other defected CCMs shows this same type of catalyst loss is not exhibited in all the defected areas (MCLD) and that it depends on defect dimensions, thickness and location. Although the structural changes at BOL are difficult to estimate, they ultimately affect the integrity of the catalyst layer in the CCM electrode.

The propagation of defects at the corners of the MCLD appears to proceed by the development of sharp cracks and degradation at its edges. A study by Pestrak et al. showed that deformation of the electrolyte membrane has a strong influence on the structural changes of the catalyst layers in CCMs [144]. The results observed in our study support this idea that the deformation of the membrane has a direct influence on the areal growth of the catalyst layer defect from MOL to EOL. On the basis of Figures 5-6b and 5-6c (also captured in transmitted mode in Figure 5-10b), cracks appear to form and pass through the MCLD between MOL-1 and MOL-2 after the membrane has been deformed. This crack propagation leads to the large areal growth rate of 11.25% from MOL-1 to MOL-2). On the other hand, examination of Figures 5-6c and 5-6d indicates that some cracks (i.e., the ones furthest to the right) have merged between MOL-2 and

EOL presumably due to membrane shrinkage, allowing some portions of the defect to shrink along with the cracks. Interestingly, less pink appears in these merged cracks present at EOL than in the cracks appearing at MOL-2 from which they formed.

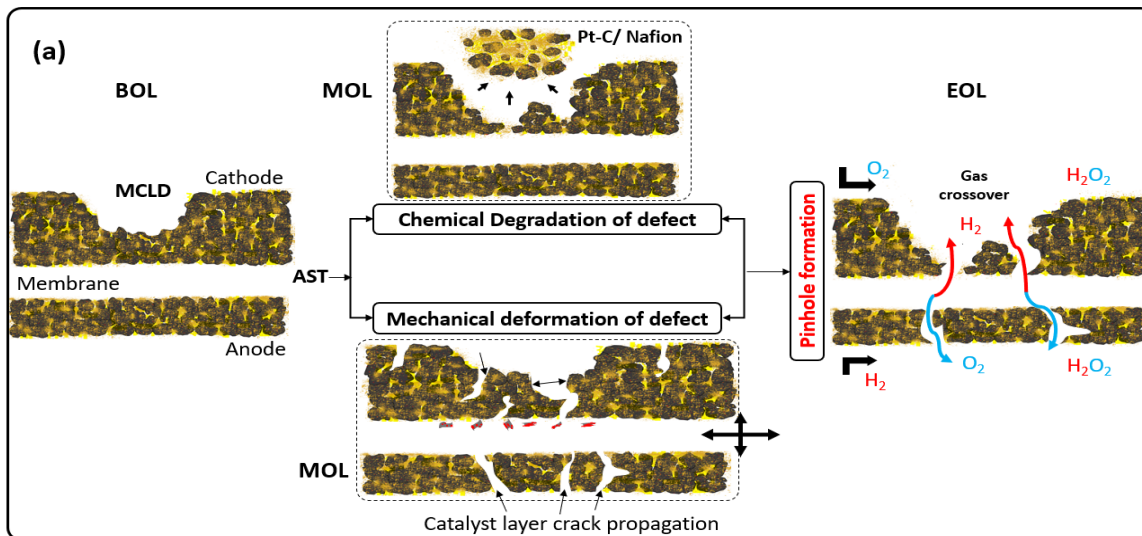


Figure 5-11: Schematic showing the possible ways that defects in the cathode layer can propagate via chemical and mechanical degradation and eventually lead to gas crossover through pinholes.

Electrode failure is intrinsically linked to degradation of both the catalyst layer and membrane, where one event may lead to occurrence of another event and also exacerbate other problems. The present study focused on events leading to electrode failure that occur through propagation of CCM defects. Figure 5-11 is a schematic showing the influence of chemical and mechanical degradation on catalyst layer defects and their effects on developing pinholes. As seen from the previous section, chemical degradation inside the catalyst layer defects (MCLD) is non-homogeneous due catalyst erosion/washout that leads to thinning/zero catalyst. The mechanical deformation of membrane during hydration/dehydration leads to wider crack opening/propagation in the catalyst layers in both anode and cathode. Both events cause structural damage to the catalyst layers.

When catalyst material is lost at the defect (MCLD/cracks), the reaction gases (hydrogen/air) can permeate through defects and react on the opposite electrodes as discussed in section 2.5.2.1.1. Gas crossover can lead to H_2O_2 /radical formation and ionomer decomposition in the catalyst layer and polymer membrane, ultimately causing cracks and micro-pinholes in the membrane (Figure

5-9b). Since the gas permeation rate depends on the size of these defects, defects tend to grow at different rates under the same operating conditions. As depicted in Figure 5-11, more decomposition of ionomer occurs on the cathode side than the anode side [68]. First, due to its smaller size, H₂ can permeate faster from the anode side to the cathode than O₂ can in the opposite direction. In addition, since the platinum loading on the cathode is higher than it is on the anode, more reaction between O₂ and crossover H₂ occurs on the cathode side than between H₂ and crossover O₂ on the anode side. Two products of this reaction are H₂O₂ and heat, both of which promote polymer decomposition.

5.4.3.3.1.2 Effect of ionomer leaching in catalyst layer

Ionomer distribution and the ionomer network in the catalyst layers are critical factors affecting the structural integrity of catalyst layers and fuel cell performance. Figure 5-7b shows the variation in the cumulative fluoride emission measured over the course of the 100-hour AST for CCM-1, CCM-3 and 25-hour AST for CCM-2. According to Figures 5-6b and 5-6c, significant erosion occurs over the first 10 hours (from BOL to MOL-1), while severe crack propagation occurs over the next 40 hours (from MOL-1 to MOL-2). The variation of the fluoride emission over the course of the AST in Figure 5-7b supports these observations because the fluoride ion release rate is highest from 0 to 40 hours, when 53.3% of the total amount of the fluoride ion leached over the 100-hour period is released. This correlation suggests that catalyst erosion and crack propagation from MOL-1 to MOL-2 contribute significantly to fluoride ion emission. Recent studies by Singh et al [91] and Macauley et. al. [113] have shown that membrane defects and catalyst layer defects lead to increased gas crossover and fluoride emission. This supports our observation that ionomer leaching may also occur through catalyst layer cracks or MCLDs particularly during the initial period of operation. Lastly, defective sites in the catalyst layer are the likely locations where hydrogen and oxygen cross over and several forms of catalyst layer degradation can take place [65][145]. In this situation, both the catalyst and the electrolyte membrane experience ionomer degradation that shortens the PEMFC life.

5.4.3.3.2 Crack degradation (mechanical) of catalyst layer

It is also important to understand the mechanical structural changes of catalyst layers that are caused by the plastic deformation of the electrolyte membrane. Kyung-Lim et al. studied the effect of electromechanical deformation on the propagation of catalyst layer cracks with electrodes

of varying thickness [146]. Electromechanical deformation is measured using a tensile test in which the membrane is elongated and tested for normalized electrical resistance. Their results showed that thicker CLs have a higher normalized resistance than thinner CLs in the CCM. The higher electrical resistance of thicker CLs was attributed to the critical elongation of cracks during initiation and the number and dimensions of cracks generated on the CL surface [1][5] [24] [26]. The fracture mechanics of thin films show that the critical elongation occurring in the catalyst layer increases as its thickness decreases.

Crack formation is affected not only by electrode thickness but also by uniform and linear hygrothermal expansion of the membrane due to water retention and swelling [96]. To demonstrate the effect of hygrothermal expansion, we select regions ROI-1 and ROI-2 from Figure 5-4b for further analysis. These regions are useful for this purpose because they are located at different distances from the gas inlet where water from the humidified reaction gases tends to accumulate. ROI-1 is closer to the gas inlet than ROI-2 and so would be expected to contain more water and undergo more hygrothermal expansion and subsequent mechanical deformation. Analysis of the images in Figure 5-12 confirm this expectation. Many more cracks appear at ROI-1 which has a higher water concentration (Figure 5-12b) than at ROI-2 which contains less water (Figure 5-12a).

The areal density of cracks can be considered to provide a good measure of the dimensional changes of cracks in catalyst layers. Areal density is defined as the ratio of crack area to the total electrode area of the CCM [6]. Examination of an aged CCM at MOL-1, MOL-2 and EOL shows that the cathode consistently contains many more cracks than does the anode. In this experiment, the crack areal density is measured from the stitched microscopic images shown in Figures 5-4a and 5-4b to be $9.2 \pm 2.8 \%$ at MOL-1 and $28.7 \pm 8.4\%$ at EOL. Analysis of these images also yields approximate widths of the cracks that propagate during the aging process (BOL \rightarrow EOL). These values are reported below in Table 5-2.

Table 5-2: Average width of cracks in the CCL of CCM-1 formed during OCV-AST.

Aging intervals	BOL	MOL-1 (10 hr)	MOL-2 (50 hr)	EOL (100 hr)
Average crack width (μm)	No cracks	5 – 20	15 – 50	50 – 100

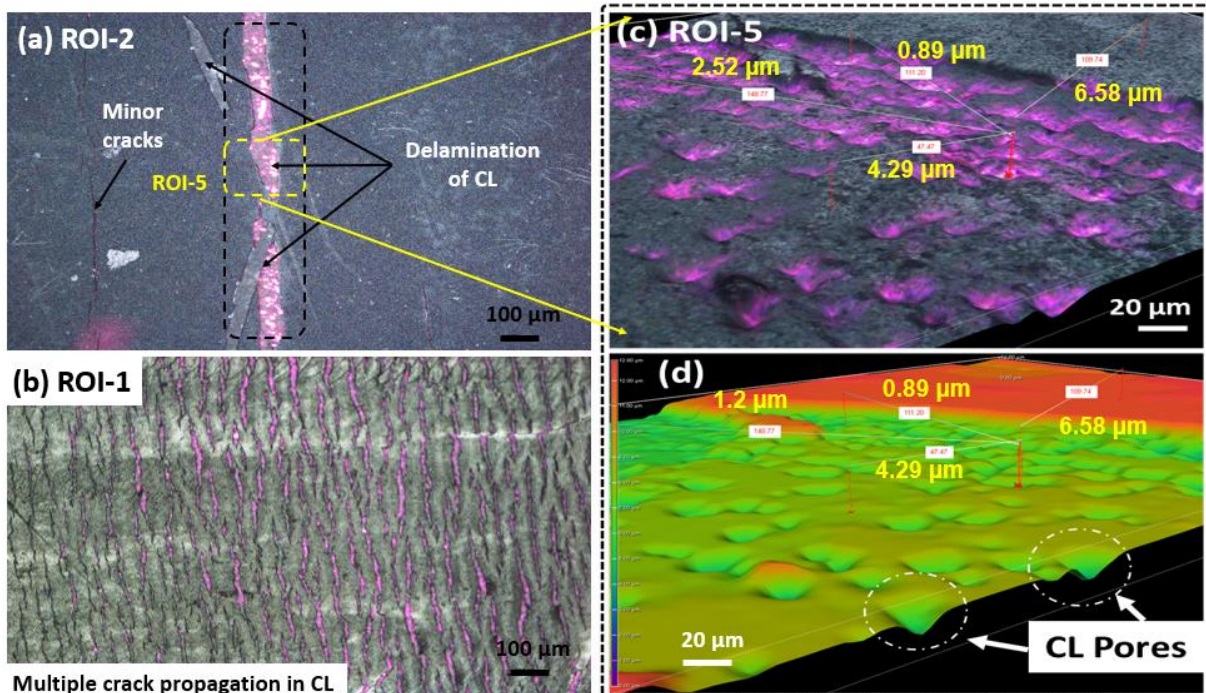


Figure 5-12: Microscopic images of crack propagation on the CCLs at EOL: (a) delaminated catalyst layer at ROI-2, (b) multiple crack propagation at ROI-1; the pink area in the image represents the thinnest region, (c) 3D enlarged view of delaminated and degraded catalyst layer at ROI-5 and (d) color mapping of delaminated area at ROI-5 showing catalyst layer pores.

Even after 100 hours of OCV-AST operation, it is observed that cracks have not propagated significantly in the vertical direction (i.e., with respect to their depth) and penetrate ~ 50% - 70% of their thickness in Figure 5-12a. (Note: The depth profile of delaminated catalyst layer in CCL was discussed in section 4.4.3.3). Closer examination at 100x magnification has been conducted on a specific delaminated region labelled ROI-5 within ROI-2 (Figure 5-12a). A view of ROI-5 is illustrated in Figure 5-12c and 5-12d showing that a portion of the catalyst layer has detached from the surface crack. The numbers on the image represent the catalyst layer thicknesses remaining on the membrane at different locations after delamination has occurred. Several Z-profile measurements have been done across the delaminated areas on the CCM (inlet, middle and outlet areas) to estimate the remaining thickness. This analysis reveals that the average thickness of delaminated CLs varies from 2 μm to 6 μm (some of these regions are shown in Figure 5-12a). As noted previously, the pink areas in Figure 5-12c represent the thinnest areas where the transmitted light can pass through the damaged portions. These damaged areas are also associated with pores or openings that form at the surface of the CL. It should be noted that pores are not intentionally introduced into this type of CL by manufacturers during fabrication. The particular color scheme

shown in Figure 5-12 is also used for the MCLD in Figure 5-6. The orange areas represent the non-defected catalyst, while the green areas correspond to defected catalyst remaining after delamination. The possible causes for the surface delamination may be traced back to hot pressing step during fabrication. The uppermost catalyst surface that is first exposed to the hot plates during CCM fabrication presumably has a strong and uniform contact bond with Pt/C catalyst particles and ionomer composite in the catalyst layers [147]. When the heat penetrates to the lower portions of the catalyst layer, the ionomer network in the catalyst layer will also develop strong bonds with the ionomer in the electrolyte membrane [22][139]. At the interface between the lower catalyst layer and membrane, some portions of the ionomer migrate into the membrane and leave behind large pores in the lower catalyst layer. This is also consistent with the idea that CCMs strongly interact with the CL and polymer membrane to reduce the contact resistance between adjacent layers [7]. When the membrane becomes humidified, it swells and experiences stress. This sets up a pressure difference between the upper and lower portions of the catalyst layer that can lead to delamination in the middle of the catalyst layer. The delamination occurs depending on the ionomer network in the catalyst layers. Some of the factors that influence delamination are CL thickness, membrane swelling and ionomer concentration in the CL. On the cathode, the maximum delamination is observed to remove 70% of the catalyst layer thickness. However, on the anode, delamination is rarely observed. If the ACL were delaminated, it would likely be completely removed since it is very thin. The differences in delamination between the cathode and anode can be attributed to their individual catalyst layer thicknesses. The dotted circles in Figure 5-12d indicate damaged area that appears as pores in the catalyst layer after delamination. To investigate the size distribution of these features, image analysis is conducted on non-defected and defected area (delaminated areas). The diameters are measured to be $\sim 1 - 2.5 \mu\text{m}$ in non-defected areas, whereas they are more than 5 times as large with diameters of $\sim 5 - 25 \mu\text{m}$ in defected areas. Large pores are not favourable for fuel cell operation because they act as dead zones where less catalyst is available for an electrochemical reaction to occur and facilitate gas crossover and water flooding. From our overall examination of CCMs at BOL, MOL-1, MOL-2 and EOL, catalyst erosion is observed only in the defected areas i.e., inside MCLDs and inside delaminated catalyst layers. No evidence of erosion is found on non-defected areas. These observations are particularly important for the development of catalyst coatings and integrity of catalyst layer fabrication. Although

experiments in this study have been done at a particular RH and temperature, experiments under conditions of RH cycling would also be useful. These are described in Chapter 6.

5.4.4 IR investigation of MCLD propagation

As discussed in section 4.3.3, we conducted IR thermography to investigate MCLD propagation and identify hotspots. Figure 5-13 shows the IR images of defected CCM-1 at BOL and EOL. No hotspot is observed in the vicinity of the MCLD when tested at BOL (Figure 5-13a). Although not included here, a hot spot still has not appeared in this region at MOL-1 and MOL-2. However, the situation has changed by the time that EOL is reached and the evidence of a hot spot (yellow region) close to the MCLD is clearly evident (Figure 5-13b). The surface temperature in these regions is analysed using FLIR IR tools software available with the IR camera. Figure 5-13c presents the temperature profile across the MCLD along the line marked by the dotted arrows in Figures 5-13a and 5-13b before and after aging. These results show that the surface temperature across the MCLD is the same (i.e., 22.5°C) as in other parts of the catalyst layer at BOL, providing evidence that thin catalyst layer defects have little impact on the fuel cell at BOL. As the sample ages, the MCLD in CCM-1 degrades preferentially, as shown previously in Figures 5-6a – d and discussed in section 5.4.3.1. This allows more H₂ to permeate through the thinner/zero catalyst regions of the MCLD from the anode and react with O₂ at cathode to generate heat. The elevated temperature is captured by the IR camera as a hotspot. The yellow curve in Figure 5-13c shows the temperature distribution across the aged MCLD. The thermography analysis shows that the surface temperature increases to a peak at 25.5°C about midway along the dashed arrow, suggesting that H₂ has crossed the thinnest area of the defect. However, on the basis of the IR thermography alone, it is difficult to conclude that a pinhole has actually formed. Overall, an increase in the surface temperature of the cathode catalyst layer in the vicinity of the MLCD from 22.5°C to 25.5°C is observed as it ages from BOL to EOL. The variation of temperature across the defect also depends on the severity of the defect developed during the manufacturing process. Thus, IR thermography analysis of defected CCMs provides useful information in characterizing the evolution of the MCLD.

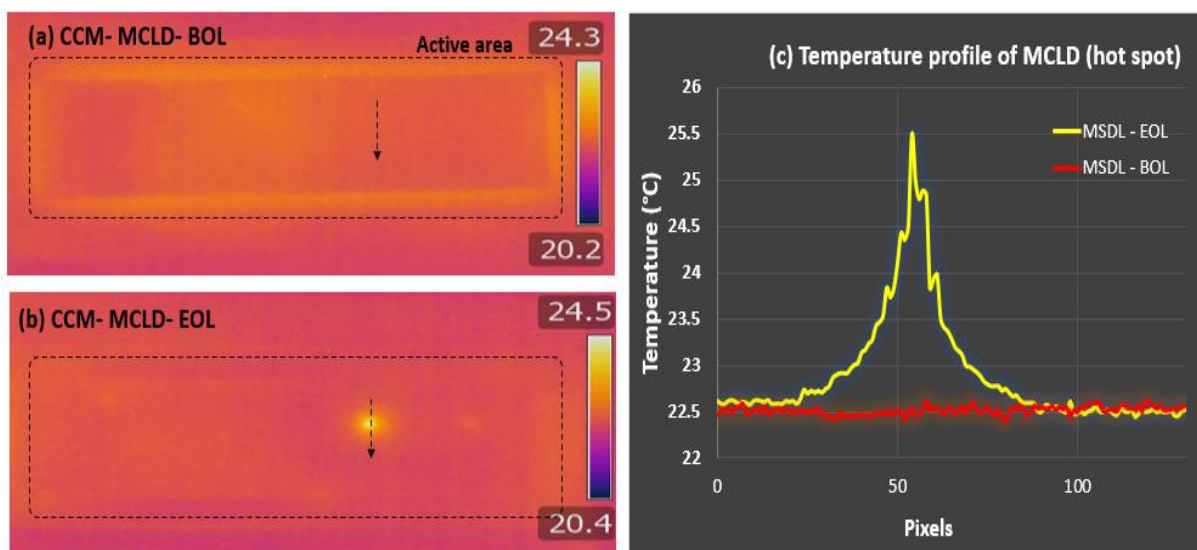


Figure 5-13: IR thermographic response of CCM containing a MCLD at (a) BOL, (b) MOL-2 and (c) EOL (after polarization analysis). (d) Surface temperature profiles along the dashed arrow line indicated in (a) and (b).

5.5 Conclusions

This chapter has focused on the morphological changes of catalyst layer defects in CCMs (manufacturing defects) under operating conditions and their effects on overall performance. The proposed protocol for investigating defects is a non-destructive method that is advantageous in providing an areal visualization and failure locations of catalyst layer defects in pristine and aged CCMs.

1. Propagation of catalyst layer defect

Overall, it was observed that the effect of chemical and mechanical degradation inside the defected areas are higher and degrade more quickly at initial hours and stabilizes in later stages of operation. The areal dimensions and lost catalyst zones inside the MCLD were quantified and examined at regular time intervals and were correlated to performance loss. The OCV results showed that the performance of defected CCMs degrade at a rate of 1.58mV/hr(CCM-1), 2.98mV/hr(CCM-2), 1.03mV/hr(CCM-3), compared to non-defected CCMs at 0.65mV/hr respectively.

2. Visualization of defect propagation

The microscopic investigation exhibits a good argument to visualize defect propagation and provides a quantitative measurement that compares defect growth and projected CCM lifetime.

The delamination effect on the catalyst layer showed that 50 – 70% of its thickness is being removed due to mechanical deformation of membrane by leaving large pores ($\sim \text{Ø}25\mu\text{m}$) on the leftover catalyst layer. Finally, IR thermography confirms the formation of gas leak across the MCLD in aged CCMs, the MCLD eventually causes intense degradation due to catalyst erosion and ionomer leaching in defected areas.

From the observations developed on defect size and orientation in CCMs, it is also recommended to investigate the impact of defect location, thickness variation, and empty catalyst sites on the lifetime of fuel cell stacks. Developments in present work aims to provide fundamental knowledge on improving the tolerance and durability of CCM electrodes against defects. Future studies will focus on MEA failure that is caused by various sizes of catalyst layer defects in CCMs and fabrication membrane damage. Thus, the current and future studies promote a non-destructive PEMFC electrode investigation method that will improve quality control systems in fuel cell technology.

6 Effect of RH AST on Manufacturing Defects: Catalyst Layer Defects and Sealant Interface Defects in PEMFC Electrode

6.1 Introduction

Although PEMFCs are impressive alternative power systems, stationary and transport applications due to their negligible carbon emissions, exhibit quick start-stop response, and demonstrate high efficiency. Cost and durability have been two main barriers to commercialization. Their cost is tied closely to the MEA electrode which represents ~70% of the total capital cost [148]. It is very important that these electrodes operate for more than 10 years of typical automotive operation, withstanding various load, stop-start, freeze-thaw and humidity cycles. When fuel cells undergo dynamic duty cycles in transit vehicles, the frequent acceleration and deceleration causes humidity fluctuations in the fuel stack that damage the membrane in the MEA. Therefore, it is essential to fabricate highly effective and high-quality MEAs that can sustain harsh conditions of the fuel cell vehicle. To meet this goal, MEA components such as CCMs, GDLs and MPLs must be fully inspected prior to stack installation. As estimated in a DOE cost analysis, 5% of stack failure rate is observed immediately after installing the MEAs at BOL due to electrode defects and poor fabrication of MEA components. This involves additional costs and time for disassembling and replacement of defected electrodes [17].

Material inspection and fundamental understanding of component failure has had a large impact in reducing the per-unit cost of the fuel cell systems. Any defect in the MEA components will ultimately increase the pressure on the membrane during hot pressing or cell operation and lead to dangerous pinholes in the MEA. Defects in MEAs commonly form in regions close to the gasket sealants. Thickness variation in individual components or improper alignment of the GDLs, CCM and gaskets will raise the stress on the thicker portions during the hot press. Consequently, pinholes tend to form in higher stress regions such as those near the sealants where the GDL fibers diffuse into the membrane [149]. These defected areas will grow during typical fuel cell operation particularly at high cell voltage, high cell temperature, high stack pressure and low RH. Fluctuations in operating conditions cause chemical and mechanical stresses and promote degradation. However, it is still not clearly understood whether electrode failure is caused more by pre-existing MEA/CCM defects than by the various stresses on the electrode during cell

operation. Therefore, analysis of electrode degradation using ASTs should enable a better understanding of failure mechanisms under chemical and/or mechanical stress in a shorter time period [150][66]. Several studies have showed that chemical degradation of the electrolyte membrane is accelerated under OCV operated at high temperature and low RH [112]. Under relatively low humidity conditions, membrane becomes dry enough for the ionic resistance to decrease significantly and gas crossover to rise on either side of the electrode. This condition favours formation of hydrogen peroxide and radical attack that decomposes the ionomer in the catalyst layers and membrane. Chemical degradation mainly occurs at weak spots in the electrodes such as defected areas and leads to cell failure.

Mechanical stability of the membrane is crucial for the durability of an effective MEA. An effective way to evaluate MEA mechanical stability and durability is to apply RH cycles (wet and dry) at a high temperature while holding the cell at OCV. During RH cycling, the constrained electrode in a fuel cell stack experiences stress due to swelling and shrinkage [151]. The repetition of RH cycles reduces the bond strength of the membrane and catalyst layer interface, increases the interfacial contact resistance (i.e., ohmic resistance) and significantly reduces the cell performance during aging [8-12]. During long-term operation, many components are expected to fail by any number of modes where one event can cause/increase the impact or occurrence of another [65]. Previous literature has demonstrated the influence of chemical and mechanical degradation on global thinning of MEA components. However, there is no clear evidence of real catalyst layer defects nor the root cause of initiation and propagation during cell operation [104]. Figure 6-1 shows various chemical and mechanical degradation modes operating during steady-state RH and cyclic RH AST during OCV operation.

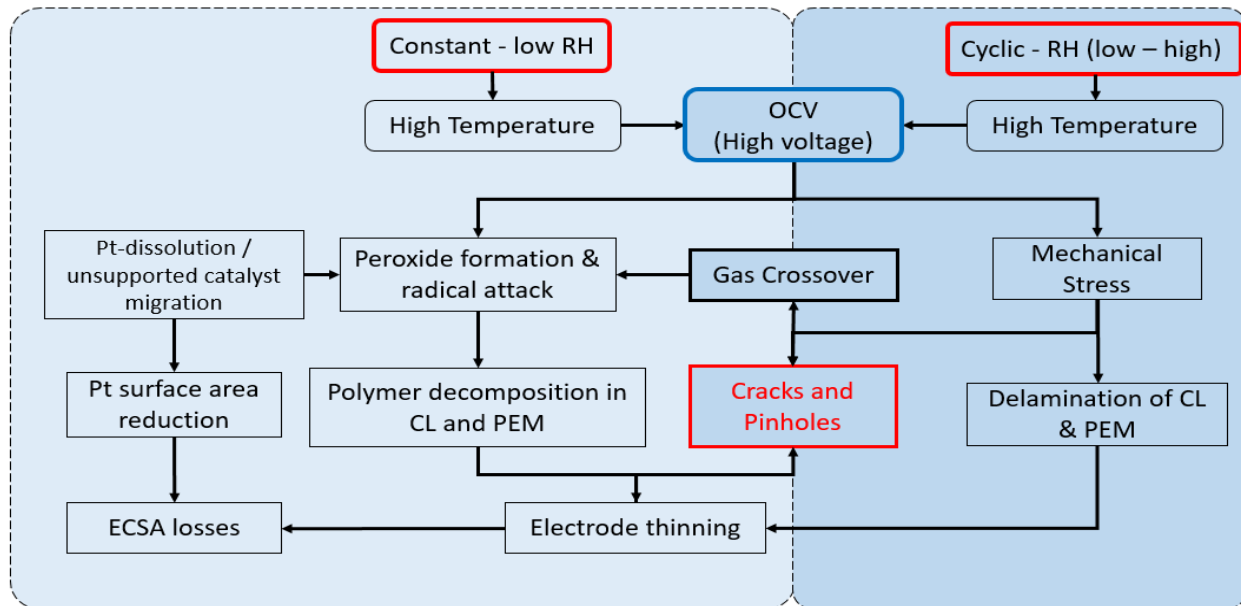


Figure 6-1: Modes of degradation in MEA operated under constant-low RH and RH cycling during OCV causing defects in PEMFC electrode.

Although studies showed that chemical and mechanical ASTs are useful for screening the overall durability of MEA, the role of pre-existing electrode defects is still not clearly understood. Thus, a research gap exists in understanding how BOL manufacturing defects affect the overall cell performance and propagate during typical fuel cell operation at high temperatures and variable humidity conditions. In this chapter, case studies of 3 defects are analysed as a part of MEA quality control: (1) missing catalyst layer defects (MCLD), (2) gasket/CCM interface defects (sealant pinhole defects), and (3) scratches/cuts in the CCM. Among the various CCM defects discussed in Chapter 4, these defects are chosen since they have been commonly recognised by electrode manufacturers during CCM fabrication. The durability of MEAs with and without defects are tested under two OCV-AST conditions: (i) steady-state low RH and (ii) cycles of low/high RH at a high stack temperature of 90°C. The extent of chemical and mechanical degradation of electrode defects and information regarding MEA component failure mechanisms can be gleaned from these ASTs and visual inspection of defects. The AST protocols developed in this work are based on the standard DOE procedures and feedback from our industrial partner. Details of the research framework are shown in Figure 6-2 and the step-by-step AST procedure used for MEA analysis is shown in Figure 6-3.

6.2 Research Framework

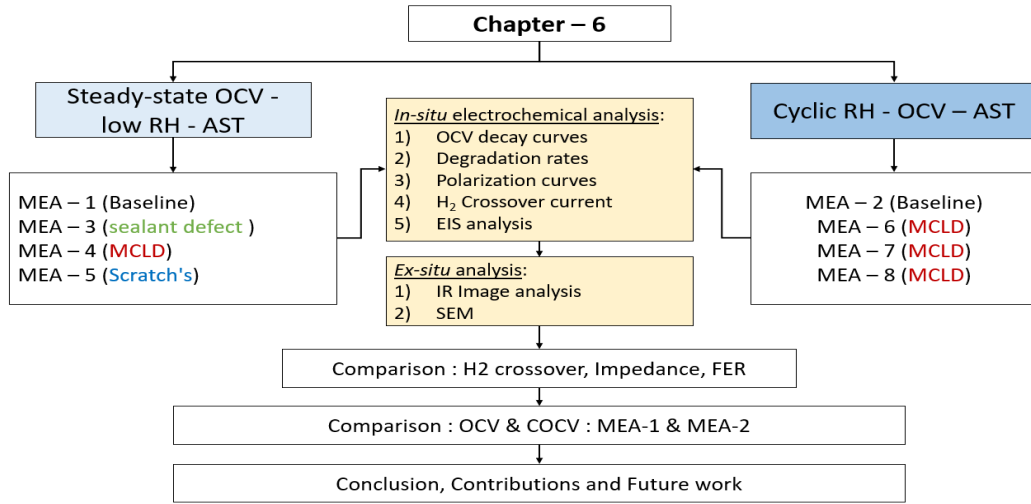


Figure 6-2: Framework for MEA analysis followed in this part of study.

6.3 Test Procedure

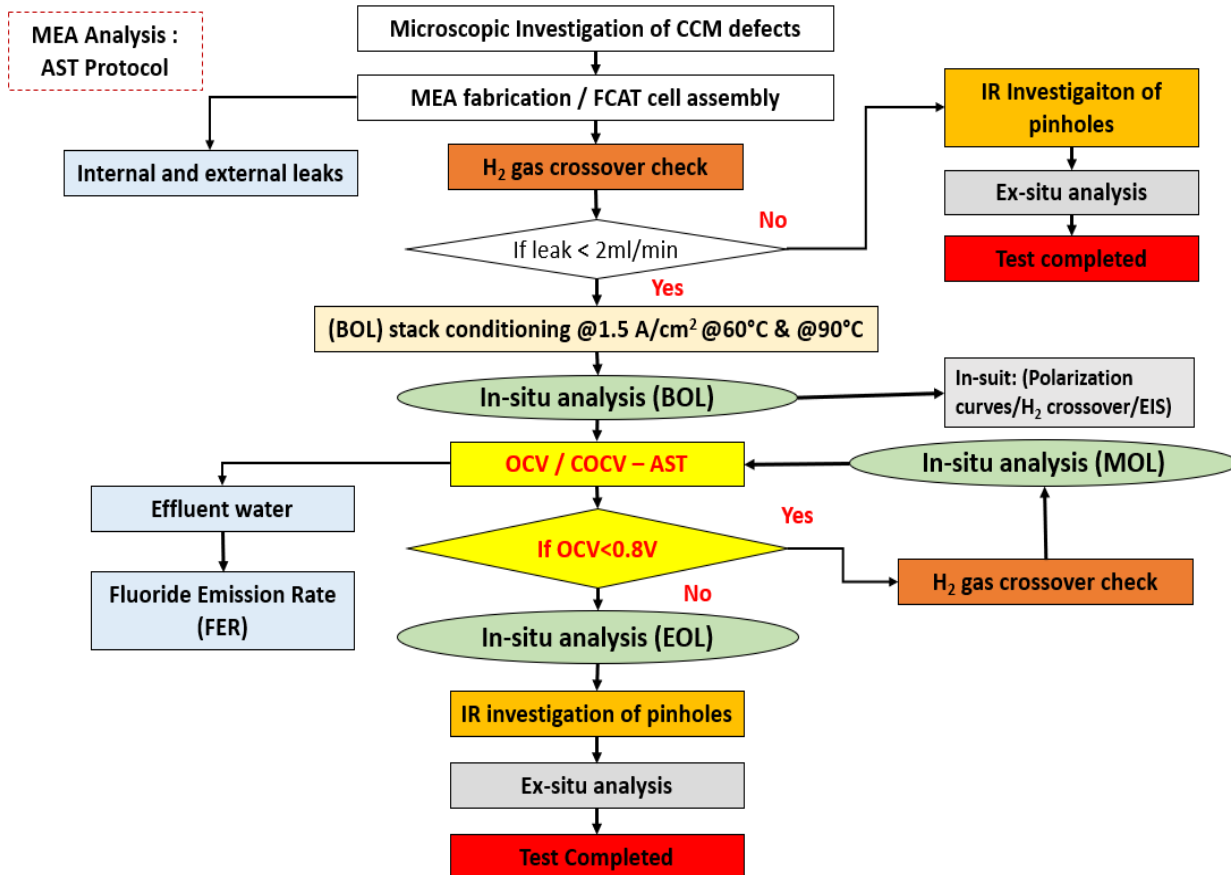


Figure 6-3: Experimental AST protocol for MEA degradation analysis.

Figure 6.3 outlines the flowchart of the AST protocol for OCV and COCV test. After examining the catalyst layer defects with an optical microscope, the defected CCMs are then used as components in the MEAs to be evaluate the electrochemical analysis. For a detailed procedure regarding the fabrication of MEA, please refer to section 2.4 of chapter-2. Once fabricated, the MEAs are examined by IR thermography for pinhole detection prior to cell assembly. An external and internal leak test is performed to check for any leaks that would disrupt constant stack pressure during operation. A leakage rate $\leq 2 \text{ mL min}^{-1}$ is acceptable for the experiment to proceed. If the leak rate exceeds 2 mL min^{-1} , the test is terminated and the MEA is examined by IR thermography for EOL pinhole detection. The electrochemical characterization of H_2 gas crossover of MEA is carried out using linear sweep voltammetry by scanning from 0.1 V to 0.65 V at a scan rate of 2 mV sec^{-1} while supplying H_2 to the anode and N_2 to the cathode. In order to equilibrate the membrane, the MEA is subject to BOL conditioning[24] at a current density of 1.5 A m^{-2} at 100% RH for a duration of 12 hours at 60°C and 1 hour at 90°C prior to the OCV / COCV AST. Following this conditioning, the stack undergoes *in-situ* H_2 gas crossover EIS and polarization measurements. Once these diagnostic checks are completed, the OCV/COCV AST is implemented. The steady-state OCV AST is conducted at a stack temperature of 90°C , with 30% RH on both sides (anode/cathode) of the membrane. The RH cycling experiment is done at a stack temperature of 90°C , while the gas at the cathode is cycled from a wet to dry state (80% to 20% RH at a dew point = 90°C) every 5 mins. Figure 6.4 shows the various RH cycles applied during (i) MEA conditioning, (ii) study-state OCV low RH – AST and (iii) cyclic OCV-AST experiments.

The stack voltage is continuously monitored during the cell operation. While the stack is held at OCV, effluent water samples from the anode and cathode chambers are collected every 10 hours to measure FER resulting from chemical degradation of the membrane. The *in-situ* diagnostics are performed to check the health of the MEA at MOL every 20 hours or whenever a sudden drop in the OCV is observed. The experiment is terminated when the voltage reaches 0.8V, as per the DOE standard electrode EOL condition. The test is completed once the EOL *in-situ* diagnostics have been performed. The MEA is then investigated by IR thermography to detect EOL pinhole/hotspots and *ex-situ* examination by SEM.

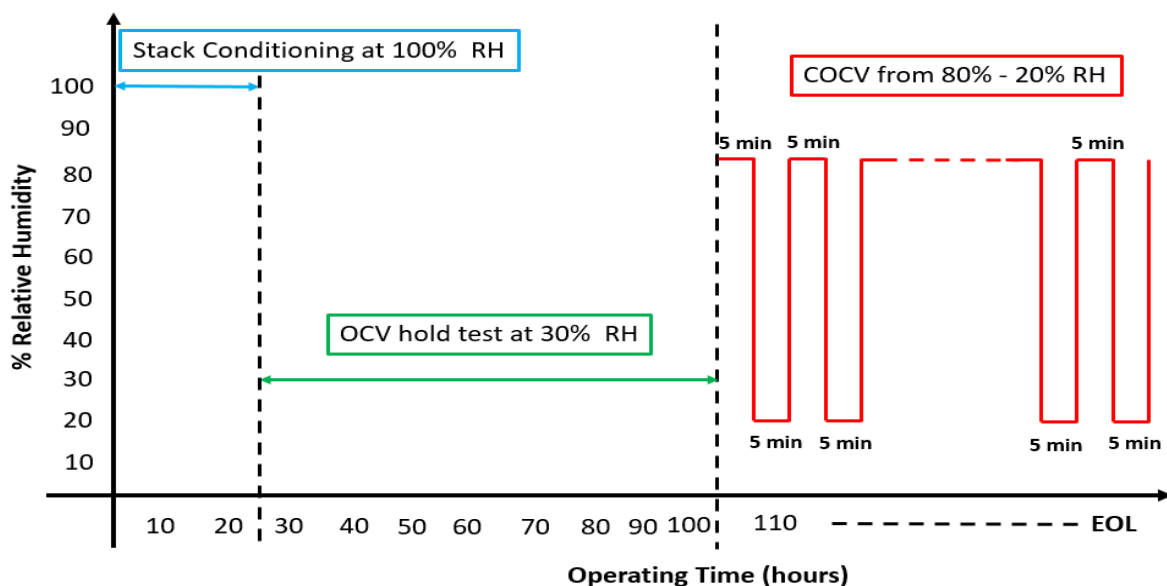


Figure 6-4: Schematic of various RH cycles used during electrode/stack conditioning (blue-100%RH), steady-state OCV (green-30%RH) and RH cycling (red – 80% - 20% RH).

Table 6-1: Summary of MEAs used in this chapter.

Sample	No. of CL defects (MCLD) and % catalyst lost inside defect	Avg. CL thickness lost in MCLD (μm)	OCV / COCV - AST	RH – AST	No. of hours operated (h)
MEA – 1	No defects	Baseline	OCV	30%	157
MEA – 3	1	NQ	OCV	30%	70
MEA – 4	1 – 48% 2 – 60%	~ 3.82 ~ 5.45	OCV	100% 30%	25 ,75
MEA – 5	1	NQ	OCV	30%	110
MEA – 2	No defects	Baseline	COCV	80%-20% RH cycling	150
MEA – 6	1 – 70%	~ 5.61	OCV + COCV	100% - RH – OCV & 80%-20%-RH cycling	100, 54
MEA – 7	1 – 28%	~ 2.24	COCV	80%-20%-RH cycling	83
MEA – 8	1	NQ	COCV	50%-20%-RH cycling	110

Note: Image showing defects in CCMs are given in Appendix section 10.5. NQ – not quantified since these MEAs were manufactured by industrial partner; defects in CCMs are therefore not quantified prior to fabrication.

Eight MEAs, each having an active area of 48 cm^2 , are examined in this study under specific operating AST conditions summarized in Table 6.1. It should be noted that the membranes

used in this study are reinforced with a porous polymer matrix, nanofibers or inorganic reinforcement that provides strong mechanical stability for the membrane [153]. MEA-1 and MEA-2 contain CCMs without any defects on the anode and cathode prior to the experiment and so serve as baseline samples. MEA-3 was analysed in case study 1, which consists of MCLD and sealant interface defects (CCM/gasket interface), and is also used to examine the evolution of an artificial pinhole ($\sim 90 \mu\text{m}$) during aging. MEA-4, MEA-6, MEA-7 and MEA-8 were analysed as a part of case study 2 solely on MCLD, no sealant interface defects are identified in this samples at BOL. MEA-5 is analysed as a part of case study 3 on catalyst layer scratches. Since MEA-3, MEA-5 and MEA-8 have been fabricated by the manufacturer, microscopic defect characterization was not performed on these samples. Information regarding the specifics of the composition of the components and CCM/MEA fabrication conditions are not disclosed to protect the manufacturer confidentiality and intellectual property issues. A detailed visual inspection of MCLDs for MEA-4, MEA-6 and MEA-7 are shown in this work. Other observations made during the OCV and COCV tests include calcium contaminant accumulation on the cathode GDL (across flow channels) during the OCV hold test and a visible burn across MEA sealants during the COCV test.

6.4 OCV-hold diagnostic test at low RH

Table 6-2: Description of overall test analysis and samples used for OCV hold test.

Samples Name	No of CL defects and % of defect	Anode/cathode RH (%)	OCV (V)	No. of. hours operated (h)	Interrupted hours (h)	Voltage degradation rate (mV h^{-1})
MEA – 1	No defects (baseline)	30% / 30%	0.945	157	0, 38, 80, 120, 157	0.910
MEA – 3	1 – ND	30% / 30%	0.932	70	0, 7, 24, 45, 57, 70	1.24
MEA – 4	2 – 48% & 60%	30% / 30%	0.944	75	0, 28, 60, 75	2.19
MEA – 5	1 – ND	30% / 30%	0.950	108	0, 27, 44, 62, 96, 108	1.85

Note: Image showing defects in CCMs are given in Appendix section 10.5.

The OCV-hold test at constant low RH is designed to accelerate the chemical degradation of MEA that decomposes the polymer in the reinforced membrane matrix and catalyst layers. The samples listed in Table 6-2 are used to study the chemical durability of MEA at a constant

mechanical stress i.e., low RH. The durability tests range from 100 hours to 200 hours, which includes assembly of cell, preconditioning of MEA and *in-situ* analysis. One of the major issues during the OCV-AST are MOL interruptions, either intentional or unintentional, that occur due to safety inspections and MOL diagnostic tests to assess the MEA health. The interruptions during OCV-hold tests can either negatively or positively affect cell performance due to reversible and irreversible losses caused by material degradation, which will be discussed later in this chapter. During aging, as the membrane breakdown, and its OCV performance decreases until it reaches the pass or fail criteria of 0.8 V. However, the OCV increases after reaching 0.8 V due to reversible voltage loss effects, the experiment is still terminated as per the manufacturer protocol requirement when the cell reaches 0.8 V. This decision has been made to standardize the quality control assessment of MEA effectiveness.

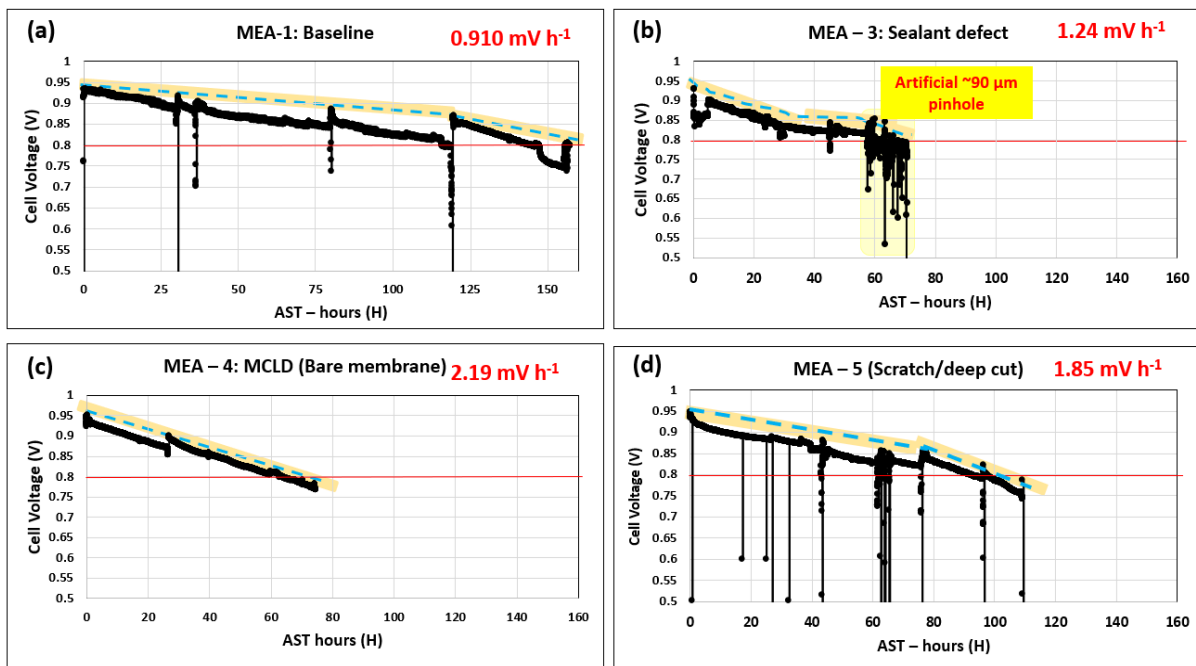


Figure 6-5: OCV degradation curves of defected and non-defected MEAs: (a) MEA-1 baseline (no defects) (b) MEA-3, 1 intentional pinhole introduced at 70 hours (c) MEA-4, 2-MCLD in CCL as shown in Figure 5-4c. (d) MEA-5, 1 scratch defect.

The decay of the OCV of MEA-1, MEA-3, MEA-4 and MEA-5 over the duration of the AST is presented in Figure 6-5. The OCV of MEA-3 over the first five hours is hindered by back pressure issues with the fuel cell test station, causing complications with reaching the set value of 260 kPa

on the cathode. The OCV curves for all MEAs show similar trends, presumably due to the loss of material components in the membrane and catalyst layers. However, the performance of MEAs which have defects at the outset deteriorates much more rapidly than the base case MEA. This allows us to distinguish the failure mechanisms of MEAs into two categories: (i) more gradual degradation of electrolyte membrane and catalyst layer due to chemical stress leading to slow electrode failure (>150 hours of AST) by developing a pinhole in thin degraded membrane. and (ii) physical damage leads to fast electrode failure (typically 55 – 110 hours of AST) through sealant interface defects, exacerbated by sufficient compression of stack endplates to initiate damage (pinhole) in the membrane. The first type of degradation is observed in the base case of MEA-1 (Figure 6-5a), which reaches EOL after > 150 hours of OCV-AST. The second type is observed in the cases of MEA-3, MEA-4 and MEA-5, which reach EOL more rapidly in between 55 - 110 hours of OCV AST. More about the failure mechanisms of these MEAs is discussed in sections 6.5.1 – 6.5.4.

It is interesting that the initial OCVs of these MEAs at BOL are essentially the same, with an average value of ~ 0.945 V. Thus, the initial OCV is not a good indicator of the state of MEA in these cases. As shown in Figure 6-5, a sharp drop in the OCV is observed when the AST is interrupted at MOL for electrochemical characterization to obtain polarization curves and EIS spectra and measure H₂ crossover, but then recovers when the AST is resumed. Close analysis of the change of the OCV during this interruption period is very informative and enables the reversible and irreversible losses of the electrode to be distinguished. The OCV degradation rates measured in this study are commonly reported in the literature. For instance, Kundu et.al.[111] and Mehmood et.al.[154] reported similar degradation rates during cell interruption. To explain in more detail, the period (MOL-1) in the OCV curve of MEA-1 from 0 hours up to the first interruption at 30 hours is shown as an example in Figure 6.6. The overall degradation rate during the first 30 hours is measured to be ~ 3.16 mV h⁻¹. The irreversible voltage loss is indicated in green (from A to C in Figure 6-6), while reversible loss is indicated in red (from B to C in Figure 6-6). Each interruption is characterized by two sharp downward spikes when the AST is interrupted and one upward spike when it is resumed. It should be noted that the upward spike reaches a voltage higher than the OCV measured just prior to the interruption. The irreversible losses are estimated from the difference between this spike and the OCV at t=0 and are attributed to permanent degradation of MEA components such as the membrane and catalyst layer (from A to

C in Figure 6-6). The reversible voltage loss is estimated from the difference between this upward spike and the first downward spike where the OCV just before the AST is interrupted (from B to C in Figure 6-6). The reversible voltage loss can be attributed to such phenomena as catalyst surface oxidation and water flooding in the MEA, that are completely or partially undone when the AST is interrupted and the MEA undergoes electrochemical characterization. The reversible voltage loss can be attributed to such phenomena as catalyst surface oxidation and water flooding in the MEA, which are completely or partially undone when the AST is interrupted and the MEA undergoes electrochemical characterization. The total degradation rate corresponds to the sum of reversible and irreversible decay rates. However, it is important to distinguish between these two types of OCV loss and estimate the irreversible voltage decay because it is directly associated with membrane thinning and loss of active catalyst surface area.

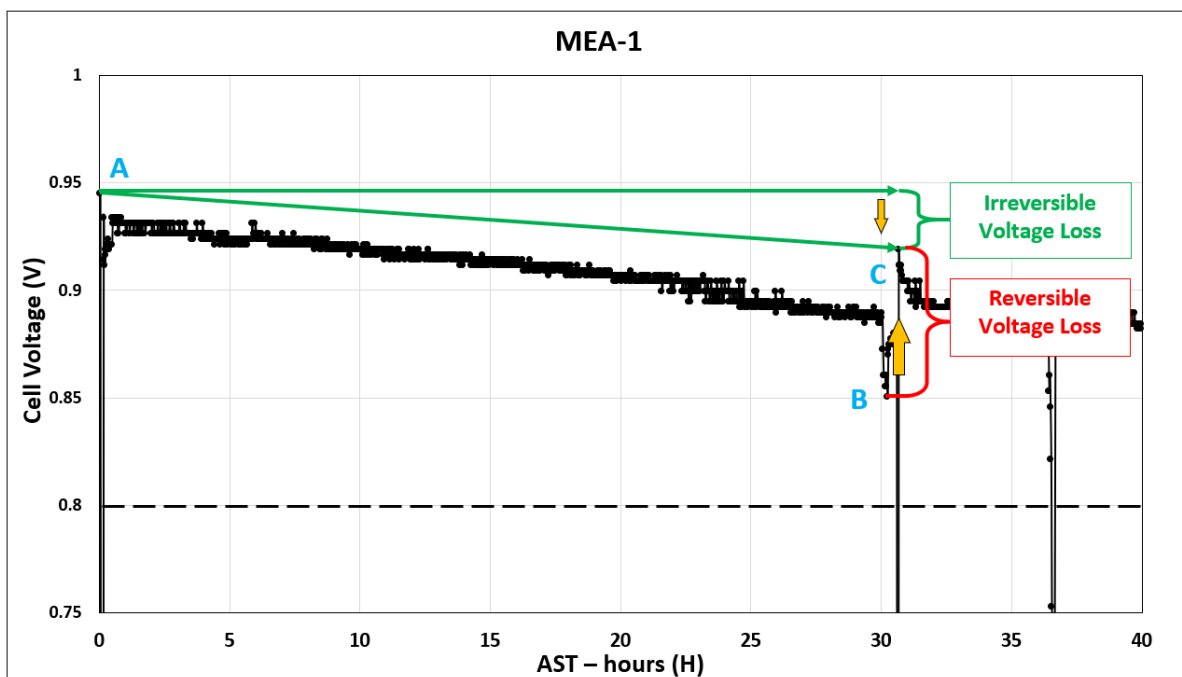


Figure 6-6: Analysis of the OCV curve for MEA-1 during the first period (MOL-1) to differentiate the reversible and irreversible losses. The irreversible voltage loss is indicated in green (A to C) and the reversible loss in red (B to C).

The degradation rates of MEA-1, MEA-3, MEA-4 and MEA-5 are 0.910 mV h^{-1} , 1.24 mV h^{-1} , 2.19 mV h^{-1} , 1.85 mV h^{-1} respectively. The rates of OCV degradation obtained in this study are higher than those reported previously using a similar type of membranes, which have varied between 0.001 and 0.7 mV h^{-1} [155][10]. This difference is likely due to the operating conditions

(temperature, RH, pressure and gas flowrate) during the AST. The ASTs used during the previous studies were carried out lower temperature, higher RH, lower pressure and lower flowrates, all of which should lower degradation rates and longer lifetimes. It should be noted that the differences in the MEA themselves will affect the degradation rates. However, in this context, the focus is to study the evolution of manufacturing defects influencing the cell performance on similar types of MEAs. The AST in our study is carried out at high temperature (90°C), high gas inlet pressure of anode/cathode (250/270Kpa), high flow rates (2/10 SLPM) and low humidity (30/30 %RH). Therefore, we expect our AST conditions to significantly accelerate aging of the CCM/MEA components. Similar observations were also reported in the literature [5,12,17-19].

6.4.1 Performance of MEA-1

The initial investigation of MEA-1 with IR thermography at BOL reveals no hotspots, indicating a good condition for OCV-AST analysis. During the aging of MEA-1, several voltage losses corresponding to its structural changes in electrode are observed. Figure 6-7a shows the breakdown of the total OCV decay rates of MEA-1 into the irreversible and reversible contributions during four intervals of the AST. The blue bars denote the irreversible and permanent losses (i.e., due to structural damage in the MEA components during the OCV-AST). Irreversible losses give a good indication of the extent of material degradation in the electrode [154]. The orange bars correspond to the reversible and temporary losses i.e., due to water flooding, catalyst surface oxidation and surface contamination [111][157]. Although reversible losses dominate over irreversible losses, these losses are recovered by purging dry N₂ during the MOL interruption to remove excess water in the catalyst layers. The black bar with green lines represents the total reversible and irreversible losses.

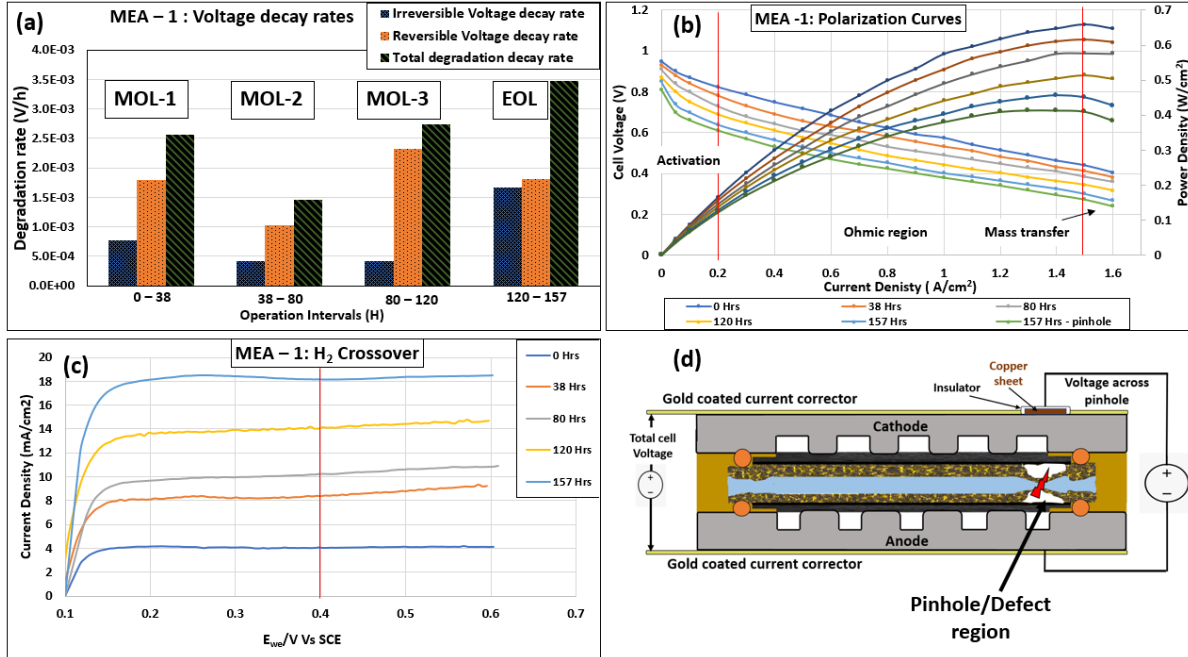


Figure 6-7: MEA-1 performance: (a) breakdown of irreversible (blue), reversible (orange) and total (green) OCV decay rates during the AST, (b) polarization curves and (c) H₂ crossover current measured at different points during the AST. (d) Schematic of voltage recording from total cell and across pinhole/defect region.

From Figure 6-5a, it is found that the total voltage decay from 0.945V to 0.802V at decay rate of 0.910 mV h⁻¹. IR examination on MEA-1 at MOL-2 (80 AST hours), a small hotspot is identified (Figure 6-8b) where its OCV drops to 0.884 V. The hotspot is found at the edge of the gasket/CCM interface located at the top left corner of the electrode. It is likely that this damage is caused by mechanical stress due to rupture of membrane at sealant/gasket/CCM interface. A possible mechanism for failure due to sealant damage is discussed in section 4.4.1.2. A schematic showing the cross-sectional view of the sealant defects in MEA is shown in Figure 6-8a. As the MEAs are installed in the stack, the silicon gaskets prevent potential gas leak and provide sufficient stack compression for the fuel cell. Any variations in the thickness of the MEA components (CCM/GDL) across the gasket leads to development of stress zones in the MEA during the stack compression as shown in Figure 6-8a, location-1. These stress zones are expected to cause faster membrane degradation and eventually develop into pinholes, as shown in location 2 and 3. Further discussion of the degradation of sealant defects at BOL, MOL and EOL is included later in this section. Figure 6-8c confirms the growth of the pinhole first observed at MOL-2 and the formation of new pinholes by the time EOL is reached. As a result of pinhole growth, the irreversible decay

rate increased by 4 times at EOL to a rate of 1.67 mV h^{-1} . Two major pinholes are identified across the top left and top center areas of the electrode. The IR thermographs clearly show that the sealant areas are more vulnerable to chemical degradation at the edge interface sections of the MEA, which is the area where CCM/GDL is sealed with gasket. Figure 6-8d shows a digital image of the cathode surface of MEA-1 after EOL, revealing physical damage of the teflon gasket caused by the exothermic combustion of H_2 with O_2 . The magnified image in Figure 6-8d (inside the yellow box) shows the damaged area in the MEA.

Table 6-3: OCV and H_2 crossover current density at different stages during the AST.

AST (hours)	OCV (V)	H_2 crossover (mA cm^{-2}) @ 0.4V
0 hrs	0.948	2.0
38 hrs	0.918	8.28
80 hrs	0.884	10.18
120 hrs	0.867	14.04
157 hrs	0.805	18.0

Figure 6-7b shows polarization curves for MEA-1 at various times during the AST. The results show a small drop in cell performance over time in each of the activation, ohmic and mass transfer regions of the polarization curves. These curves also show a decrease in the OCV over time, which is consistent with that observed previously in Figure 6-5a. This trend obviously is a consequence of the degradation and pinhole formation discussed above (Figure 6-8b-d). The loss of OCV can be attributed to the steady increase of H_2 crossover through the degraded membrane from $\sim 4 \text{ mA cm}^{-2}$ at BOL to $\sim 18 \text{ mA cm}^{-2}$ at EOL (Figure 6-7c). For better comparison, the total cell voltage and voltage across the pinhole region have both been measured at EOL (157 hours) (Figure 6-7d). The voltage across the pinhole region was measured by placing a $15\mu\text{m}$ thick copper sheet with area of 0.5 cm^2 on top of the gold-coated current collector across the pinhole region in MEA. The y-axis in the blue polarization curve at 157 hours (Figure 6-7b) corresponds to the cell voltage, while the y-axis in the green curve corresponds to the cell voltage as measured at the hotspot-region 3 identified in Figure 6-8c at 157 hours. The cell voltage measured across the hotspot-region 3 (0.81) is 4.7% lower than the total cell voltage (0.85V). From all observations made on MEA-1, the growth of the pinhole in the membrane decreases the OCV by 14.7% and 40.6% in the mass-transfer region from BOL to EOL.

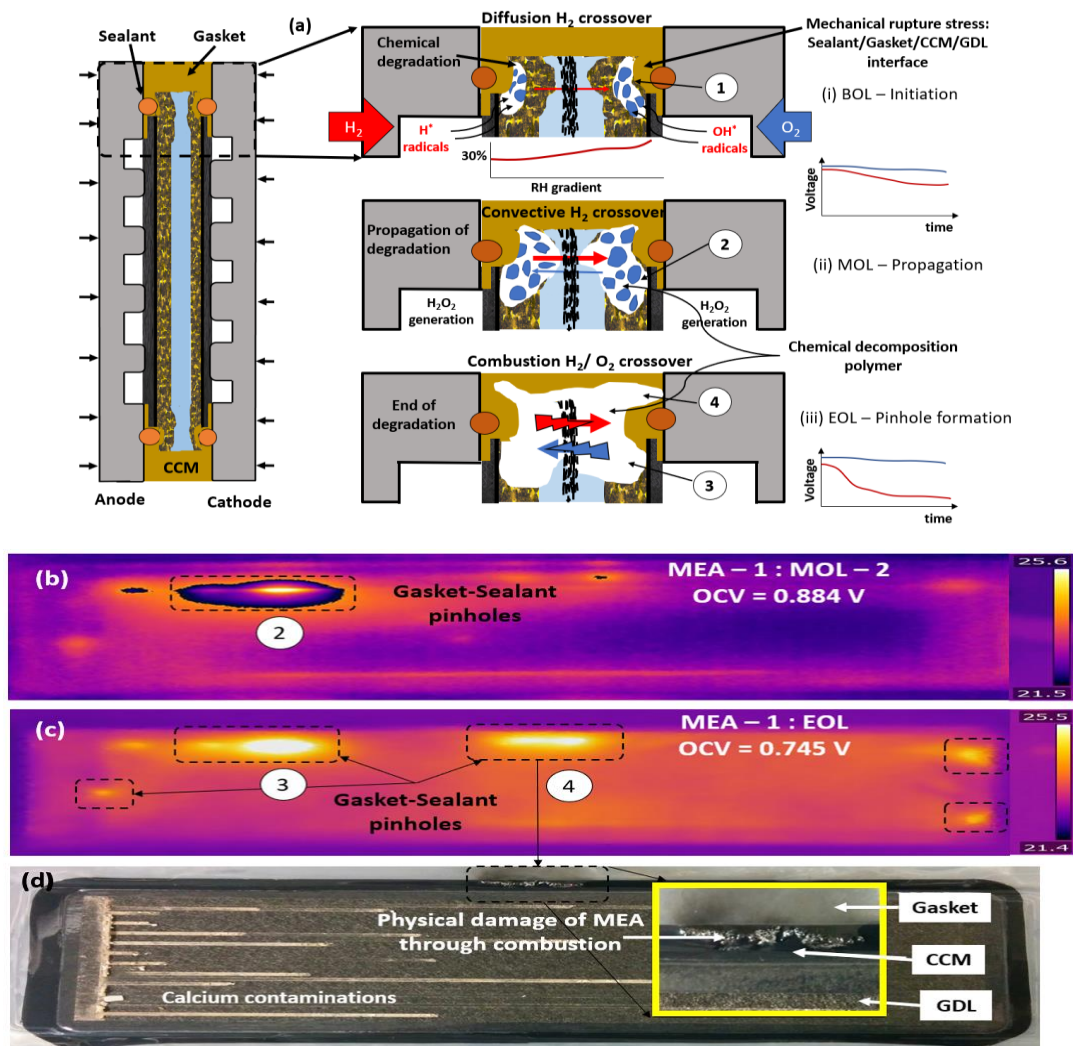


Figure 6-8: MEA-1 (a) Schematic of sealant/gasket/CCM/GDL interface defects in MEA (i) BOL initiation of defects across sealant (orange circles) interface area (ii) MOL propagation of defects (radicals/ H_2O_2 generation) (iii) EOL pinhole formation (H_2/O_2 crossover); IR image of MEA-1 captured at (b) MOL-2 and (c) EOL. (d) Digital image of MEA-1 captured after EOL; magnified image shows burned area of MEA due to H_2/O_2 combustion and calcium contaminant precipitated on the GDL (white).

Figure 6-8a presents a schematic of the various stages of defect initiation, propagation and pinhole formation in MEA-1. Failure likely occurs due to several events during the AST, such as (i) compression of bipolar plates on the MEA, (ii) non-uniform thickness of MEA components and (iii) non-uniform hydration of the active area and gasket/CCM/GDL interface. Degradation of MEA-1 during the different stages of aging may proceed due to the following causes:

(1) **BOL initiation:** Although reinforced membranes have better chemical and mechanical properties and are less sensitive to mechanical failures during wet and dry conditions [158], thicker portions of the MEA are compressed to a greater extent by the bipolar plates and develop internal

stress particularly within the membrane. When the RH is low, the moisture level will likely vary over the electrode surface and gasket/CCM edge interfaces. As aging continues, voids form in the stressed areas near the gasket/CCM interface that facilitates the formation of water droplets along the edge of MEA and polymer degradation (Figure 6-8a). Lai et.al. [159] reported that a RH gradient is an important parameter that affects degradation of the membrane, making it very difficult to estimate the local stress in the membrane. The water droplets in the void areas slowly generate H^* and OH^* radicals in the anode and cathode ionomer layers of the CCM [160].

(2) **MOL propagation:** As a result of radical attack in the stressed areas, chemical decomposition of polymer occurs on either side of the electrode and membrane thickness is reduced. The thinned areas facilitate gas crossover that further accelerates OH^- and peroxide generation and chemical degradation of the membrane [161]. In addition, the constrained membrane also experiences clamping stress from the gasket sealants (Figure 6-8a), leading to mechanical stress in the CCM. Both chemical and mechanical stresses initiate pinhole formation in the MEA (e.g., region 2 in Figure 6-8a). Figure 6-8b shows the IR image of hot-spots caused by H_2 crossover through the pinhole present at MOL-2 after 80 hours of the AST.

(3) **EOL degradation:** As the amount of gas crossover increases during the AST, the direct interaction of H_2 and O_2 will lead to their combustion across the pinhole, which degrades the anode and cathode ionomers in the reinforced membrane without damaging the PTFE reinforcement layer [153]. As shown in Figure 6-8a, region 3 is a chemically degraded area in the CCM covered by the GDL. The damage to this area in MEA-1 is evident in the growth of the area and surface temperature from $\sim 24.5^\circ C$ to $26.8^\circ C$ of the hotspot first present at MOL-2 until EOL after 157 hours. Region 4 depicts the damaged portion near the gasket/CCM interface due to mechanical stress from the sealant and hot bipolar plate ($90^\circ C$). The damage in such a region is likely due mostly to variations of the thickness of the local areas of MEA components. It is very critical for electrode developers to improve the accuracy of thickness measurements of the component layers by determining the thickness over the entire substrate surface rather than at only a single point.

6.4.2 Performance of MEA - 3

Quality control inspection at the component level is key and absolutely necessary for the production of high quality MEAs. As per electrode developers' information, $\sim 20\%$ of MEAs exhibit lower than expected performance due to sealant interface defects causing gas leaks during

stack operation. To the best of our knowledge, the experiment on MEA-3 is the first reported study conducted to investigate the impact of sealant/gasket/CCM interface defects and artificial pinholes. Inspection of MEA-3 by IR imaging at BOL prior to the OCV-hold AST reveals four hot-spot stressed regions (Figure 6-9a). Regions 1, 2 and 4 are located in the portions contacted by the gasket and only region 3 lies within the active area of the electrode. The initial OCV of MEA-3 at BOL is measured to be 0.935V. As the sample ages during the AST, its OCV decreases relatively quickly and reaches 0.8 V after only 57 hours. IR examination at MOL-4 shows significant propagation of defects in regions 1 and 2 across the gasket/CCM interface (Figure 6-9b). On the other hand, no further growth of the hot-spots in regions 3 and 4 are observed. Regions 1 and 2 are presumably more stressed during the AST than regions 3 and 4, which might cause faster chemical degradation of ionomer in the membrane and accelerate gas crossover. As a result of the gas leak through the degraded areas, the anode pressure of MEA-3 drops by 10 kPa (from 270 kPa to 260 kPa) during interval MOL-4.

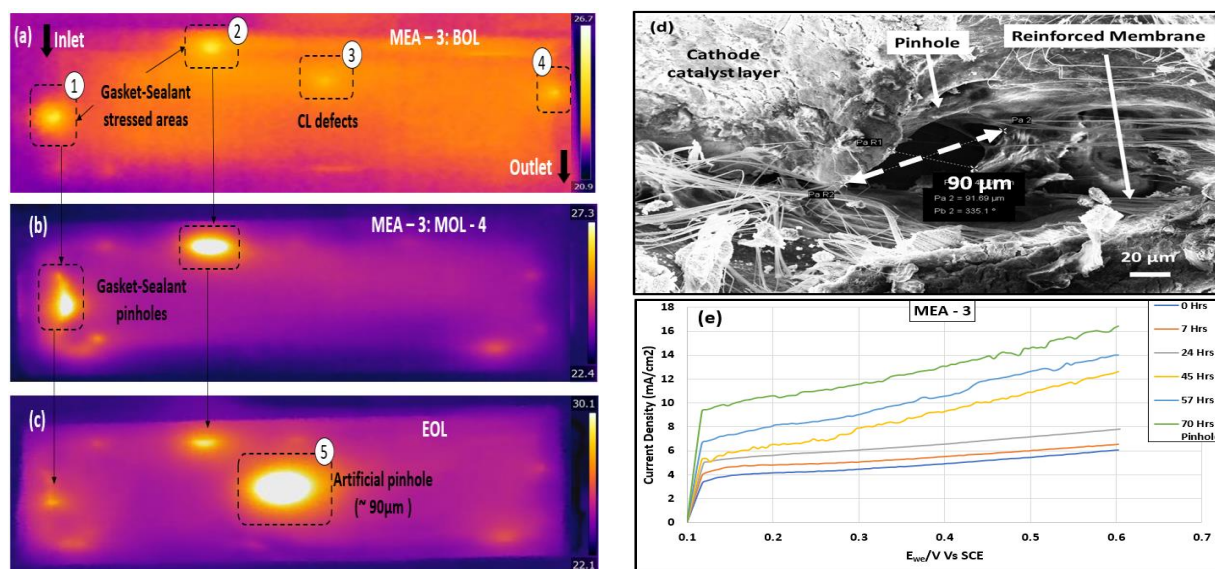


Figure 6-9: MEA-3 IR examination at (a) BOL, (b) MOL-4 and (c) EOL; (d) SEM image of artificial pinhole ($\sim 90\mu\text{m}$) in CCM formed using a micro-needle and; (e) variation of H₂ crossover current density during the course of aging.

After MOL-4 is reached, an artificial pinhole has been introduced in the center of the MEA using a micro-needle with diameter $\sim 90\mu\text{m}$ (Figures 6-9c,d). A number of previous researchers have investigated the effect of artificial pinholes on cell performance. Breakthrough of the micro-hole can clearly be seen through the CCM/reinforcement layer. Not surprisingly, the $\sim 90\mu\text{m}$ pinhole

has a significant effect on the OCV, which drops almost immediately by 165 mV from 0.838 V to 0.673 V (Figure 6-5b). Furthermore, the OCV begins to become very unstable and fluctuate widely. It is also observed that both irreversible and reversible effects showed similar decay rates (Figure 6-10a-EOL). This large fluctuation of voltage is likely due to gas leakage through the artificial pinhole in region 5 (Figure 6-9c) where the reinforced PTFE barrier is broken. This causes a pressure drop of 10 kPa across the electrode. IR analysis at EOL shows that the surface temperature has risen from 24.2°C (non-defected area) to 35.8°C (at the artificial pinhole). At the same time, the hot-spots in regions 1 and 2 shrink once the artificial pinhole is introduced (compare Figures 6-9b and 6-9c), indicating that the large amount of gas leaking through the pinhole in region 5 reduces the amount crossing regions 1 and 2. This observation also suggests that the PTFE reinforcement in region 1 and 2 layer has not been severely degraded during the course of the AST. This reinforced layer is able to maintain a gas barrier, which may explain why degradation to the point where hot-spots appear does not necessarily cause cell failure. Figure 6-9e shows clear evidence of increase in H₂ crossover current as a result of leakage through pinhole.

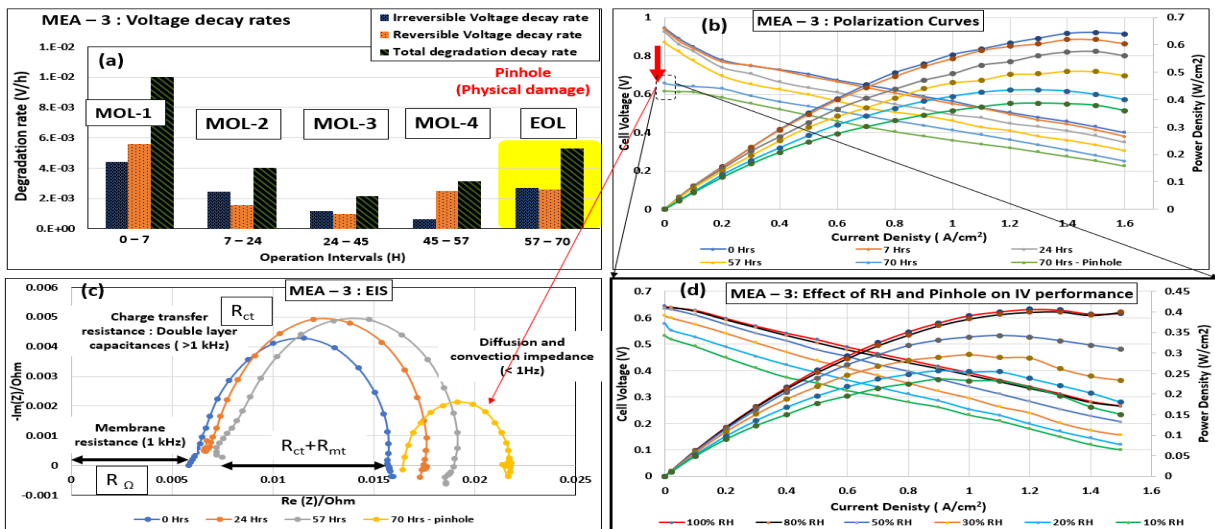


Figure 6-10: MEA-3 performance: (a) breakdown of irreversible (blue), reversible (orange) and total (green) OCV decay rates during the AST; (b) polarization curves obtained during the AST; red arrow indicates the drop in OCV after artificial pinhole is introduced, the black dashed circle shows the voltage difference between total cell voltage (blue curve) and voltage drop across pinhole region (green curve) the schematic of voltage measuring points is shown in Figure 6-7d (c) EIS spectra and (d) polarization curves across artificial pinhole region at various RHs.

Figure 6-10 presents the results of the electrochemical analysis of MEA-3 at various stages of aging. From Figure 6-10a, it is found that the OCV drops most rapidly during the initial hours

(MOL-1) of the AST, not surprising due to the presence of sealant interface defects at BOL. Over the period from BOL to MOL-4, the OCV drops by 120mV from 0.93V to 0.809V. Once artificial pinhole is introduced, the irreversible OCV loss in particular increases. Figure 6-9d shows the SEM surface view of artificial pinhole showing a diameter of 90 μm . As expected, the introduction of the artificial pinhole affects the polarization performance (Figure 6-10b) particularly at low current densities rather than at high current densities. The OCV measured at 57 hours is 0.870V, but drops to 0.655V at 70 hours. Examination of the polarization curves over the entire current range indicates that the slopes of I-V curves have not changed significantly in comparison to the OCV drop alone. The decrease in performance is most severe after the artificial pinhole is introduced. The performance evolution across the artificial pinhole is analysed by measuring the cell voltage across the pinhole region-5 in figure 6-9c. The blue curve represents the polarization of the cell (OCV = 0.655 V) at EOL, while the green curve corresponds to the polarization measured across the artificial pinhole region (OCV = 0.615 V) as per the schematic shown in Figure 6-7d.

The effect of pinhole as a function of RH is an important subject of debate in PEMFC for membrane durability. The relative change in the humidity of the membrane causes swelling/shrinking, which in turns affects the size of the pinhole [88]. It is expected that the membrane will absorb moisture in a fully humidified condition and swell, thereby reducing the size of the pinhole. The gas crossover decreases as the size of the pinhole closes. On the other hand, when membrane undergoes dry operation, the pinhole size and resulting gas crossover increase. The effect of pinhole under various RH conditions is presented in Figure 6-10d. From our observation, no significant effect is observed when the RH is varied between 100% and 80%. However, when the RH decreases further to 50%, 30%, 20% and 10%, the OCV drops from 0.635V to 0.630V, 0.599V, 0.577V and 0.519V, respectively. The drier the membrane, the greater is gas crossover through pinholes. The cell performance also decreases across all three regions i.e., activation, ohmic and mass transport regions primarily because of the reduction of the H^+ conductivity through the membrane. However, the reduction in the OCV is larger than the cell voltage when high current densities are applied.

Figure 6-10c shows the EIS spectra of MEA-3 measured at 100 mA cm^{-2} (5 A) at the various intervals during the AST[162,163]. It is recommended that the comparison of EIS is better

at low current densities than high current densities in order to eliminate noise due to mass transfer effects. The corresponding high frequency resistance (HFR) and low frequency resistance (LFR) obtained from these Nyquist plots are summarized in Table 6-4. Relatively little change in the membrane resistance (R_{Ω}) is observed between 0 hours (5.8 m Ω) and 57 hours (7.5 m Ω). We believe the small increase in resistance may be attributed to the slow growth of interface defects (region 1 and 2) from BOL to MOL-4, as shown in the IR images (Figures 6-9a and b). However, the situation changes dramatically when the 90 μ m pinhole is introduced in MEA-3. The yellow curve in Figure 6-10c represents the response after the pinhole is introduced at 70 hrs. The R_{Ω} is found to increase from 7.5 m Ω to 16.4 m Ω . On the other hand, the charge transfer resistance R_{ct} (i.e., diameter of arc in EIS spectrum) increased over the period from 0 hours to 57 hours of the AST until the artificial pinhole is introduced. We believe that the charge transfer increase is mainly caused by catalyst degradation. After the artificial pinhole is implemented, it is found that the magnitude of the impedance curve noticeably decreases. Subsequently, it is likely that some internal current, which is induced by gas crossover through the pinhole, causes smaller impedance magnitude of the pinhole in MEA at 70 hours than that of the pinhole in MEA at 57 hours. Since impedance magnitude decreases with increasing internal current at a given electrode, the decrease in impedance after the introduction of the artificial pinhole is a good indication of the presence of internal current [164]. From the Nyquist plot shown in 6-8c, it is observed that ohmic resistance dominates the charge transfer resistance due to the formation of the pinhole in the membrane.

Table 6-4: OCV, H₂ crossover current density, HFR and LFR of MEA-3 during course of AST.

Age (hrs)	OCV (V)	H ₂ crossover (mA cm ⁻²) @ 0.4 V	EIS (m Ω)	
			HFR (R_{Ω})	LFR ($R_{ct} + R_{mt}$)
0	0.94	4.5	5.8	15.7
24	0.90	8.3	6.4	17.6
57	0.81	11.0	7.5	18.9
70 – pinhole	0.79	12.0	16.4	21.7

Where R_{Ω} = membrane resistance, R_{ct} = charge transfer resistance, R_{mt} = mass transfer resistance

6.4.3 Performance of MEA - 4

Although catalyst layer coating defects are of great importance to CCM electrode manufacturers and developers in order to produce high quality MEAs, very limited information on

their impact on cell performance and lifetime is available in the literature. Therefore, the main focus of this research is to investigate how significantly catalyst layer defects lower the performance and affect the lifetime of the cell. The investigation of MEA- 4 allows us to specifically study the effect of an MCLD in which a small portion of the catalyst layer is missing (MCLD) from the CCM due to faulty manufacturing and bare membrane inside the MCLD is exposed to incoming reactant gases. The CCM used in MEA-4 is first examined with an optical microscope to identify the catalyst layer defects. Two defects are identified over an active area of $\sim 48 \text{ cm}^2$, i.e., defect-1 and defect-2 on the CCL as shown in Figure 5-4c. First the sample was aged in the custom-designed cell over a duration of 25 hours of OCV at 60°C to study the morphological changes of defects (MCLD) as discussed in section 5.4.3.3.2. Later the defected CCM was hot-pressed with GDLs to form MEA and aged in the FCAT cell as discussed in section 6.3 to do the electrochemical analysis. Before hot-pressing the MEA, the surface features of defect-2 were closely examined with the optical microscope, it is observed that a small section of the catalyst layer was found to be completely missing inside the MCLD. This section of bare membrane has developed cracks and micro-pinhole on the surface during the 25 hours of OCV test. An overview of bare membrane region prior to hot press is shown in Figure 5-10. After the fabrication of MEA-4, the sample is operated under constant low RH for 75 hours of AST. The electrochemical analysis during this period is reported in Figure 6-12. After the 75 hours of AST, the sample met the EOL criteria discussed in section 6.3. Following the EOL, the GDLs are carefully detached from the CCM and microscopic surface analysis on bare membrane in defects-2 is further investigated after AST to study the morphological changes of defect. Figure 6-11a illustrates the schematic of cross-sectional view of CCM defect (MCLD) undergoing chemical and mechanical stress that leads to degradation of polymer in the membrane and develops in to cracks and pinholes. Figure 6-11b and 6-11e shows surface view of the degraded bare membrane area during the OCV AST, the bright dots inside the red dotted circles represents Pt that presumably has dissolved under OCV and low RH conditions, migrated and re-precipitated in the membrane [87], [113]. The degraded locations in the membrane is shown in purple color in Figure6-11c. The effect of Pt dissolution in the membrane on catalyst layer durability is subject to debate. From the microscopic surface analysis of the degraded bare membrane two observations are made: (i) catalyst/Pt dissolution, whereby Pt particles dissolve from the catalyst layer and migrate in the polymer matrix [33,70,165,166] and (ii) ionomer decomposition in membrane developing into micro-pinholes.

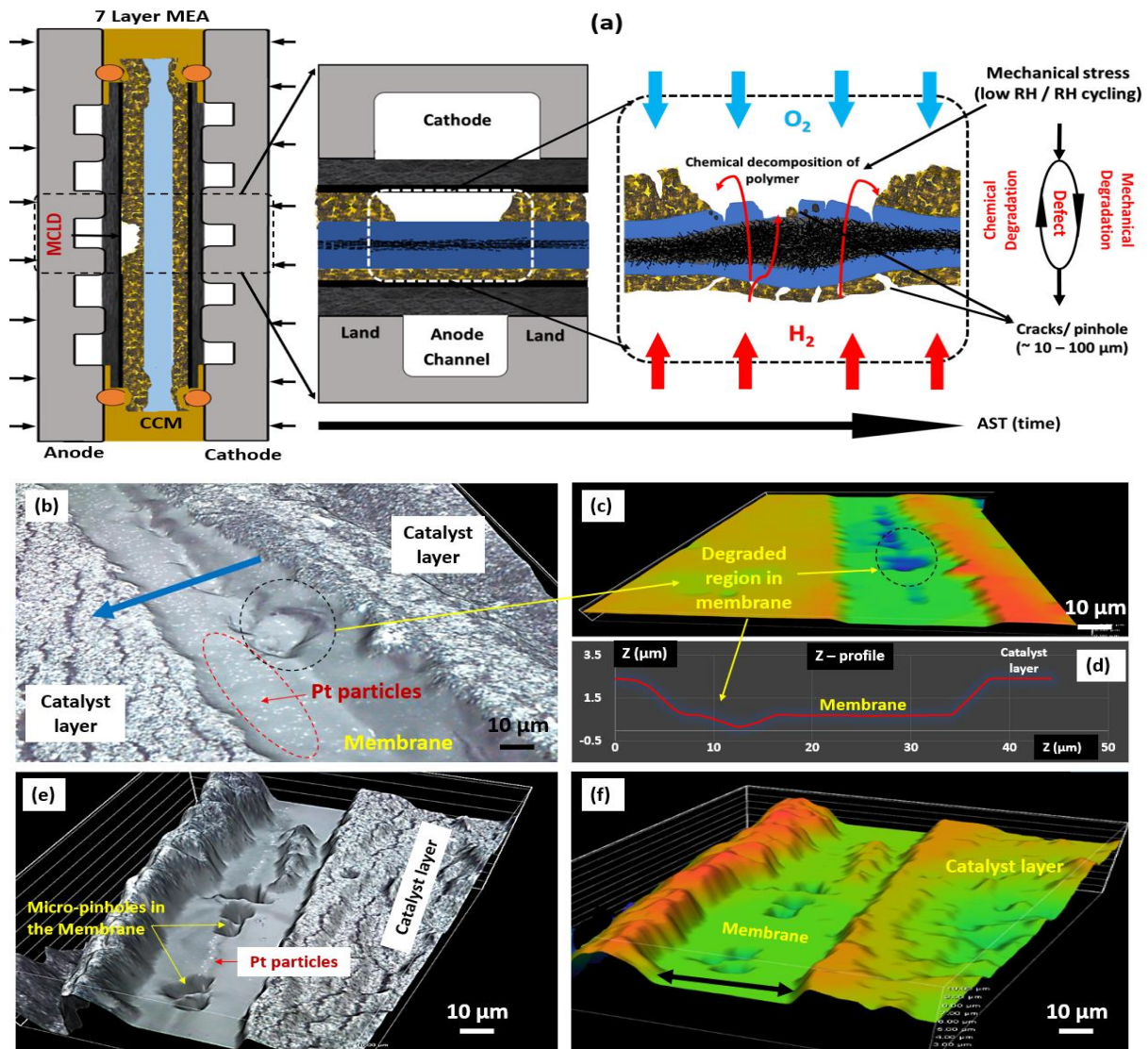


Figure 6-11: MEA-4 (a) Schematic of chemical and mechanical stress on catalyst layer defect (zero catalyst area/bare membrane – cross sectional view) in CCM causing defect to develop into cracks and pinholes; (b) Microscopic image of degraded catalyst layer defect (MCLD), showing the surface view of bare membrane/zero catalyst area, the white dots inside the red dotted circle represents the dissolution Pt-particles from the catalyst layer in to the membrane during the OCV AST; (c) represents the 3D view of color mapping of defect in Figure (b), where orange represents the catalyst layer, green represents the bare membrane and purple represents the degraded area in the membrane developing into micro-pinholes. (d) Z-profile along the blue arrow in Figure (a), (e) degraded areas in the membrane developing into micro-pinholes. (f) 3D view of image in Figure (e).

1. **Catalyst/Pt dissolution:** The red dotted circle in Figure 6-11a shows the Pt particles detached from the catalyst layer and dissolved in to the membrane ionomer during OCV AST under low RH. One of the possible causes for the Pt dissolution is expected (a) due to

catalyst sintering, as discussed in 5.4.3.2. (b) Oxide species of Pt, causing Pt dissolves from cathode catalyst layer and migrate through ion-exchange sites in the polymer membrane through a concentration effect. Where Pt catalyst particles oxidized to PtO by combining with water molecule and convert into Pt^{2+} . The Pt^{2+} ions then further deposit into membrane due to thermodynamically preferred potential gradient direction for positive metallic ions (less negative cathode to more negative anode) [122]. As the AST progresses, the defected areas (bare membrane zones) degrade which presumably increases hydrogen gas crossover and causes local hotspots across the defect. The increase in local temperature can lead to melting of ionomer in catalyst layer causing the catalyst/Pt particles to be isolated from the layer and dissolve into membrane. The blue area in Figure 6-11c shows a thin degraded region in the membrane. The Z-profile in Figure 6-11d presents the variation in thickness of bare membrane along the blue arrow in Figure 6-11a. Several studies have shown that catalyst migration and Pt dissolution into the electrolyte membrane can accelerate the chemical degradation of the membrane via radical formation [33,70,165,166].

2. **Ionomer decomposition:** The dotted circles in Figure 6-11b represents the micro-pinholes in the degraded membrane captured after 75 hours of OCV AST. It is expected that both the micro-pinholes are initiated by chemical decomposition of ionomer during OCV aging [71,101,142]. By measuring the dimensional features of the membrane holes, it is found that $\sim 20 \mu\text{m}$ diameter and $5.8 \mu\text{m}$ depth is developed due to degradation of the membrane. Further examination of the CCM using IR thermography confirms that the feature in defect-2 appears as a hot-spot (see Figure Appendix 10.3). This finding strongly confirms the gas leak through the pinholes. Figure 6-11f shows the color mapping of defected area corresponding to the image in figure 6-11e.

In conclusion, the membrane defects affect cell performance more severely than catalyst layer defects. Even a sub-micron defect can allow permeation of hydrogen from anode to cathode and develop dangerous pinholes that lead to EOL of the PEMFC electrode.

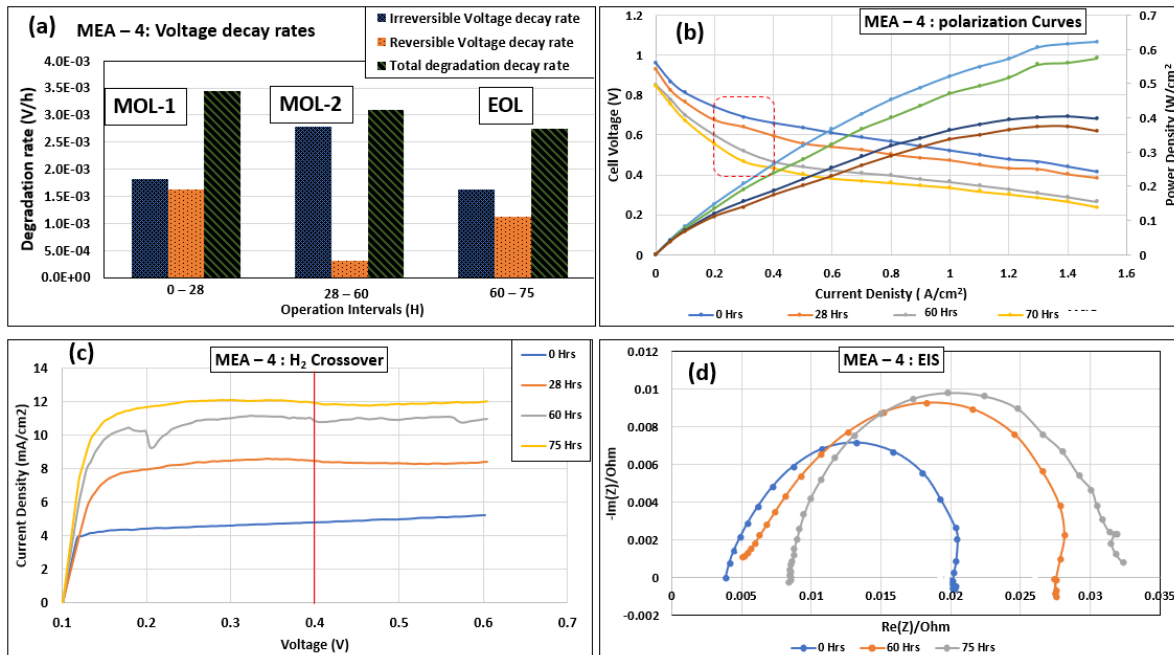


Figure 6-12: MEA-4 performance: (a) breakdown of irreversible (blue), reversible (orange) and total (green) OCV decay rates during the AST; (b) polarization curves obtained during the AST; red dotted area indicates the difference in the ohmic portion of curves. (c) H₂ crossover currents and (d) Nyquist EIS plots during the course of aging.

Figure 6-12 shows the electrochemical measurements of MEA-4 and Table 6-5 lists the parameters obtained from these experiments. Irreversible decay of the OCV (blue bar in Figure 6-12a) dominates reversible decay during all three intervals of the AST. This reflects the rapid degradation of MEA-4, which may lead to the development of surface cracks and pinholes exacerbated by high gas crossover through the catalyst layer defects. The formation of a pinhole/hotspot in the catalyst layer defect across ROI-1 is supported by the increase in H₂ crossover current (Figure 6-12c) and IR thermograph (see Appendix section 10.3). From the polarization curves in Figure 6-12b, little shift in ohmic region between 0.2 A cm⁻² and 0.4 A cm⁻² is observed with a significant performance loss of 32.2% across 0.3 A cm⁻². We believe the voltage losses in the ohmic region are associated with structural changes in the catalyst layers through cracks, propagation of MCLD or delamination of the catalyst layer/membrane interface that increases the MEA ohmic resistance [167][168][160]. Analysis of the EIS spectra indicate that R_Ω and R_{ct} gradually increase from BOL to EOL. It is expected that, during the low RH AST operation, the ionomer in catalyst layer and membrane chemically degrades fast, which can lead to accelerate propagation of electrode defects,

especially bare membrane (zero catalyst areas) to develop pinholes [140]. The overall degradation rate of MEA-4 is measured to be 2.19 mV h⁻¹ during the OCV-AST.

Table 6-5: OCV, H₂ crossover current density, HFR and LFR of MEA-4 during course of AST.

Age (hrs)	OCV (V)	H ₂ crossover (mA cm ⁻²) @ 0.4 V	EIS (mΩ)	
			HFR (R _Ω)	LFR (R _{ct} + R _{mt})
0	0.93	4.5	3.8	20.1
28	0.90	8.3	-	-
60	0.81	11.0	5.1	27.5
75	0.79	12.0	8.5	32.3

The possible causes for defect propagation leading to failure mode in MEA-4 are discussed below:

1) **Lower extent of electrochemical reaction across defects:** The local concentration of reaction gases in non-defected catalyst areas vary from that in defected areas (zero catalyst areas/bare membrane). Studies have shown that the concentration of reaction gases gradually decreases as one moves from the top-most surface at the catalyst layer/GDL interface to the bottom-most layer at the catalyst layer/membrane interface [167]. When a catalyst deficiency exists, e.g., zero catalyst/ thin catalyst layers/bare membrane, the gas concentration increases across defected areas due to little or no electrochemical reaction. These conditions accelerate degradation via catalyst erosion and the formation of surface cracks, tears or blisters in the membrane. This in turn gradually increases the driving force for gas crossover through defects.

2) **Hydrogen crossover:** This phenomenon is very critical in thinner membranes (<25 μm) considering its mechanical properties with respect to premature failure. The direct crossover of gases chemically decomposes the polymer in the membrane through H₂O₂/radical attack. Although chemical degradation is considered the primary cause for membrane degradation, the mechanical stress due to dehydration (low RH AST) further accelerates defect propagation [168]. As a result, both chemical and mechanical stresses lead to propagation of local defects in MEA.

6.4.4 Performance of MEA – 5

MEA-5 is a 3rd case study focusing on catalyst layer defects such as scratches or cuts in the CCM. An example of scratches with deep cuts and surface cuts are shown in Figure 6-13a and Appendix Figure 10-5. The graphical view of MEA-5 showing the location of this defect is shown in Figure 6-13c. Two types of scratches are commonly observed on cathode catalyst layers: (i)

surface cuts and (ii) deep cuts. From our previous investigations (see section 4.4.3.1 of chapter-4), surface scratches have very little/negligible impact on defect propagation due to lower variability in defect thickness $\pm 0.5\mu\text{m}$. The thickness of the surface cut is found to be approximately $\sim 1.2\mu\text{m}$. On the other hand, deep cuts in catalyst layer are concerning and require more attention in selecting high-quality CCMs. The dotted circle in Figure 6-13a shows a deep cut, with the deep cut region in the catalyst layer (magenta colour) that directly exposes bare membrane to the gases. The Z-profile in Figure 6-13b taken along the blue arrow in Figure 6-13a shows that the cut penetrates to a depth of $\sim 4\mu\text{m}$. Manufacturers should be aware of this type of scratch and the extent to which they affect PEMFC performance. If CCMs rolls are investigated with a reflected microscope, the operators should inspect the range and severity of scratches by varying the transmitted light between 5% and 20% during analysis. The higher the reflected light intensity inside the defect, the more critical is the defect.

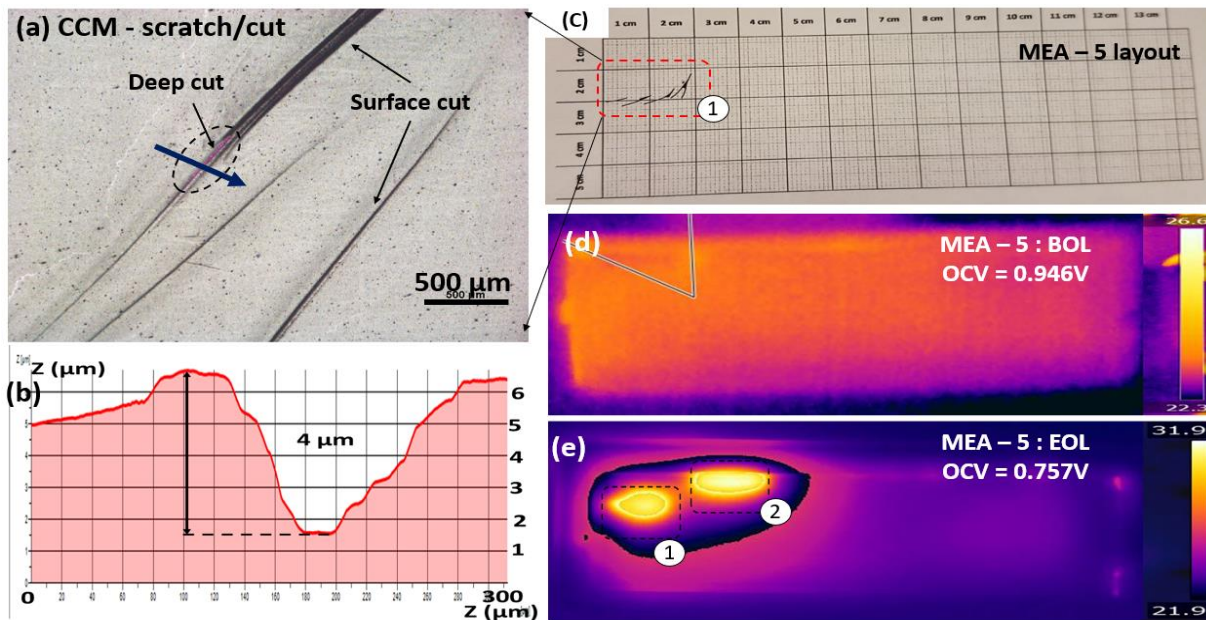


Figure 6-13: MEA-5 (a) Optical image showing scratches on the catalyst layer; the dotted circle area indicates a deep cut, while the dark line denotes a surface scratch; (b) Z-profile across the blue arrow in (a) showing a deep scratch with depth of $4\mu\text{m}$; (c) layout of MEA-5 showing location of defect in CCM; IR images of MEA-5 at BOL (d) and EOL (e) showing two pinholes 1 and 2.

IR examination of MEA-5 prior to the OCV-AST does not reveal any hotspots (Figure 6-13b), indicating that no gas should leak across the membrane at the outset. During the AST, the OCV of MEA-5 degrades at a rate of 1.85 mVh^{-1} until it reaches EOL after 110 hours. The AST is

interrupted at 35, 75, and 110 hours for electrochemical analysis to characterize the extent of degradation. The results of the electrochemical analysis of MEA-5 are shown in Figure 6-14 and corresponding values are listed in Table 6-6. The irreversible components of the OCV decay rates for MEA-4 and MEA-5 are similar, with values of 1.83 mVh^{-1} and 1.93 mVh^{-1} , respectively, during the initial stages of the AST at MOL-1. It is expected that H_2 permeation through both MEAs are approximately the same due to the presence of catalyst layer defects. The decay rate during MOL-2 is measured to be 0.65 mV h^{-1} , assuming slow degradation of defects in the electrode between 35 and 75 hours. When EOL is reached, the irreversible decay rate has increased four-fold, attaining a degradation rate of 2.79 mV h^{-1} in the interval from 75 to 110 hours. The higher degradation rate suggests that a significant structural change in the electrode has occurred, leading to higher H_2 leakage and a lower OCV. The IR imaging at EOL (Figure 6-13e) confirms the presence of two major hotspot regions, one at the same location as the defects shown in Figure 6-13c and the other near the sealant/gasket interface. Interestingly, the area of these hotspots is much larger than those in the other MEAs. From image analysis, the area of region-1 (catalyst layer scratch) is measured to be $\sim 1.29 \text{ cm}^2$ and region-2 (gasket/sealant interface) is measured to be 1.79 cm^2 . The larger areas of the hotspot indicate a greater extent of damage in the membrane caused due to catalyst layer scratch and sealant defects due to CCM mishandling. This is confirmed by H_2 crossover current densities that are about an order of magnitude larger (118.6 mAcm^{-2} after 75 hours and 146.4 mA cm^{-2} after 110 hours) than that observed for the previous MEAs (Figure 6-14c). The rapid increase in H_2 crossover current indicates a high crossover rate and a high internal short circuit between anode and cathode.

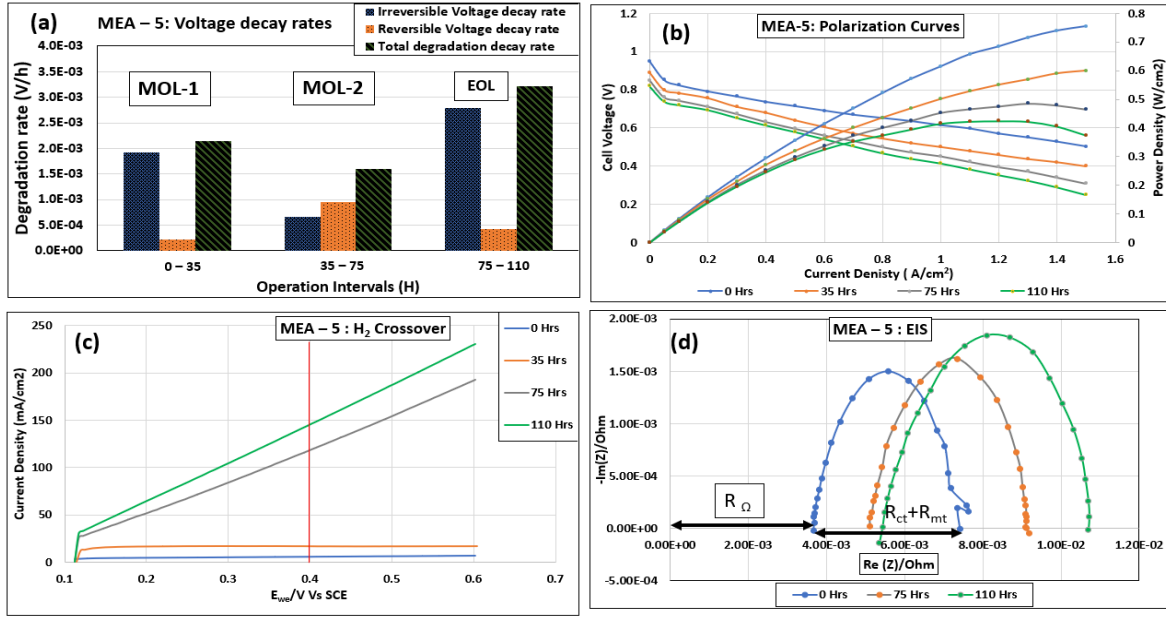


Figure 6-14: MEA-5 performance: (a) breakdown of irreversible (blue), reversible (orange) and total (green) OCV decay rates during the AST; (b) polarization curves, (c) H₂ crossover currents and (d) Nyquist EIS plots (@ 100 mA cm⁻²) obtained during aging.

Table 6-6: OCV, H₂ crossover current density, HFR and LFR of MEA-5 during course of AST.

Age (hrs)	OCV (V)	H ₂ crossover (mAcm ⁻²) @ 0.4V	EIS (mΩ)	
			HFR (R _Ω)	LFR (R _{ct} + R _{mt})
0	0.946	4.82	3.67	7.41
35	0.878	16.40	-	-
75	0.851	118.6	5.12	9.19
110	0.757	146.4	5.44	10.70

The polarization curves for MEA-5 in Figure 6-14b show that 50.3% of the cell voltage is lost over the current density at 1.5A/cm² where mass transfer is dominant. Increase in mass-transfer losses is most likely caused by the propagation of damaged areas (region-1 and region-2 in Figure 6-13e) that do not contribute to any electrochemical reaction and facilitate water accumulation at higher current densities. The EIS results also confirms the growth of membrane resistance from 3.67 mΩ (BOL) to 5.44 mΩ (EOL), respectively, as shown in Figure 6-14d and Table 6-6. The IR results strongly support the conclusion that the irreversible loss of OCV in MEA-5 originates primarily in the catalyst layer and CCM/gasket interface defects. Although these

defects have a small effect on cell performance at BOL, their impact grows dramatically and leads to fuel cell failure as they propagate during the AST.

6.5 COCV diagnostic test during RH cycling

The RH cycling protocol was designed and implemented to accelerate both chemical and mechanical degradation of the membrane and catalyst layer defects. ASTs involving the application of RH cycles (wet/dry) over short intervals at high temperature are particularly useful for assessing membrane durability in PEMFC stacks operating under realistic conditions. Under high RH conditions, the membrane swells and buckles in-plane due to the constraining pressure by the bipolar plates, leading to catalyst layer cracks and delamination of GDL/catalyst layer/membrane interface. On the other hand, under low relative humidity conditions, the membrane shrinks and loses stiffness and strength. Also when it is not highly hydrated, the membrane is more prone to chemical degradation and a weaker inter-layer bond strength of MEA components. The repeated humidity cycling of high and low RH conditions induces internal and external stress on the membrane reduces the ductility of the membrane and develops pinholes to reach its EOL.

The RH of the reaction gases is cycled from 80% (wet) to 20% (dry) on the cathode side and maintained at 80% on the anode side throughout the experiment. The decision to select 80% RH over 100% is to reduce the possibility of water flooding in the membrane. On the other hand, 20% RH is selected over 0% to prevent extreme drying of the membrane which can lead to large residual tensile stress at 90°C [119][118]. This approach of testing MEAs is of great interest to electrode developers and membrane researchers and commonly used [67]. Figure 6-15 shows the OCV response (red curve) of MEA-2 superimposed on the applied RH cycles (black) during the AST. The particular waveform used consists of RH = 80% for 10 mins followed by RH = 20% for another 10 mins on the cathode side.

As a result of lowering the RH from 80% to 20%, the OCV drops by 22 mV. The decrease in OCV occurs as a result of electrode stress and slow oxygen reduction reaction (ORR) kinetics due to the low water content in the electrode. Khattra et.al showed that during RH cycling, the longer hold time at lower humidity leads to considerable chemical and mechanical stress in the polymer membrane that leads to faster degradation of the electrode [169]. A study from Neyerlin. et. al

reported that ORR kinetics is slower at lower RH due to the presence of less water in the catalyst layer ionomer which restricts the proton transfer rate in the electrode and increases the overpotential of the electrode [170]. Similar work by Xu et al. showed a ~85 mV drop in the OCV when RH was switched from 100% to 40%. They proposed that the increase in overpotential is due to decrease in proton activity in the catalyst layer under low RH.

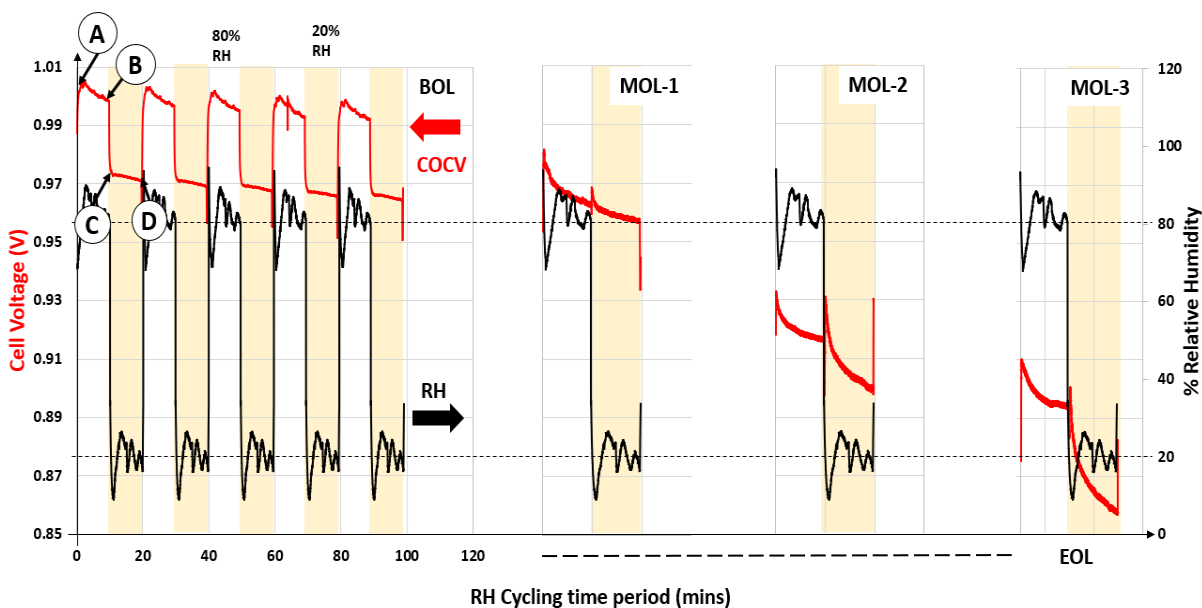


Figure 6-15: RH cycle waveform (black) and OCV response (red) of MEA-2 (baseline) during AST.

When MEA-2 is hydrated to 80% RH (point A in Figure 6-15), it takes up water and swells, resulting in large in-plane compressive stress. During the wet-hold period at 80% RH (A to B), the in-plane compressive stress relaxes with small variation of the water content in the membrane, this leads to fairly minor deviations in OCV during this part of the cycle from BOL to EOL [169]. The switch from 80% to 20% RH (B to C) reduces the water content in the membrane and significantly decreases the in-plane compressive stress.

The switch from 80% to 20% RH (B to C) reduces the water content in the electrode both in catalyst layer and electrolyte membrane. This leads to faster decay of the OCV that appears throughout the AST. During the dry-hold period at 20% RH (C to D), the membrane shrinks and reduces its thickness, enabling more H₂ crossover to occur. The change in OCV correlates with the dynamic changes of the hygro-expansion and elongation of Nafion membrane as a function of RH reported by Lai et. al. [159]. Majsztrik et. al. found that Nafion expands 14% from its original

state when fully hydrated and shrinks up to 11% when dehydrated. When cycled between 80% to 20% RH, the elastic deformation of membrane is expected to change by 6.5% [169].

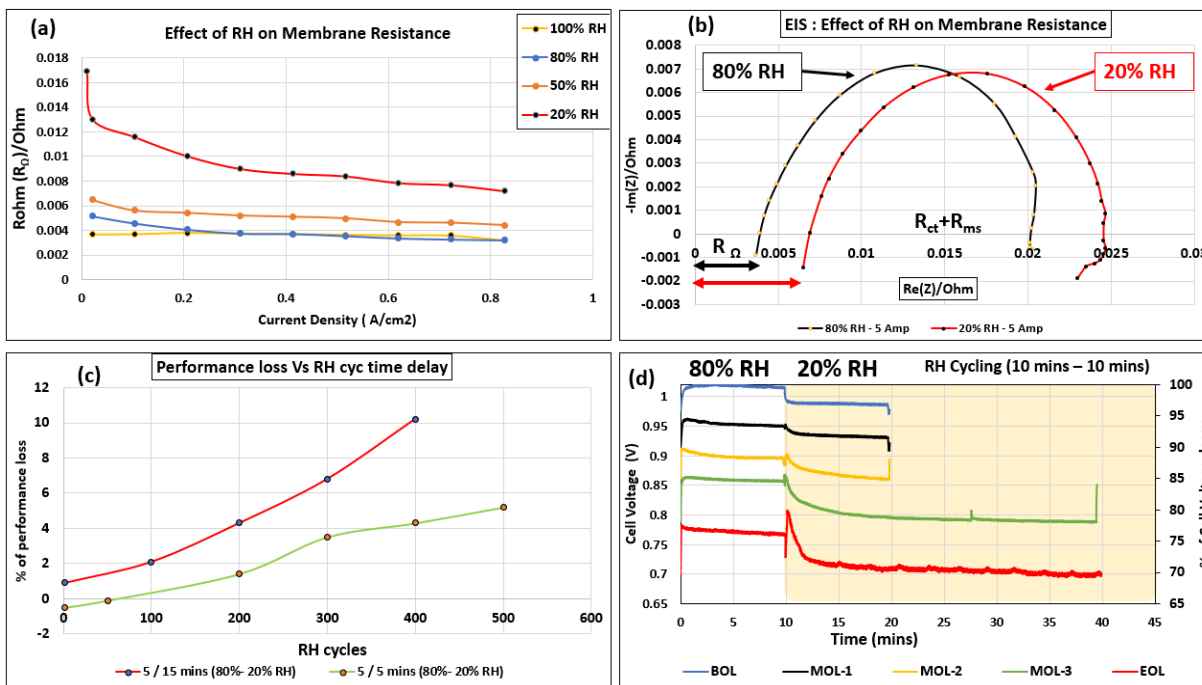


Figure 6-16: Comparison of (a) membrane resistance R_{Ω} obtained from EIS; (b) EIS spectra obtained at 80% and 20% RH; (c) performance loss with respect to RH time delay and; (d) comparison of COCV curves from BOL to EOL, showing the effect of extended dry operation on steady decrease in OCV.

The sensitivity of the membrane to different RH levels has also been investigated. Figure 6-16a shows a comparison of R_{Ω} obtained by EIS on MEA-2- BOL at various current densities at RH levels of 100, 80, 50 and 20%. The membrane resistance increases from 0.0037Ω to 0.0169Ω when the RH decreases from 100% to 20%. The gradual increase in R_{Ω} is due to an increase in ionic resistance caused by dehydration of the membrane. A comparison of the EIS spectra obtained at 80% and 20% RH is shown in Figure 6-16b, revealing an increase in the membrane resistance by 4.4% as RH is reduced due to lower water content in the membrane and less contact between ionomer and carbon particles in the catalyst layer. The optimum transition cycling time (i.e., time period for the RH to change from dry to wet) is not clearly discussed in the DOE test protocol as it depends on the particular membrane and stack operations. Therefore, we study the effects of the transition cycling time on cell performance by varying the duration of the dry portion of the RH cycles. The results showed that an increase in the transition time from 5 min to 15 min for a wet period of 5 min reduces the 12.5% of OCV performance. As the dry operating period is extended,

the OCV loss of the cell significantly increases. Figure 6-16d shows a comparison of the OCV as a function of RH cycling (80% RH and 20% RH) with extended dry period. It is clearly seen from green and red curves, OCV declines steadily with increasing dry operating time. The results of defected and non-defected MEAs operated under COCV-AST are listed in below Table 6-7.

Table 6-7: Description of overall test analysis and samples used for COCV test.

Sample	No. of CL defects and % of defect	RH cycle (cathode)	OCV (V)	No. of. hours operated (hr)	Interrupted hours (hr) – (stopped for electrochemical analysis)	OCV degradation rate (mV h ⁻¹)
MEA – 2	No defects (baseline)	80% - 20%	0.95	150	0, 26, 44, 64, 80, 110,130, 150	1.26
MEA – 6	1 – 70%	100% - 50% 80% - 20%	0.95	54	0, 16, 32, 43, 54	4.21
MEA – 7	2 – 28%	80% - 20%	1.05	84	0, 22, 36, 54, 83	2.26
MEA – 8	1 – ND	80% - 20%	0.95	110	0, 50, 100, 110	1.61

Note: The location of the defect locations in these MEAs are shown in Appendix section 10.5.

Not surprisingly, MEA-2 (baseline), with no defects in the CCM, exhibits the longest lifetime of 150 hrs, with the lowest OCV degradation rate of 1.26 mV h⁻¹ over 700 RH cycles (Figure 6-17a). MEA-6, with one MCLD exhibits the lowest lifetime of 54 hours, with the highest degradation rate of 4.21 mV h⁻¹ over 162 RH cycles. To study the magnitude of chemical degradation on CCM defects (MCLD), the COCV-AST is modified for MEA-7 and MEA-8, with an extended dry operating period of 5/15 min and 5/25 min wet/dry phase.

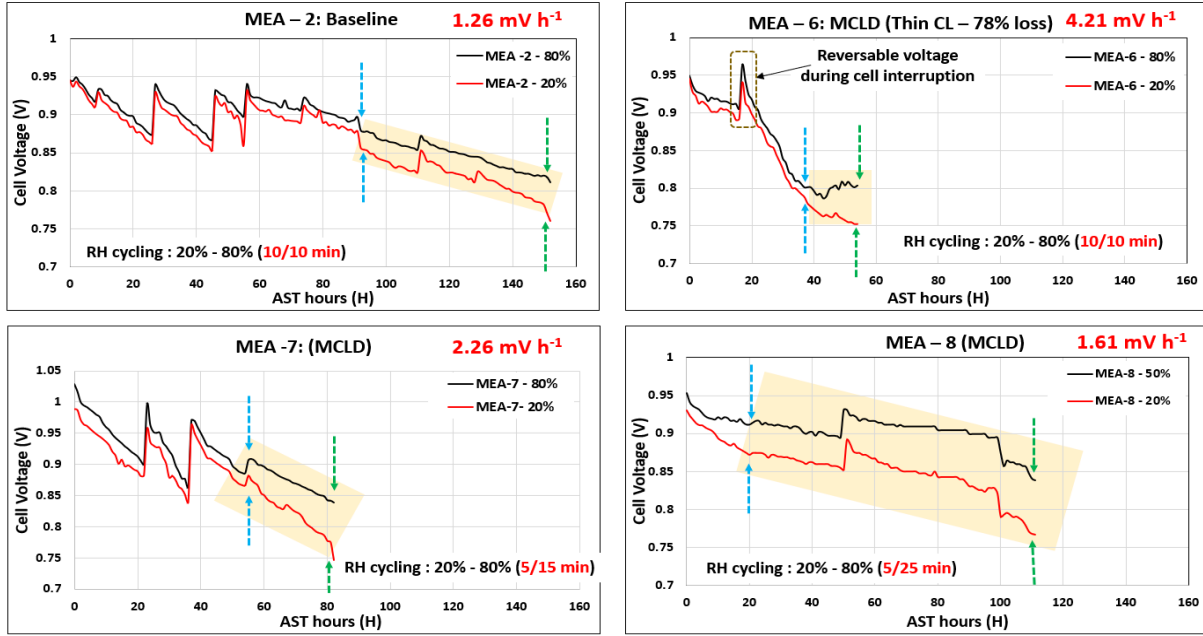


Figure 6-17: OCV decay curves isolated from the COCV curves shown in Figure 6-15 during the course of RH cycling AST; black line represents the voltage response at 80% RH, red line represents the voltage response at 20% RH.

The voltage curves shown in Figure 6-17 are isolated voltage curves shown in Figure 6-15 to show declining voltage behaviour of under 80% RH and 20% RH. The black curves in the plots represent the OCVs recorded during wet conditions, i.e., 80% RH, where the membrane is saturated with water providing good ionic conductivity, with less mechanical and chemical stress. The red curve represents the voltage during dry conditions, i.e., 20% RH, when the membrane shrinks and experiences high in-plane mechanical stress. In each of the cases shown here, the difference in the OCVs measured under wet and dry conditions is relatively small at the outset of the AST, but begins to grow at a later stage. It is likely that the decrease in OCV is caused by degradation of the membrane [83]. The shaded regions in Figure 6-17 highlight when the voltage difference between wet/dry conditions becomes larger. The blue arrows indicate the onset of material degradation leading to early failure of the electrode that is further investigated using FER measurements. The green arrows represent the EOL caused by material degradation that accelerates gas leakage through damaged areas/electrode defects.

6.5.1 Performance of MEA-2

As discussed earlier, MEA-2 is fabricated with a CCM with no defects on the anode or cathode and so is considered as the baseline case for the COCV-AST. The OCV decay of MEA-2

is studied over the following sequence of conditions: (i) cycles operating for 10 min at 80% RH and then 10 min at 20% for the duration of 92 hrs and (ii) cycles operating for 10 min at 80% RH and then an extended dry period of 15 min at 20% RH from 92 to 157 hours. The purpose of extending the dry operation time is to assess the chemical stability of the membrane at low RH. Analysis of the data in Figure 6-17a shows that short cycling (5/5) leads to slower degradation (0.95 mV hr^{-1}), whereas extended cycling (5/15) causes the degradation rate to increase ~ 2.2 -fold to 2.21 mV/hour . The extended dehydration period leads to a loss of ionic conductivity in the membrane, higher ohmic resistance and gradual decrease of OCV. The breakdown of the reversible and irreversible components of the OCV loss of MEA-2 over the course of the COCV-AST is presented in Figure 6-18a. The irreversible component (blue bar) exhibits slow steady growth for the first 92 hrs when the dry period is 5 min. However, after the dry period is extended to 15 mins, the decay rate slightly increases from 110 to 130 hrs but then rises more sharply thereafter between 130 and EOL at 157 hrs. As will be shown from IR imaging, significant degradation of the MEA occurs during this period of last interval when OCV decays most rapidly.

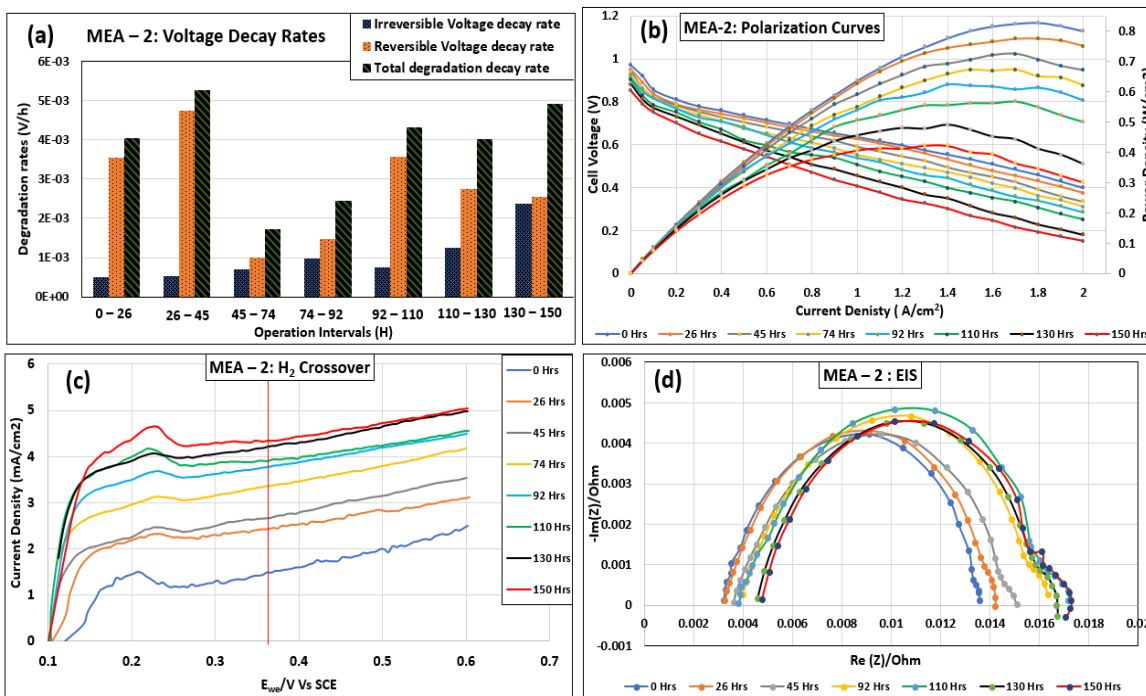


Figure 6-18: MEA-2 performance: (a) breakdown of irreversible (blue), reversible (orange) and total (green) OCV decay rates during the AST; (b) polarization curves, (c) H₂ crossover currents and (d) Nyquist EIS plots (@ 100 mA cm^{-2}) obtained during aging.

Table 6-8: OCV, H₂ crossover current density, HFR and LFR of MEA-2 during course of AST.

Age (hrs)	No. of RH cycles (80% - 20%)	OCV (V)	H ₂ crossover (mA cm ⁻²) @ 0.4V	EIS (mΩ)	
				HFR (R _Ω)	LFR (R _{ct} + R _{mt})
0	0	0.97	1.59	3.26	13.58
26	150	0.95	2.54	3.35	14.22
45	275	0.94	2.81	3.68	15.09
74	450	0.92	3.45	-	-
92	550	0.91	3.90	3.99	16.35
110	610	0.89	4.01	3.85	17.18
130	675	0.87	4.29	4.56	16.74
150	725	0.82	4.59	4.78	17.45

Figure 6-18b presents the polarization curves recorded at 0, 26, 45, 74, 92, 110, 130 and 150 hours during the COCV-AST and Table 6-8 summarizes the parameters obtained from the electrochemical characterization. From 0 to 150 hours of AST, the OCV decreases by 14.3% from 0.975 V to 0.835 V. This effect is presumably due to an increase in gas crossover through the pinhole defects shown in the IR images in Figures 6-19a-c. Interestingly, examination of the corresponding H₂ crossover currents (measured at 0.4 V) over the course of the AST in Figure 6-18c shows no apparent correlation with the change in OCV and the IR images. On the other hand, the cell voltage at a current density of 2 A cm⁻² decreases significantly by 62.5% from 0.4 V to 0.15 V between BOL and EOL. The larger performance loss at high current densities (i.e., mass transfer region) is expected due to structural damages of the catalyst layer and electrolyte membrane (i.e., catalyst layer cracks, delamination and pinholes). Figure 6-18c shows the Nyquist plots of MEA-2 obtained during the ASTs. The increase in diameter of the semicircle in Figure 6-18c indicates the growth of charge transfer resistance as a result of catalyst layer damage or catalyst degradation.

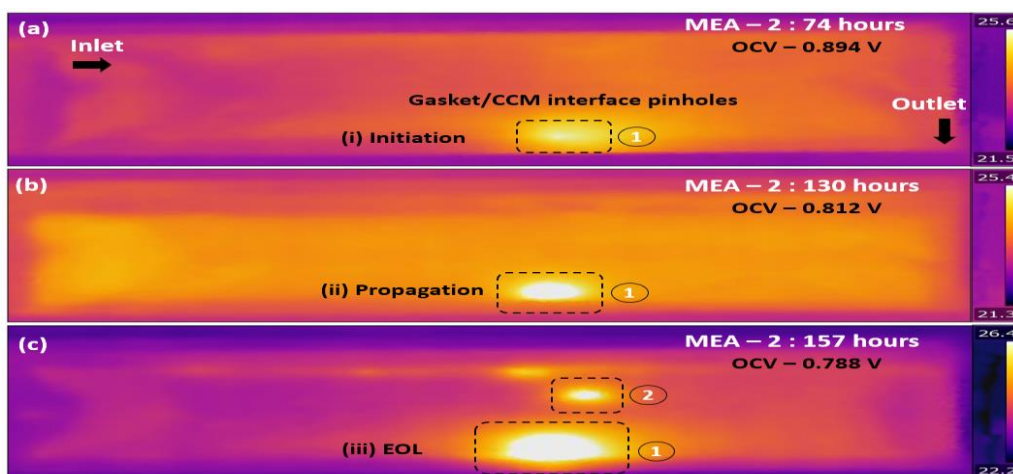


Figure 6-19: MEA-2 IR thermographs captured at (a) 74, (b) 130 and (c)157 hrs of AST.

The IR thermographs in Figure 6-19 indicate that hydration and dehydration during RH cycling at a high temperature initiates mechanical membrane failure particularly near the gasket/CCM interface (region-1). With the increase in dry time at 92 hours, the defect in region-1 continues to grow. By the time the AST reaches EOL, a second pinhole in region-2 has appeared at the center of the MEA and the defect in region-1 has grown significantly (Figure 6-19c). Taken together, these results suggest that the life span of MEA is greatly influenced by the length of time that the membrane is in a dehydrated state.

6.5.2 Performance of MEA-6

As noted previously, MEA-6 is examined to investigate the impact of RH cycling when an MCLD catalyst layer defect is initially present. The MEA-6 is fabricated using the CCM-1, the overview of stitched microscopic image is shown in Figure 5-4a. First, this particular defected CCM was initially operated at low temperature 60°C in a custom-designed test cell, to study the morphological changes of MCLD and corresponding catalyst layer defects in the CCM at regular intervals 10hours, 50 hours and 100 hours. This provides valuable insight information of degradation of catalyst layer defects and root cause for the evolution of defect over its aging period. After 100 hours of OCV operation, the CCM is assembled into an MEA and then subjected to the COCV-AST. Considering the structural damages and safe operation of the aged CCM, RH cycles consisting of 100% RH for 10 min followed by 50% RH for another 10 min are applied over a duration of 16 hrs. No significant changes in OCV are observed during these 100%-50% RH cycles (48 total cycles). Consequently, the RH AST used previously for the other MEAs (i.e., 80% - 20%

RH cycles 10min/10min) is then applied to MEA-6 until it reaches EOL. As a result of the change in AST, the irreversible component of the OCV decay rate increases by ~12-fold over the period from 16 to 32 hrs (Figure 6-20a). At the end of 32 hours, the OCV reaches 0.804 V, close to the EOL. The experiment is continued for another 54 hrs (162 RH cycles) until the OCV reaches 0.752 V, with degradation rate of $\sim 4.21 \text{ mV h}^{-1}$. After the EOL, the GDLs were carefully disassembled and CCM was separated for optical analysis (see section 4.3.2) to study the effect of RH cycling on the catalyst layer and MCLD. Microscopic inspection showed that several regions in the anode and cathode catalyst layers developed cracks and delaminated. When the delamination occurs in the anode catalyst layer, it removes all of the catalyst layer to expose the membrane. This is expected since the thickness of the anode catalyst layer is 3x times thinner than the cathode. The delamination mechanism in catalyst layers is discussed in section 5.4.3.3.2. On the other hand, delamination on the cathode side removes 30 – 70% of its initial thickness. The changes of the morphology of the MCLD were also investigated after the RH cycling AST and are discussed later in section 6.5.2.1. It is also observed that the mechanical stress in MEA during RH cycling also causes excess compression under the land area where sections of the MPL are separated from the GDL and remain on the catalyst layer surface. From the entire microscopic observation on CCM, the RH cycling AST cause significant structural damage in catalyst layer through cracks and delamination.

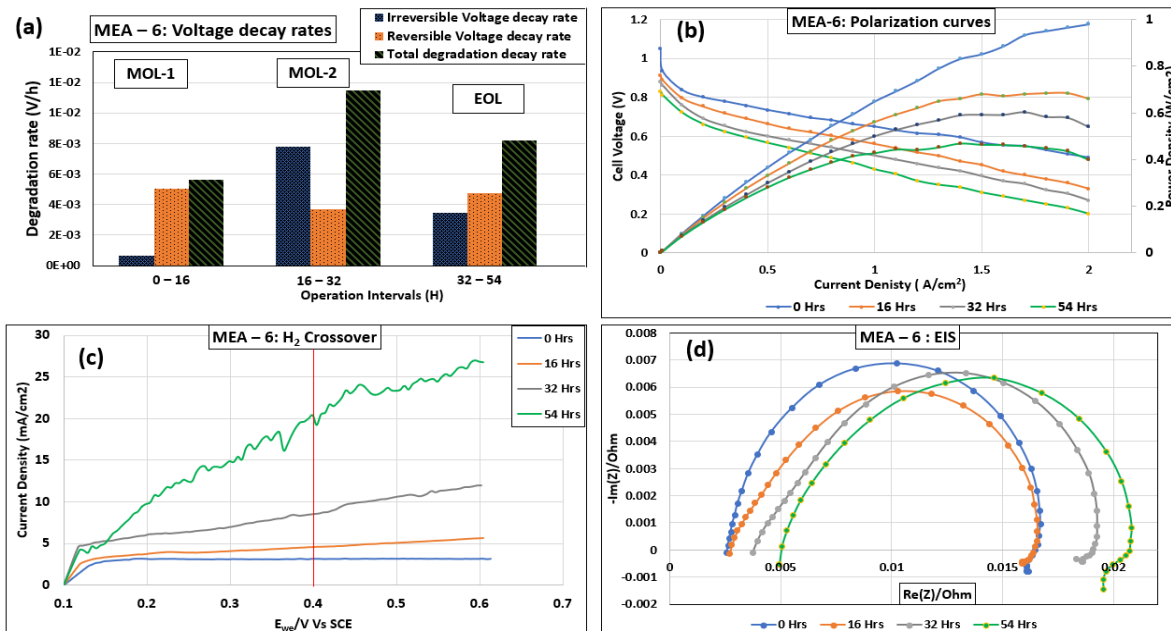


Figure 6-20: MEA-6 performance: (a) breakdown of irreversible (blue), reversible (orange) and total (green) OCV decay rates during the AST; (b) polarization curves, (c) H₂ crossover currents and (d) Nyquist EIS plots (@ 100 mA cm⁻²) obtained during aging.

Figure 6-20b shows the changes in the polarization curves measured at $t = 0, 16, 32$ and 54 hrs during the COCV-AST. A steady decrease is observed in the polarization performance over time. However, the drop in cell voltage in the activation region ($0.01 - 0.25$ A cm⁻²) is smaller than elsewhere in the curve. This indicates that the active catalyst in the catalyst layer is not as severely affected by the AST as other components. A larger performance loss is observed in both the ohmic region (0.25 A cm⁻² – 1.5 A cm⁻²) (i.e., 39.9% drop of the cell voltage from 0.614 V to 0.369 V at a current density of 1.2 A cm⁻²) and mass-transfer region (1.5 A cm⁻² – 2 A cm⁻²) (i.e., 50% drop of the cell voltage from 0.401 V to 0.201 V at a current density of 2 A cm⁻²). It is expected that these losses are most likely due to structural and interfacial changes in the catalyst layer and electrolyte membrane due to cracks and delamination during RH cycling. The combined chemical and mechanical stress during RH cycling leads to propagation of catalyst layer cracks and defected areas (e.g., MCLD) and delamination of the catalyst layer. It is expected that catalyst layer cracks and propagation of MCLD increase the ohmic losses in MEAs.

The H₂ crossover currents in Figure 6-20c show good agreement with the trends observed for the irreversible OCV decay and IR thermographs Figure 6-21. From 0 to 16 hrs during the AST, the

crossover current density remains below 5 mA cm^{-2} . After 32 hours, the crossover current density increases to 8.58 mA cm^{-2} at 0.4V (red line in image 6-18) and the irreversible OCV decay rate increases ~ 7 -fold. At EOL, the crossover current has increased to 20.52 mA cm^{-2} at EOL. This is also confirmed by IR thermography results as shown in Figure 6-21. Figure 6-21(a) shows the MEA-6 before RH cycling with a small hotspot located at the MCLD. After 96 RH cycles (32 hours), a second hotspot (region 2) is developed across the sealant interface area (Figure 6-21b). After 162 RH cycles (54 hours), the hotspot in region 2 (Figure 6-21c) has grown significantly at the same time that the OCV is measured to be 0.775V and EOL is reached. This is also confirmed from EIS results, where the membrane resistance increases from $2.69 \text{ m}\Omega$ to $5.05 \text{ m}\Omega$ from BOL to EOL. The summary of OCV losses, H_2 crossover and EIS results is presented in Table 6-9.

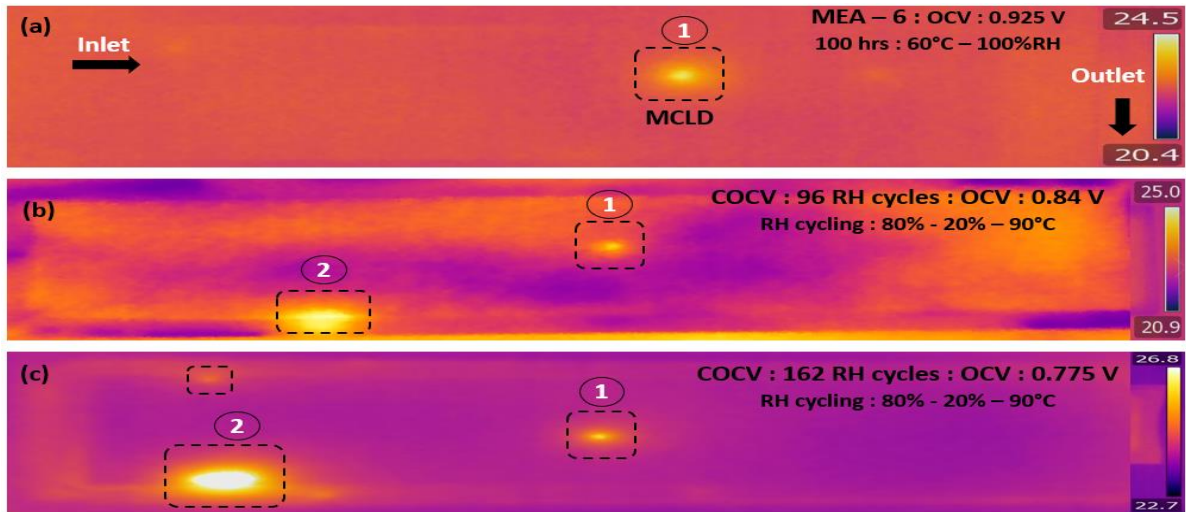


Figure 6-21: MEA-6 IR investigation captured at (a) BOL (b) MOL-1 and (c) EOL. IR thermographs of MEA-6 captured at (a) prior to COCV test, (b) after 96 RH cycles (32 hrs) and (c) after 162 RH cycles (54 hrs of AST).

Table 6-9: OCV, H_2 crossover current density, HFR and LFR of MEA-6 during course of AST.

Age (hrs)	No. of RH cycles (80% - 20%)	OCV (V)	H_2 crossover (mA cm^{-2}) @ 0.4V	EIS ($\text{m}\Omega$)	
				HFR (R_Ω)	LFR ($R_{ct} + R_{mt}$)
0	0	0.10	3.17	2.69	16.37
16	48	0.91	4.58	2.74	16.45
32	96	0.88	8.58	3.75	19.18
54	162	0.83	20.52	5.05	20.72

6.5.3 Effect of RH cycling on catalyst layer defects

Figures 6-22a-c show optical images of the MCLD in the CCM used in MEA-6. Figure 6-22a shows the catalyst layer immediately after fabrication of the CCM, while Figure 6-22b is captured after 100 hours of the OCV operated at 100% RH in a custom test cell operated at 60°C (section 5.4.3.1). The same MCLD after 162 RH cycles at COCV at 90°C is shown in Figure 6-22c. The microscopic images (Figure 6-22C) show that the area inside the MCLD has developed severe cracks in comparison to that observed prior to RH cycling (Figure 6-22b). This shows evidence that catalyst layer defects have grown much faster during RH cycling than during the AST at constant RH. It is believed that during RH cycling, the repetitive switching from wetter gases to drier gases increases the mechanical stress in the membrane that further accelerates the degradation of the of the MCLD. These defected regions are expected to be the least resistant to humidity changes and therefore more prone to damage during fuel cell operation.

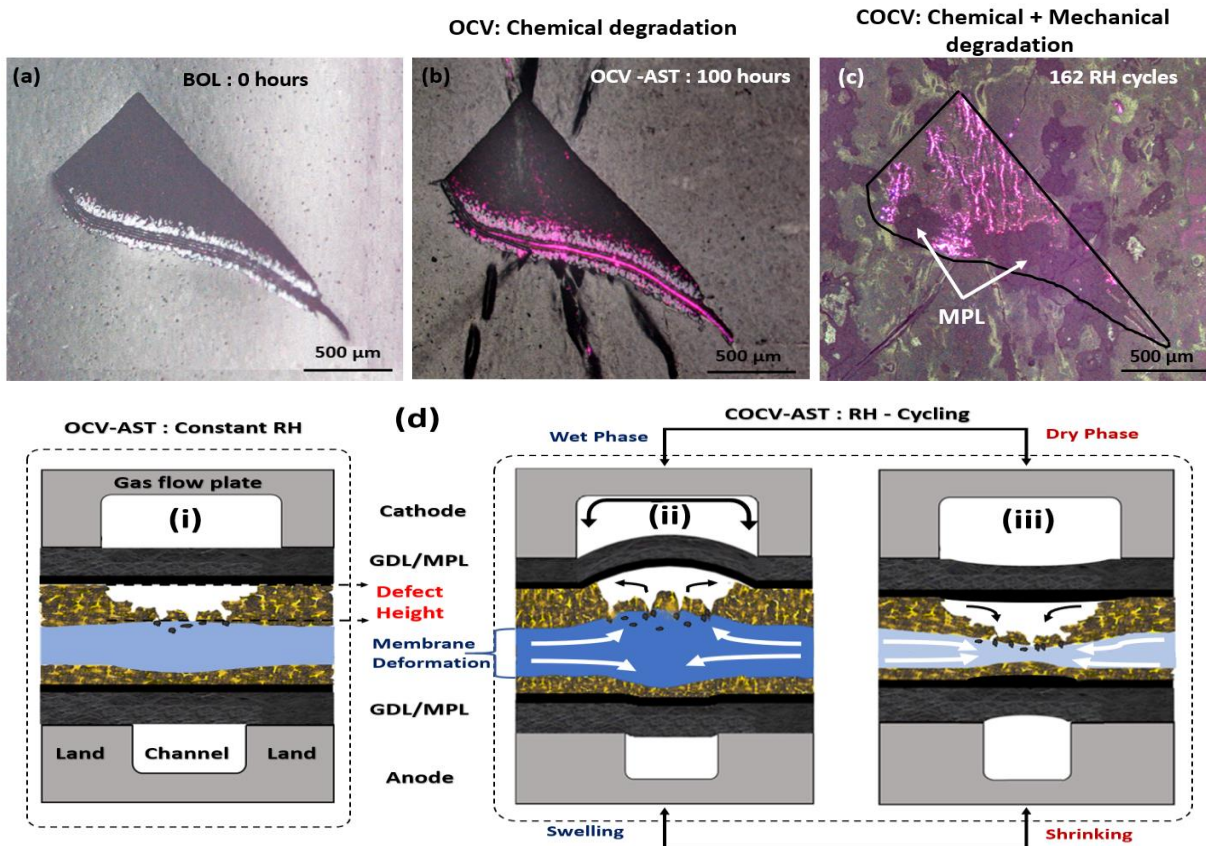


Figure 6-22: MEA-6 - Optical images of MCLD at (a) BOL, (b) after 100 hrs of OCV at 60°C and 100%RH, (c) after 54 hrs of COCV at 90°C (162 RH cycles) (d) schematic of MCLD during OCV and COCV ASTs.

By observing the Figure 6-22c the MCLD has undergone several structural changes (i.e., CL cracks and catalyst erosion) inside the defect during RH cycling AST. The defect will be subjected to high levels of mechanical stress since the membrane tensile properties change depending on the wet/dry conditions [159]. However, after several RH AST cycles, the ability of the membrane to stretch is reduced and so fractures appear on the defect surface that appears as pink area inside the defect. Figure 6-22d schematically depicts membrane expansion expected during both the OCV AST at constant RH and the OCV AST when RH is cycled. During operation at constant RH and high temperature, the mechanical stress in the membrane is relatively small and it is the electrode that is severely affected by chemical degradation (Figure 6-22d(i)). The effect of chemical degradation on MCLD defects is studied in section 5.4.3.1. During wet/dry cycling, the repetitive expansion and contraction of the membrane induces both chemical and mechanical stress that results in faster degradation of catalyst layer defects through cracks as well as catalyst erosion (Figure 6-22d(ii) and (iii)). The defect is expected to propagate more under RH cycling than at constant RH. Image analysis of the MCLD before and after RH cycling in Figures 6-22b and c reveals that the total area of the defect has stretched to a maximum of 1.25 times its original area. This shows that catalyst layer defects are observed to have immense structural changes due to plastic deformation of the membrane. In addition to the areal growth of the MCLD, the catalyst inside the MCLD is eroded during the RH cycling, causing a 33.2% increase in the pink area before and after RH cycling. From overall observation, we conclude that the combined mode of chemical and mechanical stress during RH cycling accelerates the removal of unsupported catalyst particles in weak catalyst areas, and develops deep catalyst layer cracks, delamination and pinholes. No significant effect on FER is observed by comparing the FER results for MEA-6 and MEA-8; after 54 hours of AST, MEA-6 showed $6.38 \mu\text{mol}/\text{cm}^2$ whereas MEA-8 showed $7.26 \mu\text{mol}/\text{cm}^2$. Therefore, defects in CCMs are very susceptible to propagate during harsh cell operating conditions.

6.5.4 Performance of MEA-7 and MEA-8

The experiments on MEA-7 and MEA-8 are the extended 2nd case study on the effect of RH cycling on pre-existing MCLDs, where both the CCMs used in MEA-7 and MEA-8 consist of MCLD in the cathode catalyst layer developed during the decal transfer process (as discussed in 2.4.1). The graphical overlay of the defect and its location on MEA-7 is shown in Figure 6-23a. The MCLD is first examined with an optical microscope (Figure 6-23b) before fabrication of the

MEA. Figure 6-23c shows the magnified view of an edge of this catalyst layer defect (MCLD) at 50x magnification, while the corresponding Z-profile is shown in Figure 6-23d. The Z-profile shows that the edge of the MCLD has a depth of $\sim 6 \mu\text{m}$. Interestingly, no transmitted light is observed inside the defect in the optical image of Figure 6-23b or c. This indicates that the catalyst inside MCLD is packed, so there has been no extreme thinning inside the MCLD where no transmitted light (pink area) is appeared in the defect. Therefore, it is expected that $\sim 75\%$ ($\sim 6 \mu\text{m}$) of the catalyst layer has been lost from this portion of the CCM during decal transfer process and that $\sim 25\%$ ($\sim 2 \mu\text{m}$) still remains everywhere within the defect. The dry period during the RH cycling AST for MEA-7 and MEA-8 has been increased to study the effect of chemical stress in particular on cell performance. The dry time during the RH cycles are raised to 15 min for MEA-7 and to 25 mins for MEA-8. The wet time is 5 min in all cases. Thus, MEA-7 experiences wet conditions during 25% of the AST and dry conditions during 75%, while MEA-8 is wet during only 17% of the AST and dry for the remaining 83%.

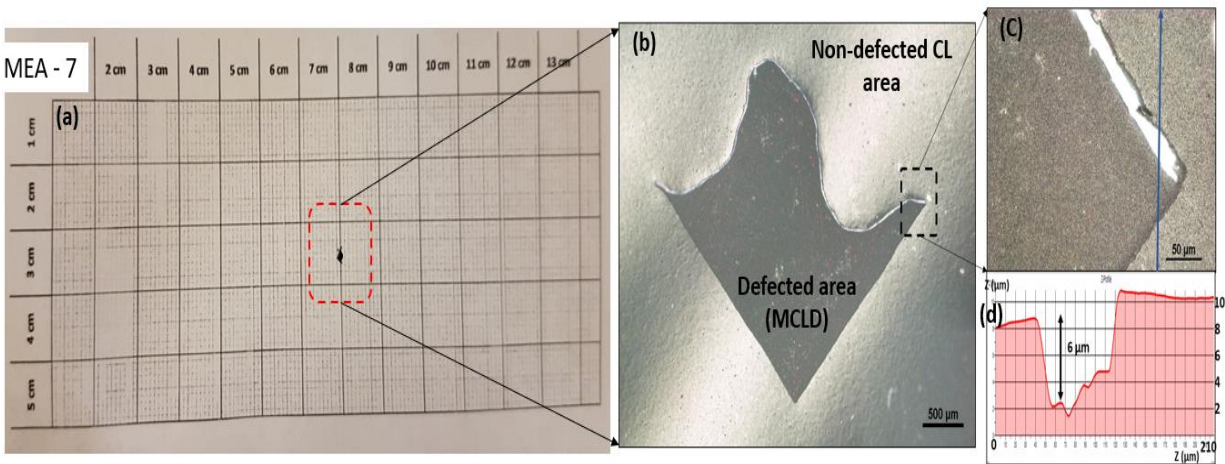


Figure 6-23: MEA-7 (a) Graphical view of catalyst layer defect(MCLD) located in CCL in CCM, (b) optical image of MCLD, (c) edge of MCLD (dashed region in (b)) magnified at 50X resolution and (d) Z-profile along the blue arrow in (c) showing the depth of the defect.

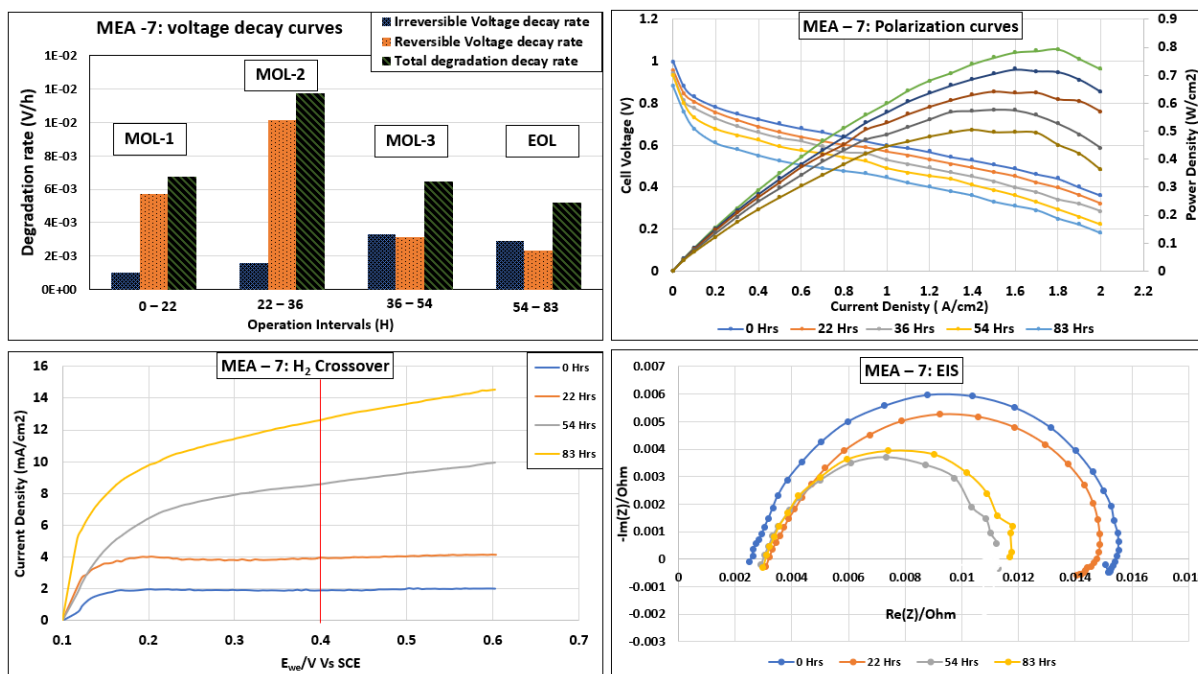


Figure 6-24: MEA-7 performance: (a) breakdown of irreversible (blue), reversible (orange) and total (green) OCV decay rates during the AST; (b) polarization curves, (c) H₂ crossover currents and (d) Nyquist EIS plots (@ 100 mA cm⁻²) obtained during aging.

Table 6-10: OCV, H₂ crossover current density, HFR and LFR of MEA-7 during course of AST.

Age (hrs)	No. of RH cycles (80% - 20%)	OCV (V)	H ₂ crossover (mA cm ⁻²) @ 0.4V	EIS (mΩ)	
				HFR (R _Ω)	LFR (R _{ct} + R _{mt})
0	0	1.01	1.92	2.49	15.40
22	66	0.96	3.97	3.09	14.75
36	108	0.94	-	-	-
54	162	0.93	8.62	2.97	11.67
83	208	0.88	12.58	2.85	10.95

MEA-7 is operated for 208 RH cycles until EOL and degrades at an average rate of 2.26 mV h⁻¹. Figure 6-24 shows the electrochemical results obtained for MEA-7 and Table 6-10 summarises the estimates for OCV, H₂ crossover current and EIS equivalent circuit parameters. Analysis of the OCV decay (Figure 6-24a) reveals that the irreversible component is quite low and stable during MOL-1 and MOL-2 (0 to 36 hrs), but gradually increases ~2-fold by MOL-3 and EOL (36 to 83 hrs). From the polarization curves in Figure 6-24b, the cell voltage decreases by ~ 22.5% in the ohmic region and ~48% in the mass-transfer region from BOL to EOL. The extended dry cycling

should reduce the ductility of the membrane and catalyst layer interfaces. Although SEM examination of MEA-7 and MEA-8 was not conducted, results for MEA-2 operated with 10 min (wet)/10min (dry) cycles show that membrane thinning occurs unevenly so that its thickness varied from 7.28 μm to 14.85 μm . These SEM results are discussed in section 6.7. Mukandan et.al [109] reported similar effect in which membrane degradation is faster when operating under dry conditions over a long period. The RH cycles in this earlier study were varied only from 30sec/45sec and 2min/2min which is much shorter than those used in our ASTs. As discussed in section 6.6, the FER values for MEA-8 (5/25min-cyc) are slightly higher than that of MEA-2(10/10min-cyc). Figure 6-24c shows the growth of the H_2 crossover current as a result of gas leak in the electrode during RH cycling.

The impedance curves in Figure 6-24d show the opposite trend when compared to previous results. EIS results show a small increase in the HFR from 2.49 $\text{m}\Omega$ to 2.86 $\text{m}\Omega$ presumably caused by growth of catalyst layer defects and membrane resistance. While the trend of EIS spectra decreases at 54 and 83 hours where the mass transfer resistance decreases from 15.4 $\text{m}\Omega$ at BOL to 10.95 $\text{m}\Omega$ at EOL. It is expected the chemical and mechanical stress during RH cycling might decrease the stability of catalyst layer and membrane via degradation process, especially that the extend dry phase during RH cycling (5/15 min each cycle) might chemically accelerate the membrane degradation. The combined degradation in MEA can lead to develop cracks and pinholes that could increase the mass transfer losses at 54 and 83 hours. Reshetenko et.al.[101] reported that catalyst layer defects are more prone to chemical degradation and develop in to pinholes. They showed the membrane propagation of catalyst layer defects leads to higher mass transfer resistance.

MEA-8 is tested for 264 RH cycles until EOL and exhibits an average degradation rate of 2.19 mV h^{-1} . As shown in Figure 6-26a, an MCLD is observed in MEA-8 at BOL and IR investigation conformed no hotspot at BOL. The irreversible, reversible and total components of OCV degradation in MEA-8 gradually increase during the course of the AST (Figure 6-24a). From the FER analysis as discussed in section 6.6, showed the MEA-8 has higher FER in compared to MEA-2, MEA-6 and MEA-7 operated in COCV-AST. This trend represents the large fraction of ionomer is degraded in MEA-8 that presumable due to extended dry period during RH cycling (5/25 min each cycle). This result supports the expectation that the extended dry period of 25

min during the AST leads to more chemical degradation of the membrane. The IR images shown in Figures 6-26b-d strongly confirm the propagation of defected areas in MEA-8 during RH cycling AST and the development of hotspot defects after 50, 100 and 110 hours. It is important to note that no hotspot is observed in the MCLD at BOL. As shown in Figure 6-26b, a hot-spot develops at the MCLD (region-1) by 50 hrs of the AST. As the AST continues, It is expected that mechanical stability of the membrane decreases due to continuous wet/dry cycling and therefore chemical degradation accelerated the weak zones in the membrane to develop pinholes. Figures 6-26c and 6-26d clearly show that degradation is also initiated near the gasket/CCM interface through chemical and mechanical stress. Although MEA-7 and MEA-8 are manufactured with same type and design the electrode durability also depends on ASTs. In this case, when the dry cycling time is increased from 50% to 83% of the total AST, the overall degradation rate of MEA-8 (2.19 mV h^{-1}) increases ~ 1.7 -fold relative to MEA-2 (1.36 mV h^{-1}). Comparison of the polarization curves in Figures 6-24b and 6-25b shows that the increase in % dry time in MEA-8 does not significantly reduce its performance compared to that of MEA-7. A very large growth of the H_2 crossover current density from 11.7 mA cm^{-2} to 30.0 mA cm^{-2} is observed between 50 and 110 AST hours (Figure 6-25c), as would be expected from the development of a number of hotspots revealed in the IR thermographs. By comparing the IR results in Figure 6-26 and EIS analysis in Figure 6-25c the formation of hotspot in the MEA over aging period matches the trend of EIS spectra where the growth of pinhole in membrane corresponds to increase in membrane resistance at HFR. The noise observed in yellow curve (110 hours) is presumable due to gas crossover through the defects causing mass transfer losses in the electrode.

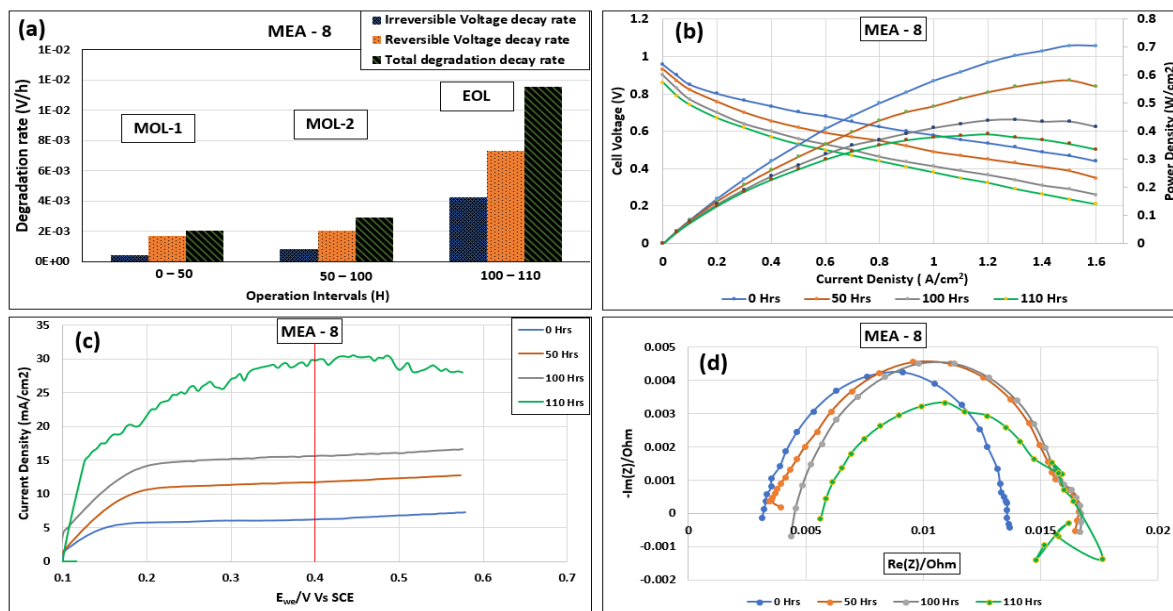


Figure 6-25: MEA-8 performance: (a) breakdown of irreversible (blue), reversible (orange) and total (green) OCV decay rates during the AST; (b) polarization curves, (c) H₂ crossover currents and (d) Nyquist EIS plots (@ 100 mA cm⁻²) obtained during aging.

Table 6-11: OCV, H₂ crossover current density, HFR and LFR of MEA-8 during course of AST.

Age (hrs)	No. of RH cycles (80% - 20%)	OCV (V)	H ₂ crossover (mAcm ⁻²) @ 0.4V	EIS (mΩ)	
				HFR (R _Ω)	LFR (R _{ct} + R _{mt})
0	0	0.96	6.183	3.11	13.56
50	120	0.93	11.74	3.52	17.62
100	240	0.90	15.62	4.58	17.75
110	264	0.86	29.98	5.62	17.90

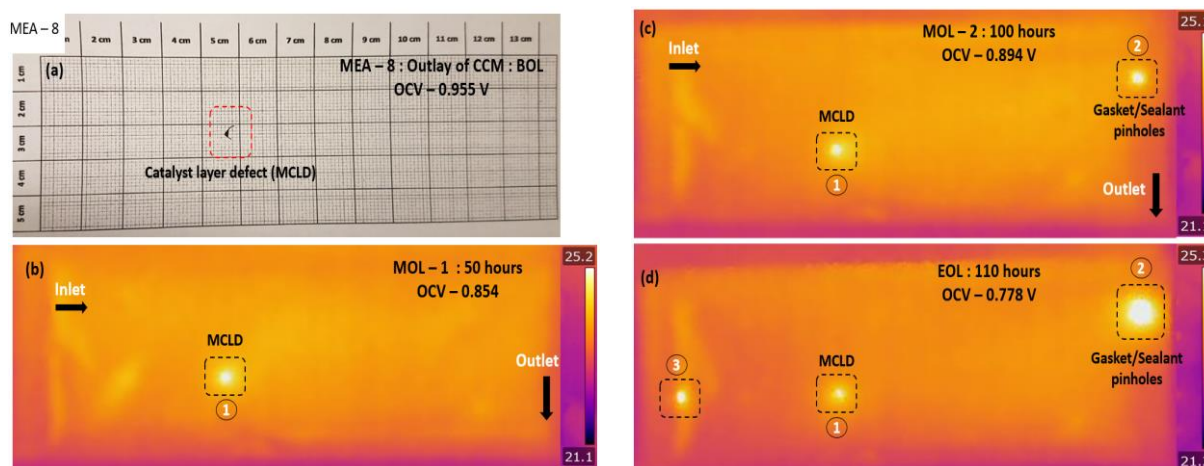


Figure 6-26: MEA-8 (a) Optical image of catalyst layer defect; IR images of MEA-8 at (a) MOL-1 – 50 hours, (b) MOL-2 – 100 hours and (c) EOL- 110 hours.

6.6 Effect of constant and cyclic RH on membrane degradation observed by fluorine emission analysis

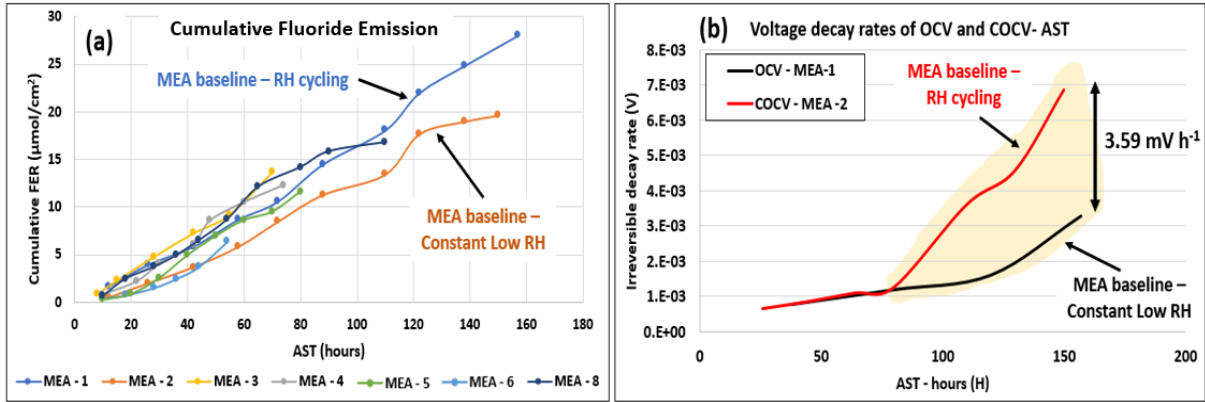


Figure 6-27: (a) Cumulative fluoride emission release for MEA operated under constant low RH and cyclic RH (b) Comparison of irreversible voltage decay rate of MEA-1 and MEA-2 operated under OCV and COCV-AST.

Fluoride ion emission is one of the important indicators of chemical degradation of membrane that was periodically monitored during MEA aging (OCV and COCV experiments). Figure 6-27a shows the cumulative fluoride ion release for MEAs operated during the AST. The emission rate of a membrane can be evaluated by comparing the slopes of the graphs. From the above FER results, it is observed that MEA-2 (baseline) operated under cyclic RH exhibits a somewhat higher emission rate than MEA-1 (baseline) operated at constant low RH. An increase in FER signifies faster chemical degradation of the ionomer in the MEA and thinning of the membrane. As membrane becomes thinner, more gas crosses over from one side to the other and reduces the cell potentials. The increase in the FER is found to be approximately proportional to the voltage degradation rates as shown in Figure 6-27b. Figure 6-27b shows the voltage decay rates of MEA-1 (OCV) and MEA-2 (COCV) operated over a duration of 150 hours of AST. Both MEA-1 and MEA-2 experience similar irreversible voltage decay over the first 80 hours of the AST. However, after this point, the decay rate of MEA-2 increases significantly between 80 and 150 hours. This indicates the major degradation in MEA-2 occurs after 80 hours of COCV-AST. Taken together, the results in Figure 6-19 indicate that more chemical degradation and irreversible damage to the MEA occur during operation with RH cycling than at constant low RH.

6.7 Effect of constant and cyclic RH on CCM observed by SEM

Fracture sites in the degraded membrane are indicative of most damage to the MEA. Figure 6-28 shows SEM images of damaged sites in CCM. Figure 6-28(a) shows a cross-sectional view of a CCM at BOL. Figure 6-28(b) shows the cross-sectional view of CCM (same type as in Figure 6-20a) used in MEA-5 operated over a duration of 110 hours at constant low RH. In this case, a CCL crack is shown in white dotted circle. By observing the cathode ionomer layer inside the white dotted circle, a micro-hole is developed in the cathode ionomer layer that might originate from the CCL crack. The cathode ionomer layer in the BOL sample has a thickness of 5 μm , whereas the cathode ionomer layer in the EOL sample is 3.59 μm . Figure 6-28 (c) and (d) show cross-sectional views of the CCM used in MEA-2 operated over a duration of 157 hours under cyclic RH (20% - 80%). The major damage in the membrane is observed between the reinforced ePTFE layer and ionomer layers of anode and cathode. The thickness of the reinforced layer changes significantly depending on location, where its average thickness varies from 1.42 μm to 14.83 μm compared with a measured thickness of 2.5 μm at BOL. It is believed that this dramatic change is caused by mechanical stress from membrane swelling and shrinkage during RH cycling. It is also observed that few regions in the catalyst layers are delaminated from the membrane. The rapid changes in membrane thickness could lead to greater membrane ohmic resistance and decrease the durability of the membrane and overall performance of the cell.

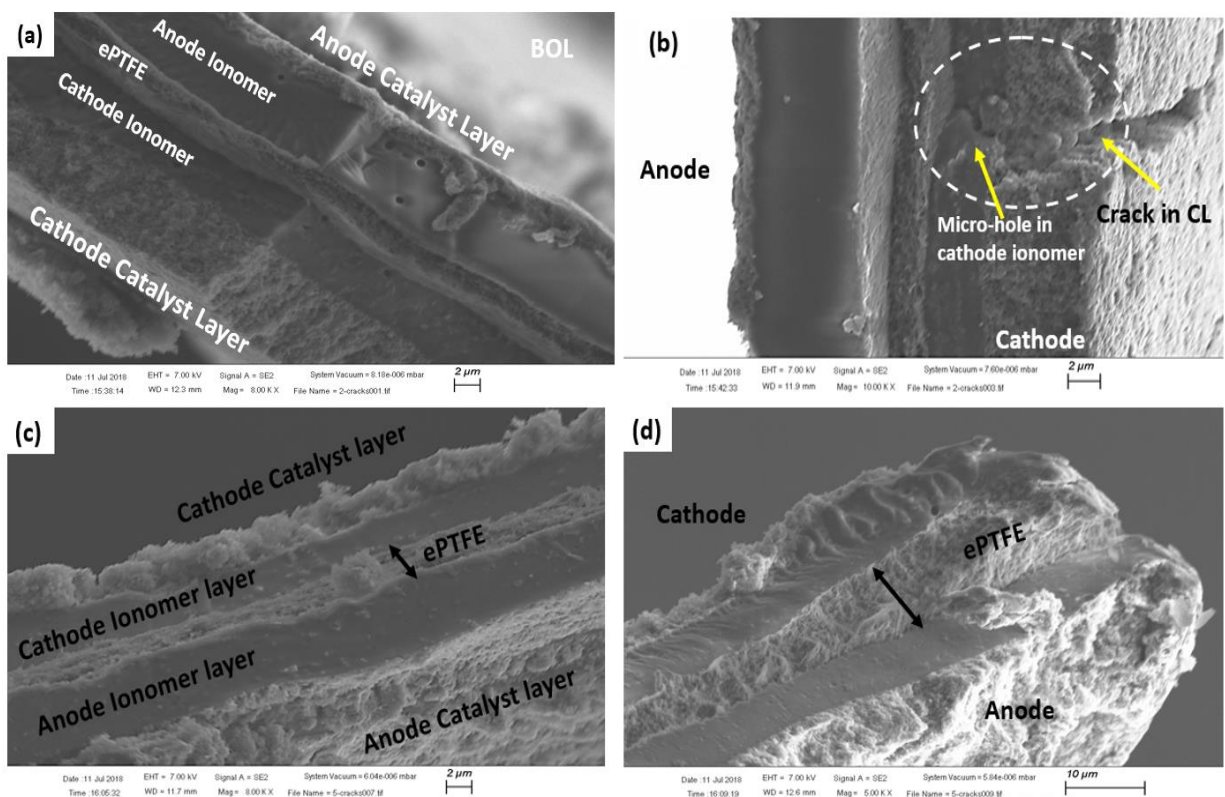


Figure 6-28: Cross sectional view of (a) CCM at BOL; (b) CCM (MEA-4) operated under constant low RH for 75 hours of OCV-AST (white dotted circle indicates micro-hole in cathode ionomer developed at end of catalyst layer crack); CCM (MEA-2) operated at cyclic RH (80% -20%) for 150 hours of COCV-AST shown at two magnifications (c) and (d).

6.8 Conclusions

The present chapter focused on the durability of MEAs with and without defects (i.e., sealant interface defects, MCLD and scratches/deep cuts) present at BOL and the effect of chemical and mechanical stresses on overall MEA degradation and electrode life-time.

1. AST protocol for aging MEAs

The AST protocols have been implemented to accelerate the evolution of electrode defects using steady-state OCV at low RH and RH cycling to introduce combined chemical and mechanical stresses. The ASTs significantly degrades the local defects in the MEA and reduces the cell performance. RH cycling was found to have a higher degradation effect than constant low RH where the overall COCV decay rate (1.24 mVh^{-1}) is higher than OCV at low RH (0.910 mVh^{-1}) over a duration of 150 AST hours. During the initial half of the RH cycling AST, OCV of MEA-

2 showed a mild decay rate of 0.74 mVh^{-1} indicating the early stage of defect degradation, followed by an increased decay rate of 2.4 mVh^{-1} in the later stage of defect degradation stage leading to electrode failure.

2. MEA defect propagation

The steady-state low RH AST promotes significant degradation of the membrane and catalyst layer defects, developing pinholes across areas where the membrane experiences the highest mechanical stress. The IR results confirm that the sealant interface defects showed faster damage in the MEA due to highest mechanical stress across the sealant/gasket/CCM interface. Scratch/deep cuts and empty CL with bare exposed membrane showed pinhole formation in the MEA. On the other hand, the RH cycling AST showed two major effects on MEA defects: (i) mechanical stress in the MEA components during wet/dry cycling accelerated structural damage of the thin catalyst layer defect (MCLD) (ii) degradation of ionomer in the COCV is higher than OCV at constant low RH. The extended RH cycling with a longer dry regime gradually reduces the strength of the electrolyte membrane and develops membrane pinhole during AST. The cell performance as observed from OCV curves decreases ~ 1.5 times while subject to RH cycling compared to constant low RH-AST, confirming that combined chemical and mechanical stresses accelerated the catalyst layer defects and decrease the life-time of membrane. The AST protocol implemented in this study allows for screening of MEA durability of electrodes for heavy duty fuel cell stack applications.

7 Defect Analysis in Gas Diffusion Layers (GDL): Quality Control Approach

7.1 Introduction

The gas diffusion layer (GDL) is an important component of the MEA since it is critical to gas distribution, water management, electron transport and heat distribution during cell operation. GDLs represents ~ 5-10% of the fuel cell stack cost of PEMFC stacks [34]. Since the GDL acts as an interface between the bipolar gas flow fields and catalyst layers of CCM, it must provide good electric contact and impart strong mechanical stability to the MEA. A GDL is specifically designed to have a porous structure that allows uniform distribution of reaction gases to the active sites of the catalyst and removes heat from the electrode [45]. It also plays a crucial role in water management by ensuring sufficient humidification of the membrane, enabling reactants to reach catalyst sites and promoting drainage of liquid water and escape of water vapour from the catalyst layer. This is challenging in fuel cells as flooding by water may occur at high current density and block the active sites of the electrocatalyst.

To minimize water flooding and electrical contact resistance to the active catalyst layer, a thin micro-porous layer (MPL) composed of carbon paste and hydrophobic agent polytetrafluoroethylene (PTFE) is coated on one side of GDLs [46]. The MPL plays a prominent role in PEMFC performance and durability. Carbon paste and PTFE in the MPL improve the mass transport properties for water removal as well as the electric contact between the catalyst layer and GDL. Several studies have investigated the effects of carbon powder type, amount of PTFE loading, thickness (i.e., carbon loading) and pore size distribution of the MPL in order to improve its mechanical and chemical properties [171–175]. The material functionality of MPL is mainly controlled by surface morphology, which is commonly affected by surface defects that directly affect the in-plane and through-plane conductivity of the substrate. The surface morphology of the MPL is smoother than that of the GDL (carbon fiber matrix) due to a finer and more uniform pore size distribution. On the other hand, the surface roughness of the MPL which is higher than that of the catalyst layer predominantly affects the interfacial contact between the MPL and the catalyst layer [42]. Therefore, any surface defects in the MPL can lead to ohmic and mass transfer losses

and reduce cell performance. Studies have shown that the more PTFE that is present in the MPL, the more effective is the water management in the MEA and the better is the polarization performance of the cell. At the same time, excess loading of PTFE in GDL/MPL substrates can lead to a non-uniform distribution and increase the local resistance at the MPL surface. The other common problem is the non-homogeneous dispersion of the carbon slurry paste within the ML during the coating process and to the non-uniform evaporation of solvents in MPL during the sintering process. This uneven drying of the substrate can affect the morphology of the MPL by generating cracks and interlayer voids on the MPL surface.

7.1.1 Fabrication of GDL/MPL substrates

GDLs used in this study have been directly supplied by a manufacturing industry partner as a part of a research collaboration into the study of MPL cracks and the mechanical durability of the MPL surface. The chemical compositions of these GDLs and MPLs which were fabricated by our industrial partners are confidential. We report physical, optical, and electrical properties of the MPL surface in this chapter. A mechanically and chemically durable GDL is developed by immersing the base GDL (porous carbon papers) in a 5 - 7 wt% PTFE solution diluted with water for ~ 2 - 4 min and then drying it at room temperature for 24 hours. The MPL slurry is prepared first by mechanically mixing carbon black (meso/micro porous carbon, Vulcan XC, high surface area carbon), distilled water and isopropyl alcohol (IPA) using a mixing stirrer until they are finely dispersed. Finally, the required concentration of PTFE of ~20- 30 wt.% is added to the MPL slurry paste and stirred for 4 to 5 hours. The MPL slurry can be coated on the GDLs using various coating techniques such as doctor blade, spray coating, compression molding or knife coating methods[176–178]. The freshly coated MPL slurry on GDL substrate is then heated in an oven by ramping the temperature at a rate of 5°C/min from room temperature to 100°C and hold for 1 hours followed by, 240°C for 2 hours and then sintered at 350°C for 2 hours. It is expected that the cracks in the MPL surface develop during the drying process, depending upon the uniformity of coating, viscosity of the slurry, thickness variations in GDL substrate, overlap coating and volume of the MPL slurry. Figure 7-1 shows the step-by-step procedure involved in fabricating the GDL/MPL substrate. Defects such as cracks, inter-layer voids, carbon clusters, dents, inter-layer cracks and delamination of the MPL can arise from many sources during the fabrication[176,177]. The red dotted area represents the possible causes of MPL cracks formed during the coating and sintering process. Surface cracking on the MPL is a major concern for GDL manufacturers since it usually

adversely affects cell performance. Specifically, void areas in MPL affects the electrical conductivity, water flooding or degrades the catalyst layer during the operation of the cell.

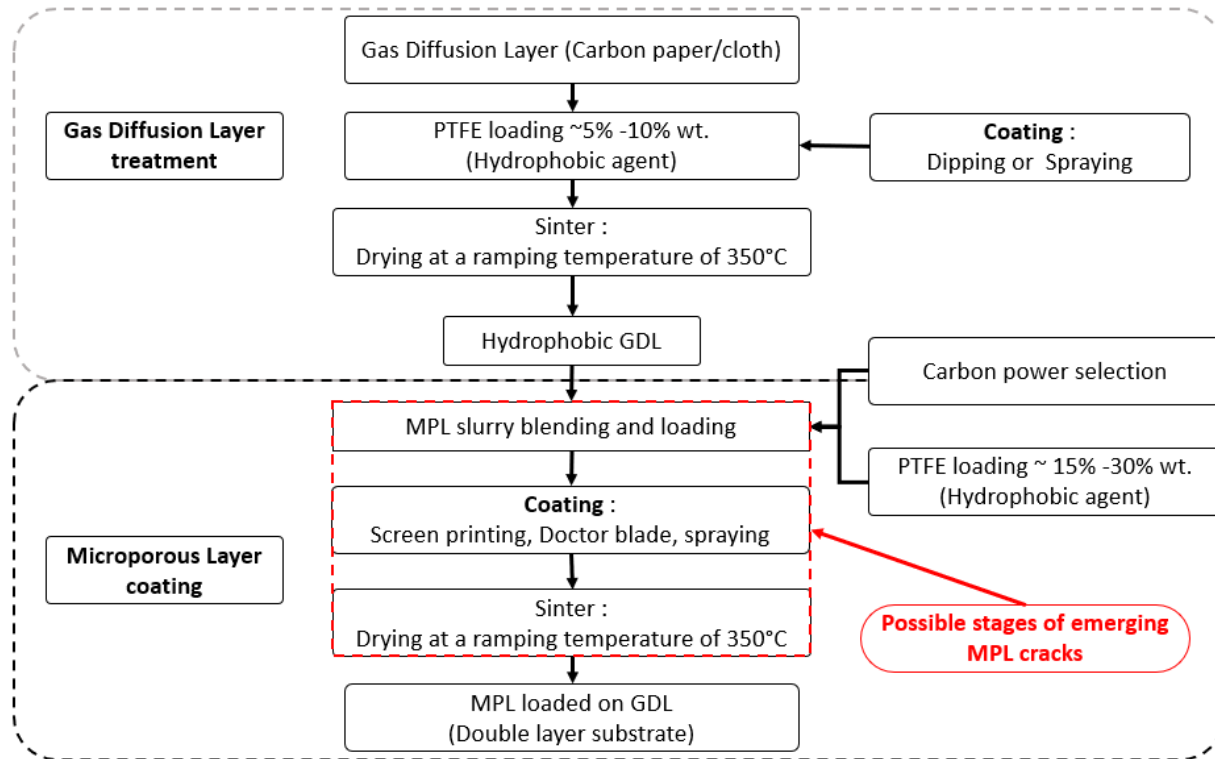


Figure 7-1: Steps used to fabricate the GDL and MPL. The red dotted area indicates steps where defects/cracks in the MPL can develop.

Studies have shown that structural changes/defects in the MPL can affect cell performance as follows: (i) water accumulation within defects/cracks, (ii) raise the electrical contact resistance in MEA and (iii) features on the MPL surface can damage the catalyst layer when the two are compressed together. Water can accumulate within interfacial gaps where the catalyst layer contacts the cracked areas of the MPL. As a result, the intended gas transfer and electrochemical reaction cannot occur at these affected sites and the electric resistance of the MEA increases. Good contact between the MPL and catalyst layer surface is critical for effective electrical conductivity and lessening the likelihood of flooding. The interfacial contact between the MPL and catalyst layer depends on the applied stack compression pressure. As the compression pressure increases, the contact resistance decreases. As noted previously, the MPL surfaces are rougher than that of the catalyst layer and control the interfacial structure. Therefore, when the stack is compressed during operation, features on the MPL surface can impinge and damage the catalyst layer.

Cracks/defects on the MPL can be transferred to the catalyst layer and permanently damage the CCM or even promote cell failure.

Due to the complex nature of the GDL/MPL material, defects differ by their size and shape depending on the manufacturing process. Therefore, the manufacturing industry requires rapid and advanced tools to identify the defects in a short duration of time during the manufacturing process [8]. The goal of improving the quality control in GDL materials is to identify all of the defects on the substrate at a web speed of 30 ft min⁻¹ during mass production. Although Bender et al. from NREL has implemented an IR camera in the rolling system to detect surface cuts on the size range of ~0.5cm, any smaller defect will remain undetected [9]. Hizir et al. measured crack dimensions on the GDL/MPL using gold sputtering, but this method is destructive and expensive [42]. Reshetenko et.al reported the effect of PTFE variation in the GDL using EIS method [163] and Prass et.al showed the effect of compressing the rougher MPL surface on the catalyst layer and studied the indentation of MPL cracks on the catalyst layers, but both the studies have not shown any evidence on how MPL defects affect the cell performance [102]. Although the determination of the effects of GDL defects on cell performance is extremely critical for GDL manufacturers and developers, it has been difficult to investigate and control due to difficulties in detecting sub-micron features and low visual contrast. Therefore, a research gap exists in identifying local defects in GDL/MPL with high accuracy and high resolution and correlating these defects to overall cell performance.

Control of MPL properties (e.g., chemical composition, mechanical stability, surface morphology, thermal and electrical properties) and material functionality is of great interest for GDL manufacturers and developers. The research described in this chapter focuses on the surface morphological defects on GDL/MPL substrates. The aim of this work is to develop a non-destructive method of investigating GDL defects that affect the performance of fuel cells. In the first phase of the research, IR thermography is developed and applied as a non-destructive tool to identify defects in the GDL that can be implemented in a continuous production line. This setup can identify defects with a minimum size range of 1 mm x 1 mm in less than one minute. In the second phase of the research, GDL/MPL substrates are aged by applying relative humidity (RH) cycling – ASTs in a custom-designed test cell over 600 cycles. Under these conditions,

electrochemical degradation of the catalyst layer/MPL is not significant. A different AST would be required and the MEA would have to be disassembled to investigate electrochemical degradation. Excess air flow rates are supplied to the test cell under two RH cycling periods to accelerate the mechanical degradation of the MPL surface (discussed in section 7.4.1). Crack propagation on the MPL surface is investigated using reflected light microscopy and the electrical conductivity of MPL surface is studied using in-plane and through-plane measurements. The contact angle of the MPL surface is measured to characterize the loss of its hydrophobic content as a result of degradation in the GDL substrate. In addition, polarization cell performance is compared for fresh and aged GDLs to examine the effect of crack propagation due to mechanical degradation of the GDL/MPL surface on cell performance.

7.2 Research Framework

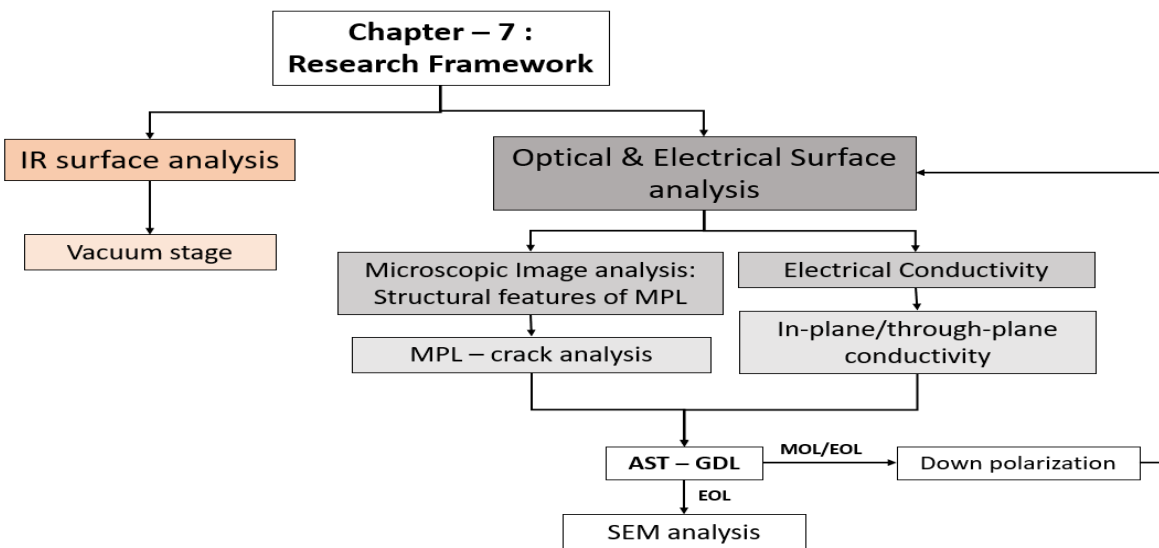


Figure 7-2: Framework for research on GDL quality control in this chapter.

7.2.1 Objective of GDL defect analysis

Figure 7-2 shows the research framework adopted in this study of GDL quality control. The main objective of this research is to detect defects on the GDL/MPL electrode using IR thermography with DC excitation method by pulling cold air suction through defects under vacuum. This test setup is newly developed in this work and will be discussed in detail in section 7.3.1. Defects with size from $\sim 200 \mu\text{m}$ to $\sim 500 \mu\text{m}$ on the MPL can be identified using this method of inspection. As no industrial standards for common defect sizes currently exist, this size range is selected to be representative of common defects. After IR investigation, the second stage of

research focuses on a microscopic surface analysis of MPL cracks and electrical conductivity (in-plane) of GDL/MPL. The final stage of the research is aimed at developing and applying an AST to age GDLs in a custom-design test cell operating at a temperature of 80°C. Crack propagation, electrical conductivity and electrochemical performance of aged GDL are characterized at EOL. This experiment provides a better understanding of defect propagation in MPLs and its impact on overall cell performance. This chapter also describes the progress made toward improving GDL quality control.

7.3 IR Examination of GDL Defects

The use of DC excitation in conjunction with IR thermography has previously been reported by Das et al.[8] who used a reaction-flow-through technique by passing 0.4% H₂ to a gas diffusion electrode (GDE) to excite the defects in a reactive environment and Aieta et al.[16] who applied 21 V to a GDE substrate to study the thermal response of thickness variations (artificial defects) of catalyst layers. These methods could only detect defects larger than 2 mm and ignores defects below this range. The quality control challenges exist in identifying defects below 1 mm range in MEA components and speed of data acquisition during the in-line process. Therefore, the aim of this work is to identify local sub-millimeter defects in the GDL/MPL in a short inspection time.

Experiments were performed by passing DC current to the GDL-MPL surface to generate heat, while cold air is pulled down through the GDL using a vacuum pump electrically isolated from the current by a porous ceramic plate as shown in Figure 7-3a. As current is passed through the sample, temperature variations are monitored with an IR camera placed 1 meter away from the setup in a dark environment. The temperature difference on the GDL surface is recorded carefully using an IR camera and the defected areas are identified as cold spots on the IR thermograph.

7.3.1 Experimental set-up: DC excitation using vacuum stage

Figure 7-3a shows a schematic of the IR setup developed to detect sub-millimeter defects on the GDL substrates. GDL with different surface defects are placed on a porous ceramic plate with approximate pore sizes of 10 μm to 15 μm. Thermal heat is generated on the GDL surface by applying a DC current of 1-2 A using a BioLogic model VMP3 potentiostat to copper sheets connected to both ends of the GDL. In this work, 1 A is applied to GDL samples with an active area of 12 cm x 4 cm. As current flows through the GDL, heat is generated on the surface. Any

variations in the temperature distribution on the surface are attributed to differences in local resistance of the GDL/MPL matrix according to Ohm's law. It is expected that local defects such as large cracks, voids or deep scratches lead to higher in-plane resistance. When DC current is applied to the MPL surface, a smaller temperature difference is observed across the defected areas than the non-defected areas due to high local in-plane resistance of defects causing low current to flow within the defected area resulting low temperature change in the thermography image [16].

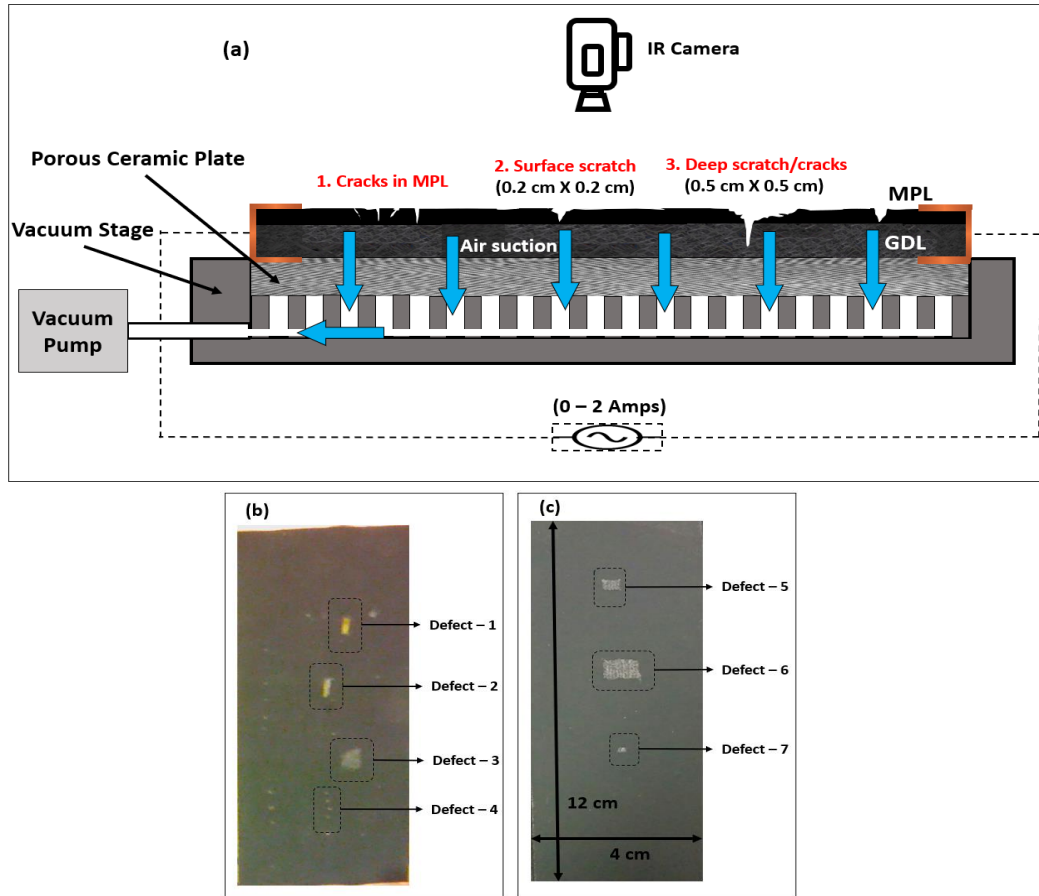


Figure 7-3: (a) Schematic of experimental setup designed with vacuum stage for IR investigation of GDL defects. (b, c) Digital images of GDL showing defects 1-7 within the active area of 12 cm x 4 cm. Table 7-1 lists dimensions of defects shown in figures b and c.

Table 7-1: Dimensions of defects shown in Figure 7-3b and c.

Defect numbers	Dimensions of defect
D - 1	100% removal of GDL & MPL
D - 2	100% removal of MPL & 50% removal of GDL
D - 3	4 mm x 4 mm - MPL
D - 4	0.25 mm - MPL
D - 5	2 mm x 2 mm - MPL
D - 6	5 mm x 5 mm - MPL
D - 7	1 mm x 1 mm - MPL

For defect analysis, artificial defects were created by scraping MPL surface using a lab scalpel to form various non-uniformity of MPL defects. Figures 7-3a and b present digital images of two GDL samples with different dimensions of defects on the MPL surface. The purpose of testing different sizes of defects is to analyse the sensitivity of the experimental setup to identify millimeter and sub-millimeter defects. A detailed description of defects is shown in Table 7-1. It should be noted that defect 1 (D-1) is made by removing a complete section of GDL and MPL, defect 2 (D-2) is made by removing 100% MPL and 50% GDL and defects 3-7 (D-3, D-4, D-5, D-6 and D-7) are made by removing 100% MPL.

The first set of experiments is performed on GDL using the DC excitation method without vacuum stage to study the thermal response of the various defects on GDL/MPL. This method was adapted from the literature to investigate the MPL defects[16]. Figures 7-4a and c show the thermal responses of defected GDL when 1 A DC current is supplied to the sample. Only D-1 and D-2 can be clearly observed in the IR image when no vacuum is applied. Two observations can be made:

i) The temperature of the defect is expected to vary depending on the depth of damage to the defect. Since D-1 (i.e., a small section of both GDL and MPL layers is entirely removed) and D-2 (100% and 50% removal of MPL and GDL, respectively) are more severe than the other defects (D-3 to D-7), zero or negligible current is expected to flow in these regions causing cold spots across D-1 and D-2 (blue areas) with a temperature difference of 10°C between non-defected and defected areas. Therefore, temperature decreases as the severity of the defect increases, a similar trend as that reported by Aieta et al [16].

ii) On the other hand, defects D-3 to D-7 are introduced to the MPL without any damage to the GDL. Since current can flow through the GDL (carbon fiber paper) and bypass the MPL, it would be expected to flow across these smaller defects on the MPL. Therefore, no temperature difference is observed across defects D-3 to D-7.

From our previous observations and feedback from the GDL manufacturer, defects such as D-1 and D-2 are not commonly observed during the fabrication process. However, defects D-3 to D-7 are commonly recognized in the MPL. The non-uniformity of MPL defects varies from manufacturer to manufacturer due to coating methods, sample handling process and packing

materials. Regardless of their size, defects in the GDL/MPL would be expected to reduce the performance of the cell. Since the DC excitation method alone cannot detect defects D-3 to D-7, it is important to improve the technique so that these defects can also be identified. The next stage of our research is focused on improving this method by incorporating a vacuum stage.

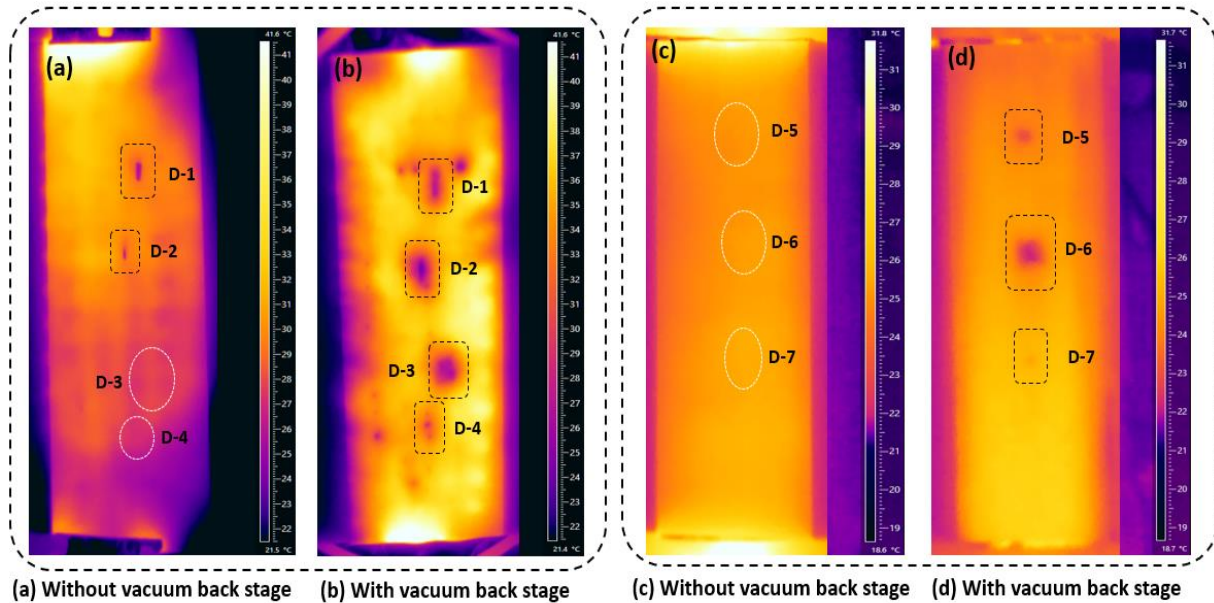


Figure 7-4: IR images of defected GDLs: (a) and (c) are captured without a vacuum, (b) and (d) are captured with a vacuum.

A vacuum stage is introduced in order to detect defects smaller than a millimeter, as shown in Figure 7-3a. The GDL substrate is placed on a flat ceramic porous plate clamped to a vacuum stage/vacuum chuck made from polycarbonate material. The vacuum pump is connected at the center of the stage to provide uniform suction of air through the porous plate. The ceramic plate has a uniform distribution of 10-15 μm pores and a thickness of 5 mm. When the vacuum pressure and DC current supply are turned on, the GDL sample is evenly attached to the surface of the porous plate without any deformation and static electric current is supplied to the GDL. A uniform suction force is developed through the GDL porous material that depends on the vacuum pressure. Any vibration of the GDL will cause noticeable surface noise or drop in temperature. Figures 7-4b and d show the thermal responses of the same two defected GDLs shown in Figures 7-4a and c when the air is pulled through the GDL using vacuum pressure. In comparing Figures 7-4 a and c (without vacuum) with Figures b and d (with vacuum), the smaller defected regions in the GDL/MPL (i.e., D-3 to D-7) are clearly observed when vacuum is applied. Due to the uniform

suction of air, it is expected that thinner areas in the GDL substrate offer higher gas permeability that allows more air to pass through defected areas and results in a colder surface. At a higher vacuum, the permeation rate of gases through defected areas in turn increases the local electrical resistance of the defect. This drives the flow of current across the edge of the defect and the temperature drop at the center of the defect. An example of a larger GDL area (30 cm x 20 cm) investigated using the vacuum stage method is shown in Appendix Figure 10-6.

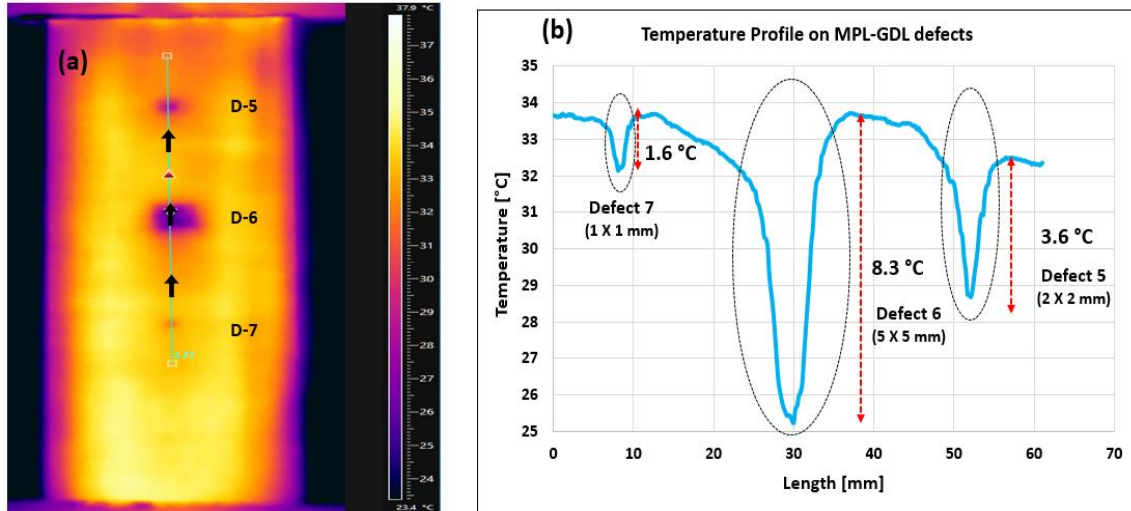


Figure 7-5: IR image of GDL showing defects D-5 to D-7. (b) Temperature line profile across the defects shown in Figure 7-5a.

Figure 7-5a shows the thermal response of the GDL shown in the digital image in Figure 7-3c. Figure 7-5b shows the temperature profile along the green line passing through D-5, D-6 and D-7 in Figure 7-5a. This plot clearly shows the drop in surface temperature at the defect. Furthermore, the larger the defect, the greater is the temperature decrease. The temperature drops across D-7 (1 mm x 1 mm), D-5 (2 mm x 2 mm) and D-6 (5 mm x 5 mm) are measured to be 1.6, 3.6 and 8.3°C, respectively. In each case, the temperature decreases from the edge to the center of the defect. This shows that the net flux of current at the center decreases as a result of loss of conductive material (i.e., defect in MPL), allowing higher permeation of gases through the GDL fibers. The temperature decrease of 8.3°C across D-6 across 5 mm square defect shows that this temperature is ~ 3 times larger than the literature value of 2.6°C [16]. Table 7-2 shows the comparison of thermal response on MPL defect to the current literature values. The IR defect detection method developed in this work takes less than 1 minute to scan a GDL surface with an active area of 30 x 20 cm.

Table 7-2: Comparison of temperature response on MPL defects with literature values.

Range of defects	IR detection temperature across defects (°C)	
	This study	Literature
5 x 5 mm	8.3	4.8 [179]
2 x 2 mm	3.6	1.5 [16]
1 x 1 mm	1.6	Not detectable

This method of investigating GDL/MPL defects should provide useful information for fuel cell electrode developers in materials selection for GDLs that are often used for high power density applications. For example, it is known that MEAs in heavy-duty fuel cell stacks are operated at high inlet gas pressure and high current density. In this situation, any defects in GDL will lead to (i) non-uniform distribution of reaction gases on the catalyst layer surface, (ii) non-uniform distribution of current at local areas and (iii) uneven water removal in the MEA i.e., defects facilitate water flooding zones. These effects ultimately decrease cell performance in the mass transfer-controlled region and promote dangerous pinhole formation in CCMs, as shown in Chapter 6. The proposed non-destructive and non-contact method is able to detect defects with various sizes at a resolution of $\sim 1 \text{ mm}^2$ on the MPL surface. This method takes less than a minute to visually inspect the GDL/MPL substrate with an active area of 600 cm^2 and holds great promise for use in on-line quality control processes.

7.4 MPL Crack Analysis

In this work, surface morphology (optical visualization) and electrical properties of the GDL/MPL cracks are carried in the following steps:

1. Acceleration stress test (AST) protocol is developed to age the GDL/MPL surface by cycling reaction gas (air) from 100% RH to 0% RH. The effect of RH on MPL degradation is studied using two wet/dry cycles (5 min/5 min and 5 min/10 min) at a cell temperature of 80°C in a custom-designed test cell.
2. MPL cracks are inspected using optical microscopy before and after AST. From microscopic analysis, the dimensions of defects such as crack area, percentage of defect area covered by cracks and average width of cracks are examined in fresh and aged GDLs.
3. Finally, electrical conductivity of GDL/MPL substrates are measured at BOL and EOL using:

a. in-plane measurements using a standard four-point probe

7.4.1 Implementation of AST

The separation of GDLs from MEA sub-components is a complex process to analyse the degradation of MPL in *in-situ* experiments. Therefore, the AST used in this work is developed to mechanically degrade the GDL/MPL substrates in a custom-design test cell to study the crack propagation in the MPL surface. The samples are aged in a test cell (shown schematically in Figure 7-6a) in which the MPL surface is oriented toward the incoming reaction gas from the flow-channel plate. The test cell design is slightly different from the single cell used to characterize PEMFC performance since the objective is to investigate crack propagation in the MPL surface through mechanical degradation. The active area of the GDL used in this experiment is 48 cm². Gaskets used in the test cell are 10% less thick than the GDL samples in order to enable 10% uniform through-plane compression. The end plates of the test cell are made from transparent polycarbonate material. This allows the operator to view the GDL surface during wet/dry cycling periods. This method of investigation enables any accumulation of water to be directly observed in the GDL samples during wet and dry conditions. Transparent fuel cells have been previously used to characterize water management in PEM fuel cells [180–182]. Figure 7-6b shows the polycarbonate test cell that is connected to the G-50 fuel cell test station used in this study. Air is supplied as the fuel at a flow rate of 12 L min⁻¹ through the flow channels and its RH is cycled from 80% to 0% (dew point temperature - 80°C) according to the two waveforms noted in the previous sub-section to accelerate MPL degradation. Table 7-3 lists the operating conditions used for the ASTs on two GDLs from the same batch. The main aim of developing these wet and dry ASTs is to study two major changes in the GDL/MPL surface:

- (i) Wet and dry cycling decreases the hydrophobic concentration in the GDL/MPL substrate and leads to carbon corrosion (oxidation of carbon) over the AST [173].
- (ii) Carbon corrosion leads to loss of material that can change the surface structure (i.e., propagation of cracks) and electrical properties of the MPL.

In the first half of both AST-1 and AST-2, the GDLs are operated at 80% RH for 5 min to provide sufficient water to the MPL surface to simulate the conditions of water flooding at the cathode at high current densities. In the second half of the cycles, the air is switched to 0% RH for 5 min during AST-1 and 10 min in AST-2 to study the influence of dry operating conditions on

crack propagation in MPL surface. Figure 7-6c shows the GDL surface during dry operating conditions, while Figure 7-6d shows the GDL surface under 80% RH conditions. These images clearly show that the channels are fully covered with water droplets compared to the land under wet conditions, but not under dry conditions. The regions under the channel are readily exposed to the reaction gases and mechanically stressed compared to those under the land.

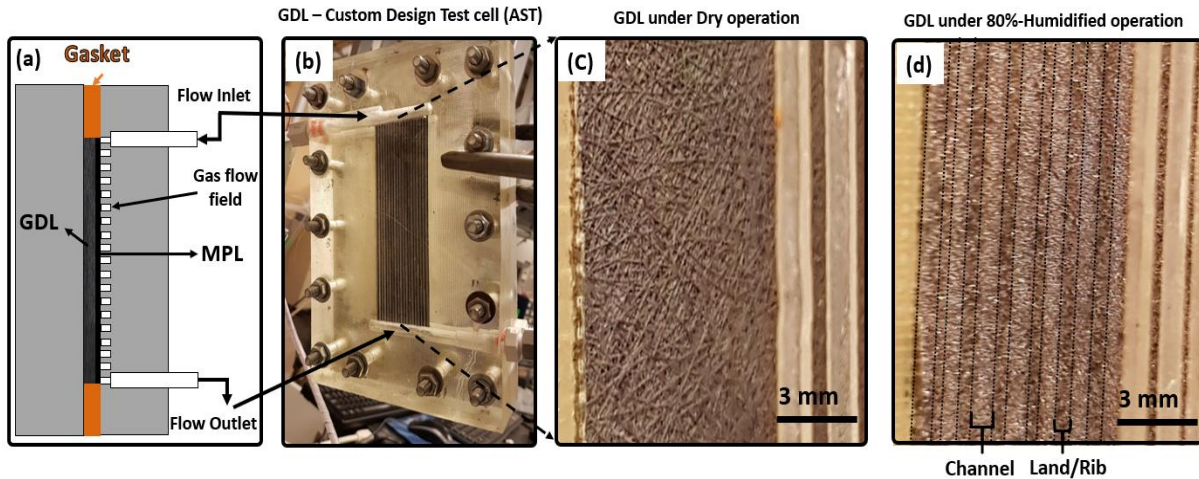


Figure 7-6: (a) Schematic of custom-design test cell for RH cycling AST. (b) Digital image of test cell connected to fuel cell test station. Images of GDL surface when operating cell under (c) 0% and (d) 80% RH.

Table 7-3: Operating conditions applied for aging GDLs.

Operating conditions	Operating parameters
Reaction gases	Air
Flow rate of gases	12 SLPM (standard liters per minute)
Operating pressure	150 kPa
Operating temperature	80°C
GDL compression	10% of initial thickness
RH cycling	0% - 80%
AST – 1 (transient time)	5 min – 5 min (600 cycles)
AST – 2 (transient time)	5 min – 10 min (600 cycles)

7.4.2 Microscopic investigation of MPL cracks

The morphology of the MPL samples was examined using reflected optical microscopy before and after the ASTs to observe the distribution of surface cracks. The reflected microscope is operated in transmitted light mode whereby white light is shone on the GDL backing layer and

the MPL surface faces toward the objective lens. This technique helps to locate through-plane cracks in the GDL/MPL. Through-plane cracks have deep valleys and allow transmitted light to pass through the defected area. These defects are considered as deep cracks or pinholes in the GDL. Cracks that do not allow transmitted light are considered as surface cracks. This method enables non-destructive characterization of the surface defects in GDL/MPL substrates. Figures 7-7a and b show microscopic images of MPL surface cracks captured at 5x magnification at BOL. Figures 7-7c and d show SEM images of surface cracks and interlayer void formation in MPL captured at 500x and 200,000x magnification, respectively. Surface cracks are clearly observed on the fresh MPL layer presumably formed during the fabrication process i.e., coating, drying or handling. Park et al reported that one of the major causes of generating cracks on the MPL surface is due to an uneven distribution of PTFE binder in the carbon slurry ink [176]. This variation of binder concentration changes the viscosity and phase stability of slurry ink over the coating process and generates surface cracks in the MPL during thermal drying [42,102]. The higher viscosity of the slurry provides close packing of carbon particles and reduces the pore size in the MPL. However, during drying, the close packing leads to deep crack or pinholes in the MPL [183]. Defect 1 in Figure 7-7a is a deep crack or through-plane crack in the MPL which allows light to be transmitted through the defected area. On the other hand, when the viscosity of the carbon slurry becomes too low, air bubbles tend to form and ink can penetrate into the GDL fibers and cause puddle-shape or circle-shape defects as shown in defect 2 in Figure 7-7 [184]. The entrapped air bubbles also develop inter-layer voids inside the MPL cracks during thermal sintering. Defects 2, 3 and 4 in Figure 7-7b appear to be surface cracks since they do not permit transmission of light. Defect 2 in Figure 7-7b and defect 6 in Figure 7-7c are examples of puddle-shape cracks that might be formed by entrapped air bubbles. Defect 5 in Figure 7-7c is an interlayer void defect shown in an enlarged view in Figure 7-7d. This higher resolution image clearly shows that the crack penetrates deeply into the surface and leads to more cracks further within the MPL. Fabrication of a uniform hydrophobic phase and crack-free GDL/MPL surface is extremely difficult specially for larger batch processes where the production scale of GDL substrates is $\sim 120 \text{ m}^2$ [183] later the GDLs are cut in to specific size as per the active area of the MEA. A better understanding of the effect of coating defects on cell performance should enable PEMFC developers to modify the operating conditions to improve the durability of electrodes.

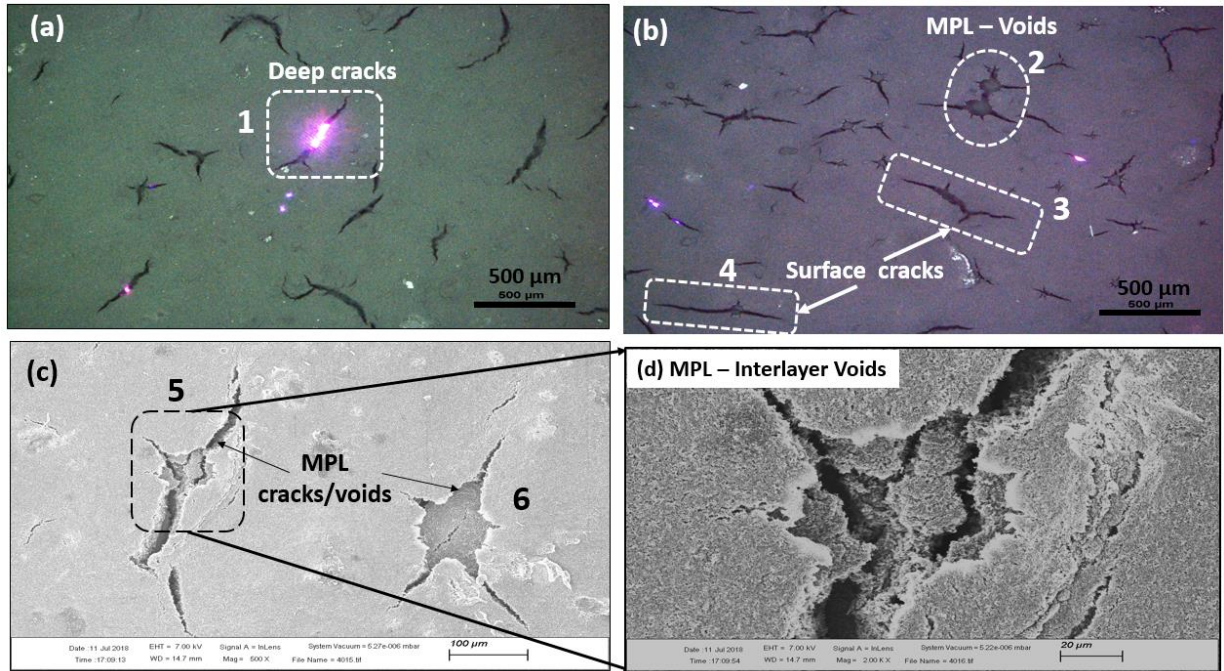
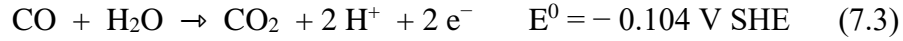
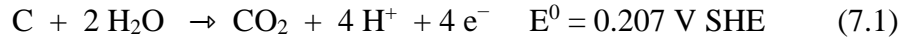


Figure 7-7: Microscopic images of MPL surface at BOL showing (a) deep cracks (through-plane crack) (b) surface cracks (in-plane cracks) (c) SEM image of MPL surface cracks (d) SEM image of interlayer inside the crack.

Three different regions of the GDL have been investigated (i.e., inlet, center and outlet) to study defect propagation after being subjected to the ASTs. Figures 7-8a and b present microscopic stitched images (5x magnification) of the entire 1 cm x 1 cm active area of fresh and aged MPL surfaces of same sample but captured at different location, respectively, after AST-2. From Figures 7-8a and b, cracks in the MPL surface are observed to propagate in both the in-plane and through-plane directions as it ages. Through-plane cracks pass through the GDL and MPL thickness and appear in magenta color inside the black enclosed areas. To eliminate distortions (shading or noise) in the image, a FFT-bandpass filter is applied to better visualize the image contrast. Degradation of the MPL surface through crack propagation is a highly complex process and so it may be useful to categorize cracks based on their area using imaging software ImageJ.

Figure 7-8c shows the frequency distribution of cracks with respect to their area in a fresh sample and a sample aged according to AST-1 and AST-2. A large number of cracks fall in the range from 0 to 100 μm^2 at BOL. As the samples are aged by RH cycling during ASTs, smaller cracks merge together and increase in size. As a result, both the number of cracks decreases (black dotted area in Figure 7-8c) and the area of cracks increases (red dotted area in Figure 7-8d) after aging. It is

known that the carbon is thermodynamically unstable under conditions such as high current densities, potential cycling, humidity cycling, high flow rates and water flooding conditions. The following equations describe possible oxidation reactions of carbon in the presence of water:



During the AST, it is expected that carbon loss in the MPL is accelerated by oxidation and promotes crack propagation. Chun et al [184] showed that RH cycling at higher flow rates (10 LPM) accelerates the mechanical degradation of the MPL surface and decreases the weight of the GDL by 60%. The higher flow rates of air causes carbon erosion in the MPL surface which in turn leads to delamination of the MPL/GDL sublayer and further increases in the ohmic and mass-transfer resistance of the cell. Under high humidity conditions, it is expected that water accumulates inside the cracked area due to its lower local capillary pressure, specifically in puddle-shaped cracks and inter-layer void cracks. When cell switches from wet to dry operating conditions, water is discharged from the cracks and enhances the carbon corrosion, causing damage in the MPL surface. The mechanical stress during the RH cycling AST leads to propagation of cracks in MPL surface both in-plane and through-plane directions. This allows the boundaries of neighboring cracks to connect or merge together. As a result, the area of the cracks increases and the areal density of cracks decreases significantly. Figure 7-8d shows a bar graph of the total area covered by cracks depending on their area. From the image analysis, it is found that total defect area covered by cracks on fresh MPL is 3.2%, 5.4% after AST-1 and 7.2% after AST-2. The results from Figure 7-8d clearly show that the total crack area is significantly higher after the GDLs are subject to AST-2 than after undergoing AST-1. Thus, the longer the GDL operates under dry conditions, the greater is the crack propagation on the MPL surface.

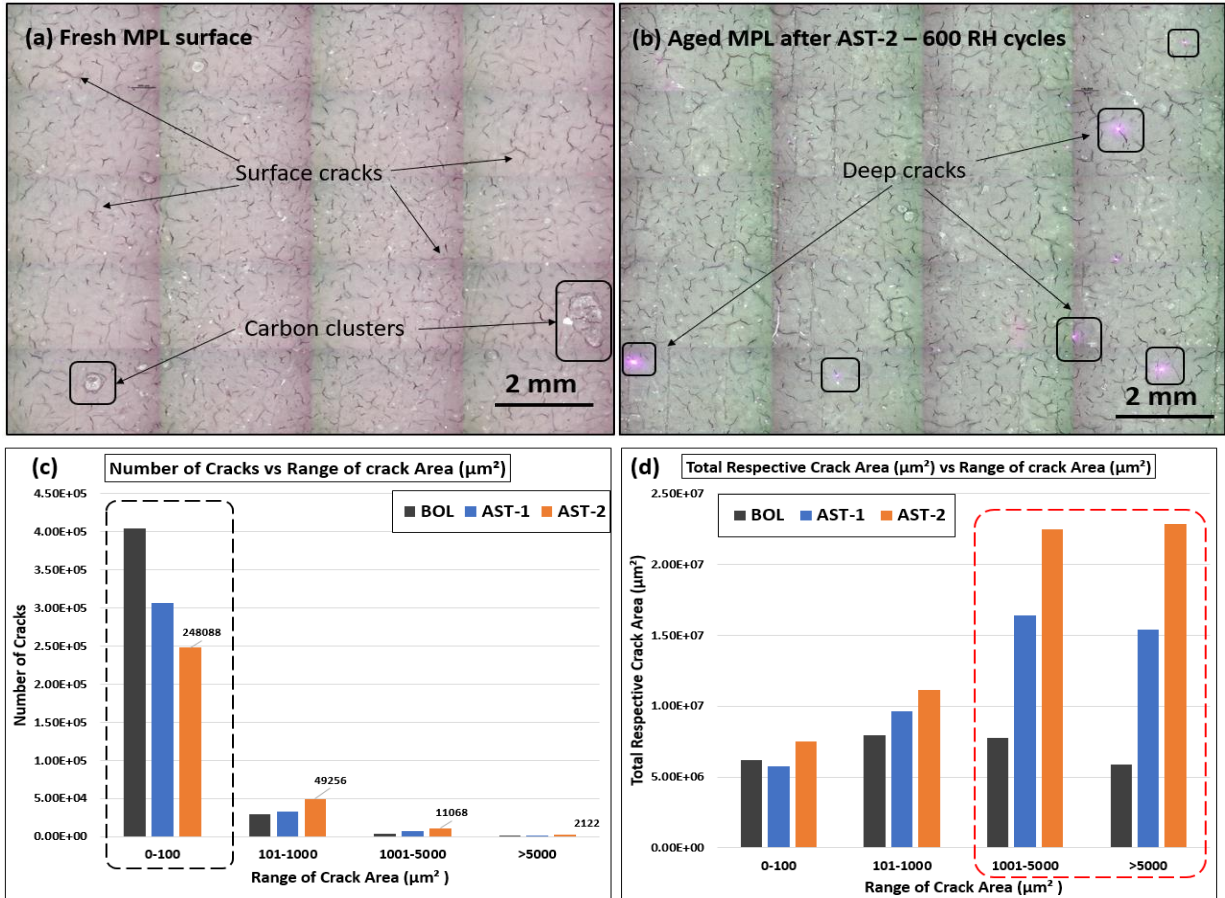


Figure 7-8: Stitched image of MPL surface: (a) fresh MPL surface covered with surface cracks and carbon clusters, (b) aged MPL surface after AST-2, (c) frequency distribution of the number of cracks according to crack area and (d) frequency distribution of the area covered by cracks according to crack area.

From the microscopic analysis, the cracks on the MPL surface are randomly oriented and connected through sub-branches of neighboring cracks. It is found that the average width of the cracks on the fresh MPL is $< 10 \pm 2 \mu\text{m}$ and increases to $18 \pm 3 \mu\text{m}$ after AST-1 and $25 \pm 5 \mu\text{m}$ after AST-2. It is expected that wider cracks play major roles in multi-phase transport issues, with the catalyst layers [185]. An example of MPL cracks (through-plane and in-plane cracks) examined under X-ray Tomography is shown in Appendix Figure 10.8 to understand the depth of cracks in thicker and thinner MPL surface. The average area of cracks increases from $725 \pm 15 \mu\text{m}^2$ at BOL to $1280 \pm 20 \mu\text{m}^2$ after AST-1 and to $1445 \pm 20 \mu\text{m}^2$ after AST-2. From close observation of the land and channel regions, no crack propagation is observed under the land area. It is also found that regions under the channel area are more vulnerable to the emergence of new cracks as well as the growth of previously existing cracks in the MPL. Since the cracks under the channel

are exposed to higher fuel flow velocities, rapid changes of humidity and mechanical intrusion of the GDL into the channel may result in different crack growth behavior. Figure 7-9a shows an MPL surface under both land and channel areas. It is clearly observed that the cracks under the land area are compressed and their widths tend to close. Therefore, no significant growth of the cracks is observed under the land region as shown in Figure 7-9a. On the other hand, the cracks under the channel expand both along their lengths and widths and merge with neighboring cracks. This can be attributed to higher flow rates and erosion along the crack edges due to water accumulation, which ultimately accelerates the propagation of BOL cracks in MPL surface [186]. We observe that puddle-shape cracks tend to form under the land region, and it was found that the average depth of puddle-shape cracks are around $5 \pm 1 \mu\text{m}$ with a diameter of $25 \pm 4 \mu\text{m}$. Puddle-shape cracks refers to the circular openings in the crack, an example is shown in Figure 7-7C (region 6). Generally, crack propagation on the GDL/MPL in actual fuel cell operation depends on stack compression pressure, inlet gas flowrates and membrane expansion pressure (depending on RH cycling). It is believed that the pressurized gases in flow field plate mechanically stretch the GDLs with in the channel area, this stretch causes propagation of cracks in MPL surface. Whereas cracks in MPL under the land region is confined therefore negligible propagation is observed. From close investigation of the MPL surface, several dents on the surface are also observed as bright areas although we notice no change in their area during aging. However, it is believed that dents on the MPL surface have no effect on the material properties as well as on the cell performance [42]. It is also observed that GDL fibers are visible in deeper cracks. These observations strongly demonstrate that through-plane cracks can penetrate the entire MPL thickness and reach the GDL/MPL interface. The frequency of through-plane cracks in the aged sample is not uniform over the entire surface, showing deviations from one region to another.

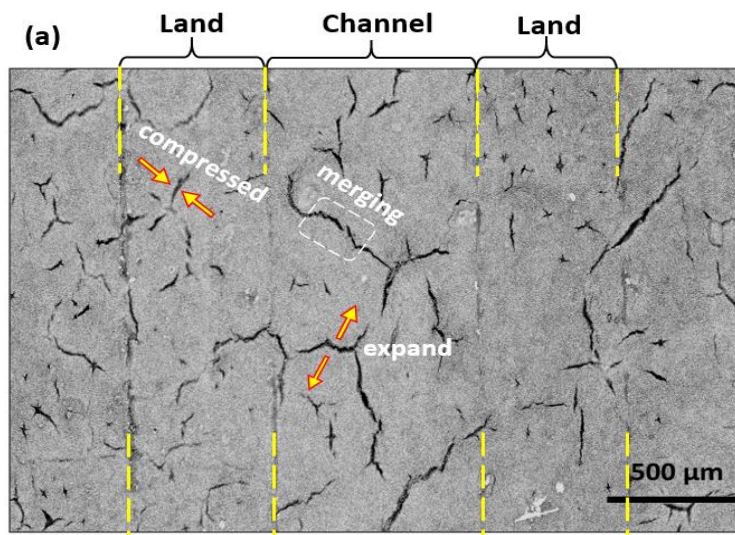


Figure 7-9: (a) Microscopic image of cracked MPL surface under channel and land regions.

The key observations from microscopic investigation of MPL cracks in the fresh and aged samples are:

1. The cracks that appear at BOL merge during the AST to form larger branches of the crack network. It is believed that edges of cracks are prone to carbon corrosion and carbon erosion, which may cause an increase in the aspect ratio of cracks (length, width and depth). The emergence of new cracks on the MPL surface is also observed, which might be due to mechanical stretching of GDL and carbon corrosion.
2. It is expected that inter-layer voids at BOL have propagated into deeper cracks and develop through-plane cracks at EOL. The majority of deeper cracks are observed in aged GDL operated under AST-2 rather than AST-1.
3. The propagation rate of cracks in MPL surface is observed to be higher under the channels than under the lands as shown in Figure 7-9a. This effect is expected since the area under the channel is fully exposed to the high flow rates of wet and dry gases and thus a higher rate of water accumulation, contributing to the erosion along with the edges of the cracks. This ultimately accelerates the propagation of cracks. A similar effect on the catalyst layer surface has been reported by Kim et al [187].

7.4.3 Effects of crack propagation in MPL

Crack propagation on the MPL surface also reduces the in-plane electrical conductivity and increases the intercontact resistance between the catalyst layer and the MPL. The larger cracked

area in the MPL surface reduces the contact area with the MPL and the active catalyst layer in the MEA. It is expected that the reduced contact area between MPL and catalyst layer is caused primarily by in-plane cracks rather than through-plane cracks that may affect electron transport between two interfaces. Figure 7-10a shows the schematic of an MEA with cracks in the MPL that causes gaps between the MPL and catalyst layers. Figure 7-10b shows a schematic of in-plane and through-plane cracks causing diffusion barriers for oxygen transport and electron flow from the MPL surface to the cathode catalyst layer, particularly at higher current densities.

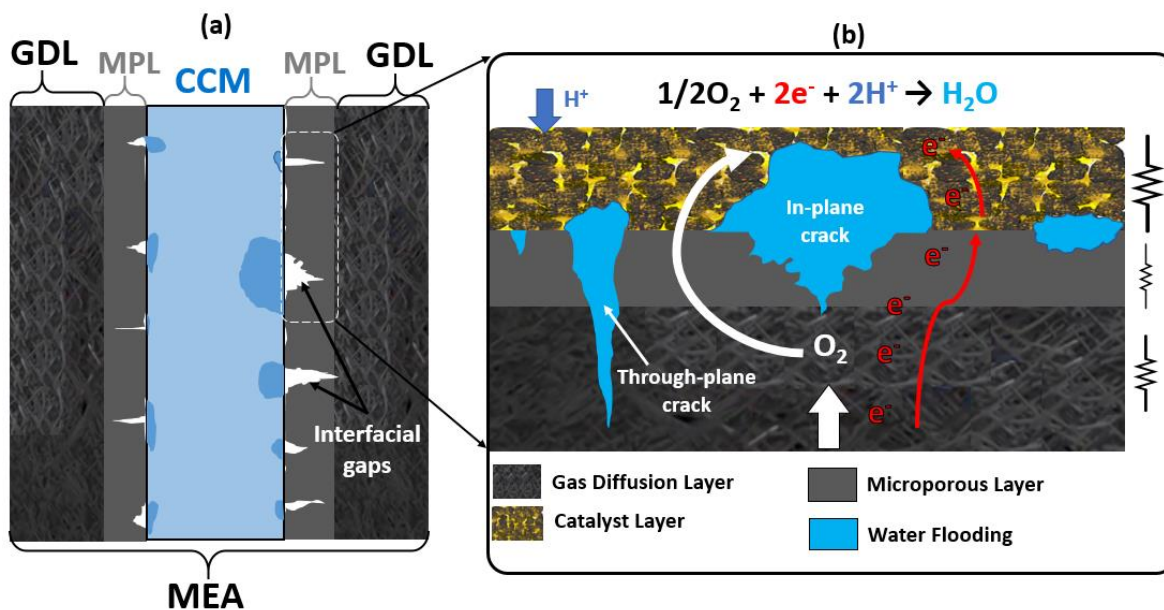


Figure 7-10: (a) Schematic of MEA showing cracks in MPL that lead to interfacial gaps between the CCM and catalyst layer. (b) Schematic of in-plane and through-plane cracks causing diffusion barriers for gas and electron transport to the catalyst layer.

During fuel cell operation at low current densities, MPL cracks might have a beneficial effect by facilitating permeation of reaction gases to the catalyst layer surface. However, at higher current densities, water produced at the cathode tends to accumulate and fill MPL cracks, thereby inhibiting access of the reaction gases to the catalyst sites. The presence of cracks across the MPL cracks and catalyst layer tends to lengthen the path of electrons to the catalyst sites (Figure 7-10b). In the absence of electrochemical reactions (i.e., after fuel cell shut-down), it is also expected that interfacial gaps due to both in-plane and through-plane cracks facilitate water accumulation between MPL/catalyst layer interface and propagate catalyst layer degradation.

7.4.4 Effect of GDL degradation on polarization performance

The cell performances of fresh and aged GDLs containing fresh CCMs have been assessed to determine the effect of degradation of GDLs alone. CCMs used in this study are defect-free and in good condition. Figure 7-11a shows the polarization performance of three GDLs used at the cathode i.e. (i) pristine GDL, (ii) aged GDL after AST-1 and (iii) aged GDL after AST-2. The cell performances of cells containing aged GDLs are slightly lower than that of cells with a fresh GDL particularly in the ohmic and mass-transfer regions. It is found that the cell voltage in the mass transfer region (i.e., at a current density of 1.5 A cm^{-2}) decreases by 12.4% and 23.1% relative to that obtained with a pristine GDL when the GDL has been aged according to AST-1 and AST-2, respectively. We speculate that two major phenomena contribute to this performance loss – (i) in-plane and through-plane crack propagation on the MPL surface and (ii) loss of PTFE concentration in the GDL/MPL during the aging process. Both of these defects facilitate water flooding at high current densities.

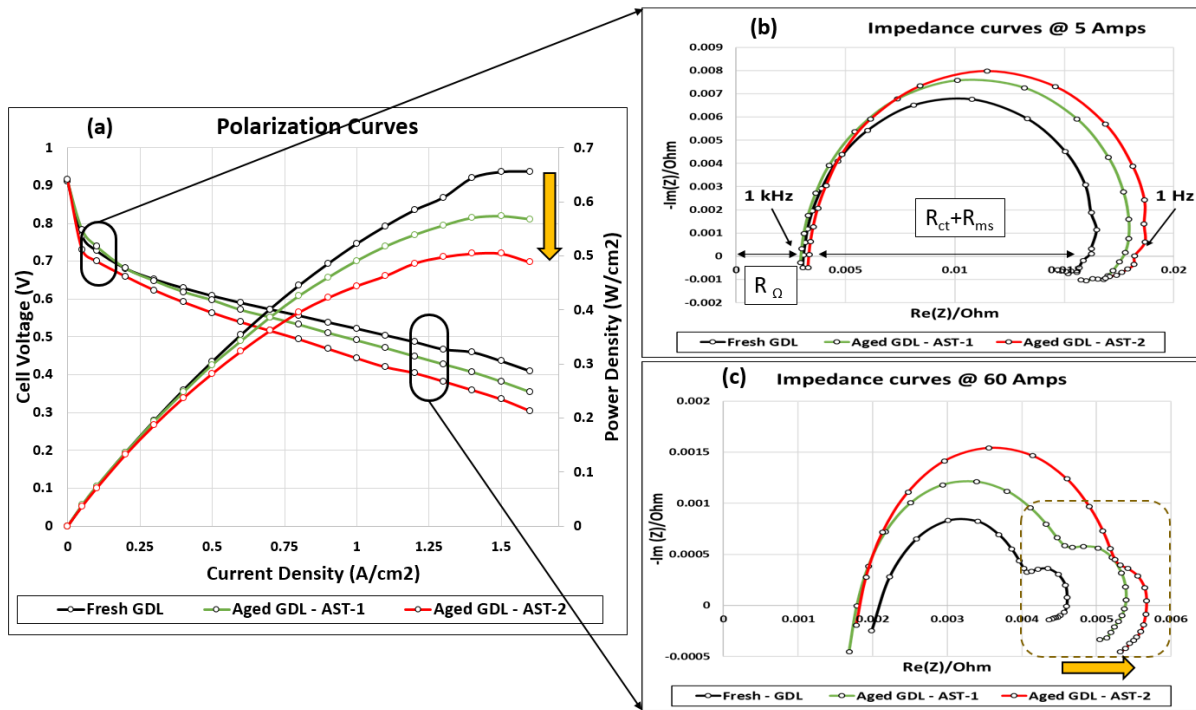


Figure 7-11: (a) Polarization and power density curves of fresh and aged GDLs. (b) EIS curves obtained at low current (5 A) and (c) high current (60 A).

Figures 7-11b and c show the EIS curves of fresh GDL and aged GDLs obtained at 0.1 A cm^{-2} (5 A) and 1.25 A cm^{-2} (60 A), respectively. The corresponding HFR (R_{Ω}) and LFR ($R_{ct} + R_{ms}$) values obtained from these curves are listed in Table 7-4. As shown in Figure 7-11b, no major change of

the ohmic resistance is observed in the HFR region upon aging at a low current density of 0.1 A cm⁻². A small shift in the low frequency region is observed due to mass-transfer losses. The increase in the diameter of the large loop may relate to changes in structural features (crack propagation in the MPL) of the GDLs aged during AST-1 and AST-2 which in turn leads water flooding. By observing the EIS curves in figure 7-11c at low frequency region, where the smaller semi-circle inside the dotted square can be attributed due to the oxygen diffusion limitation at high current density at 1.25 A/cm² (60 A), The fact that the smaller arc formation is expected due to increase in cathode over potential caused by water flooding effect in the aged GDL-AST-2. Our experimental results are compared with Ciureanu et.al [105] and Reshetenko et.al [106] demonstrating the impact of MPL defects causing concentration gradient of oxygen due to water flooding.

Table 7-4: Polarization performance and parameters obtained from EIS analysis of cells containing fresh and aged GDLs.

	voltage at 1.5 A cm ⁻² (V)	EIS at 0.1 A cm ⁻² - (mΩ)		EIS at 1.5 A cm ⁻² - (mΩ)	
		HFR - R _Ω	LFR- (R _{ct} + R _{ms})	HFR - R _Ω	LFR- (R _{ct} + R _{ms})
fresh GDL	0.43	3.0	16.2	2.2	4.6
aged GDL (after AST-1)	0.38	3.0	17.7	1.9	5.4
aged GDL (after AST-2)	0.34	3.2	18.1	1.91	5.7

7.5 Electrical Characteristics of GDL/MPL Substrates

An important characteristic of the GDL/MPL is its ability to transport current between the catalyst layer and bipolar plates. As discussed earlier, the crack propagation in the MPL surface significantly affect the electrical properties of the GDL. Electrical characteristics of MPL surface have been measured using four-point probe method as discussed in section 3.2.2.1.3.1.

7.5.1 In-plane electrical measurements

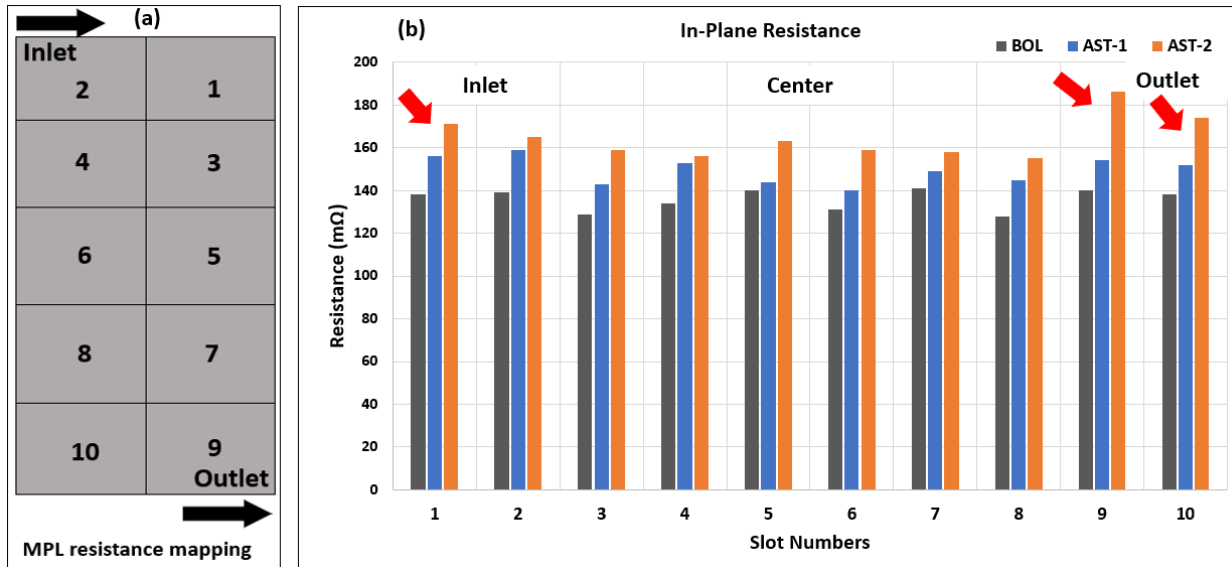


Figure 7-12: (a) Schematic of MPL surface (top view) divided into 10 regions or slots for in-plane resistance measurements, (b) In-plane resistance measurements obtained in the 10 slots using the four-point probe, the red arrows indicate the resistance at inlet and outlet.

The average in-plane resistance of fresh and aged GDLs is shown in Figure 7-12. For detailed in-plane measurements, the entire MPL surface is divided into 10 equal area regions or slots (each slot covers an active area of 2 x 1.4 cm) as shown in Figure 7-12a and the in-plane resistance of each of these slots averaged over 20 measurements is determined (200 points in total) from slot to slot as shown in Figure 7-12b. The average in-plane resistances over the entire MPL surface at BOL, AST-1 and AST-2 are 135.8, 149.5 and 164.6 mΩ, respectively. These results show that the in-plane surface resistance increases by 13.7 mΩ and 28.8 mΩ when a fresh MPL is aged according to AST-1 and AST-2, respectively. It is found that the in-plane resistance in the MOL outlet region has increased from 140 mΩ to 185 mΩ (slot-9) and 178 mΩ (slot-10), these areas also showed a noticeable crack growth under channel area. We believe that the increases in surface resistance is due to the growth of crack length and aspect ratio (length to depth). These results are also consistent with our previous microscopic observation that the area of the cracks increases significantly when sample are aged under the different RH cycles during AST-1 and AST-2. It is also observed that the local resistance under the flow channel is measured to be ~ 169 mΩ, which is higher than the value of 151 mΩ under the lands. This shows that the material loss in the channels is greater than under the lands and this is expected to increase the ohmic resistance in MEA.

7.6 Conclusions

Defect investigation is critical for PEMFC components, specifically GDL/MPL substrates, that play such a key role in determining MEA performance. Defects in the GDL can reduce the cell performance at earlier stages of stack operation. In this research work, *ex situ* investigation of GDL/MPL defects has been conducted using IR thermography. MPL defects are found to be an important cause for losses in cell performance. The defects in the GDL/MPL surfaces have been successfully investigated using three *ex-situ* methods. The findings from this study can be summarized as follows:

1. IR characterization

The experimental setup for IR investigation involves the application of a DC excitation method using a vacuum stage. A large number of experiments have been conducted by introducing artificial defects with size 5 x 5 mm, 2 x 2 mm and 1 x 1 mm on the MPL surface to study the temperature response of DC current. Our data suggest that this experimental setup using the vacuum stage technique can detect temperature changes of 1.6°C in defects as small as 1 x 1 mm. The measurements from this study are about twice as sensitive as those reported in the literature values for defect detection in GDL substrates.

2. Microscopic examination

An RH cycling AST protocol has been developed to study crack propagation on an MPL surface via mechanical degradation. This involves the application of 600 wet-dry RH cycles to age the GDL with two different dry periods (5/5-min and 5/10-min – wet/dry cycles). After 600 RH cycles, the cell voltage decreases significantly by 23.1% at 1.5 A cm⁻². We have also analyzed morphological features of MPL cracks in fresh and aged GDLs. The microscopic analysis reveals that significant growth of MPL cracks occurs in the aged samples. Two types of crack propagation have been observed i.e., surface (in-plane) cracks and deep cracks (through-plane) cracks. The most severe crack propagation on the MPL surface is observed when the GDL/MPL is aged according to AST 2 (5/10 min - wet/dry) and the defect area covered by cracks increases from 3.2 to 7.2%. Crack propagation is majorly affected under the channel, then the land area. Therefore, the channel-to-land width ratio is also an important factor for crack propagation mitigation. It is expected that in-plane cracks are potentially dangerous for gas diffusion and electron transport between the MPL and CL.

3. Electrical resistance measurements

The in-plane electrical resistance increases from 135.8 to 164.6 m Ω when the GDL/MPL substrate is aged under AST-2 RH cycling. The highest in-plane resistance is measured under the channels with an average of 169 m Ω for channels and 151 m Ω for lands. From these results, it appears that mechanical stress caused by RH cycling increases the electrical resistance of GDL/MPL substrates.

Investigation of crack orientations using present AST methods provides useful information for GDL developers to understand the effect of crack propagation in MPL on cell performance and eliminate the diffusion barrier in MEAs caused by water flooding. Although it is difficult to eliminate the cracks during the fabrication process, correct precautions should be followed to reduce the degradation of the MPL by purging with nitrogen after the shutdown of the PEMFC stack to remove water in the cracks.

8 Conclusions and Recommendations

The final chapter summarizes the highlights of major conclusions emerging from the research.

8.1 Conclusions

One of the critical barriers for advancing the manufacturing of PEM fuel cell systems is the development of quality control analysis to produce defect-free MEA components. In most cases, no standard quality control measurements have been established or correlation of quality control parameters with durability and performance. Therefore, the focus of this research has been on the various defects in MEA components and correlate their propagation to cell performance. In particular, this work has explored real defects in MEA components that are commonly generated during manufacturing production. The main objectives of this work are listed below.

➤ CCM Defect Analysis

1. Investigation of real manufacturing defects in MEA components (CCMs and GDLs) and their classification based on geometry
2. Development of a non-destructive method of investigating catalyst layer defects (MCLD) in the CCMs and its use to better understand the mechanism by which these defects degrade the cell
3. Development of accelerated stress protocols to age the defected electrode, study defect propagation and relate this to the resulting cell performance

As a first step, a non-destructive and non-contact method of identifying and characterizing defects in commercial CCMs has been developed. Further work also examined the mechanical propagation of catalyst layer defects when the cell is operated in a non-reactive environment (N_2/N_2). This work found six types of catalyst layer defects, with catalyst layer cracks and MCLDs being the most commonly observed ones. The characteristic features of these defects were investigated and classified based on their dimensions. The above work was published in *International Journal of Energy Research*.

Secondly, a novel test protocol was developed to age (chemical degradation) the defects (MCLD) in CCMs without any confounding effects due to external damage from flow field plates and GDL

indentation. The proposed method enables areal visualization of morphological changes and failure locations of the catalyst layer defects in pristine and aged CCMs. It was observed that degradation of MCLD occurs most rapidly during the initial stages of the AST and tends to stabilize in later stages of the operation. The areal dimensions and degraded catalyst zones inside the MCLD were quantified and examined at regular time intervals and correlated to cell performance loss. Developments in present work aims to provide fundamental knowledge on improving the tolerance and durability of CCM electrodes against defects and providing a high level of quality analysis for better productivity of CCM electrodes.

➤ **MEA Defect Analysis**

Thirdly, the effects of various defects (i.e., sealant interface defects, MCLD, scratches/cuts and membrane pinholes) and their propagation under chemical and mechanical stresses on overall MEA degradation and electrode life-time was studied. Two AST protocols involving operation at constant low RH and wet/dry RH cycles at OCV to introduce combined chemical and mechanical stresses were implemented to accelerate the evolution of MEA defects. It was found that RH cycling dramatically over a duration of 150 AST hours reduced the overall cell performance by 1.26 mV h^{-1} in comparison to constant low RH which led to a loss of 0.910 mV h^{-1} . The rate of OCV decay was found to be a useful diagnostic tool for the prediction of the cell EOL, as confirmed by other diagnostic tests i.e., H_2 crossover, polarization curves and IR thermography. From our observations, the total cell performance was much more severely affected by sealant interface defects, empty catalyst zones and deep scratches/cracks rather than by missing/thin catalyst layer defects. The impact of MEA defects on cell performance were prioritized as Sealant interface defects > Scratch/deep cuts in CL > Empty CL defects > Thin/missing CL defects. Thus, the AST protocol implemented in this study should enable the screening for MEA durability of electrodes intended for heavy-duty fuel cell stack applications.

➤ **GDL Defect Analysis**

The final topic in this thesis involved an investigation of defects in GDL-MPL substrates. MPL defects are among the most important causes of ohmic and mass transport losses in MEAs. In this study, we examined MPL defects on commercial GDL-MPL substrates using IR thermography,

microscopic surface analysis and electrical conductivity measurement. The IR setup involved the use of DC excitation and a vacuum stage to detect MPL defect as small as 1 X 1 mm. The detection limit from the thermal response of these measurements was found to be two times lower than that previously reported in the literature. The research also focused on developing an aging protocol for GDL-MPL substrates. Crack propagation in MPL surface was characterised using microscopic examination. As the GDL-MPL substrate was aged by RH cycling AST (5/10 min- wet/dry), the defected area covered by MPL cracks increased from 3.2 to 7.2% from BOL to EOL. Lastly, the in-plane electrical conductivities of GDL-MPL substrates were examined before and after aging. The in-plane electrical resistance of the MPL surface increased from 135.8 to 164.6 m Ω . Interestingly, crack propagation in MPL surface was observed under the channel area rather than land area. Crack growth on the MPL surface led to a 23.1% decrease in cell performance in the mass transfer control region (i.e., at a current density of 1.5 A cm⁻²).

In general, the formation of defects during manufacturing of the catalyst layer/MPL or any MEA component will depend on many factors, including the method of fabrication (coating/hot press), structure of electrode (thickness of catalyst layer/MPL/ pore size distribution), type of materials used (catalyst loading/ionomer concentration/ PTFE distribution). The methodologies presented in this thesis are highly relevant for investigating defect parameters and addressing some of the problems that manufacturing defects in MEA components have on performance loss in PEM fuel cells. Based on this study, we can put together the defect chart in Figure 8-1 to summarize the impact of MEA defects (i.e., catalyst layer, membrane and GDL-MPL defects) on the initial and final cell performance and on the operating lifetimes of MEAs.


Defect study in MEA componetns	Impact on initial cell performance	Impact on final cell performance	Lifetime of MEA
Missing/Thin Catalyst Layer Defects	Little/No Impact	Moderate Impact	Moderate Impact
Empty Catalyst Layer Defects	Little/No Impact	Significant Impact	Significant Impact
Sealant Interface Defects (Gasket/GDL/CCM)	Moderate Impact	Significant Impact	Significant Impact
Deep cracks/Scratch (Deep cuts)	Little/No Impact	Significant Impact	Significant Impact
CL/MPL cracks	Little/No Impact	Moderate Impact	Moderate Impact, Future work
Thin/Zero MPL layers	Little/No Impact	Moderate Impact	Future work
Coating/Manufacturing defects (Droplets/Oil marks/CL blusters)	Little/No Impact	Little/No Impact, Future work	Little/No Impact, Future work
Catalyst Loading variations/Ionomer concentration in CCM/Location of defects (Inlet/middle/outlet)	Future work	Future work	Future work
PTFE loading in GDL-MPL/MPL thickness variations/ Porosity of GDL	Future work	Future work	Future work
			

Figure 8-1: Defect chart summarizing the impacts of various defects in MEA components on overall cell performance and life-time as determined in this study.

8.2 Contributions to MEA quality control development

The following section summarizes the major research contributions for fuel cell electrode manufacturing:

The methodology and test protocols developed in Chapters 4 and 5 provide non-destructive and non-contact methods for inspection of catalyst layer defects in CCMs that can be installed in the manufacturing production line. This method based on optical reflectometry should provide useful information for catalyst layer developers to determine the location and dimensions of defects generated during the production process. The aging protocol developed for defect propagation in CCMs should yield fundamental knowledge on the growth of defects under chemical and mechanical stress during cell operation. The six types of catalyst layer defects reported in Chapter 4 can be used for quality control measurements. We believe our analysis reduces the gap between manufacturing and the impact of defects formed during manufacturing on cell performance which should enable manufacturers to make better decisions regarding the selection/rejection of CCMs prior to MEA fabrication.

The research also focused on investigating the effects of various manufacturing defects on MEA life-time using two AST methods (i.e., constant low RH and wet/dry RH cycles). The RH test protocol developed in this work assessed the durability of MEA defects intended for automotive applications where the temperature, pressure, gas composition and humidity are expected to change rapidly. This new AST protocol is aimed at enabling faster screening of defect formation and propagation in MEAs caused by manufacturing with the ultimate goal of increasing MEA performance, efficiency and durability.

The IR test setup developed in this work can detect GDL-MPL defects on the order of 1 mm in size in less than 1 min. Our testing method can be used as an accurate and fast response on-line quality control tool for GDL sheets or continuous GDL rolls.

8.3 Recommendations for future work

Defects in CCMs and GDLs vary in their nature and formation depending on the type of manufacturing process. The impact of MEA defects on cell performance also depend on their size (length, width and aspect ratio), location (inlet, middle and outlet), conditions of operation and the component in which they exist (catalyst layer, membrane, GDL and MPL). In the present work, only certain types of defects (CL cracks, MCLD, zero catalyst loading, scratch/deep cuts and sealant interface defects) were investigated due to limited supply from the manufacturer. The following recommendations are suggested for future research to further improve quality control of MEAs.

8.3.1 Catalyst layer development

1. The impacts of irregularities in the geometry of catalyst layer defects (i.e., thickness and size of affected regions) and particular location of defects (e.g., below the land, below the channel, gas inlet, middle and outlet) on cell performance under various operating conditions should be investigated.
2. A defect degradation model should be developed to predict the effect of thickness irregularities, catalyst loading and catalyst degradation on lifetime of the MEA components.

3. Although the present research is focused on cathode catalyst layers, it is also important to study the effect of defects on the anode catalyst layer and degradation of membrane defects under typical chemical and mechanical stresses on cell performance should be further investigated.
4. Propagation/degradation of catalyst layer defects under the compression of flow field plate land/channel should be studied.

8.3.2 GDL-MPL development

1. The role of the MPL coating in crack formation is not yet completely understood. Future work should be aimed at characterizing MPL cracks generated under the combinations of different MPL slurry, coating and drying conditions. A detailed crack analysis accounting for crack width, narrow cracks, voids and through-plane/in-plane effects and its impact on gas permeability would also be useful.
2. Future work is also required to investigate the effect of MPL thickness, penetration of MPL into GDL, PTFE loading/distribution and porosity of GDLs on total cell performance.
3. The effect of compression on the GDL-MPL surface under the flow field land and channel is also recommended to investigate the mechanical properties of the GDL substrates.
4. The impact of MPL defects on catalyst layer and the structural features of GDL-MPL on the electrode durability should be investigated for the development of GDL substrates. X-ray tomography is recommended for a detailed inspection of MPL intrusion into the GDL and the internal GDL structure affecting the permeability of gases.

9 References

- [1] C. Song, Fuel processing for low-temperature and high-temperature fuel cells: Challenges, and opportunities for sustainable development in the 21st century, *Catal. Today*. 77 (2002) 17–49. doi:10.1016/S0920-5861(02)00231-6.
- [2] S.G. Chalk, J.F. Miller, Key challenges and recent progress in batteries, fuel cells, and hydrogen storage for clean energy systems, *J. Power Sources*. 159 (2006) 73–80. doi:10.1016/j.jpowsour.2006.04.058.
- [3] S. Sharma, S.K. Ghoshal, Hydrogen the future transportation fuel: From production to applications, *Renew. Sustain. Energy Rev.* 43 (2015) 1151–1158. doi:10.1016/j.rser.2014.11.093.
- [4] M.P. Arcot, K. Zheng, J. Mcgrory, M.W. Fowler, M.D. Pritzker, Investigation of catalyst layer defects in catalyst - coated membrane for PEMFC application: Non - destructive method, *Int. J. Energy Res.* (2018) 1–18. doi:10.1002/er.4107.
- [5] Gutoff.E.B, E.. Cohen, K. G.I, Coating and drying defects: troubleshooting operating problems, Wiley-Interscience. (2006).
- [6] P. Rupnowski, M. Ulsh, B. Sopori, High Throughput and High Resolution In-Line Monitoring of PEMFC Materials by Means of Visible Light Diffuse Reflectance Imaging and Computer Vision, in: *Am. Soc. Mech. Eng.*, 2015: p. V001T04A002. doi:10.1115/fuelcell2015-49212.
- [7] S. Kundu, M.W. Fowler, L.C. Simon, S. Grot, Morphological features (defects) in fuel cell membrane electrode assemblies, *J. Power Sources*. 157 (2006) 650–656. doi:10.1016/j.jpowsour.2005.12.027.
- [8] P.K. Das, A.Z. Weber, G. Bender, A. Manak, D. Bittinat, A.M. Herring, M. Ulsh, Rapid detection of defects in fuel-cell electrodes using infrared reactive-flow-through technique, *J. Power Sources*. 261 (2014) 401–411. doi:10.1016/j.jpowsour.2013.11.124.
- [9] M. Ulsh, B. Sopori, V. Aieta, N, G. Bender, Challenges to High-Volume Production of Fuel Cell Materials: Quality Control M. Ulsh, *Electrochem. Soc.* 50 (2012) 919–926. doi:10.1149/05002.0919ecst.
- [10] C. Lim, L. Ghassemzadeh, F. Van Hove, M. Lauritzen, J. Kolodziej, G.G. Wang, S. Holdcroft, E. Kjeang, Membrane degradation during combined chemical and mechanical accelerated stress testing of polymer electrolyte fuel cells, *J. Power Sources*. 257 (2014) 102–110. doi:10.1016/j.jpowsour.2014.01.106.
- [11] R. Banan, A. Bazylak, J. Zu, Effect of mechanical vibrations on damage propagation in polymer electrolyte membrane fuel cells, *Int. J. Hydrogen Energy*. 38 (2013) 14764–14772. doi:10.1016/j.ijhydene.2013.08.136.
- [12] M.M. Mench, E.C. Kumbur, N. Veziroglu, *Polymer Electrolyte Fuel Cell Degradation*, Academic Press, 2011.
- [13] A. Kusoglu, A.Z. Weber, *A Mechanistic Model for Pinhole Growth in Fuel-Cell*

- Membranes during Cyclic Loads, *ECS*. 161 (2014) E3311–E3322. doi:10.1149/2.036408jes.
- [14] J.T. Gostick, M.A. Ioannidis, M.W. Fowler, M.D. Pritzker, Pore network modeling of fibrous gas diffusion layers for polymer electrolyte membrane fuel cells, *J. Power Sources*. 173 (2007) 277–290. doi:10.1016/j.jpowsour.2007.04.059.
- [15] W. Zhang, C. Wu, Effect of Clamping Load on the Performance of Proton Exchange Membrane Fuel Cell Stack and Its Optimization Design: A Review of Modeling and Experimental Research, *J. Fuel Cell Sci. Technol.* 11 (2013) 020000. doi:10.1115/1.4026070.
- [16] N. V. Aieta, P.K. Das, A. Perdue, G. Bender, A.M. Herring, A.Z. Weber, M.J. Ulsh, Applying infrared thermography as a quality-control tool for the rapid detection of polymer-electrolyte-membrane-fuel-cell catalyst-layer-thickness variations, *J. Power Sources*. 211 (2012) 4–11. doi:10.1016/j.jpowsour.2012.02.030.
- [17] DOE, B.M. Institute, Manufacturing Cost Analysis of Polymer Electrolyte Membrane (PEM) Fuel Cell Systems for Material Handling Applications, DOE Rep. (2017) 1–137.
- [18] A. Tavassoli, C. Lim, J. Kolodziej, M. Lauritzen, S. Knights, G.G. Wang, E. Kjeang, Effect of catalyst layer defects on local membrane degradation in polymer electrolyte fuel cells, *J. Power Sources*. 322 (2016) 17–25. doi:10.1016/j.jpowsour.2016.05.016.
- [19] M. Mandal, A. Valls, N. Gangnus, M. Secanell, Analysis of Inkjet Printed Catalyst Coated Membranes for Polymer Electrolyte Electrolyzers, *J. Electrochem. Soc.* 165 (2018) 543–552. doi:10.1149/2.1101807jes.
- [20] I.S. Park, W. Li, A. Manthiram, Fabrication of catalyst-coated membrane-electrode assemblies by doctor blade method and their performance in fuel cells, *J. Power Sources*. 195 (2010) 7078–7082. doi:10.1016/j.jpowsour.2010.05.004.
- [21] S. Yilmaztürk, T. Gümüolu, G.A. Ari, F. Öksüzömer, H. Deligöz, Fabrication and performance of catalyst-coated membranes by layer-by-layer deposition of catalyst onto Nafion for polymer electrolyte membrane fuel cells, *J. Power Sources*. 201 (2012) 88–94. doi:10.1016/j.jpowsour.2011.10.116.
- [22] C.Y. Jung, W.J. Kim, S.C. Yi, Optimization of catalyst ink composition for the preparation of a membrane electrode assembly in a proton exchange membrane fuel cell using the decal transfer, *Int. J. Hydrogen Energy*. 37 (2012) 18446–18454. doi:10.1016/j.ijhydene.2012.09.013.
- [23] M.B. Sassin, Y. Garsany, B.D. Gould, K.E. Swider-Lyons, Fabrication Method for Laboratory-Scale High-Performance Membrane Electrode Assemblies for Fuel Cells, *Anal. Chem.* 89 (2017) 511–518. doi:10.1021/acs.analchem.6b03005.
- [24] M. Knowles, D. Baglee, A. Morris, Q. Ren, The state of the art in fuel cell condition monitoring and maintenance, *World Electr. Veh. J.* 4 (2011) 487–494.
- [25] M. Ulsh, B. Sopori, V. Aieta, N. G. Bender, Challenges to High-Volume Production of Fuel Cell Materials: Quality Control M. Ulsh, *Electrochem. Soc.* 50 (2012) 919–926.

- [26] G. Bender, W. Felt, M. Ulsh, The Spatial Performance Effect of Electrode Defects in PEMFC, *Electrochem. Soc.* (2012) 1588–1588.
- [27] Toyota Fuel Cell Vehicle, https://www.toyota-global.com/innovation/environmental_technology/fuelcell_vehicle/. (2019).
- [28] J. Zhang, PEM fuel cell electrocatalysts and catalyst layers: Fundamentals and applications, 2008. doi:10.1007/978-1-84800-936-3.
- [29] H. Tawfik, Y. Hung, D. Mahajan, Polymer Electrolyte Fuel Cell Degradation, 2012. doi:10.1016/B978-0-12-386936-4.10005-3.
- [30] Y. Wang, K.S. Chen, J. Mishler, S.C. Cho, X.C. Adroher, A review of polymer electrolyte membrane fuel cells: Technology, applications, and needs on fundamental research, *Appl. Energy*. 88 (2011) 981–1007. doi:10.1016/j.apenergy.2010.09.030.
- [31] Matthew M. Mench, Fuel Cell Engines, John Wiley & Sons, Inc., 2008. doi:10.1002/9780470209769.
- [32] Y. Wang, K.S. Chen, J. Mishler, S.C. Cho, X.C. Adroher, A review of polymer electrolyte membrane fuel cells: Technology, applications, and needs on fundamental research, *Appl. Energy*. 88 (2011) 981–1007. doi:10.1016/j.apenergy.2010.09.030.
- [33] L. Dubau, L. Castanheira, F. Maillard, M. Chatenet, O. Lottin, G. Maranzana, J. Dillet, A. Lamibrac, J.C. Perrin, E. Moukheiber, A. Elkaddouri, G. De Moor, C. Bas, L. Flandin, N. Caqué, A review of PEM fuel cell durability: Materials degradation, local heterogeneities of aging and possible mitigation strategies, *Wiley Interdiscip. Rev. Energy Environ.* 3 (2014). doi:10.1002/wene.113.
- [34] B.D. James, J.M. Moton, W.G. Colella, Mass Production Cost Estimation of Direct H₂ PEM Fuel Cell Systems for Transportation Applications: 2013 Update, ASME 2014 12th Int. Conf. Fuel Cell Sci. Eng. Technol. Collocated with ASME 2014 8th Int. Conf. Energy Sustain. (2014) V001T07A002–V001T07A002.
- [35] K. Artyushkova, S. Pylypenko, M. Dowlapalli, P. Atanassov, Structure-to-property relationships in fuel cell catalyst supports: Correlation of surface chemistry and morphology with oxidation resistance of carbon blacks, *J. Power Sources*. 214 (2012) 303–313. doi:10.1016/j.jpowsour.2012.04.095.
- [36] T.R. Ralph, M.P. Hogarth, Catalysis for Low Temperature Fuel Cells. Part 1: The Cathode Challenges, *Platin. Met. Rev.* 46 (2002) 3–14. <http://www.platinummetalsreview.com/dynamic/article/view/pmr-v46-i1-003-014>.
- [37] Y.J. Wang, W. Long, L. Wang, R. Yuan, A. Ignaszak, B. Fang, D.P. Wilkinson, Unlocking the door to highly active ORR catalysts for PEMFC applications: Polyhedron-engineered Pt-based nanocrystals, *Energy Environ. Sci.* 11 (2018) 258–275. doi:10.1039/c7ee02444d.
- [38] B. Smitha, S. Sridhar, A.A. Khan, Solid polymer electrolyte membranes for fuel cell applications - A review, *J. Memb. Sci.* 259 (2005) 10–26. doi:10.1016/j.memsci.2005.01.035.
- [39] W. Liu, K. Ruth, G. Rusch, Membrane Durability in PEM Fuel Cells, *J. New Mater.*

- Electrochem. Syst. 4 (2001) 227–232. doi:10.1002/fuce.200320239.
- [40] J. Ting-Chu, J. Guo-Bin, K. Shih-Tsung, C. Pei-Hung, C. Shih-Hung, Diagnosis of PTFE-Nafion MEA degradation modes by an accelerated degradation technique, *Int. J. Energy Res.* 35 (2010) 1274–1283. doi:10.1002/er.
- [41] S. Kundu, M.W. Fowler, L.C. Simon, R. Abouatallah, N. Beydokhti, Open circuit voltage durability study and model of catalyst coated membranes at different humidification levels, *J. Power Sources.* 195 (2010) 7323–7331. doi:10.1016/j.jpowsour.2010.05.027.
- [42] F.E. Hizir, S.O. Ural, E.C. Kumbur, M.M. Mench, Characterization of interfacial morphology in polymer electrolyte fuel cells: Micro-porous layer and catalyst layer surfaces, *J. Power Sources.* 195 (2010) 3463–3471. doi:10.1016/j.jpowsour.2009.11.032.
- [43] Y.-H. Cho, H.-S. Park, J. Kim, Y.-H. Cho, S. Won Cha, Y.-E. Sung, The Operation Characteristics of MEAs with Pinholes for Polymer Electrolyte Membrane Fuel Cells, *Electrochem. Solid-State Lett.* 11 (2008) B153. doi:10.1149/1.2937450.
- [44] W. Vielstich, H. Yokokawa, *Handbook of Fuel Cells - Fundamentals Technology and Applications*, John Wiley & Sons, 2009.
- [45] J. Park, H. Oh, T. Ha, Y. Il, K. Min, A review of the gas diffusion layer in proton exchange membrane fuel cells : Durability and degradation, *Appl. Energy.* 155 (2015) 866–880. doi:10.1016/j.apenergy.2015.06.068.
- [46] T. Kitahara, T. Konomi, H. Nakajima, Microporous layer coated gas diffusion layers for enhanced performance of polymer electrolyte fuel cells, *J. Power Sources.* 195 (2010) 2202–2211. doi:10.1016/j.jpowsour.2009.10.089.
- [47] P.J. Hamilton, B.G. Pollet, Polymer electrolyte membrane fuel cell (PEMFC) flow field plate: Design, materials and characterisation, *Fuel Cells.* 10 (2010) 489–509. doi:10.1002/fuce.201000033.
- [48] O.A. Alo, I.O. Otunniyi, Hc. Pienaar, Manufacturing methods for metallic bipolar plates for polymer electrolyte membrane fuel cell, *Mater. Manuf. Process.* 34 (2019) 927–955. doi:10.1080/10426914.2019.1605170.
- [49] C. Alegre, L. Álvarez-Manuel, R. Mustata, L. Valiño, A. Lozano, F. Barreras, Assessment of the durability of low-cost Al bipolar plates for High Temperature PEM fuel cells, *Int. J. Hydrogen Energy.* 4 (2018) 0–11. doi:10.1016/j.ijhydene.2018.07.070.
- [50] B. Koraishy, J. Meyers, K. Wood, Manufacturing of membrane electrode assemblies for fuel cells, in: *Researchgate.Net*, 2010: pp. 1–13.
- [51] V. Mehta, J.S. Cooper, Review and analysis of PEM fuel cell design and manufacturing, *J. Power Sources.* 114 (2003) 32–53. doi:10.1016/S0378-7753(02)00542-6.
- [52] S. Shahgaldi, I. Alaefour, X. Li, Impact of manufacturing processes on proton exchange membrane fuel cell performance, *Appl. Energy.* 225 (2018) 1022–1032. doi:10.1016/j.apenergy.2018.05.086.
- [53] M. Stähler, A. Stähler, F. Scheepers, M. Carmo, D. Stolten, A completely slot die coated

- membrane electrode assembly, *Int. J. Hydrogen Energy*. 44 (2019) 7053–7058. doi:10.1016/j.ijhydene.2019.02.016.
- [54] C. Pak, D.J. You, K.H. Choi, H. Chang, High Performance Membrane Electrode Assemblies by Optimization of Processes and Supported Catalysts, *Hydrog. Energy Challenges Perspect.* (2012) chapter 10. doi:10.5772/53683.
- [55] G.J.M. Janssen, E.F. Sitters, Performance of thin-film cathodes for proton-exchange-membrane fuel cells based on high-surface-area carbon supports, *J. Power Sources*. 171 (2007) 8–17. doi:10.1016/j.jpowsour.2006.11.008.
- [56] J.M. Song, S. Suzuki, H. Uchida, M. Watanabe, Preparation of high catalyst utilization electrodes for polymer electrolyte fuel cells, *Langmuir*. 22 (2006) 6422–6428. doi:10.1021/la060671w.
- [57] S. Shukla, K. Domican, K. Karan, S. Bhattacharjee, M. Secanell, *Electrochimica Acta Analysis of Low Platinum Loading Thin Polymer Electrolyte Fuel Cell Electrodes Prepared by Inkjet Printing*, *Electrochim. Acta*. 156 (2015) 289–300. doi:10.1016/j.electacta.2015.01.028.
- [58] R. Lin, X. Cai, H. Zeng, Z. Yu, Stability of High-Performance Pt-Based Catalysts for Oxygen Reduction Reactions, *Adv. Mater.* 30 (2018) 1–8. doi:10.1002/adma.201705332.
- [59] D.S. Hwang, C.H. Park, S.C. Yi, Y.M. Lee, Optimal catalyst layer structure of polymer electrolyte membrane fuel cell, *Int. J. Hydrogen Energy*. 36 (2011) 9876–9885. doi:10.1016/j.ijhydene.2011.05.073.
- [60] C. Pak, D.J. You, K.H. Choi, H. Chang, High Performance Membrane Electrode Assemblies by Optimization of Processes and Supported Catalysts, *Hydrog. Energy Challenges Perspect.* (2012) 259–278. doi:10.5772/53683.
- [61] H. Tang, S. Wang, M. Pan, S.P. Jiang, Y. Ruan, Performance of direct methanol fuel cells prepared by hot-pressed MEA and catalyst-coated membrane (CCM), *Electrochim. Acta*. 52 (2007) 3714–3718. doi:10.1016/j.electacta.2006.10.053.
- [62] T. V. Reshetyenko, G. Bender, K. Bethune, R. Rocheleau, Effects of local variations of the gas diffusion layer properties on PEMFC performance using a segmented cell system, *Electrochim. Acta*. 80 (2012) 368–376. doi:10.1016/j.electacta.2012.07.031.
- [63] M.S. Saha, D.K. Paul, B.A. Peppley, K. Karan, Fabrication of catalyst-coated membrane by modified decal transfer technique, *Electrochem. Commun.* 12 (2010) 410–413. doi:10.1016/j.elecom.2010.01.006.
- [64] The United States Council for Automotive Research, USCAR Fuel cell tech team cell component accelerated stress test protocols - Revised May 26, 2010, 2010. http://www1.eere.energy.gov/hydrogenandfuelcells/pdfs/component_durability_may_2010.pdf.
- [65] L. Placca, R. Kouta, Fault tree analysis for PEM fuel cell degradation process modelling, *Int. J. Hydrogen Energy*. 36 (2011) 12393–12405. doi:10.1016/j.ijhydene.2011.06.093.
- [66] J. Wu, X.Z. Yuan, J.J. Martin, H. Wang, J. Zhang, J. Shen, S. Wu, W. Merida, A review of

- PEM fuel cell durability: Degradation mechanisms and mitigation strategies, *J. Power Sources*. 184 (2008) 104–119.
- [67] S. Vengatesan, K. Panha, M.W. Fowler, X.Z. Yuan, H. Wang, Membrane electrode assembly degradation under idle conditions via unsymmetrical reactant relative humidity cycling, *J. Power Sources*. 207 (2012) 101–110. doi:10.1016/j.jpowsour.2012.01.133.
- [68] S. Kreitmeier, P. Lerch, A. Wokaun, F.N. Büchi, Local Degradation at Membrane Defects in Polymer Electrolyte Fuel Cells, *J. Electrochem. Soc.* 160 (2013) F456–F463. doi:10.1149/1.023306jes.
- [69] G. Bender, W. Felt, M. Ulsh, Detecting and localizing failure points in proton exchange membrane fuel cells using IR thermography, *J. Power Sources*. 253 (2014) 224–229. doi:10.1016/j.jpowsour.2013.12.045.
- [70] S.R. Dhanushkodi, S. Kundu, M.W. Fowler, M.D. Pritzker, Study of the effect of temperature on Pt dissolution in polymer electrolyte membrane fuel cells via accelerated stress tests, *J. Power Sources*. 245 (2014) 1035–1045. doi:10.1016/j.jpowsour.2013.07.016.
- [71] M. Bodner, C. Hochenauer, V. Hacker, Effect of pinhole location on degradation in polymer electrolyte fuel cells, *J. Power Sources*. 295 (2015) 336–348. doi:10.1016/j.jpowsour.2015.07.021.
- [72] X.Z. Yuan, S. Zhang, S. Ban, C. Huang, H. Wang, V. Singara, M. Fowler, M. Schulze, A. Haug, K. Andreas Friedrich, R. Hiesgen, Degradation of a PEM fuel cell stack with Nafion[®] membranes of different thicknesses. Part II: Ex situ diagnosis, *J. Power Sources*. 205 (2012) 324–334. doi:10.1016/j.jpowsour.2012.01.074.
- [73] M. Jourdani, H. Mounir, A. El Marjani, Compilation of factors affecting durability of proton exchange membrane fuel cell (PEMFC), *Proc. 2014 Int. Renew. Sustain. Energy Conf. IRSEC 2014*. (2014) 542–547. doi:10.1109/IRSEC.2014.7059906.
- [74] A.S. Alavijeh, M. Goulet, R.M.H. Khorasany, J. Ghataurah, C. Lim, M. Lauritzen, E. Kjeang, G.G. Wang, R.K.N.D. Rajapakse, Decay in Mechanical Properties of Catalyst Coated Membranes Subjected to Combined Chemical and Mechanical Membrane Degradation, (2015) 204–213. doi:10.1002/fuce.201400040.
- [75] A. Collier, H. Wang, X. Zi Yuan, J. Zhang, D.P. Wilkinson, Degradation of polymer electrolyte membranes, *Int. J. Hydrogen Energy*. 31 (2006) 1838–1854. doi:10.1016/j.ijhydene.2006.05.006.
- [76] L. Ghassemzadeh, K. Kreuer, J. Maier, K. Mu, Chemical Degradation of Nafion Membranes under Mimic Fuel Cell Conditions as Investigated by Solid-State NMR Spectroscopy What if there is no metal ion? Will Nafion still be degraded by treatment?, *J. Phys. Chem. C*. 114 (2010) 14635–14645.
- [77] G.S. Hwang, H. Kim, R. Lujan, R. Mukundan, D. Spornjak, R.L. Borup, M. Kaviani, M.H. Kim, A.Z. Weber, Phase-change-related degradation of catalyst layers in proton-exchange-membrane fuel cells, *Electrochim. Acta*. 95 (2013) 29–37. doi:10.1016/j.electacta.2013.02.017.
- [78] J. St-Pierre, D.P. Wilkinson, S. Knights, M.L. Bos, Relationships between water

- management, contamination and lifetime degradation in PEFC, *J. New Mater. Electrochem. Syst.* 3 (2000) 99–106.
- [79] M.K. Kadirov, A. Bosnjakovic, S. Schlick, Membrane-derived fluorinated radicals detected by electron spin resonance in UV-irradiated nation and Dow ionomers: Effect of counterions and H₂O₂, *J. Phys. Chem. B.* 109 (2005) 7664–7670. doi:10.1021/jp044987t.
- [80] S. Mu, P. Zhao, C. Xu, Y. Gao, M. Pan, Detaching behaviors of catalyst layers applied in PEM fuel cells by off-line accelerated test, *Int. J. Hydrogen Energy.* 35 (2010) 8155–8160. doi:10.1016/j.ijhydene.2009.12.182.
- [81] R. Shimoi, Takashi Aoyama, A. Iiyama, Development of Fuel Cell Stack Durability Based on Actual Vehicle Test Data: Current Status and Future Work, *Int. J. Engines.* 2 (2009) 960–970. <http://www.jstor.org/stable/26308446>.
- [82] A. Sadeghi Alavijeh, R.M.H. Khorasany, A. Habisch, G.G. Wang, E. Kjeang, Creep properties of catalyst coated membranes for polymer electrolyte fuel cells, *J. Power Sources.* 285 (2015) 16–28. doi:10.1016/j.jpowsour.2015.03.082.
- [83] S. Vengatesan, M.W. Fowler, X.Z. Yuan, H. Wang, Diagnosis of MEA degradation under accelerated relative humidity cycling, *J. Power Sources.* 196 (2011) 5045–5052. doi:10.1016/j.jpowsour.2011.01.088.
- [84] H.F.M. Mohamed, Y. Kobayashi, C.S. Kuroda, A. Ohira, Impact of heating on the structure of perfluorinated polymer electrolyte membranes: A positron annihilation study, *Macromol. Chem. Phys.* 212 (2011) 708–714. doi:10.1002/macp.201000693.
- [85] R.A. Silva, T. Hashimoto, G.E. Thompson, C.M. Rangel, Characterization of MEA degradation for an open air cathode PEM fuel cell, *Int. J. Hydrogen Energy.* 37 (2012) 7299–7308. doi:10.1016/j.ijhydene.2011.12.110.
- [86] M. Uchimura, S.S. Kocha, The Impact of Cycle Profile on PEMFC Durability, 11 (2007) 1215–1226. doi:10.1149/1.2781035.
- [87] M. Uchimura, S. Sugawara, Y. Suzuki, J. Zhang, S.S. Kocha, Electrocatalyst Durability under Simulated Automotive Drive Cycles, *Electrochem. Soc.* 16 (2008) 225–234.
- [88] S. Kreitmeier, M. Michiardi, A. Wokaun, F.N. Büchi, Factors determining the gas crossover through pinholes in polymer electrolyte fuel cell membranes, *Electrochim. Acta.* 80 (2012) 240–247. doi:10.1016/j.electacta.2012.07.013.
- [89] M. Jouin, R. Gouriveau, D. Hissel, M.C. Péra, N. Zerhouni, Degradations analysis and aging modeling for health assessment and prognostics of PEMFC, *Reliab. Eng. Syst. Saf.* 148 (2016) 78–95. doi:10.1016/j.ress.2015.12.003.
- [90] M. Hu, G. Cao, Research on the long-term stability of a PEMFC stack: Analysis of pinhole evolution, *Int. J. Hydrogen Energy.* 39 (2014) 7940–7954. doi:10.1016/j.ijhydene.2014.03.072.
- [91] Y. Singh, F.P. Orfino, M. Dutta, E. Kjeang, 3D visualization of membrane failures in fuel cells, *J. Power Sources.* 345 (2017) 1–11. doi:10.1016/j.jpowsour.2017.01.129.

- [92] G. De Moor, C. Bas, N. Charvin, E. Moukheiber, F. Niepceron, N. Breilly, J. Andr??, E. Rossinot, E. Claude, N.D. Albrola, L. Flandin, Understanding membrane failure in PEMFC: Comparison of diagnostic tools at different observation scales, *Fuel Cells*. 12 (2012) 356–364. doi:10.1002/face.201100161.
- [93] S. Kreitmeier, P. Lerch, a. Wokaun, F.N. Buchi, Local Degradation at Membrane Defects in Polymer Electrolyte Fuel Cells, *J. Electrochem. Soc.* 160 (2013) F456–F463. doi:10.1149/1.023306jes.
- [94] S.M. Kim, C.-Y. Ahn, Y.-H. Cho, S. Kim, W. Hwang, S. Jang, S. Shin, G. Lee, Y.-E. Sung, M. Choi, High-performance Fuel Cell with Stretched Catalyst-Coated Membrane: One-step Formation of Cracked Electrode, *Sci. Rep.* 6 (2016) 26503. doi:10.1038/srep26503.
- [95] J. Xie, D.L. Wood, K.L. More, P. Atanassov, R.L. Borup, Microstructural Changes of Membrane Electrode Assemblies during PEFC Durability Testing at High Humidity Conditions, *J. Electrochem. Soc.* 152 (2005) A1011. doi:10.1149/1.1873492.
- [96] R. Banan, J. Zu, A. Bazylak, Humidity and temperature cycling effects on cracks and delaminations in PEMFCs, *Fuel Cells*. 15 (2015) 327–336. doi:10.1002/face.201400118.
- [97] V. Stanic, M. Hoberecht, Mechanism of pin-hole formation in membrane electrode assemblies for PEM fuel cells, *Prot. Conduct. Membr. Fuel Cells IV.* (2006) 391–401.
- [98] M. Ulsh, B. Sopori, N. V Aieta, G. Bender, Challenges to High-Volume Production of Fuel Cell Materials: Quality Control, *ECS Trans.* 50 (2013) 919–926. doi:10.1149/05002.0919ecst.
- [99] P. Reinholdtsen, B. Khuri-Yakub, T. The Effects of Surface Roughness on Subsurface Defect Detection using Acoustic Microscopy, *Edward L.Ginz. Lab. Stanford, Calif.* 94305. (n.d.) 485–491.
- [100] D.R.P. Morris, S.P. Liu, D. Villegas Gonzalez, J.T. Gostick, Effect of Water Sorption on the Electronic Conductivity of Porous Polymer Electrolyte Membrane Fuel Cell Catalyst Layers, *ACS Appl. Mater. Interfaces*. 6 (2014) 18609–18618.
- [101] T. V. Reshetyenko, G. Bender, K. Bethune, R. Rocheleau, Application of a segmented cell setup to detect pinhole and catalyst loading defects in proton exchange membrane fuel cells, *Electrochim. Acta.* 76 (2012) 16–25. doi:10.1016/j.electacta.2012.04.138.
- [102] S. Prass, S. Hasanpour, P.K. Sow, A.B. Phillion, W. Merida, Microscale X-ray tomographic investigation of the interfacial morphology between the catalyst and micro porous layers in proton exchange membrane fuel cells, *J. Power Sources*. 319 (2016) 82–89. doi:10.1016/j.jpowsour.2016.04.031.
- [103] M. Uish, M. Porter, J. C. Bittinat, D. G. Bender, Defect Detection in Fuel Cell Gas Diffusion Electrodes Using Infrared Thermography, *Fuel Cells*. 16 (2016) 170–178. doi:10.1002/face.201500137.
- [104] K. Panha, M. Fowler, X.Z. Yuan, H. Wang, Accelerated durability testing via reactants relative humidity cycling on PEM fuel cells, *Appl. Energy*. 93 (2012) 90–97. doi:10.1016/j.apenergy.2011.05.011.

- [105] M. Ciureanu and R. Roberge, Electrochemical impedance study of PEM fuel cells. Experimental diagnostics and modeling of air cathodes, *J. Phys. Chem B* 105 (2001) 3531-3539.
- [106] T. V. Reshetyenko, G. Bender, K. Bethune, R. Rocheleau, Effects of local variations of the gas diffusion layer properties on PEMFC performance using a segmented cell system, *Electrochim. Acta.* 80 (2012) 368–376. doi:10.1016/j.electacta.2012.07.031.
- [107] R. Lin, E. Gülzow, M. Schulze, K.A. Friedrich, Investigation of Membrane Pinhole Effects in Polymer Electrolyte Fuel Cells by Locally Resolved Current Density, *J. Electrochem. Soc.* 158 (2011) B11. doi:10.1149/1.3504255.
- [108] X.Z. Yuan, H. Li, S. Zhang, J. Martin, H. Wang, A review of polymer electrolyte membrane fuel cell durability test protocols, *J. Power Sources.* 196 (2011) 9107–9116. doi:10.1016/j.jpowsour.2011.07.082.
- [109] R. Mukundan, A.M. Baker, A. Kusoglu, P. Beattie, S. Knights, A.Z. Weber, R.L. Borup, Membrane Accelerated Stress Test Development for Polymer Electrolyte Fuel Cell Durability Validated Using Field and Drive Cycle Testing, *J. Electrochem. Soc.* 165 (2018) F3085–F3093. doi:10.1149/2.0101806jes.
- [110] H. Wang, X.-Z. Yuan, H. Li, PEM Fuel Cell Diagnostic Tools, CRC Press, 2017. <https://www.crcpress.com/PEM-Fuel-Cell-Diagnostic-Tools/Wang-Yuan-Li/p/book/9781138113343>.
- [111] S. Kundu, M. Fowler, L.C. Simon, R. Abouatallah, Reversible and irreversible degradation in fuel cells during Open Circuit Voltage durability testing, *J. Power Sources.* 182 (2008) 254–258. doi:10.1016/j.jpowsour.2008.04.009.
- [112] E. Endoh, S. Terazono, H. Widjaja, Y. Takimoto, Degradation Study of MEA for PEMFCs under Low Humidity Conditions, *Electrochem. Solid-State Lett.* 7 (2004) A209. doi:10.1149/1.1739314.
- [113] N. Macauley, A.S. Alavijeh, M. Watson, J. Kolodziej, M. Lauritzen, S. Knights, G. Wang, E. Kjeang, Accelerated Membrane Durability Testing of Heavy Duty Fuel Cells, 162 (2015) 98–107. doi:10.1149/2.0671501jes.
- [114] S. Zhang, X.Z. Yuan, J.N.C. Hin, H. Wang, J. Wu, K.A. Friedrich, M. Schulze, Effects of open-circuit operation on membrane and catalyst layer degradation in proton exchange membrane fuel cells, *J. Power Sources.* 195 (2010) 1142–1148. doi:10.1016/j.jpowsour.2009.08.070.
- [115] M. Yandrasits, M. Lindell, S. Hamrock, G. Haugen, E. Fort, D. Peppin, A. Komlev, K. Kalstabakken, Chemical Stability of Perfluorobis (sulfonyl) imide-Acid (PFIA) Ionomers in Open Circuit Voltage (OCV) Accelerated Test Conditions, *J. Electrochem. Soc.* 165 (2018) 3261–3270. doi:10.1149/2.0301806jes.
- [116] V.A. Sethuraman, J.W. Weidner, A.T. Haug, L. V. Protsailo, Durability of Perfluorosulfonic Acid and Hydrocarbon Membranes: Effect of Humidity and Temperature, *J. Electrochem. Soc.* 155 (2008) B119. doi:10.1149/1.2806798.
- [117] C. Lim, A.S. Alavijeh, M. Lauritzen, J. Kolodziej, S. Knights, E. Kjeang, Fuel Cell

- Durability Enhancement with Cerium Oxide under Combined Chemical and Mechanical Membrane Degradation, *ECS Electrochem. Lett.* 4 (2015) F29–F31. doi:10.1149/2.0081504eel.
- [118] P. Zihrul, P. Weber, J. Durst, H.A. Gasteiger, F. Hasché, Impact of Hydrogen Bleeding into the Cathode Feed of a PEM Fuel Cell, *J. Electrochem. Soc.* 164 (2017) F209–F216. doi:10.1149/2.0161704jes.
- [119] Q. Lin, S. Shi, L. Wang, S. Chen, X. Chen, G. Chen, In-plane biaxial cyclic mechanical behavior of proton exchange membranes, *J. Power Sources.* 360 (2017) 495–503. doi:10.1016/j.jpowsour.2017.06.040.
- [120] X.-Z. Yuan, C. Song, H. Wang, J. Zhang, *Electrochemical Impedance Spectroscopy in PEM Fuel Cells*, Springer US, 2010.
- [121] R. Borup, J. Meyers, B. Pivovar, Y.S. Kim, R. Mukundan, N. Garland, D. Myers, M. Wilson, F. Garzon, D. Wood, P. Zelenay, K. More, K. Stroh, T. Zawodzinski, J. Boncella, J.E. McGrath, M. Inaba, K. Miyatake, M. Hori, K. Ota, Z. Ogumi, S. Miyata, A. Nishikata, Z. Siroma, Y. Uchimoto, K. Yasuda, K.I. Kimijima, N. Iwashita, Scientific aspects of polymer electrolyte fuel cell durability and degradation, *Chem. Rev.* 107 (2007) 3904–3951. doi:10.1021/cr050182l.
- [122] Y. Shao, G. Yin and Y. Gao, Understanding and approaches for the durability issues of Pt-based catalysts for PEM fuel cell, *J. Power Sources.* 171 (2007) 558–566. doi:10.1016/j.jpowsour.2007.07.00.
- [123] A.E. Dolinko, Non-destructive visualization of defect borders in flawed plates inspected by thermal load, *J. Phys. D. Appl. Phys.* 41 (2008) 205503. doi:10.1088/0022-3727/41/20/205503.
- [124] M. Hamour, J.C. Grandidier, A. Ouibrahim, S. Martemianov, Electrical conductivity of PEMFC under loading, *J. Power Sources.* 289 (2015) 160–167. doi:10.1016/j.jpowsour.2015.04.145.
- [125] A. Arvay, E. Yli-rantala, C. Liu, X. Peng, P. Koski, L. Cindrella, P. Kauranen, P.M. Wilde, A.M. Kannan, Characterization techniques for gas diffusion layers for proton exchange membrane fuel cells e A review, *J. Power Sources.* 213 (2012) 317–337. doi:10.1016/j.jpowsour.2012.04.026.
- [126] Y. SINGH, Electrical Resistivity Measurements: a Review, *Int. J. Mod. Phys. Conf. Ser.* 22 (2013) 745–756. doi:10.1142/S2010194513010970.
- [127] M.K. Raja, S. Mahadevan, B.P.C. Rao, S.P. Behera, T. Jayakumar, S.P. Behera, T. Jayakumar, B. Raj, Influence of crack length on crack depth measurement by an alternating current potential drop technique, *Meas. Sci. Technol.* 21 (2010). doi:10.1088/0957-0233/21/10/105702.
- [128] S.V. Venkatesan, M. El Hannach, S. Holdcroft, E. Kjeang, Probing nanoscale membrane degradation in fuel cells through electron tomography, *J. Memb. Sci.* 539 (2017) 138–143. doi:10.1016/j.memsci.2017.05.073.
- [129] E. Carcadea, M. Varlam, D.B. Ingham, M.S. Ismail, L. Patularu, A. Marinoiu, D. Schitea,

- The effects of cathode flow channel size and operating conditions on PEM fuel performance: A CFD modelling study and experimental demonstration, *Int. J. Energy Res.* (2018) 1–16. doi:10.1002/er.4068.
- [130] G. Ding, M.H. Santare, A.M. Karlsson, A. Kusoglu, Numerical evaluation of crack growth in polymer electrolyte fuel cell membranes based on plastically dissipated energy, *J. Power Sources*. 316 (2016) 114–123. doi:10.1016/j.jpowsour.2016.03.031.
- [131] P. Berg, A.A. Kulikovskiy, A model for a crack or a delaminated region in a PEM fuel cell anode: analytical solutions, *Electrochim. Acta*. 174 (2015) 424–429. doi:10.1016/j.electacta.2015.05.189.
- [132] Dupont Fuel Cell Store, DuPont™ Nafion® PFSA Membranes NR-211 and NR-212, Fuelcellstore. (2010) 1–5. <http://www.fuelcellstore.com/spec-sheets/nafion-211-212-spec-sheet.pdf>.
- [133] T. Arlt, I. Manke, C. Tötzke, D. Gerteisen, J. Scholta, H. Rieseemeier, M. Klages, J. Banhart, R. Alink, J. Haußmann, H. Markötter, Influence of cracks in the microporous layer on the water distribution in a PEM fuel cell investigated by synchrotron radiography, *Electrochem. Commun.* 34 (2013) 22–24. doi:10.1016/j.elecom.2013.04.006.
- [134] T. Uchiyama, H. Kumei, T. Yoshida, Catalyst layer cracks by buckling deformation of membrane electrode assemblies under humidity cycles and mitigation methods, *J. Power Sources*. 238 (2013) 403–412. doi:10.1016/j.jpowsour.2013.04.026.
- [135] Y. Matsui, T. Suzuki, P. Deevanhxay, S. Tsushima, S. Hirai, crack generation in catalyst layer and micro porous layer by wet-dry cycles and its impact on pemfc performance, in: *ASME 2013 11th Int. Conf. Fuel Cell Sci. Eng. Technol.*, 2013: pp. 1–5.
- [136] S. Mu, C. Xu, Y. Gao, H. Tang, M. Pan, Accelerated durability tests of catalyst layers with various pore volume for catalyst coated membranes applied in PEM fuel cells, *Int. J. Hydrogen Energy*. 35 (2010) 2872–2876. doi:10.1016/j.ijhydene.2009.05.022.
- [137] F. Jing, M. Hou, W. Shi, J. Fu, H. Yu, P. Ming, B. Yi, The effect of ambient contamination on PEMFC performance, *J. Power Sources*. 166 (2007) 172–176. doi:10.1016/j.jpowsour.2006.12.103.
- [138] D. You, Y. Lee, H. Cho, J.-H. Kim, C. Pak, G. Lee, K.-Y. Park, J.-Y. Park, High performance membrane electrode assemblies by optimization of coating process and catalyst layer structure in direct methanol fuel cells, *Int. J. Hydrogen Energy*. 36 (2011) 5096–5103. doi:10.1016/j.ijhydene.2011.01.068.
- [139] M. Yazdanpour, A. Esmailifar, S. Rowshanzamir, Optimization of catalyst ink composition for the preparation of a membrane electrode assembly in a proton exchange membrane fuel cell using the decal transfer, *Int. J. Hydrogen Energy*. 37 (2012) 11290–11298. doi:10.1016/j.ijhydene.2012.04.139.
- [140] A. Phillips, M. Ulsh, J. Porter, G. Bender, Utilizing a Segmented Fuel Cell to Study the Effects of Electrode Coating Irregularities on PEM Fuel Cell Initial Performance, *Fuel Cells*. 17 (2017) 288–298. doi:10.1002/face.201600214.
- [141] U.S. Department of Energy, DOE CELL COMPONENT ACCELERATED STRESS

TEST, 2010.

- [142] H. Gunji, M. Eguchi, F. Sekine, Y. Tsutsumi, Gas-leak-induced pinhole formation at polymer electrolyte membrane fuel cell electrode edges, *Int. J. Hydrogen Energy*. 42 (2017) 562–574. doi:10.1016/j.ijhydene.2016.11.038.
- [143] Y. Singh, F.P. Orfino, M. Dutta, E. Kjeang, 3D Failure Analysis of Pure Mechanical and Pure Chemical Degradation in Fuel Cell Membranes, *J. Electrochem. Soc.* 164 (2017) F1331–F1341. doi:10.1149/2.0451713jes.
- [144] M. Pestrak, Y. Li, S.W. Case, D. a. Dillard, M.W. Ellis, Y.-H. Lai, C.S. Gittleman, The Effect of Mechanical Fatigue on the Lifetimes of Membrane Electrode Assemblies, *J. Fuel Cell Sci. Technol.* 7 (2010) 041009. doi:10.1115/1.4000629.
- [145] G. De Moor, C. Bas, N. Charvin, J. Dillet, G. Maranzana, O. Lottin, N. Caqué, E. Rossinot, L. Flandin, Perfluorosulfonic acid membrane degradation in the hydrogen inlet region: A macroscopic approach, *Int. J. Hydrogen Energy*. 41 (2016) 483–496. doi:10.1016/j.ijhydene.2015.10.066.
- [146] K.-L. Jang, S. Kim, B.-H. Jeong, J.-G. Oh, B.K. Hong, T.-S. Kim, Electromechanical diagnostic method for monitoring cracks in polymer electrolyte fuel cell electrodes, *Int. J. Hydrogen Energy*. 42 (2017) 11644–11653. doi:10.1016/j.ijhydene.2017.02.010.
- [147] Q. Meyer, N. Mansor, F. Iacoviello, P.L. Cullen, R. Jervis, D. Finegan, C. Tan, J. Bailey, P.R. Shearing, D.J.L. Brett, *Electrochimica Acta* Investigation of Hot Pressed Polymer Electrolyte Fuel Cell Assemblies via X-ray Computed Tomography, *Electrochim. Acta*. 242 (2017) 125–136. doi:10.1016/j.electacta.2017.05.028.
- [148] B. James, 2018 Cost Projections of PEM Fuel Cell Systems for Automobiles and Medium-Duty Vehicles, 2018.
- [149] S. Kreitmeier, G.A. Schuler, A. Wokaun, F.N. Büchi, Investigation of membrane degradation in polymer electrolyte fuel cells using local gas permeation analysis, *J. Power Sources*. 212 (2012) 139–147. doi:10.1016/j.jpowsour.2012.03.071.
- [150] S. Zhang, X. Yuan, H. Wang, W. Mérida, H. Zhu, J. Shen, S. Wu, J. Zhang, A review of accelerated stress tests of MEA durability in PEM fuel cells, *Int. J. Hydrogen Energy*. 34 (2009) 388–404. doi:10.1016/j.ijhydene.2008.10.012.
- [151] N.S. Khattra, Z. Lu, A.M. Karlsson, M.H. Santare, F.C. Busby, T. Schmiedel, Time-dependent mechanical response of a composite PFSA membrane, *J. Power Sources*. 228 (2013) 256–269. doi:10.1016/j.jpowsour.2012.11.116.
- [152] Y. Huang, R. Solasi, Y. Zou, M. Feshler, T.H. Madden, Mechanical Endurance of Polymer Electrolyte Membrane and PEM Fuel Cell Durability, *J. Polym. Sci. Part B Polym. Phys.* 44 (2006) 2346–2357. doi:10.1002/polb.20863.
- [153] S. Subianto, M. Pica, M. Casciola, P. Cojocar, L. Merlo, G. Hards, D.J. Jones, Physical and chemical modification routes leading to improved mechanical properties of perfluorosulfonic acid membranes for PEM fuel cells, *J. Power Sources*. 233 (2013) 216–230. doi:10.1016/j.jpowsour.2012.12.121.

- [154] A. Mehmood, M.G. An, H.Y. Ha, Physical degradation of cathode catalyst layer: A major contributor to accelerated water flooding in long-term operation of DMFCs, *Appl. Energy*. 129 (2014) 346–353. doi:10.1016/j.apenergy.2014.05.016.
- [155] P. Pei, H. Chen, Main factors affecting the lifetime of Proton Exchange Membrane fuel cells in vehicle applications: A review, *Appl. Energy*. 125 (2014) 60–75. doi:10.1016/j.apenergy.2014.03.048.
- [156] M. Jouin, M. Bressel, S. Morando, R. Gouriveau, D. Hissel, M.C. Péra, N. Zerhouni, S. Jemei, M. Hilairret, B. Ould Bouamama, Estimating the end-of-life of PEM fuel cells: Guidelines and metrics, *Appl. Energy*. 177 (2016) 87–97. doi:10.1016/j.apenergy.2016.05.076.
- [157] R. Borup, J. Meyers, B. Pivovar, Y.S. Kim, R. Mukundan, N. Garland, D. Myers, M. Wilson, F. Garzon, D. Wood, P. Zelenay, K. More, K. Stroh, T. Zawodzinski, J. Boncella, J.E. McGrath, M. Inaba, K. Miyatake, M. Hori, K. Ota, Z. Ogumi, S. Miyata, A. Nishikata, Z. Siroma, Y. Uchimoto, K. Yasuda, K.I. Kimijima, N. Iwashita, Scientific aspects of polymer electrolyte fuel cell durability and degradation, *Chem. Rev.* 107 (2007) 3904–3951. doi:10.1021/cr050182l.
- [158] Y. Tang, A. Kusoglu, A.M. Karlsson, M.H. Santare, S. Cleghorn, W.B. Johnson, Mechanical properties of a reinforced composite polymer electrolyte membrane and its simulated performance in PEM fuel cells, *J. Power Sources*. 175 (2008) 817–825. doi:10.1016/j.jpowsour.2007.09.093.
- [159] Y.-H. Lai, C.K. Mittelsteadt, C.S. Gittleman, D.A. Dillard, Viscoelastic Stress Analysis of Constrained Proton Exchange Membranes Under Humidity Cycling, *J. Fuel Cell Sci. Technol.* 6 (2009) 021002. doi:10.1115/1.2971045.
- [160] T.R. Ralph, D.E. Barnwell, P.J. Bouwman, A.J. Hodgkinson, M.I. Petch, M. Pollington, Reinforced Membrane Durability in Proton Exchange Membrane Fuel Cell Stacks for Automotive Applications, *J. Electrochem. Soc.* 155 (2008) B411. doi:10.1149/1.2838163.
- [161] S. Kundu, M.W. Fowler, L.C. Simon, R. Abouatallah, N. Beydokhti, Degradation analysis and modeling of reinforced catalyst coated membranes operated under OCV conditions, *J. Power Sources*. 183 (2008) 619–628. doi:10.1016/j.jpowsour.2008.05.074.
- [162] S. Asghari, A. Mokmeli, M. Samavati, Study of PEM fuel cell performance by electrochemical impedance spectroscopy, *Int. J. Hydrogen Energy*. 35 (2010) 9283–9290. doi:10.1016/J.IJHYDENE.2010.03.069.
- [163] T. V Reshetenko, J. St-Pierre, K. Artyushkova, R. Rocheleau, P. Atanassov, G. Bender, M. Ulsh, Multianalytical Study of the PTFE Content Local Variation of the PEMFC Gas Diffusion Layer, *J. Electrochem. Soc.* 160 (2013) F1305–F1315. doi:10.1149/2.104311jes.
- [164] J.-M. Le Canut, R.M. Abouatallah, D.A. Harrington, Detection of Membrane Drying, Fuel Cell Flooding, and Anode Catalyst Poisoning on PEMFC Stacks by Electrochemical Impedance Spectroscopy, *J. Electrochem. Soc.* 153 (2006) A857. doi:10.1149/1.2179200.
- [165] M. Watanabe, H. Yano, H. Uchida, D.A. Tryk, Achievement of distinctively high durability at nanosized Pt catalysts supported on carbon black for fuel cell cathodes, *J. Electroanal.*

- Chem. 819 (2018) 359–364. doi:10.1016/j.jelechem.2017.11.017.
- [166] W. Bi, G.E. Gray, T.F. Fuller, PEM Fuel Cell Pt / C Dissolution and Deposition in Nafion Electrolyte, (2007) 20–23. doi:10.1149/1.2712796.
- [167] P. Chippar, K. Oh, W.-G. Kim, H. Ju, Numerical analysis of effects of gas crossover through membrane pinholes in high-temperature proton exchange membrane fuel cells, *Int. J. Hydrogen Energy*. 39 (2013) 1–9. doi:10.1016/j.ijhydene.2013.05.117.
- [168] P. Vanya, J. Sharman, J.A. Elliott, Mesoscale simulations of confined Nafion thin films, *J. Chem. Phys.* 147 (2017). doi:10.1063/1.4996695.
- [169] N.S. Khattra, A.M. Karlsson, M.H. Santare, P. Walsh, F.C. Busby, Effect of time-dependent material properties on the mechanical behavior of PFSA membranes subjected to humidity cycling, *J. Power Sources*. 214 (2012) 365–376. doi:10.1016/j.jpowsour.2012.04.065.
- [170] K.C. Neyerlin, H.A. Gasteiger, C.K. Mittelstaedt, J. Jorne, W. Gu, Effect of Relative Humidity on Oxygen Reduction Kinetics in a PEMFC, *J. Electrochem. Soc.* 152 (2005) A1073. doi:10.1149/1.1897368.
- [171] J.T. Gostick, M. A. Ioannidis, M.W. Fowler, M.D. Pritzker, On the role of the microporous layer in PEMFC operation, *Electrochem. Commun.* 11 (2009) 576–579. doi:10.1016/j.elecom.2008.12.053.
- [172] G. Chen, H. Zhang, H. Ma, H. Zhong, Electrochemical durability of gas diffusion layer under simulated proton exchange membrane fuel cell conditions, *Int. J. Hydrogen Energy*. 34 (2009) 8185–8192. doi:10.1016/j.ijhydene.2009.07.085.
- [173] S. Yu, X. Li, J. Li, S. Liu, W. Lu, Z. Shao, B. Yi, Study on hydrophobicity degradation of gas diffusion layer in proton exchange membrane fuel cells, *Energy Convers. Manag.* 76 (2013) 301–306. doi:10.1016/j.enconman.2013.07.034.
- [174] L. Cindrella, A.M. Kannan, J.F. Lin, K. Saminathan, Y. Ho, C.W. Lin, J. Wertz, Gas diffusion layer for proton exchange membrane fuel cells-A review, *J. Power Sources*. 194 (2009) 146–160. doi:10.1016/j.jpowsour.2009.04.005.
- [175] M. Han, J.H. Xu, S.H. Chan, S.P. Jiang, Characterization of gas diffusion layers for PEMFC, *Electrochim. Acta.* 53 (2008) 5361–5367. doi:10.1016/j.electacta.2008.02.057.
- [176] S.B. Park, Y. Il Park, Fabrication of gas diffusion layer (GDL) containing microporous layer using fluorinated ethylene propylene (FEP) for proton exchange membrane fuel cell (PEMFC), *Int. J. Precis. Eng. Manuf.* 13 (2012) 1145–1151. doi:10.1007/s12541-012-0152-x.
- [177] W.M. Yan, C.Y. Hsueh, C.Y. Soong, F. Chen, C.H. Cheng, S.C. Mei, Effects of fabrication processes and material parameters of GDL on cell performance of PEM fuel cell, *Int. J. Hydrogen Energy*. 32 (2007) 4452–4458. doi:10.1016/j.ijhydene.2007.02.003.
- [178] J. Park, H. Oh, T. Ha, Y. Il Lee, K. Min, A review of the gas diffusion layer in proton exchange membrane fuel cells: Durability and degradation, *Appl. Energy*. 155 (2015) 866–880. doi:10.1016/j.apenergy.2015.06.068.

- [179] E.C.S. Transactions, T.E. Society, Defect Detection in Fuel Cell Gas Diffusion Electrodes Using Infrared Thermography D.C. Bittinat, 58 (2013) 495–503. doi:10.1002/fuce.201500137.
- [180] M.I. Rosli, D.J. Borman, D.B. Ingham, M.S. Ismail, L. Ma, M. Pourkashanian, Transparent PEM Fuel Cells for Direct Visualization Experiments, *J. Fuel Cell Sci. Technol.* 7 (2010) 061015. doi:10.1115/1.4001353.
- [181] J. Wu, X. Zi Yuan, H. Wang, M. Blanco, J.J. Martin, J. Zhang, Diagnostic tools in PEM fuel cell research: Part II. Physical/chemical methods, *Int. J. Hydrogen Energy.* 33 (2008) 1747–1757. doi:10.1016/j.ijhydene.2008.01.020.
- [182] A. Bazylak, Liquid water visualization in PEM fuel cells: A review, *Int. J. Hydrogen Energy.* 34 (2009) 3845–3857. doi:10.1016/j.ijhydene.2009.02.084.
- [183] E.S. De Castro, V. Gurau, High Speed, Low Cost Fabrication of Gas Diffusion Electrodes for Membrane Electrode Assemblies, 2010.
- [184] J.H. Chun, D.H. Jo, S.G. Kim, S.H. Park, C.H. Lee, S.H. Kim, Improvement of the mechanical durability of micro porous layer in a proton exchange membrane fuel cell by elimination of surface cracks, *Renew. Energy.* 48 (2012) 35–41. doi:10.1016/j.renene.2012.04.011.
- [185] M. Ulsh, Fuel Cell MEA Manufacturing R & D, (2013) 1–29.
- [186] A. Pokhrel, M. El Hannach, F.P. Orfino, M. Dutta, E. Kjeang, Failure analysis of fuel cell electrodes using three-dimensional multi-length scale X-ray computed tomography, *J. Power Sources.* 329 (2016) 330–338. doi:10.1016/j.jpowsour.2016.08.092.
- [187] S. Kim, B.K. Ahn, M.M. Mench, Physical degradation of membrane electrode assemblies undergoing freeze/thaw cycling: Diffusion media effects, *J. Power Sources.* 179 (2008) 140–146. doi:10.1016/j.jpowsour.2007.12.114.

10 Appendix

10.1 Leak test

The basic leak test is performed at BOL, MOL and EOL to measure the total gas leakage rate from all the sources, i.e., each coolant, fuel and oxidant port, hydrogen cross-over. A schematic diagram (Figure 7.4) below shows the set-up for the H₂ cross-over circuit leak test. The same set-up and procedure are used to test for internal and external leaks. Once the MEA is assembled in FCAT cell, the leak test is performed by slowly pressurizing the fuel cell stack to 30psi using air as a source until it is locked automatically.

For the hydrogen crossover test, the hydrogen source is connected to the fuel inlet port while the fuel outlet is closed. Tubing is connected to the oxidant inlet and then submerged in a graduated cylinder. The oxidant outlet is sealed, while the coolant inlet and outlet are locked. The amount of leakage between the fuel and oxidant circuits is obtained by measuring the volume of bubbles collected in the inverted graduated cylinder. A leakage rate of 1 ml/min or less is tolerable to pass the test. For the internal and external leak tests, a soap solution is sprayed on each of the ports, connections, across the bipolar plates and MEA to locate the leak. The appearance of bubbles indicates a gas leak, which must then be addressed. The soap solution is also sprayed on the bipolar plates due to the possibility of a leak in the gaps between the plates. Measurement of H₂ gas crossover is regularly conducted (MOL) throughout the OCV-hold test experiment to make sure it does not exceed 2 ml/min. If this value is exceeded, the test is terminated and MEA is further tested *ex-situ* to identify defects such as thickness variations and pinhole spots. Table 1 shows the breakdown of the gas volumes measured during the internal and external leak tests in a case where the entire set-up is found to pass the leak test.

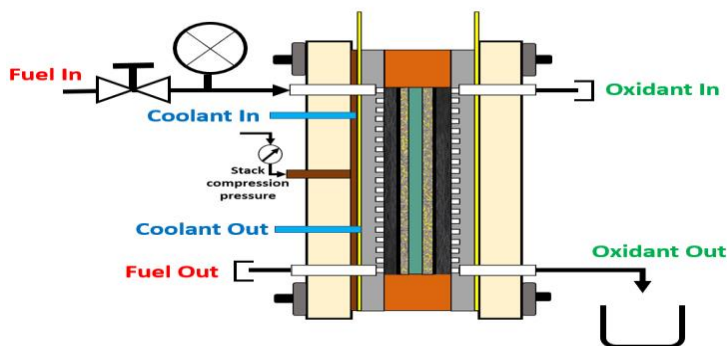


Figure 10-1: Fuel-to-oxide or hydrogen crossover leak test set-up.

10.2 MATLAB for Image Stitching:

1. Using MATLAB, run the function `[] = video(file, time, filename, ref)` where

file = the filename

time = the amount of time before taking a second image (around 15-18)

filename = the name of the images you want each image will be numbered automatically)

ref = when to start taking the images from the video (i.e. if the stage starts moving in 2 seconds, ref = 2)

1. Run file.
2. Save images to folder.
3. Open Image J.
4. Select Plugin → Stitching → Deprecated → Stich Grid of Images
5. Change grid size x to 1, grid size y to the number of images in the folder.
6. Select overlap percentage (5-8 is sufficient)
7. Select directory of the folder containing the images.
8. Change 'Filename' to the name of the images (ex. If image name is CCM_01.png, CCM_02.png etc., change file names to CCM_{ii}.png)
9. Change Output filename to desired name (ex. Video1.png)
10. Select "Create preview only"
11. Select OK.
12. Once preview shows up, if the image is fine, select Save As, select file format desired, and save image.
13. If final image is not desired, redo process but play around with the time in the MATLAB code, or change up the overlay percentage.
14. Repeat process for other videos.

Developed code for stitching

Matlab code for splitting the video (video direction going down)

```
function [] = video(file,time,filename,ref)
% This function takes the original video file and cuts the frames into
% images
% file = video name, time = how many seconds/frame to cut,
% filename = what name you want the images to be saved as
clc
v = VideoReader(file);
numberofframes = v.NumberofFrames; % number of frames in total
rate = v.FrameRate; % determines the number of frames per second
step = rate*time; % number of frames per desired time
frame = ref*rate;
num = 1;% image number
while frame <= numberofframes
    thisFrame = read(v, frame);
    image(thisFrame);
axis off
box off
```

```

set(gca,'position',[0 0 1 1],'units','normalized')
drawnow; % Force it to refresh the window.
Title = strcat(filename,'_');
if num < 10
    name = strcat('0',num2str(num));
    name = [Title num2str(name)];
else
    name = [Title num2str(num)];
end
print(name, '-dpng')%saves image into png format
frame = frame + step;
num = num +1;
end
end

```

Matlab code for splitting the video (video direction going up)

```

function [] = video3(file,time,filename,ref)
%This function takes the original video file and cuts the frames into
%images
% file = video name, time = how many seconds/frame to cut,
% filename = what name you want the images to be saved as
clc
v = VideoReader(file);
numberofframes = v.NumberofFrames; %number of frames in total
rate = v.FrameRate; %determines the number of frames per second
step = rate*time; %number of frames per desired time
frame = ref*rate;
num = 26;%image number
while frame <= numberofframes
    thisFrame = read(v, frame);
    image(thisFrame);
axis off
box off
set(gca,'position',[0 0 1 1],'units','normalized')
drawnow; % Force it to refresh the window.
Title = strcat(filename,'_');
if num < 10
    name = strcat('0',num2str(num));
    name = [Title num2str(name)];
else
    name = [Title num2str(num)];
end
print(name, '-dpng')%saves image into png format
frame = frame + step;

```

```

num = num - 1;
end
end

```

10.3 IR thermography of catalyst layer defects: CCM-2

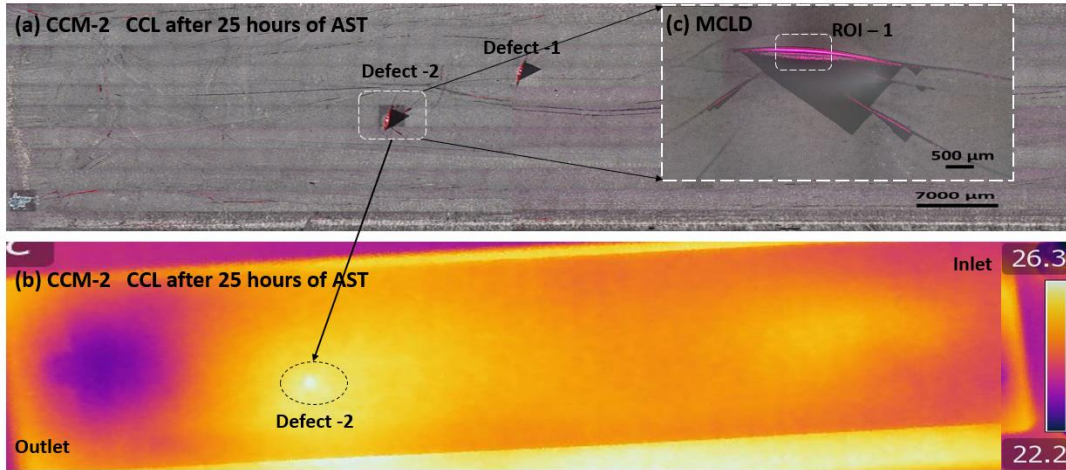


Figure 10-2: IR investigation of CCM-2 captured after 25 hour of AST: (a) digitally stitched microscopic image of CCL that has 2 MCLDs, (b) IR thermograph showing hotspot across defect-2 and (c) magnified view of defect-2.

10.4 COCV decay curves

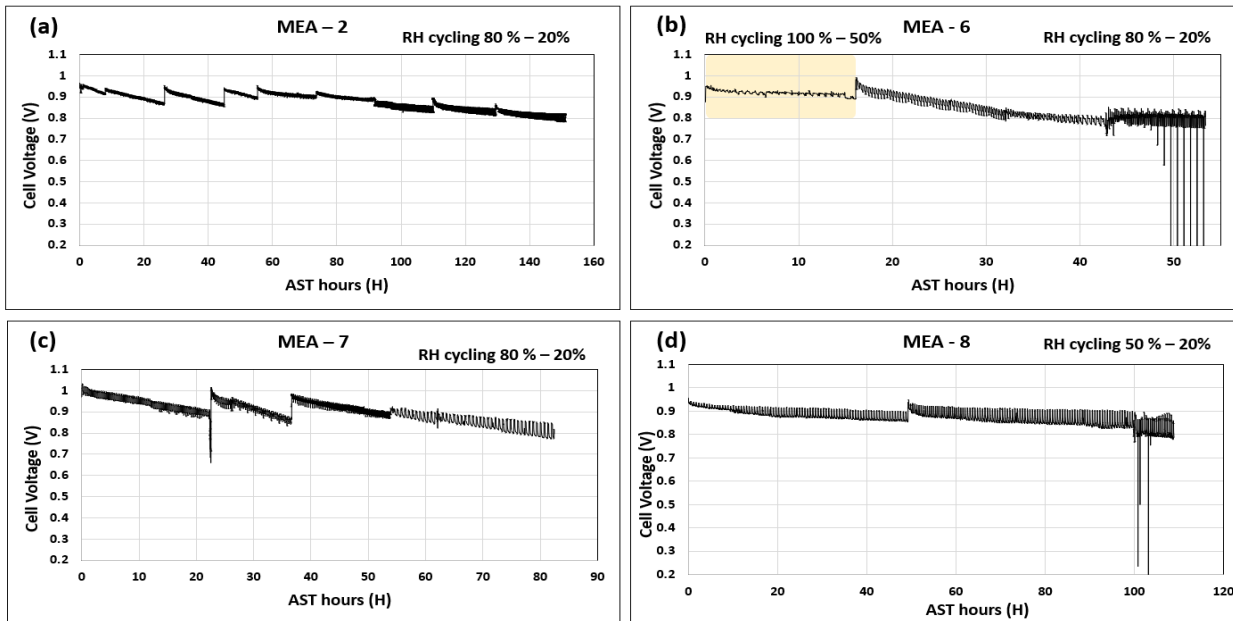


Figure 10-3: COCV decay curves recorded during RH cycling AST: (a) MEA-2 (b) MEA-6 (c) MEA-7 and (d) MEA-8

10.5 Overview of defect locations in CCM- CCL

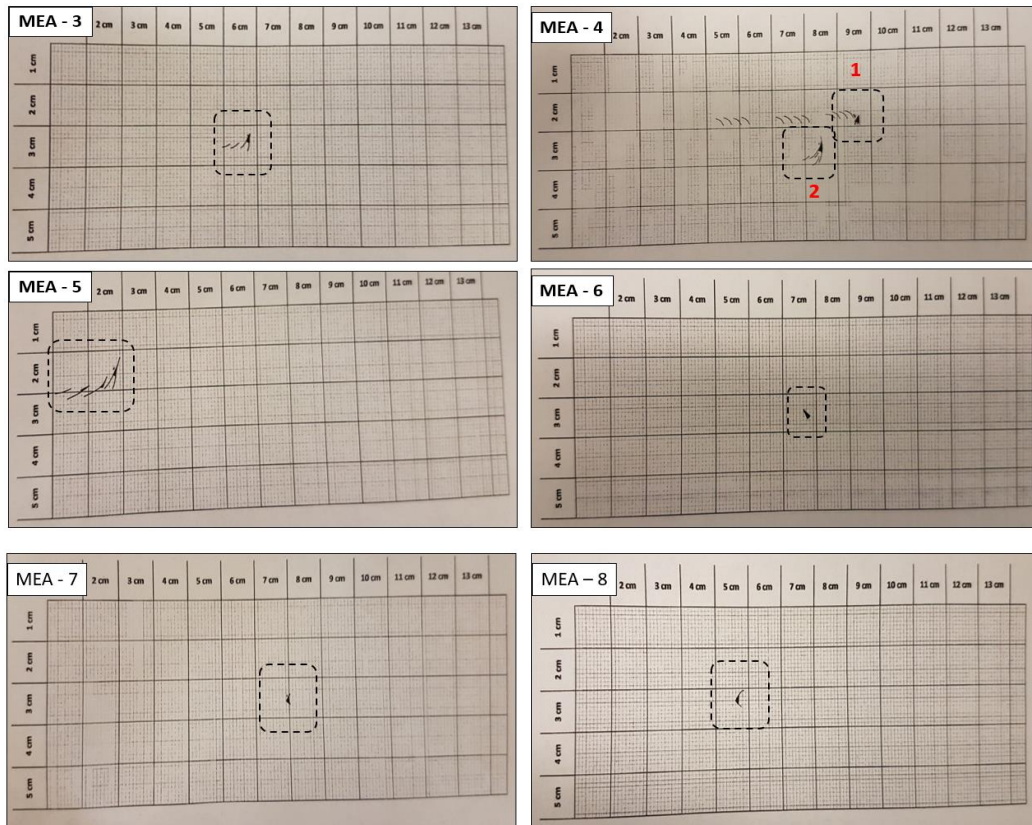


Figure 10-4: Graphical chart of CCM-used for MEAs (3 to 8), The rectangular box represents the approximate location of MCLDs on the CCL side of the CCM.

10.6 Scratch/deep cuts in catalyst layer – CCL

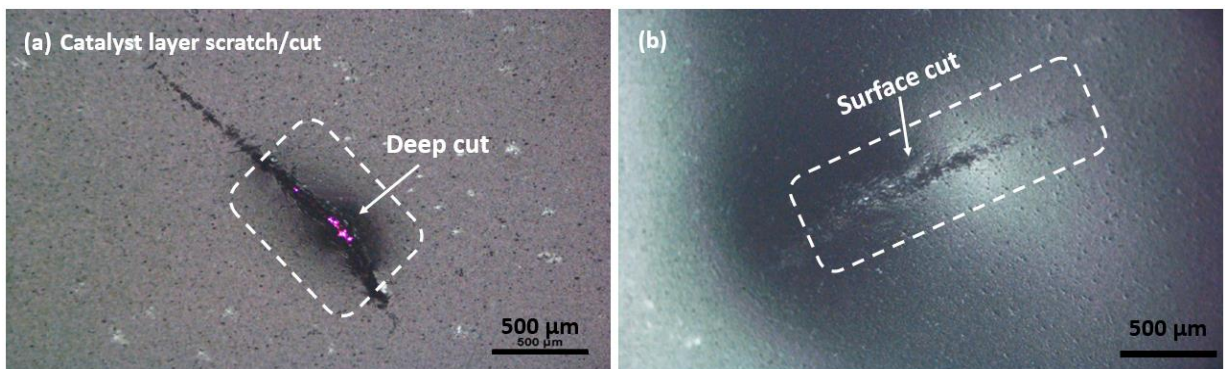


Figure 10-5: Microscopic image of scratches in the catalyst layers: (a) deep cuts and (b) surface cuts.

10.7 IR thermography set-up for GDL defect detection

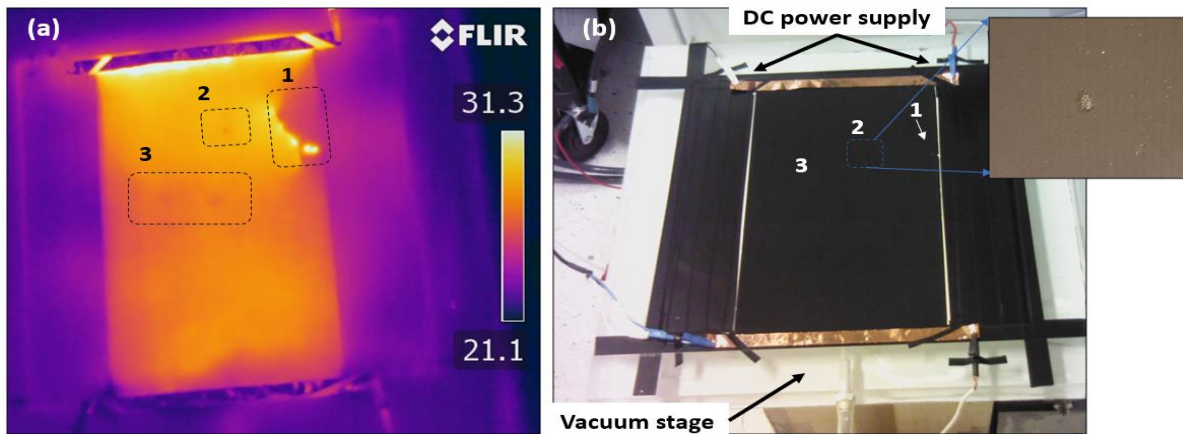


Figure 10-6: (a) Thermal response of defected GDL (30 cm X 20 cm), the corresponding digital image is shown in Figure (b), the magnified image represents the defect on the MPL (2 mm X 2 mm)

10.8 X-ray tomography of GDL-MPL substrates

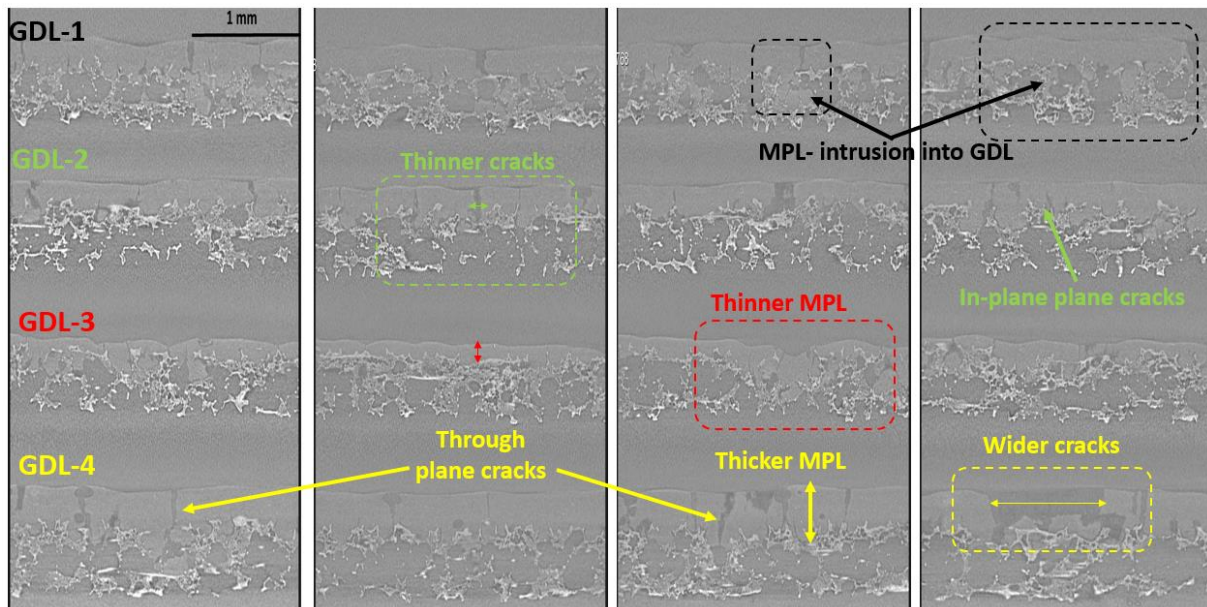


Figure 10-7: X-ray tomographic images showing variations in the MPL thickness and MPL cracks on the GDL substrate.